SERS-based Rapid Diagnostics for the Detection of Biomarkers associated with Sepsis

PhD Thesis

Emma O'Connor

Bionanotechnology
Department of Pure and Applied Chemistry
University of Strathclyde, Glasgow

December 23, 2020

This thesis is the result of the author's original research. It has been composed by the author and has not been previously submitted for examination which has led to the award of a degree.

Signed:

Date: 23/12/2020

Abstract

Worldwide, approximately 11 million people lose their lives to sepsis every year, primarily due to the condition being extremely difficult to diagnose. Therefore, early detection of sepsis is crucial for improved patient outcomes and lower mortality rates.

In this investigation, a surface enhanced Raman scattering or SERS-based rapid diagnostic platform was developed for the multiplexed detection of biomarkers associated with sepsis. Two biomarkers, C-reactive protein (CRP) and interleukin-6 (IL-6) were detected using a lateral flow immunoassay (LFIA) device combined with SERS-active gold nanoparticles. For CRP, a limit of detection (LOD) of 8 ng/mL was achieved using a portable, handheld Raman spectrometer and these results were comparable to using a benchtop microscope instrument. Additionally, the results showed that SERS was more sensitive than visible RGB analysis. The assay was also capable of semi-quantitative detection of CRP in spiked human plasma samples with a calculated LOD of 5.4 μg/mL using the handheld instrument. CRP concentrations exceeding 10 μg/mL are indicative of a disease state.

A LOD of 10.5 ng/mL was calculated for singleplex IL-6 detection. Multiplex detection of both CRP and IL-6 was also achieved on a single LFIA device using both spatially resolved and signal-resolved SERS analysis. The signal-resolved duplex detection assay, where handheld SERS analysis was performed on a single test region, was capable of quantitative detection of both biomarkers simultaneously and LODs of 7.5 ng/mL and 14.1 ng/mL were calculated for CRP and IL-6 respectively.

Additionally, the optimisation of a 3D microfluidic paper-based diagnostic, or μPAD, device for use with a SERS-based immunoassay was investigated. The flexible design of 3D μPADs offers excellent potential for multiplexing. Quantitative detection of CRP using this rapid diagnostic device was achieved however, the results showed the SERS-based LFIA was superior to the 3D μPAD for detection of CRP and IL-6.

Overall, this work has demonstrated the viability of a SERS-based LFIA rapid diagnostic, combined with a handheld Raman spectrometer, for the portable, multiplexed and fast detection of biomarkers associated with sepsis at the point-of-care.

Abbreviations

μPAD	Microfluidic paper-based analytical device
4-MBA	4-mercaptobenzoic acid
Ab	Antibody
AgNP	Silver nanoparticle
AuNP	Gold nanoparticle
AuNP-Ab	Gold nanoparticle conjugated to antibody
AuNP-Ab-CRP	Gold nanoparticle conjugated to CRP-specific antibody
AuNP-Ab-IL-6	Gold nanoparticle conjugated to IL-6-specific antibody
BSA	Bovine serum albumin
capAb	Capture antibody
CARS	Compensatory anti-inflammatory response syndrome
CFU	Colony forming units
CL	Chemiluminescence
CNS	Central nervous system
CRP	C-reactive protein
d.H_2O	water purified using Millipore Purification Systems
DAMPs	Damage-associated molecular patterns
DLS	Dynamic light scattering
DTNB	5,5’-dithio-bis(2-nitrobenzoic acid)
EDC	1-Ethyl-3-(3-dimethylaminopropyl)carbodiimide
EDTA	Ethylenediaminetetraacetic acid

ELISA	Enzyme-linked immunosorbent assay
Fab	Fragment antigen binding
Fc	Fragment crystallisable
FWHM	Full-width half-maximum
hCG	human chorionic gonadotropin
HRP	horseradish peroxidase
Ig	Immunoglobulin
IL	Interleukin
IL-6	Interleukin-6
LED	Light-emitting diode
LF	Lateral flow
LFIA	Lateral flow immunoassay
LOD	Limit of detection
LSPR	Localised surface plasmon resonance
MGITC	Malachite green isothiocyanate
MNP	Magnetic nanoparticle
NC	Nitrocellulose
NHS	*N*-hydroxysuccinimide
NP	Nanoparticle
PAMPs	Pathogen-associated molecular patterns
PBS	Phosphate buffered saline
qSOFA	Quick sequential organ failure assessment
RBITC	Rhodamine B isothiocyanate
RGB	Red green blue
RRS	Resonance Raman scattering
SERRS	Surface-enhanced resonance Raman scattering
SERS	Surface-enhanced Raman scattering
SIRS	Systemic inflammatory response syndrome
SOFA	Sequential organ failure assessment

SPR	Surface plasmon resonance
TMB	3,3’,5,5’-tetramethylbenzidine
TNF-α	Tumour necrosis factor-α
UV-vis	Ultraviolet-visible
WBC	White blood cell

Contents

List of Figures

List of Tables

Acknowledgements

Thank you to my supervisors, Karen Faulds and Duncan Graham. Thanks for your guidance, encouragement and honesty at every step. Whether it was speaking at a conference or mentoring a student, just knowing you thought I could do it, made me think I could.

Big thank you to Hayleigh and Stacey, you were there from the start and I always knew I could come to you for help and advice (and not just about science!). Thank you Will, not only for helping with chapter corrections but your sense of humour over chats with tea (or beer) kept me going over the last few months. Special thanks to Sian who got the bulk of this thesis to correct (sorry!). Your help and advice towards the end was invaluable. Thank you for running all of those human sample assays and most of all thank you for your positivity, encouragement and pep-talks in the Ark, you will be an amazing PhD supervisor one day!

Huge thanks to all members of Bionano that I had the pleasure to work with, both past and present. Thank you Anastasia and Fatima, your smiles kept me smiling even on the difficult days. Huge, big, special, infinite amounts of thanks to Kirsty, Jenny, Iona, Craig and Alex. There's not a hope I would've gotten to the end of this without you. You were there for it all; crying, complaining, drinking, singing and most importantly laughing. In you, I've found friends for life and I can't wait to get together again when this pandemic is over.

Trish, Paddy and Calum; there aren't words that I can use to express my thanks to you! You are family! From Fringegate and Marseille to that-week-in-Orkney-that-should've-been-Malta and the best craic wedding that ever has

been, I know we'll always help, support and make fun of one another (although you really should've told me about the fringe...)

Thank you Etienne, you are wonderful! Thank you for introducing me to the Scottish highlands, stinky but delicious cheese (Stinking Bishop EXCLUDED!), South Park and Still Game. I hope you know how much you helped with the final push to finish writing! You make me very happy.

Finally thank you to my parents, Frances and Noel (affectionately known as Froel) and sister, Gen. I couldn't have done most things in my life, least of all this, without your support, reassurance and love. Even with everything happening in the world today, you make me feel that in the end, everything will be ok.

1. Introduction

1.1 Sepsis

The definition of sepsis is constantly being contested and updated. Task forces of medical experts have been established to meet every few years to analyse data collected from around the world in an effort to understand the condition.[1] The most recent meeting, *'The Third International Consensus Definitions for Sepsis and Septic Shock'* which met in 2016 recommended the following updated definition -

> "Sepsis can be defined as life-threatening organ dysfunction caused by a dysregulated host response to infection."[1]

The ambiguity surrounding sepsis, its symptoms and how it can and should be diagnosed are the reasons for this continual amendment. Sepsis is the primary cause of death associated with infection worldwide and a recent study, with data collected over 27 years, indicated that global fatality figures are almost double those previously thought, with new figures indicating 11 million deaths annually can be attributed to sepsis.[2] The study provided a more accurate assessment by including newly collected data from outside the developed world.

In the UK alone, nearly 52,000 people lose their lives to sepsis every year; more than prostate, bowel and breast cancer combined.[3,4] Due to ambiguous symptoms and late-stage diagnosis, direct costs relating to sepsis treatment have been estimated to equate to £2 billion annually.[5] This significant loss of life coupled with the great financial strain on the NHS are some reasons why early diagnosis of sepsis is crucial. Unfortunately, there exists no clinical gold standard method for sepsis detection and diagnosis.

From the re-evaluation of sepsis definitions, there are generally regarded to be two "causes" of sepsis: non-infectious and infectious.[6] Non-infectious sepsis is misleading in that there is likely to be a primary infectious source, however, identification has proven difficult using clinical analysis such as blood culture. Indeed, blood culture is notorious for returning false negative results in the event of sepsis.[1,7] The symptoms of non-infectious sepsis are parallel to those presented during systemic inflammatory response syndrome or SIRS. This syndrome occurs as a normal immune response to inflammation but in the case of sepsis, hyper-inflammatory SIRS is prevalent in the early stages of the condition. Therefore non-infectious sepsis is hyper-inflammatory SIRS, clinically indicative of sepsis but with no identifiable infection present. Subsequent diagnosis of infection often occurs for non-infectious sepsis patients as the condition progresses to organ dysfunction and septic shock.[6]

Infectious sepsis is hyper-inflammatory SIRS with the identification of infection which, as mentioned, tends to be established at a later stage. Primary infection sources for sepsis are most commonly pulmonary infections with 64% of patients presenting with infections originating from the lungs. Abdominal (20%), bloodstream (15%) and genitourinary tract (14%) sources are also prevalent in sepsis patients.[6] Due to later stage identification of infection, organ dysfunction is evident as the initial exaggerated immune response has taken its toll on the body. In the next section, the pathogenesis of sepsis will be described with regards to hyper-inflammatory SIRS, the effect this has on organ and tissue dysfunction and what is likely to be occurring at a molecular level with respect to the release of cytokines and other pro- and anti-inflammatory processes.

1.1.1 Pathogenesis of Sepsis

1.1.1.1. Molecular and Cell Level Progression

Sepsis, whether it be "non-infectious" or "infectious", begins with the body's immune response to an invading pathogen.[6,7] The pathogen may be bacterial, viral or fungal and will express pathogen-associated molecular patterns or PAMPs upon invasion. These activate the innate immune system, where a range of immune cells *e.g.* macrophages, are capable of recognising PAMPs through toll-like receptors on their cell surface. Endotoxin, which is found in the cell wall of Gram-negative bacteria, is a good example of a PAMP that is targeted and "swallowed up" by macrophages. The toll-like receptors respond with the release of pro-inflammatory cytokines, predominantly tumour-necrosis factor α (TNF-α), interleukin-1 (IL-1) and interleukin-6 (IL-6). These enter the circulatory system inducing physical symptoms associated with SIRS such as fever and increased heart rate.[1,6]

Essentially, a "cytokine storm" triggers the release of acute phase proteins, such as C-reactive protein (CRP) in the liver, along with inflammatory, pro-oxidant and pro-coagulation lipids with the aim of controlling minor and localised infection.[1,6] In the case of SIRS and sepsis, the response goes beyond the normal threshold, evolving into an exaggerated, hyper-inflammatory response that is detrimental to the entire body.

1.1.1.2. Organ and Tissue Level Progression

With hyper-inflammatory SIRS inducing a cascade of complicated mechanisms in the body, the condition progresses causing major disruption of the cardiovascular system. This mainly manifests in the form of endothelial dysfunction where the inner lining or endothelium as shown in figure 1.1 (a), of arterial blood vessels is impaired. These effects include dysfunction of white blood cells *i.e.* leukocytes, which involves disrupting their response to infection and causing leukocyte adhesion.[6] Additionally, the barrier between the endothelium and the blood becomes defective resulting in tissue swelling and leakage of tissue fluids into the blood vessel *i.e.* tissue edema. Coagulation factors are also disrupted leading to procoagulation and the formation of blood clots which in turn cause dysregulated immunothrombosis and disseminated intravascular coagulation (DIC).[6] Figure 1.1 (b) highlights the events occurring in the vital organs; these processes have a profound effect on multiple organ dysfunction throughout the body.

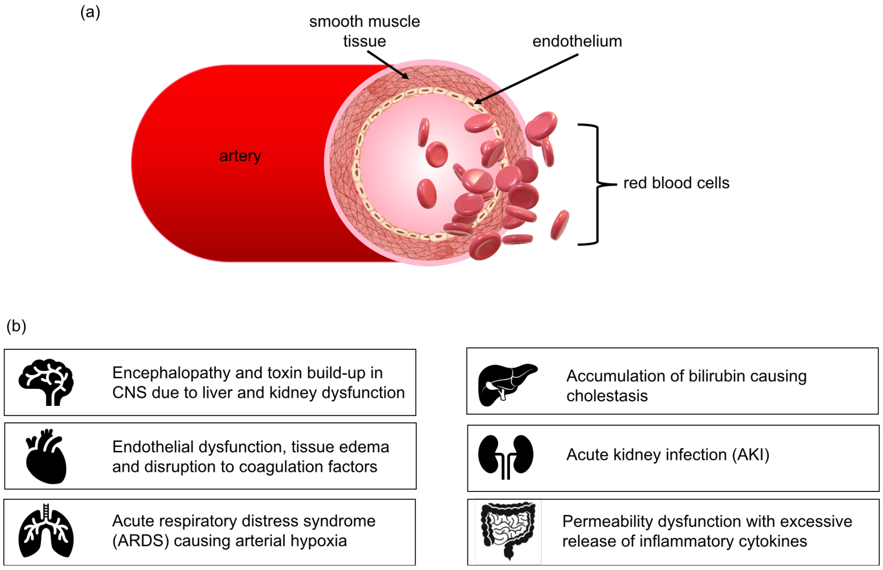

Figure 1.1: (a) Schematic representation of an artery showing the location of the endothelium, the lining between the arterial wall and the blood which experiences major dysfunction in the event of hyper-inflammatory SIRS and sepsis, (b) schematic highlighting the progression of sepsis through the organs (brain, cardiovascular system, lungs, liver, kidneys and intestines) and how these events contribute to multiple organ dysfunction and eventually septic shock. Schematics not to scale.

In the lungs, acute respiratory distress syndrome or ARDS results from reduced endothelial barrier function and tissue edema where fluid leaks into the alveoli causing arterial hypoxia. As a result, vital organs are deprived of necessary oxygen supply.[6] In the intestines, permeability dysfunction causes the rapid and excessive release of more cytokines, exacerbating systemic inflammation and further contributing to the dysfunction of multiple organs. Damage-associated molecular patterns (DAMPS) are also released as a result of organ and tissue injury, which elicit a response similar to PAMPS and add to the hyper-inflammatory response.[6]

In the liver, hepatic impairment leads to the accumulation of bilirubin resulting in cholestasis, which is the prevention of the flow of bile from the liver to the gut and consequently, excess bile begins to build-up in the body. While in the kidneys, acute kidney infection (AKI) is a commonly observed symptom of sepsis.[6]

The brain and central nervous system (CNS) are also affected and play their part in heightening the hyper-inflammatory response. Confusion, concentration-loss and delirium are all physical symptoms associated with sepsis. In the brain, enodthelial dysfunction and impaired function of the blood-brain barrier result in the brain being bombarded with inflammatory cells and cytokines, thus leading to problems with messages and signals being sent from the brain to other parts of the body. This contributes to inadequate blood flow to vital organs while kidney and liver dysfunction result in the CNS being exposed to a deluge of toxins.[6]

From this brief account of the hyper-inflammatory effects of SIRS and sepsis, it is clear that endothelial dysfunction is a major contributor to organ damage and ultimately, septic shock. Lactate levels have become a widely used indicator of organ dysfunction for sepsis as this molecule is usually processed in the liver. Therefore impairment of liver function leads to the presence of high lactate levels in the blood. For sepsis, concentrations greater than 2 mmol/L are indicative of organ dysfunction.[1]

1.1.1.3. Compensatory anti-inflammatory response syndrome (CARS)

The immune system at this stage is in a prolonged state of dysfunction and this includes a stage of compensatory anti-inflammatory response syndrome or CARS, a phenomenon first recognised by Dr Roger C Bone.[7] The initial exaggerated, hyper-inflammatory SIRS response has caused organ and tissue damage with the release of excessive amounts of pro-inflammatory cytokines, further exacerbating organ dysfunction. The immune system tries to resolve this amplified response with one that is hypo-inflammatory. It does this by releasing anti-inflammatory cytokines such as IL-10 which suppresses the function of pro-inflammatory IL-6 and neutralises TNF-α and IL-1.[6] During CARS, all of the damaged cells are cleared and PAMPs and DAMPs are removed.

These are all normal processes of the anti-inflammatory immune response. However, in the event of sepsis, the immune system has become so impaired and the organs so damaged from the initial hyper-inflammatory response, that CARS only serves to suppress the immune system further.[7] This affords opportunistic and latent pathogens the chance to infect the body. Therefore, sepsis patients are likely to fall victim to nosocomial infection and the invasion of resistant bacteria. In this way, sepsis is a self-reinforced condition.[6]

Septic shock is often described as the final event of sepsis and is defined as "a subset of sepsis in which underlying circulatory and cellular metabolism abnormalities are profound enough to substantially increase mortality"[1] At this stage, lactate levels have exceeded 2 mmol/L and this, combined with hypotension and a need for vasopressor therapy, are the variables used for the identification of septic shock.[1] Once the body goes into septic shock, the likelihood of recovery is extremely low and fatalities are attributed to multiple organ failure and the collapse of the cardiovascular system.[7]

1.1.2 Current Diagnostic Techniques

Rapid diagnosis is essential for sepsis. The condition can progress quickly to organ dysfunction and septic shock leading to much higher risk of mortality. In fact, chances of death increase by 6-10% every hour that sepsis is not diagnosed.[8] Healthcare workers rely on their own judgement coupled with sets of guidelines prepared by medical professionals for the quick diagnosis of sepsis.[1,9] Unfortunately, due to its ambiguous symptoms that overlap with many other medical conditions, sepsis remains notoriously difficult to diagnose.

In addition to this, no stand-alone, clinical, "gold standard" test exists for sepsis diagnosis. Health care professionals currently use scoring systems and symptom toolkits such as SIRS criteria checklists and the *Sequential Organ Failure Assessment (SOFA)* to diagnose sepsis in a hospital setting.[10] The Sepsis 6 Pathway is a set of treatment criteria subsequently used in cases where sepsis is strongly suspected.[11]

1.1.2.1. SIRS Criteria and the SOFA Score

Before the re-evaluation of sepsis in 2016, sepsis was diagnosed if there was evidence of infection with at least two symptoms of SIRS. The criteria for SIRS has been outlined as follows:[1]

- Temperature > 38°C or < 36°C
- Heart rate > 90 beats per min
- Respiratory rate > 20 breaths per min/arterial CO_2 pressure < 32 mm Hg
- WBC count $> 12 \text{ x } 10^9$/L or $< 4 \text{ x } 10^9$/L

If any two of these are presented by the patient and are accompanied by uncharacteristic confusion and drowsiness, then sepsis is strongly suspected and, even in the absence of an identified infection, treatment would be administered. However, the SOFA score is now more reliably used to diagnose sepsis by specifically identifying organ dysfunction. This scoring system has been used since its formulation in 1994.[12]

SOFA also uses physical and clinical symptoms as a way to diagnose sepsis. The higher the SOFA score, the higher the risk of mortality to the patient. Compared with the general hospital population, a SOFA score > 2 indicates a 10% greater risk of mortality.[10] The SOFA criteria are used to calculate a score between 0 - 24 points and are shown in figure 1.2.

It should be noted that lactate levels are also an important indicator of organ dysfunction and are used as a clinical sign of progression to septic shock

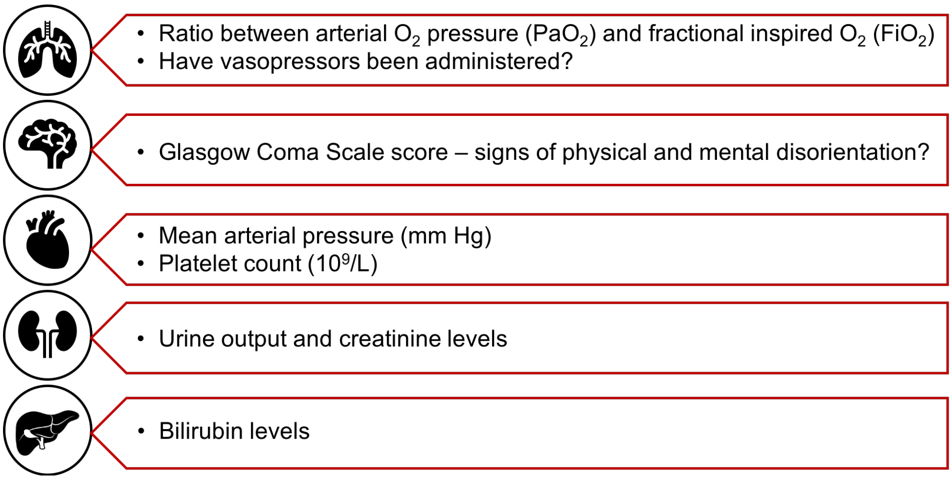

Figure 1.2: Physical and clinical symptoms used as part of the SOFA scoring system to determine the level of organ dysfunction and diagnose sepsis. The schematic shows how each of the criteria relate to the body's organ. A SOFA score of greater than 2 indicates an increased risk of mortality.[10]

when serum lactate concentrations exceed 2 mmol/L.[6] SOFA criteria includes many clinical, time-consuming tests that need to be carried out before further patient evaluation which is not ideal in a rapidly progressing condition like sepsis. Therefore a "quick" SOFA (qSOFA) has also been established, which incorporates physical symptoms only, to facilitate rapid assessment. The qSOFA looks at respiratory rate, mental status and systolic blood pressure. Even if the qSOFA score is low but sepsis is still suspected, the full SOFA will then be carried out to determine whether organ dysfunction is prevalent.[1,10]

1.1.2.2. Sepsis 6 Pathway

The Sepsis 6 Pathway is a guideline used for treatment of a patient who is strongly suspected of having sepsis due to symptoms of SIRS and following a SOFA score of greater than 2. The pathway is designed to be completed within one hour of diagnosis.[11] However, it includes two types of clinical tests that may cause delays in finding the best treatment for the patient, namely blood culture for identification of infection and serum lactate level detection. Crucially, blood culture is used to determine the type of infection which will ultimately establish the appropriate treatment. Lactate levels are also used to monitor the patient, another test where results may take hours or even days to return. Figure 1.3 outlines the 6 treatment steps as part of the pathway guideline.[11]

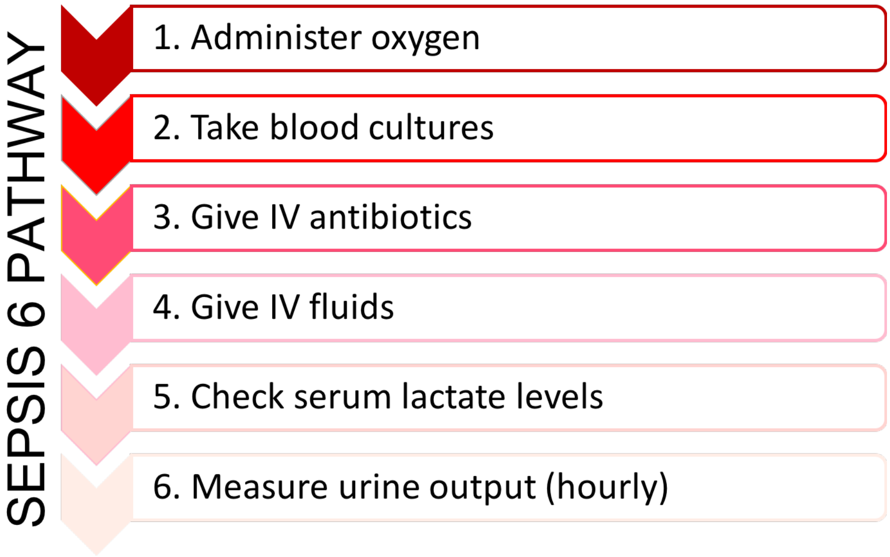

Figure 1.3: Chart showing the treatment steps taken once sepsis has been diagnosed using SIRS criteria and qSOFA/SOFA scoring system. The Sepsis 6 Pathway is a treatment guideline that must be performed within one hour of sepsis diagnosis.

It is clear from these assessment tools and guideline-based diagnosis methods that sepsis diagnosis can be extremely complicated. Additionally the condition is time-sensitive making it more difficult to treat. It should also be noted that in resource-limited settings, particularly in less developed countries, sepsis diagnosis would prove even more problematic. Sepsis can be easily treated for example with broad spectrum antibiotics or anti-viral drugs which makes early diagnosis key to successfully treating the condition.

Additionally, SIRS is not exclusively indicative of sepsis and initial symptoms of sepsis overlap greatly with several other conditions. Other factors concerning the patient also need ot be taken into account. Age, lifestyle, socio-economic status and any underlying illnesses will all effect how sepsis presents in the patient.[6]

High risk groups where the immune system is already somewhat suppressed, such as the elderly, infants and pregnant women, may initially present with different symptoms, contributing to the difficulty of diagnosing sepsis. Therefore a rapid diagnostic device capable of point-of-care sepsis diagnosis would be invaluable to decrease the risk of mortality in both a clinical setting and in the field.

1.1.3 Biomarkers

Biomarkers have gained interest in recent years as demonstrating diagnostic and prognostic value for several illnesses, including Alzheimer's and cardiovascular disease.[13] A biomarker is a molecule, protein or gene that can provide information about a persons health. Biomarkers can be diagnostic, prognostic or their levels can be used for monitoring a condition or a patient's response to a drug. Some biomarkers may be capable of all these things.[14] In the case of Alzheimer's Disease, 8 biomarkers have been identified as having diagnostic and prognostic value while for cardiovascular disease, 14 potential biomarkers have been recognised.[13] For sepsis, approximately 178 different biomarkers have been identified as being associated with the condition, none of which are specific to sepsis.[13] Therefore, for biomarker detection to be a viable method for sepsis diagnosis, a panel of biomarkers would have to be detected simultaneously in a rapid, multiplexed detection system, ideally providing aetiologic, diagnostic and prognostic information.

A few sepsis biomarkers have been mentioned already in previous sections. These include pro-inflammatory cytokines TNF-α, IL-1 and IL-6, acute phase protein CRP, organ dysfunction marker lactate and anti-inflammatory cytokine IL-10. Other biomarkers of interest include procalcitonin (PCT) which is linked to bacterial infection, soluble triggering receptor expressed on myeloid cells-1 (sTREM-1) associated with bacterial and funcgal infections, presepsin the levels of which rise in response to PAMP recognition, liposaccharide binding protein and CD64 a receptor expressed by immune cells in reponse to bacterial invasion.[15] The two biomarkers used in this study were CRP and IL-6, therefore only these will be described in detail in the following sections.

1.1.3.1. C-reactive Protein

CRP is an acute inflammatory protein discovered by Tillet and Francis in 1930.[16] It is an established biomarker of inflammation and has also demonstrated its value as a predictive biomarker of cardiovascular disease.[17–19] CRP production is upregulated by IL-6 in the liver during SIRS and its concentration has been observed to reach very high levels in the event of sepsis. The other SIRS-associated cytokines TNF-α and IL-1 also have an effect on CRP production but to a lesser extent.[20]

CRP has a pentameric structure with five identical subunits, non-covalently bound in a discoid figuration and lying in the same orientation around a central pore as shown in fig 1.4 (a).[20,21] Each subunit is made up of 206 amino acids and has a molecular mass of about 23 kDa. It is important to note that CRP exists in two isoforms, the pentameric form as mentioned but also a monomeric form where the five subunits have irreversibly dissociated. This can occur when Ca^{2+} ions are not present to stabilise the pentameric structure and in the presence of high concentrations of urea. The pentameric form of CRP was detected in this study as it has been observed to have a high serum concentration during infection. Some studies have shown CRP is also involved in inflammation and not just a marker of it.[20]

Healthy baseline CRP levels are considered to be below 3 μg/mL (mg/L) but can be dependent on factors such as age, gender and lifestyle *e.g.* weight and smoking status.[7,20,22] It is generally considered that levels greater than 10 μg/mL are indicative of a disease state while CRP concentration observed during sepsis can exceed 100 μg/mL.[13] Lower than normal levels of CRP can be indicative of acute liver injury.[23]

Clinical detection of CRP is routinely carried out using high sensitivity nephelometric assays, particularly if risk of cardiovascular disease is suspected in a patient.[20] Nephelometric assays are types of light scattering assays where scattered or reflected light from a sample is measured at an angle, usually 90° and are routine assays for detection of serum proteins. The assay takes approximately 15 - 20 mins to run and benefits from being able to detect a range of proteins quantitatively, although not simultaneously.[24] Therefore, it is a staple technique within clinical hospital labs. However, the results may take time to process when a lab is processing multiple patient samples, from multiple wards across an entire hospital. Enzyme-linked immunnoassays (ELISAs) has also been used for CRP detection but these are extremely time-consuming, taking up to a day to run, and use specialised equipment requiring handling by trained professionals.[24] Neither detection methods are capable of multiplexed detection.

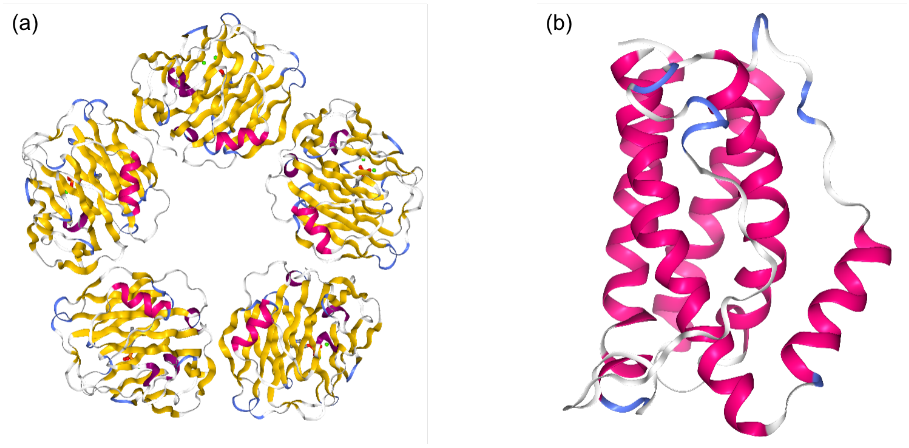

Figure 1.4: Protein structures for CRP and IL-6 biomarkers (a) CRP structure showing pentameric structure with 4 identical repeating units, CRP has a molecular weight of 150 kDa and (b) IL-6 structure showing 4-alpha-helix bundle. IL-6 has a molecular weight of 26 kDa.[25–27]

1.1.3.2. Interleukin-6

IL-6 is one of the three cytokines, along with TNF-α and IL-1, involved in the initial response of the innate immune system to infection or injury and, as mentioned, upregulates the production of CRP in the liver. It is released by immune cells like macrophages upon their interaction with PAMPs.[1,6,7] Neurons and neutrophils can also produce IL-6 in the event of inflammation.[28] IL-6 is from a family of cytokines composed of a long chain four-alpha-helix bundle (figure 1.4 (b)) with two non-identical epitopes identified for Ab binding.[28,29] Another name for IL-6 is "26 kDa protein".[30]

Baseline concentrations of IL-6 are below 5 pg/mL in healthy individuals and have been observed to be >500 pg/mL, sometimes exceeding 1 ng/mL, in the event of sepsis.[31,32] IL-6 is not currently used as a clinical biomarker and is difficult to detect as levels are so low in blood serum and plasma. Detection of IL-6 has gained particular attention recently as being an important biomarker for inflammation and infection. Unfortunately, like CRP, IL-6 is not specific to sepsis but has shown to have diagnostic and prognostic value for the condition.[7] The detection of both of these biomarkers as part of a multiplexed rapid diagnostic device would be of extreme value for point-of-care sepsis diagnosis.

Surface-enhanced Raman scattering or SERS is a very sensitive technique that has achieved single molecule detection.[33] Additionally, SERS is ideal for multiplexing. SERS is increasingly being used for the sensitive detection and quantification of biomarkers associated with disease. Rong *et al.* recently demonstrated detection of limits of 0.01 ng/mL for CRP using SERS combined with a lateral flow immunoassay. while Wang *et al.* reached 5 pg/mL limits for IL-6 in whole blood using a similar method.[34,35] Duplex detection of these biomarkers would be an encouraging preliminary step towards a multiplexed detection system. Raman scattering and SERS are explained in more detail in the following sections.

1.2 Raman Scattering

Raman scattering is named after Sir Chandrasekhara Venkata Raman. During a journey across the Mediterranean in 1921, Raman debunked Lord Rayleigh's theory that the sea was blue simply because it reflected the sky. Using a Nicol prism to filter out the light from the sun, Raman observed the clarity of the blue colour to be greatly improved which suggested the colour of the sea was itself a distinct phenomenon. Later, his student, K. R. Ramanathan, found that after sunlight was filtered through a violet glass and passed through purified water and certain alcohols, the scattered light contained wavelengths of light that were not present in the incident beam. After years of work, Raman and his students finally published their findings in 1928 and the concept of Raman scattering was born. Raman scattering however is an extremely weak effect, which is why Ramanathan originally referred to it as "weak fluorescence."[36]

When light interacts with a molecule, a number of processes can occur. The light can be absorbed and emitted by the molecule, it can be transmitted *i.e.* pass straight through the molecule or it can be scattered. Most light will undergo Rayleigh scattering which is an elastic process. This means there is no energy transfer between the incident light and the molecule and the scattered light is the same energy, frequency and wavelength as the incident light. Figure 1.5 shows this process on a Jablonski diagram where a molecule is excited to a virtual energy state representing the distortion of the electron cloud of the molecule by incident light of energy $h\nu_0$. No energy is lost during the interaction and the light scattered by the molecule is equal in energy to the incident beam.

Raman scattering is much less probable than Rayleigh scattering and is an inherently weak effect, occurring only in 1 in 10^6 instances. Raman scattering occurs when there is an energy transfer between the molecule and the incident light *i.e.* inelastic scattering. When incident light interacts with a molecule, it distorts the electron cloud, as in Rayleigh scattering. However, during Raman scattering, this distortion is accompanied by the simultaneous movement of nuclei. The electron cloud relaxes back into its original state much faster than the nuclei resulting in scattered light different in energy to that of the incident beam.

Two types of Raman scattering exist - Stokes and anti-Stokes. In Stokes Raman scattering the molecule is in the ground state and the scattered light is *lower* in energy compared with the incident light while for anti-Stokes Raman

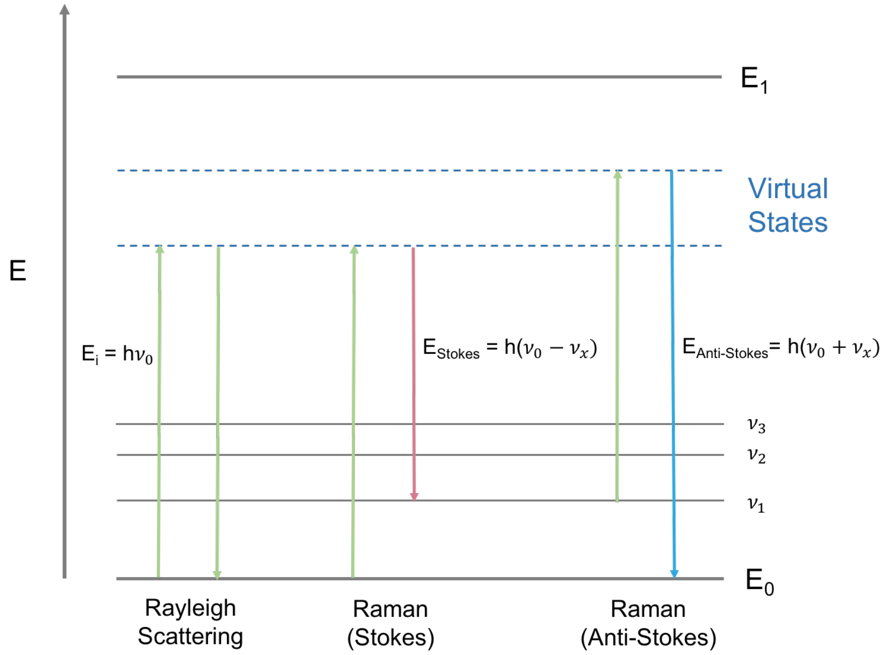

Figure 1.5: Jablonski diagram representing Rayleigh and both types of Raman scattering - Stokes and anti-Stokes. The virtual state is an "imaginary" energy state that represents the energy of the incident light and is the point at which the molecule becomes polarised. E_0 and E_1 are the energies of the ground and first excited electronic state, $h\nu_0$ is the energy of the incident light and $h\nu_x$ is an arbitrary energy equivalent to one vibrational energy unit. As shown in the diagram, in Stokes Raman scattering energy is transferred from the incident photon to the molecule and the scattered light is *lower* in energy than the incident light while anti-Stokes scattering happens when a molecule is already in an excited state, therefore energy is transferred to the incident photon from the molecule resulting in scattered light *higher* in energy than that of the incident beam. In Rayleigh scattering, there is no energy transfer and the scattered light is the same energy as the incident beam, the majority of light is scattered in this way.

scattering, the molecule is already in an excited state. This means the light scattered is *higher* in energy compared with the incident beam. Both processes are represented in the Jablonski diagram in figure 1.5.

Stokes and anti-Stokes Raman scattering are described as a shift in energy from the laser excitation energy, this shift is the difference in energy between the incident and scattered light. Stokes Raman scattering is more intense than anti-Stokes Raman scattering as it has a higher probability of occurring at room temperature. As temperature increases, so anti-Stokes intensity increases. This can be explained using the Boltzmann Distribution:

$$\frac{N_1}{N_0} = \frac{g_1}{g_0} exp(\frac{(-\Delta E)}{kT}) \tag{1.1}$$

where N_1 is the population of molecules in the first excited state, N_0 is the population of the ground state, g_1/g_0 represents the degeneracy of the states, ΔE is the difference in energy between the ground and excited state (in Raman scattering this is equivalent to one vibrational unit), k is Boltzmanns constant and T is temperature in Kelvin. At lower T *e.g.* room temperature, the majority of molecules will remain in the ground state making Stokes Raman more likely. Raman spectroscopy therefore, mostly deals with only this effect.[37]

Intense Raman scattering occurs when there is a large change in polarisabilty of the molecule. This means symmetrical molecular vibrations will result in strong Raman scattering as the distortion of the electron cloud will cause a large change in polarisabilty which induces a dipole moment in the molecule. Equation 1.2 describes the relationship between polarisability and the induced dipole with respect to the electric field of the incident light:

$$\mu = \alpha E \tag{1.2}$$

where μ is the induced dipole, α is the polarisablity of the molecule and E is the incident light.[37] The virtual state, as shown in figure 1.5, is related to the distortion of the electron cloud and is equal in energy to the incident light. It is a short-lived state that does not exist for the static molecule but is a real state of the distorted molecule where the nuclei have not had time to reach equilibrium.[37] Therefore, a change in polarisability is essential for Raman scattering and each molecule has its own unique Raman spectrum, often deemed a “molecular fingerprint”. One of the main limitations of conventional Raman spectroscopy is signal strength.[37] Therefore, many approaches have emerged with the aim of enhancing the Raman effect.

1.2.1 Enhancing the Raman Effect

The enhancement of Raman scattering is vital for improving signal sensitivity as a detection method. The intensity of Raman scattering is described in the equation 1.3:

$$I = KI_{\mathrm{L}}\alpha^2\nu^4 \tag{1.3}$$

where I is Raman intensity, K is a constant containing the speed of light, I_{L} is the laser intensity, α is the polarizability of the molecule and ν is the frequency of the laser. As shown in the equation, Raman intensity has a fourth-power dependence on the excitation frequency, ν, a factor that can be easily controlled.[37]

However, increasing the energy of the laser may have a detrimental effect depending on the sample being analysed. This is of particular importance when analysing biological samples where shorter wavelength (higher energy) electromagnetic radiation could lead to damage or destruction of the sample via photodegradation. Competing processes such as absorption and fluorescence also need to be taken into account where large background noise can result in loss of information from the Raman signal. The following sections describe other techniques that exist for signal enhancement from Raman scattering.

1.2.2 Resonance Raman Scattering

For resonance Raman scattering (RRS), the excitation wavelength is chosen to coincide with an electronic absorption band of the molecule. Both scattering and absorption will occur, with the absorption process contributing to an enhancement in Raman scattering. However, this effect is only possible with certain molecules which contain chromophores. These are coloured species with a high level of conjugation *i.e.* alternating carbon-carbon double bonds in their molecular structure.[37]

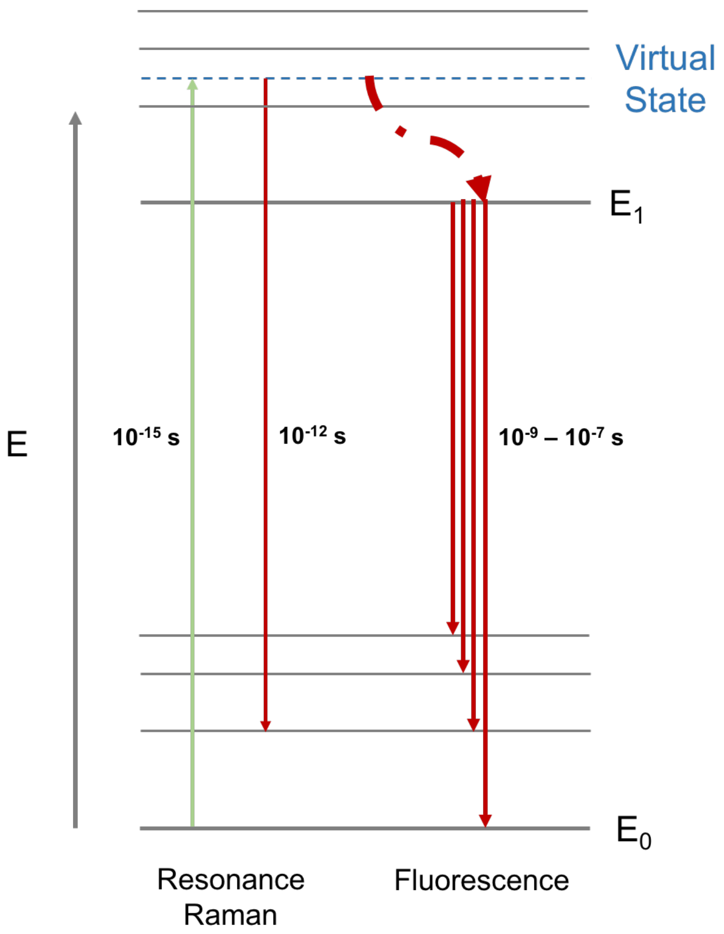

Figure 1.6: Jablonski diagram showing RRS versus fluorescence. When the excitation wavelength overlaps with the absorption wavelength of the molecule, both absorption and scattering occur. Due to the difference in timescales between the two processes, it is possible to detect only the the RRS signal and eliminate some of the fluorescence signal.

In this instance, Raman scattering can be differentiated from the combination of absorption and scattering due to the timescales of the different processes. Absorption and subsequent emission of light happen slowly compared with scattering. For absorption, the nuclei need to relax into the equilibrium geometry of the excited state before emission can occur. This is not required for Raman scattering which is essentially instantaneous, happening on a picosecond scale.[37]

Figure 1.6 compares the two processes with the aid of a Jablonski diagram. Enhancements of up to 10^6 in signal intensity have been reported for using RRS which has also proven to be more sensitive than conventional Raman scattering.

1.2.3 Surface Enhanced Raman Scattering

Surface enhanced Raman scatering (SERS) uses a roughened metallic surface to achieve Raman signal enhancements in the range of 10^6 to 10^8.[37,38] The phenomenon was first demonstrated by Fleischmann *et al.* in 1974 when investigating Raman scattering of pyridine.[37,38] The researchers found that the Raman signal for pyridine was greatly enhanced when the molecule was in close proximity to a roughened silver electrode. It is generally accepted that two effects combine to contribute to the surface enhancement: an electromagnetic effect and a chemical effect. Both the interaction of the incident light with the roughened metal surface and the molecule are important for signal enhancement.

1.2.3.1. Electromagnetic Effect

Metals on the nanoscale behave differently compared with their bulk counterparts in that they have loosely bound conduction electrons which are free to move along the surface of the metal. For roughened metal nanostructures, particularly thin films, this feature can be exploited for SERS by the generation of surface plasmon resonance (SPR). When the conduction electrons are excited by a laser, they delocalise across the surface of the metal film, travelling parallel to the interface between the metallic surface and the surrounding medium. The electrons propagate in such a way that they oscillate coherently with the incident laser wavelength and surface plasmon resonance occurs.[39,40]

Figure 1.7 depicts surface plasmon resonance of a roughened metal thin film and its effect on pyridine adsorbed to the surface. The electric component of the incident laser light, E_0 becomes enhanced by localising on the surface of the metal while retaining its initial frequency, ω_0. This localised electric field, E_{loc} can radiate both parallel and perpendicular to the surface and therefore the plasmons can scatter parallel and perpendicular, by travelling along the peaks and valleys of the roughened surface.[37,39] A molecule in close proximity to the metal surface *e.g.* pyridine can interact with the E_{loc}, resulting in a shift in frequency (ω_{vib}) of the scattered light from the incident light *i.e.* Stokes Raman scattering, ω_0 - ω_{vib}.[39]

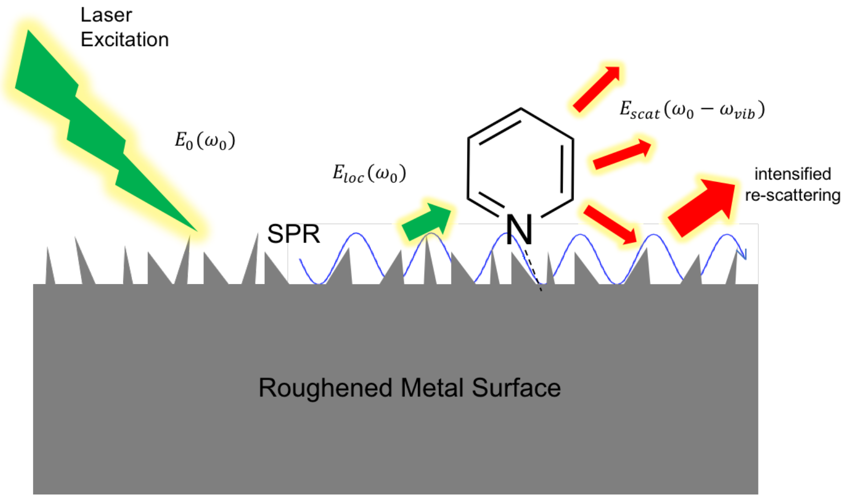

Figure 1.7: SERS electromagnetic enhancement of the Raman signal for molecule, pyridine which is only possible when the molecule is in close proximity to a roughened metal surface as shown. SPR is generated on the metal surface by incident laser light and due to the roughness of the surface, the plasmons can travel both along the surface and upwards and downwards along the peaks. This means they interact with pyridine resulting in an intensified Raman signal of the molecule. Re-scattering an also occur further contributing to the SERS signal.

An intensified Raman signal is generated for the molecule of interest. Secondary to this, scattered light from the molecule can again interact with E_{loc} on the metal surface and re-scatter, providing further signal enhancement. This is especially prevalent for areas of hotspots *i.e.* areas where the electromagnetic effect is high, for example when the molecule is located on the tip of a peak or in the valley between peaks. Silver and gold nanoparticles are particularly useful substrates in SERS measurements as their SPR peak lies in the visible region. Localised surface plasmon resonance (LSPR) can be generated using silver and gold nanoparticles and will be described in section 1.3.1.2. Electromagnetic enhancement is the dominant effect in SERS and signal enhancements of 10^2 to 10^8 have been observed for this effect.[39]

1.2.3.2. Chemical Effect and Charge Transfer

The chemical effect is considered a minor contributor to SERS with enhancements of 10^3 being reported.[38,39] This effect centres around the molecule adsorbed to the metal surface. For adsorption to occur, a type of bond must exist between the molecule and the surface which opens a two-way channel facilitating the transfer of charge. The interaction between the metal and the molecule may also change its intrinsic electronic structure by the formation of new electronic states. These states may differ from the unbound molecule in that they are closer in resonance to the excitation wavelength and upon interrogation with a laser, can transfer energy back into the metal further enhancing E_{loc}.

The existence of both effects is generally accepted and electromagnetic enhancement is thought to have a greater contribution to SERS.

1.2.4 Surface Enhanced Resonance Raman Scattering

Surface enhanced resonance Raman scattering (SERRS) combines SERS and RRS to give a technique which is highly sensitive and specific. It has several advantages over SERS including signal enhancements observed to be as high as 10^{14}. Therefore, it can achieve greater sensitivity, requires less powerful laser excitation and shorter interrogation times.[37,41] SERRS requires the presence of a chromophoric molecule (described in section 1.2.2) on the surface of the metal. When the excitation wavelength, the absorption maximum of the molecule and the frequency of the SPR peak of the metallic surface all coincide, molecular resonance enhancement compliments surface enhancement giving an intense SERRS signal unique to the molecule. The metal surface also acts as a quencher for any fluorescence from the dye molecule, widening the choice of dyes that can be used for SERRS to include commercially available chromophores. Contaminants are less significant in SERRS compared with SERS as dye molecules will be selectively enhanced over others present on the surface of the metal. If multiple dyes, each with a specific signal, are used in a detection assay to code for an array of different analytes, simultaneous, multiplexed detection that is specific and sensitive, can be achieved.[37]

1.3 Nanoparticles

Colloidal suspensions of "ruby" gold nanoparticles were investigated by Michael Faraday in 1857 when he studied their unique optical and electronic properties.[42] However, nanoparticles have been used for centuries particularly in the creation of art works. Metal nanoparticles have proved valuable for use as SERS substrates and their properties, synthesis and use with SERS/SERRS will be described in the following sections.

1.3.1 Nanoparticles as SERS substrates

As previously discussed, a roughened metal surface is the base requirement for SERS. Metal nanoparticles, particularly silver and gold, can act as appropriate substrates for intensified Raman scattering. This is largely due to their unique optical properties; both gold and silver nanoparticles have extinction maxima in the visible region of the electromagnetic spectrum and benefit from the generation of localised surface plasmon resonance (LSPR) upon laser excitation of a particular wavelength. These characteristics along with facile synthesis methods, good stability and ease of functionalisation with analyte and Raman dye molecules, means gold and silver nanoparticles are excellent substrates for SERS and SERRS.[43]

1.3.1.1. Optical Properties of Gold and Silver Nanoparticles

Plasmonic nanoparticles like gold and silver differ from other non-metallic nanomaterials due to their photophysical response. Gold nanoparticles (AuNPs) and silver nanoparticles (AgNPs) have vastly different chemical and physical properties compared with their bulk materials.[40] It is their unique optical properties, governed by their size and shape, that make them particularly valuable for nanotechnology, bionanotechnology and nanomedicine.[44] Nanoparticles are defined as materials with one dimension lying between 1 to 100 nm and can be synthesized in numerous different shapes from spherical or triangular to star shaped and rod-like.[45]

Figure 1.8 (a) shows colloidal suspensions of AuNPs increasing in size from 16 nm (deep red) to 100 nm (blue).[46] Smaller AuNPs appear red in colour because they absorb light at approximately 520 nm *i.e.* green light (figure 1.8 (b)) therefore the AuNPs appear red. AgNPs however, have an extinction maximum of approximately 400 nm meaning they appear yellow/green in colour and absorb blue light.

The existence of AuNPs and AgNPs can be found to date as far back as 4th century A.D. when the Lycurgus Cup is thought to have been fabricated. The glass part of the cup is dichroic *i.e.* it appears a different colour depending on whether it is reflecting or transmitting white light.[47] Figure 1.8 (c) shows the cup in both incidences; the glass appears green when white light is reflected from the exterior and red when white light is transmitted from the interior. This effect is caused by the scattering of light due to the presence of colloidal gold and silver suspended in the matrix of the glass; AgNPs being responsible for the green colour and AuNPs for the red. The Lycurgus cup is an iconic example of the extraordinary optical properties of both AuNPs and AgNPs.[47] It is believed the makers of the cup may never have intended for this phenomenon to be expressed in their final work and the unique interaction of the glass with light may be nothing more than an accidental phenomenon.

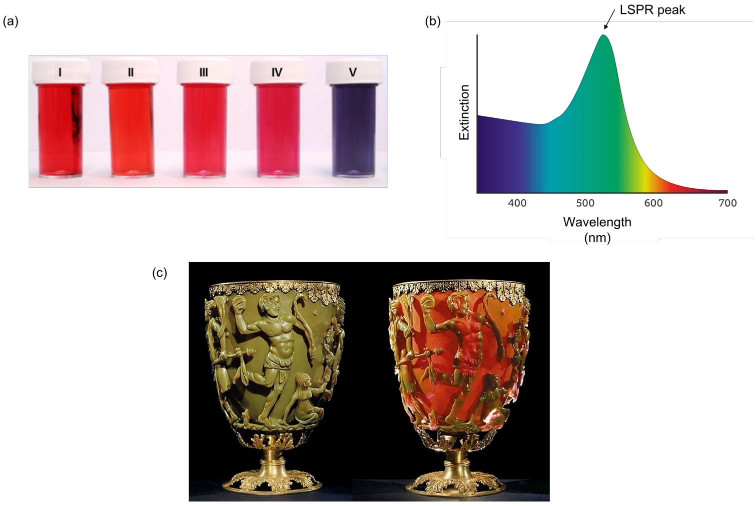

Figure 1.8: (a) AuNPs of different sizes prepared using Turkevich/Frens citrate reduction method with the following LSPR peak positions - 521 nm (I), 528 nm (II), 531 nm (III), 541 nm (IV) and 553 nm (V) indicative of increasing sizes of 16 - 100 nm of the AuNPs[46], (b) typical extinction spectrum for AuNPs with LSPR peak at approximately 520 nm showing green light is absorbed and therefore the particles appear red and (c) the iconic Lycurgus Cup. The image on the left shows green light is reflected from the outside of the cup due to scattering from silver nanoparticles while the image on the right shows the transmission of red light from inside the cup due to scattering from gold nanoparticles.[47]

1.3.1.2. Localised Surface Plasmon Resonance

The photophysical response of AuNPs and AgNPs can be attributed to their surface plasmons. Similar to SPR for thin films, localised surface plasmon resonance (LSPR) is the collective and coherent oscillation of conduction electrons across the surface of the metal following laser excitation. At a particular wavelength of incident light, the electrons reach a maximum oscillation frequency that is resonant with the laser light, the frequency at which the SPR peak for the metal is observed. Due to the confinement of the electromagnetic field by the nanoparticle, a separation of charge density is generated in the same direction as the electric field leading to light being absorbed and strongly scattered by the metal surface. Figure 1.9 represents this phenomenon showing the dipolar nature of the oscillation. Both the electromagnetic and chemical effects described for SPR are also a feature in LSPR.

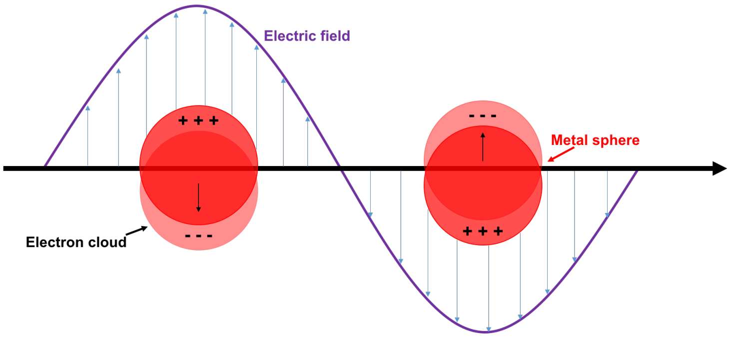

Figure 1.9: Localised surface plasmon resonance in a metal nanosphere. Electrons oscillate collectively across the surface of the nanosphere at the same frequency as the incident light generating a localised electric field confined by the dimensions of the sphere, resulting in absorption and scattering of light.

1.3.2 Nanoparticle Synthesis

The exact mechanisms which govern the formation of nanoparticles remain somewhat elusive. In addition to this, monitoring of these processes is instrumentally challenging as formation happens on an extremely small scale. It is generally accepted that nanoparticles form in three stages: nucleation, aggregation and growth. Nanoparticles typically exist in a solution phase as a homogenous dispersion of particles known as a colloidal solution. The nanoparticles are buffeted through the solution via Brownian motion where electric charges on their surface cause them to repel one another, thereby keeping them suspended in solution.

The most commonly used synthesis for AuNPs is the Turkevish-Frens method where chloroauric acid $H(AuCl_4)$ is commonly used with sodium citrate as a mild reductant.[48,49] The citrate also acts as a stabilising agent, coating the surface of the AuNPs with negatively charged citrate ions. By varying the ratios of $HAuCl_4$ and citrate used, AuNPs in a range of sizes can be synthesised.

Figure 1.10 shows a graphical representation of AuNP formation with respect to time. The reaction is a redox reaction between a metal precursor ($HAuCl_4$) and a reducing agent (sodium citrate). Under heated conditions and vigorous,

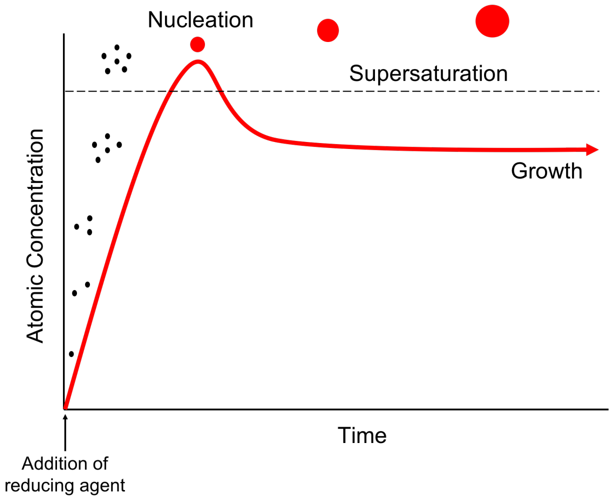

Figure 1.10: Schematic representation of AuNP formation showing the three stages associated with the phenomenon - nucleation, aggregation and growth. Au^0 concentration increases, reaching supersaturation and inducing rapid aggregation Au atomic clusters. As Au^0 concentration falls below the level of supersaturation, the growth stage begins where seeds generate nuclei formation but at a much slower rate. Once Au clusters reach a critical size, growth becomes unfavourable and the clusters begin to take on more defined shapes.[45]

continuous stirring, the sodium citrate is added to a $HAuCl_4$ solution. Oxidisation of sodium citrate to acetone dicarboxylic acid occurs, which complexes with Au^{3+} ions. The concentration of Au^{3+} rapidly decreases as zero-valent atomic gold (Au^0) is formed. As Au^0 concentration increases, it reaches a level of supersaturation, driving the formation of small clusters of Au atoms known as nuclei *i.e.* nucleation.[45] The nuclei collide, initiating the second stage of nanoparticle formation via a "rapid aggregation effect" resulting in the formation of seeds. Au^0 concentration quickly declines below the level of supersaturation and the growth step begins as seeds promote further nuclei formation but at a much slower rate. A critical size is reached beyond which further growth becomes energetically unfavourable. At this stage, the particles begin to take on more defined shapes. There is a very fast final growth step involving coagulation of smaller particles. When all the gold precursor has been used up, the process stops.[45] However, nanoparticle formation is non-linear and all three stages are happening simultaneously in the reaction solution.

Other methods of AuNPs synthesis include the Brust-Schiffrin method developed in 1994 which involves phase-transfer of $AuCl_4$ solution from toluene to water using $NaBH_4$ as a reducing agent.[50] Seeded growth and electrochemical synthesis methods have also been reported and recently "green syntheses" have been investigated in an effort to develop non-toxic and environmentally friendly synthesis methods using biological materials like enzymes and plant extracts.[51]

1.3.3 Nanoparticles and Antibodies

Functionalisation of the surface of nanoparticles with antibodies (Abs) has been a large focus in the field of biotechnology for biosensing applications.[38,52,53] Nanoparticles and Abs can have a symbiotic relationship when combined as a single entity.[53] This is especially true for AuNPs as they are considered to be biocompatible and their surfaces are easily functionalised. However, the conjugation process is not a trivial one and Abs need very specific conditions to attach to the surface of AuNPs.

Structurally, Abs are complex and differ from class to class. They are also called "immunoglobulins" and are a type of glycoprotein vital to the body's immune response. There are 5 different Ab classes - IgG, IgA, IgM, IgE and IgD, each of varying structure, which ultimately determines their functionality.[53] Figure 1.11 shows the structure of an IgG Ab, shaped like the letter "Y", which is the most abundant type of immunoglobulin, making up approximately 75% of all Abs in the body. Its function is greatly associated with long term immunity after infection or vaccination.[54]

As shown in figure 1.11, the IgG Ab consists of two heavy chains and two light chains. The heavy chains are connected at the hinge region by disulfide bridges. Each heavy chain is divided into several regions; one variable region and 3-4 constant regions joined together by intrachain disulfides with both chains connected at the hinge region by disulfide bridges. Disulfide bridges also connect

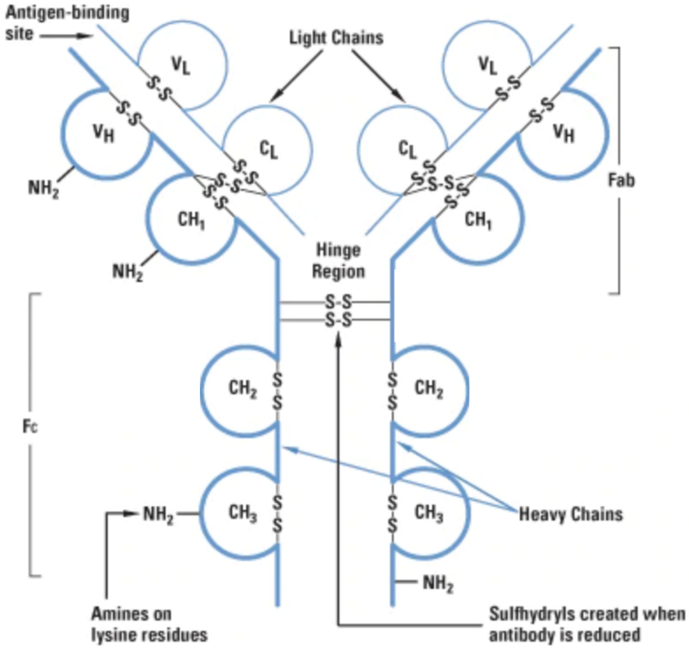

Figure 1.11: General structure of IgG antibody showing the light and heavy chains, Fab and Fc fragments. Regions marked with a "C" indicate constant regions of the structure common to all IgG Abs while "V" represents variable regions that are responsible for the specificity between different types of Abs and the antigen-binding region of the Ab. IgG Abs are covered in amino groups from lysine residues on their surface which can be used as targets for conjugation with AuNPs. Picture adapted from ThermoFisher - Chemistry of Crosslinking.[55]

the heavy and light chains, each light chain possesses one variable region and one constant region joined by intrachain disulfides. The antigen binding site is comprised of the variable regions from each chain. The Ab can be separated into two parts - the antigen recognition part or Fab fragment and the Fc fragment. The Fab fragment determines the Abs specificity and varies from Ab to Ab.[53,56] The antigen-binding regions or paratopes are located at the end of each of the "arms" of the Y-shape and there are two identical regions per Ab capable of binding two antigen species.

Amino groups are present on lysine residues covering the Ab and these are good targets for methods of functionalisation to AuNPs. Two methods are commonly used for Ab functionalisation - covalent attachment and passive adsorption.[56]

1.3.3.1. Covalent Attachment

The most frequently used covalent linkage method for the attachment of Abs to AuNPs is carbodiimide cross-coupling chemistry or EDC/NHS coupling. One such method involves the use of carboxy-thiol polyethylene glycol (CTPEG) linker molecules which are first attached to the surface of AuNPs through the thiol group. This leaves a terminal carboxylate group free for reaction with carbodiimide compound EDC which activtes the carboxylate group for direct reaction with primary amines. EDC does not leave any remnant of itself on the CTPEG linker molecule and therefore is known as a zero-length carboxy-to-amine crosslinker.[57] Figure 1.12 shows the EDC/NHS cross-coupling process for Ab attachment to AuNPs. After reacton with EDC, an O-acylisourea unstable ester intermediate is formed. Acidic conditions are favourable for this reaction and buffers which lack carboxylic acid and primary amine groups are necessary.[56,57]

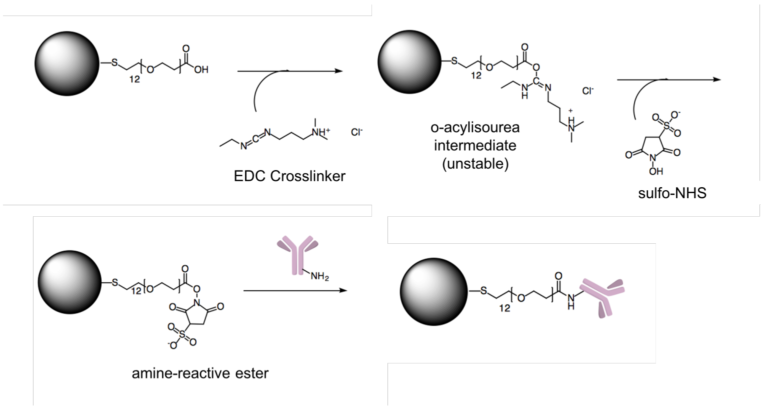

Figure 1.12: Carbodiimide cross-linking chemistry for covalent linkage of Abs to the surface of AuNPs. EDC/sulfo-NHS coupling is used to activate the terminal carboxylate group of the CTPEG linker molecule attached to the AuNP surface. Ab attachment is facilitated by the formation of an amine-reactive ester and a stable AuNP-Ab conjugate is formed by an amide bond.

NHS acts as a nucleophile and easily displaces the unstable ester intermediate to form an amine-reactive ester of greater stability. The sulfonate derivative of

NHS, sulfo-NHS is often used for this step as it is water-soluble and facilitates the formation of stable intermediates while improving the efficiency of the reaction. This means intermediates can be stored over time before cross-linking with primary amines. Conjugation can also be carried out at a physiological pH using sulfo-NHS.[57]

Once the amine-reactive ester is formed, coupling to primary amine groups abundant on the surface of the Ab facilitates functionalisation of Abs to the surface of AuNPs. Covalent attachment has the advantage of linking the Ab in such a way that its paratopes are in the correct orientation for interaction with their specific antigen species.[56,57] However, the process is time consuming and it can be difficult to achieve the optimum buffer conditions.

1.3.3.2. Passive Adsorption

Passive adsorption is the attachment of the Ab to the AuNP surface through non-covalent means. Passive adsorption occurs through electrostatic interactions between the Ab and the surface of the nanoparticle but van der Waals forces and π-π interactions also contribute to the passivation of Abs on the surface.[58] For this method, the isoelectric point (pI) of the Ab is important as is the pKa of the functional group that is being targeted *i.e.* the primary amine groups present on lysine residues covering the Ab's surface. This also means buffer conditions need to be carefully assessed before performing passive adsorption.[58,59]

It is difficult to control the orientation of the Ab on the nanoparticle surface using this technique and this is one disadvantage associated with passive adsorption. The Ab can bind in a number of ways as shown in figure 1.13. Ideally, binding will occur through the Fc region resulting in the Fab region being fully available for antigen binding. If the Ab binds side-on, flat to the surface or with the Fc region protruding upwards, the Fab region and therefore access to the paratopes of the Ab will be obscured and binding efficiency will be reduced. This will also have a detrimental impact on sensitivity during antigen detection.[59] Despite this, passive adsorption is widely used as a functionalisation technique for use with ELISAs and lateral flow immunoassay devices.[58]

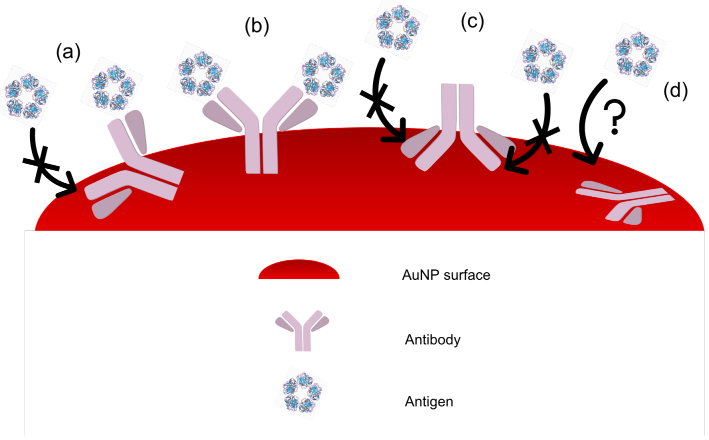

Figure 1.13: Different possible orientations in which an Ab might passivate onto AuNP surface using passive adsorption as an immobilisation technique (a) side-on leaving only a single paratope available for antigen binding, (b) tail-on, the ideal orientation for binding as it leaves both paratopes exposed, (c) head-on binding, least ideal orientation as both paratopes are blocked and the antigen cannot bind and (d) flat-on where the paratopes may be available for interaction with the antigen but it is unlikely that binding will occur.

There are many other procedures used for Ab immobilisation onto surfaces. For example, protein A and G have been used as they have a high affinity for certain types of Abs and indeed are also used for Ab purification techniques. Biotin-streptavidin systems, one of the strongest non-covalent interactions demonstrated in biology, are also popular with biotinylated Abs coupled with surfaces treated with streptavidin.[59] However, passive adsorption through electrostatic interactions was used as part of this investigation and was found to work effectively for Ab conjugation to AuNPs.

1.4 SERS-based Rapid Diagnostics for the Detection of Biomarkers associated with Sepsis

In this thesis, AuNPs were functionalised with Raman reporter molecules and conjugated to Abs for the detection of two biomarkers associated with sepsis, CRP and IL-6. Firstly, the detection of CRP was investigated using a lateral flow immunoassay test with the aim of using SERS to gain quantitative information. The assay was tested with both human blood serum and plasma samples and a handheld Raman spectrometer was compared with a benchtop Raman microscope instrument to demonstrate the viability of SERS as a point-of-care analysis technique.

Secondly, duplex detection of CRP and IL-6 on the lateral flow immunoassay platform was performed. This preliminary work would show the potential of using SERS for multiplexed detection and quantification of biomarkers, which is necessary for rapid sepsis diagnosis.

Finally, a 3D microfluidic, paper-based device platform was optimised for the detection of CRP using SERS. AuNPs used with the lateral flow immunoassay test were integrated into the platform for quantitative detection of CRP. Due to the versatile design of the device template, this 3D platform would be useful for multiplexed detection.

In all cases, SERS was compared with colourimetric RGB analysis which is commonly used with both platforms.

2. Experimental

2.1 Materials

The following chemicals were purchased from Sigma-Aldrich, UK; sodium citrate tribasic dihydrate, sodium tetrachloroaurate (III) dihydrate (Na.AuCl_4), sodium tetraborate, boric acid, bovine serum albumin (BSA), phosphate buffer powder (PB) and Tween 20. The Raman reporters malachite green isothiocyanate (MGITC) and 7-dimethylamino-4-methylcoumarin-3-isothiocyanate (RBITC) were purchased from ThermoFisher and Sigma-Aldrich respectively. C-reactive protein mouse monoclonal antibody (mAb) and interleukin-6 goat polyclonal Ab (pAb) were purchased from R&D Systems. Interleukin-6 mAb (ab9324) and human interleukin-6 protein (ab9627) were both purchased from Abcam. Human CRP was purchased from BBI Solutions. All d.H_2O (milli-q) used was purified using Millipore Purification Systems. For lateral flow strips, the FF170HP LAM 60x300mm (25mm width) backed nitrocellulose membrane was purchased from GE Life Sciences, the conjugate and absorbant pads were purchased from Merck Millipore.

2.2 Instrumentation

2.2.1 Extinction Spectroscopy

Extinction spectroscopy was carried out on an Agilent Cary 60 UV-vis spectrophotometer. Samples of 500 μL were placed in a 1 cm^3 plastic microcuvette and were scanned from 200 nm to 800 nm. A baseline measurement of d.H_2O

was performed before sample analysis.

2.2.2 DLS and Zeta Potential Measurements

A Malvern Zetasizer Nano Series was used for DLS and zeta potential measurements. 1 mL of sample was pipetted into a 2-sided 1 cm^3 plastic cuvette for DLS analysis and a Malvern Zeta Dip Cell was placed in the cuvette for zeta potential measurements.

2.2.3 SERS Measurements

2.2.3.1. Solution SERS Analysis

Solution spectra were performed using a Snowy Range Sierra Series benchtop Raman instrument with an excitation wavelength of 638 nm, a laser power of 40 mW (100%) and over a spectral range of 200 - 2000 cm^{-1}. 500 μL of sample was pipetted into a glass vial and readings were taken from the side sampling position. Matlab was used to process the data.

2.2.3.2. Raman Mapping

SERS measurements of LFIA strips and 3D μPAD membrane surfaces were carried out using a Renishaw InVia microscope witha 5X objective, an excitation wavelength of 633 nm and a laser power of 0.73 mW recorded using a portable power meter. Baseline correction, cosmic ray removal and SERS intensity maps were generated on WiRE software. Matlab were used to process the spectral data.

2.2.3.3. Handheld SERS Measurements

Handheld SERS measurements were carried out using a handheld CBEx Snowy Range instrument with an excitation wavelength of 638 nm and laser power of 27.8 mW recorded using a portable power meter.

SERS analysis of LFIA strips and 3D μPADs was performed with the aid of a removable objective lens and 3D-printed adaptor which was made to fit over the lens. The dimensions and design of the adaptor are shown in figure 3.12. Previous work with this setup was demonstrated by Mabbott *et al.*[60] A 4mm aperture opening was integrated into the top of the adaptor to allow for analysis of both devices. Matlab was used to process the data.

2.3 Gold Nanoparticles

2.3.0.1. Gold Nanoparticle Synthesis

Gold nanoparticle (AuNP) synthesis was adapted from the Turkevich method. A three-necked round bottom flask, glass stirrer and 1L graduated cylinder were soaked in fresh aqua regia for approximately 2 hours and thoroughly rinsed with water followed by rinsing with d.H_2O. 500 mL of d.H_2O was measured out in a graduated cylinder and added to a round bottom flask. 60.5 mg of $AuCl_4$ was also added to the flask while the solution was stirred vigorously. A Bunsen burner was used to heat the solution. Once boiling, 57.5 mg of sodium citrate dissolved in 5.75 mL H2O was added. The solution was boiled for a further 15 minutes. During this time the colour changed from transparent to black and finally to a deep red. Continuous stirring was maintained throughout the synthesis and while the colloidal solution was left to cool. Characterisation of AuNPs was carried out using extinction spectroscopy, dynamic light scattering (DLS) and zeta potential measurements. AuNPs of approximately 38 nm in size were formed with a zeta potential of approximately -37 mV. The concentration of the AuNPs was calculated using the Beer-Lambert law and was 0.14 nM.

2.3.0.2. AuNP Functionalisation - CRP Antibodies

AuNPs were conjugated to CRP-specific monoclonal Abs using a pH-correction method. AuNPs were corrected to pH 9 using 0.1 M Na_2CO_3. 7.5 μL of 1 Œ

10^{-5} M MGITC was made up to 10 μL in d.H_2O. 990 μL of pH-corrected AuNPs were then added, to give a final MGITC concentration of 75 nM. The sample was then shaken for 30 min. 5 μL of CRP Ab (500 μg/mL stock) was added and the sample was shaken for a further 10 min. The final Ab concentration was calculated to be 2.5 μg/mL. 500 μL of 0.5% BSA in 1XPBS (137 mM NaCl, 2.7 mM KCl, 8.1 mM Na_2HPO_4, 1.5 mM KH_2PO_4) was then added. The particles were shaken for two hours followed by centrifugation at 3223*g* for 20 min. The pellet was resuspended in 1 mL of 0.1% BSA in 10 mM phosphate buffer.

The 10 mM phosphate buffer used for the CRP-Ab functionalisation was prepared by dissolving 0.086 g of phosphate buffer powder (171.963 g/mol) in 50 mL of d.H_2O.

2.3.0.3. AuNP Functionalisation - IL-6 Antibodies

For conjugation of the IL6-specific Ab, a method developed by Wang *et al.* was used.[61] 7.5 μL of RBITC (1 x 10^{-4} M stock) was made up to 10 μL with d.H_2O. 999 μL of AuNPs was added. The final concentration of RBITC was 0.75 μM. AuNPs were then shaken for 30 min. 100 μL of 0.1 M borate buffer (pH 9) was added to the particles followed by 4 μL of IL-6 Ab (1 mg/mL stock) to give a final Ab concentration of 3.6 μg/mL. AuNP-Abs were then shaken for 2 h. 20 μL of 10% BSA was added followed by shaking for a further 30 min. The particles were centrifuged at 3223*g* for 20 min and the pellet was resuspended in 1 mL of 0.1 M borate buffer.

The 0.1 M borate buffer used for IL-6-Ab functionalisation was prepared by adding 0.15 g of sodium tetraborate to 16 mL of d.H_2O and heating to dissolve. 0.2 g of boric acid was then added and the solution was corrected to pH 9 before being made up to 20 mL with d.H_2O.

PBS Buffer

Phosphate buffered saline (PBS) recipe used to prepare 1xPBS: 137 mM NaCl, 2.7 mM KCl, 8.1 mM Na_2HPO_4, 1.5 mM KH_2PO_4.

2.4 Lateral Flow Immunoassay Devices

A schematic representation of the assembled LFIA devices used in this study is shown in figure 3.9. The strip consists of three overlapping layers: the conjugate pad, the nitrocellulose (NC) membrane and the absorbant pad. Assembly of the device began with the backed NC membrane FF170HP LAM 60x300 mm (25 mm width) purchased from GE Life Sciences. The backed membrane had adhesive regions on either side of the NC. The conjugate pad and absorbant pad purchased from Merck Millipore and were attached to these regions, ensuring that there was overlap between each layer which was essential for the running of the device.

The conjugate pad is primarily made of glass fibre while the absorbant pad acts as a wick, drawing fluid upwards through the strip. All LFIA trips were cut from the 300mm backing card to approximately 5 mm in width.

2.4.0.1. Singeplex Lateral Flow Immunoassay

Concentration studies were performed for CRP and IL-6 in a singleplex immunoassay format. The immunoassay was performed by pipetting 0.6 μL of the biomarker specific Ab (360 μg/mL of CRP-Ab from 0.5 mg/mL stock and 450 μg/mL of IL-6-Ab from 1 mg/mL stock) onto the centre of the NC membrane between the conjugate and absorbant pads and allowing the spot to dry at room temperature. 10 μL of concentrated AuNP-Abs was pipetted onto the conjugate pad prior to addition of the sample solution. Sample solutions were prepared in 1.75 mL glass vials in 100 μL of lateral flow buffer (0.5% BSA, 0.05% Tween 20 in 1.72 mg.mL phosphate buffer). The LFIA strip was placed into the vial and allowed to run until the sample solution had almost reached the top of the absorbant pad.

The following concentrations of CRP were prepared (section 3.3.2): 100, 50, 25, 20, 10, 5 and 0 ng/m from 1 mg/mL stock. The following concentrations of IL-6 were prepared (section 4.3.1.1): 100, 50, 25, 10, 5 and 0 ng/mL from 1 mg/mL stock. LF strips were washed once with 80 μL of LF buffer after the sample solution had flowed through the strip. The strips were allowed to dry before Raman and colourimetric analysis was carried out.

The assay running time was approximately 20 min not including the wash step.

2.4.0.2. Spatially-resolved Duplex Lateral Flow Immunoassay

Lateral flow strips were assembled in the same way as described for singleplex experiments. 0.6 μL of CRP-Ab and IL-6 Ab were spotted onto different regions of the NC membrane. A schematic representation showing the spatially-resolved LFIA strip is shown in figure 4.9. The IL-6 Ab was spotted closer to the conjugate pad at a concentration of 450 μg/mL while the CRP-Ab was spotted closer to the absorbant pad at a concentration of 360 μg/mL as shown.

CRP and IL-6 biomarkers were mixed together in 80 μL of LFIA buffer at a chosen concentration in 1.75 mL glass vials. 10 μL of each of the concentrated (75 nM) AuNP-Ab conjugates was added to give a final volume of 100 μL. The LFIA strip was placed into the vial and allowed to run until the sample solution had almost reached the top of the absorbant pad. LFIA strips were washed with 80 μL of LF buffer after the sample solution had flowed through the strip. The strips were allowed to dry before Raman and colourimetric analysis was carried out.

The assay running time was approximately 20 min not including the wash step.

2.4.0.3. Signal-resolved Duplex Lateral Flow Immunoassay

The LFIA devices used for the signal-resolved duplex experiments were assembled the same way as for the singleplex LFIAs. A schematic of the signal-resolved LFIA is shown in figure 4.14. CRP-Ab and IL-Ab were mixed together before being pipetted onto the NC membrane. This was done by preparing 450 μg/mL IL-6-Ab solution and 360 μg/mL CRP-Ab solution separately. 1.5 μL of each of the solutions was mixed together giving a total volume of 3 μL. 0.6 μL of the mixed solution was pipetted onto the NC membrane. By mixing the Abs together in this way, the Ab concentration was essentially diluted by half, giving final Ab concentrations of 225 μg/mL and 180 μg/mL for IL-6-Ab and CRP-Ab respectively.

The signal-resolved LFIAs were run the same way as described for the spatially-resolved LFIAs.

2.4.0.4. Colourimetric Analysis - RGB Values

LFIA strips were scanned using an 8-bit EPSON V370 Flatbed scanner at a resolution of 800 dpi. RGB analysis was performed on the scanned images using ImageJ software. The area of the NC membrane where capture Abs had been spotted on was marked before running the LFIA and this area was selected for RGB analysis. The analysis returned a value for each colour channel; red (R), green (G) or blue (B). Since AuNPs are red and absorb green light, the green channel was most sensitive to AuNPs. Each green channel was subtracted from the RGB value for white of 255 (the maximum RGB value attainable). These normalised RGB values were averaged over replicate studies for the construction of RGB calibration curves/bar charts.

2.5 3D Microfluidic Paper-based analytical devices

The materials used for the 3D μPADs were gifted by the Mace labaratory based at Tufts University, Medford, MA. Each layer of the device consisted of a template wax-printed onto Whatman Grade 4 chromatography paper with a pore size of 20 - 25 μm with the exception of the capture layer where the template was wax-printed onto Biodyne C nylon membrane with a 0.45 μm pore size. A yellow ring surrounding the capture zone was present in the design to help with visual enhancement any red colour observed from the immobilisation of AuNPs.

A schematic showing each layer and the assembly of the device is shown in figure 5.3.

Before assembling the 3D μPAD, the conjugate, incubation and capture layer had to undergo pre-treatment to ensure successful running of the device.

2.5.0.1. Pre-treatment of Layers

Conjugate Layer Treatment

In initial experiments, the conjugate layer was pre-treated with 10% BSA in 1xPBS. However, optimisation experiments showed sing the LFIA running buffer was more successful for use with the SERS-based assay for CRP detection. Therefore the conjugate layer was pre-treated with 3 μL of LFIA running buffer (0.5% BSA, 0.05% Tween 20 in 1.72 mg.mL phosphate buffer) followed by drying for 2 mins at room temperature then 5 mins @ 65°C. 5 μL of concentrated AuNP-Ab conjugates was then dried on using the same drying procedure. AuNP-Abs were centrifuged prior to drying onto the conjugate layer and resuspended in an appropriate volume of resuspension buffer (2% BSA, 10% sucrose and 0.1% Tween 20 in 1xPBS).

Incubation Layer Treatment

6 μL of blocking buffer (5 mg/mL milk powder and 0.1% Tween 20 in 1xPBS) was applied to the centre of the dogbone shape and the same drying procedure was followed as for the conjugate layer.

Capture Layer Treatment

2 μL of mouse monclonal CRP Ab was applied to the capture zone at various concentrations and the same drying procedure as described was followed. 3 μL of blocking buffer (5 mg/mL milk powder and 0.1% Tween 20 in 1xPBS) was then applied to the area and the same drying procedure performed.

The device was ready for assembly once all pre-treatment steps had been carried out. Prior to use, the device underwent cold lamination to ensure any air trapped between the layers was pressed out.

2.5.0.2. Running of the 3D μPAD

20 μL of CRP sample solution in d.H_2O/d.H_2O only control was applied to the top layer of the device to begin the running of the assay.

Once this was observed to be completely absorbed into the top layer, the 3D μPAD was washed through twice with 2 x 15 μL of wash buffer (0.05% Tween 20 in 1xPBS). After 15 mins the first three layers of the device were peeled back to reveal the capture layer. The capture zone was immediately scanned using an 8-bit EPSON V370 Flatbed scanner at a resolution of 800 dpi.

SERS analysis was performed as soon as possible after revealing of the capture layer. This was done using the CBEx handheld Raman spectrometer from Snowy Range Instruments with an excitation wavelength of 638 nm and laser power of 27.8 mW. A removable objective lens and 3D-printed adaptor were used to aid on the reading of the 3D μPAD where the 4 mm aperture opening had been specifically designed to encompass the whole region of the capture zone. Three raised regions on the top of the adaptor (figure 3.12) were designed to fit the 3D μPAD in place so that the capture region placement was correct for analysis.

Colourimetric Analysis of the Capture Zone

Colourimetric analysis of the cature layer was performed in the same way as described for LFIA devices. The scanned images of the capture layer of the 3D μPADs underwent RGB analysis using ImageJ software. The capture zone was selected using ImageJ and RGB measurements were generated for this area only (excluding the yellow ringed region).

3. Comparing benchtop and handheld Raman analyses: A SERS-based lateral flow assay for the detection of C-reactive protein

3.1 Introduction

3.1.1 Lateral Flow Assays

Lateral flow immunoassays (LFIA) are ideal for the rapid detection of biomolecules at the point-of-care. They are user-friendly and cost effective making them an attractive platform for quick diagnosis in a clinical setting. LFIAs cannot be referred to without mentioning the home pregnancy test. Developed in the 1970's and still a robust testing method used today, the hCG hormone is detected in a urine sample and the assay run time can take as little as 5 minutes.[62] The result from these kinds of tests need only generate a qualitative result *i.e.* a 'yes/no answer' and colourimetric detection is predominantly used in LFIAs as it often produces a clear and easy-to-interpret result. Gold nanoparticles are commonly used in home pregnancy tests to give a coloured response.

The term 'immunoassay' refers to a recognition interaction involving an antibody (Ab). Commonly, the Ab is immobilised onto a static surface and due to the high affinity binding and the specific nature of Abs, they are capable of capturing a wide range of targets. Once the target is bound, a second recognition reagent is used to generate a signal, the level of which can be used to determine the concentration of the target.[63] Popular signal generating species like fluorescently-labelled Abs or nucleic acids are common, including labelled aptamers. Latex beads and colloidal gold are also common.[64] In this investigation, gold nanoparticles (AuNPs) were functionalised with a Raman reporter molecule and Abs to act as signal generators or 'labels' in a LFIA. The following sections explain the architecture and working principle of conventional LFIAs, which typically use Ab-functionalised AuNPs as visual signal generators, which are used in the previously mentioned home pregnancy tests.

3.1.1.1. Device Architecture and Working Principle of a Conventional Lateral Flow Immunoassay

Conventional LFIAs consist of 4 main sections - sample pad, conjugate pad, flowing membrane and wicking/absorbant pad. Figure 3.1 (a) shows a schematic of a conventional LFIA strip. The sample pad is where the sample solution comes into contact with the strip. The material used *e.g.* cellulose, rayon, glass fibre, etc. is usually highly absorbant and maintains a continuous sample flow. This pad must possess a high tensile strength when wet and it's failure inadvertently leads to the entire device failing.[65] The sample pad overlaps with the conjugate pad, the next section on the LFIA strip.

The conjugate pad holds the 'label' species and this is what is observed when the test and control lines appear on the flowing membrane (figure 3.1 (a)). AuNPs are commonly used as conjugates in LFIAs as they can be easily functionalised with Abs and other biomolecules for the specific detection of analytes.[66] Other nanoparticles have been used as labelling species such as polystyrene beads, fluorescent particles, other metal NPs and magnetic NPs.[67–72] When the sample solution travels along the conjugate pad, it rehydrates the conjugates and continues to flow along the LFIA strip to the flowing membrane.

This membrane is the reaction matrix and is usually a porous material such as nitrocellulose. Nitrocellulose has been modified with amine groups that aid in the immobilisation of capture proteins. The test and control lines lie on the

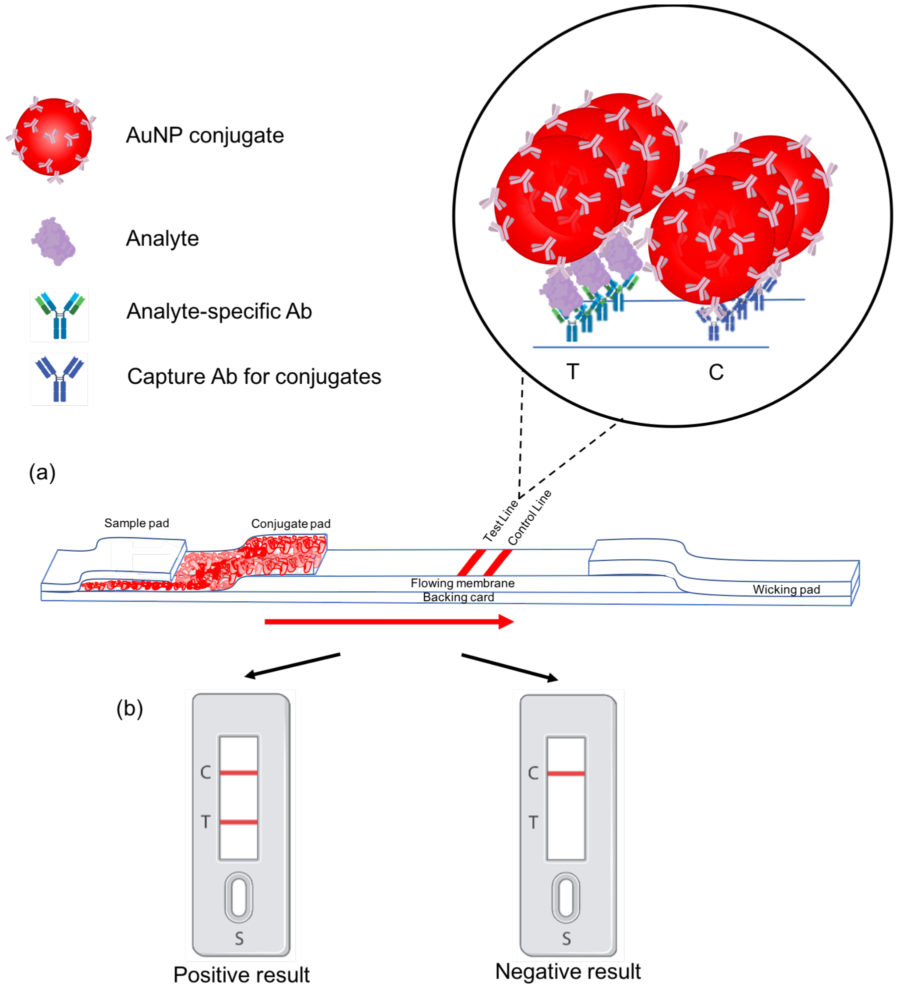

Figure 3.1: (a) Architecture of a conventional lateral flow immunoassay strip showing the test line and control line and consisting of a sample pad, conjugate pad, flowing membrane and wicking pad all placed onto a backing card, each section overlaps with the next to ensure flow of sample solution through the strip. The conjugate pad is coloured red since AuNPs are commonly used as labelling species and are dried onto the conjugate pad before use. Inset shows immunoreactions occurring at the test and control lines in the event of a positive assay and (b) visual results from running a conventional LFIA, a positive result will generate the appearance of two red lines while a negative result shows a single red line. C = control line, T = test line and S = sample inlet. Schematic not to scale.

flowing membrane and usually consist of a capture entity specific to the analyte/biomolecule (test line) followed by a species that will capture any excess conjugates (control line). The appearance of the control line shows that the device is working as intended. Flowing membranes are usually described according to capillary flow time *i.e.* flow of solvent front in seconds per 4 cm. Capillary flow time depends on the physical properties of the membrane such as pore size, pore size distribution and porosity. For example, a large pore size will result in fast movement through the membrane and therefore correlates with a low capillary flow time. If a longer incubation time was important for the workability of an assay, then a smaller pore size would be better as this would increase the capillary flow time but would also increase the time it takes to run the assay.[64,65]

The final section on the LFIA strip is the wicking/absorbant pad. This pad helps to draw all the solution through the device and past the reaction matrix where the immunoreactions have taken place. Its presence ensures that all non-bound conjugates are drawn away from the rest of the device and do not interfere with the analysis of results. The wicking pad material can be made of the same material as the sample pad and is usually thick cellulose.[65]

Many LFIA devices are housed in a specially designed cassette like those shown in figure 3.1 (b). This plastic housing can be optimally designed to have pressure points at certain regions on the device to encourage optimal flow control. These features also contribute to the reproducibility of the assay.[64,73]

The sample solution can be introduced to the device through the S inlet on the cassette which lines up with the sample pad (figure 3.1 (b)). The sample flows upwards through the device via capillary action. As the solution passes along the conjugate pad, it reimmobilises the label species or conjugates and any analyte present in the sample will bind to recognition molecules, *e.g.* Abs, functionalised to the label species or conjugates. When these analyte-conjugate complexes come into contact with the test line, they are captured by analyte-specific biomolecules, usually Abs immobilised at this location forming a coloured line of accumulated conjugates. Any conjugates not bound to the analyte will bind to capture antibodies (capAbs) on the control line, the inset in figure 3.1 (a) shows the immunoreactions taking place at the test and control lines in the event of a positive test. Any unbound conjugates, AuNPs in this example, are drawn towards the wicking pad and away from the region to be analysed.

The more analyte present in the sample solution, the more immunoreactions will occur at the test line meaning the colour of the test line will intensify with increasing analyte concentration. In the case of AuNPs being used as labelling species, an intense red colour will be visible at high analyte concentrations, at lower concentrations the colour intensity of the test line will diminish.

3.1.1.2. Advances in Visual Detection Methods

Conventional LFIAs tend to use visual techniques to analyse results, AuNPs are commonly used due to their red colour. The visual result provides qualitative information, *i.e.* the yes/no answer as to whether a target is present in the sample. However, relying on visual analysis alone means interpretation can be subjective and low detection limits and sensitivity are sacrificed. Quantitative information is also difficult to obtain using this technique. Much research has gone into improving the sensitivity of colorimetric methods while also obtaining quantitative information from colourimetric analysis. Nardo *et.al* used red, green, blue (RGB) analysis to achieve semi-quantitative detection of two mycotoxins found in wheat and food products.[74] RGB values are ideal particularly when used in combination with AuNPs as this technique works best with primary-colour labels.[62] They used red and blue coloured AuNPs to code for each of the mycotoxins and were able to successfully identify both colour responses from a single test line.[74] Red and blue AuNPs were also used alongside RGB values for the dual detection of two malaria parasite biomarkers. The authors achieved quantitative information from the RGB analysis and obtained LODs of 31.2 ng/mL and 7.8 ng/mL respectively for each biomarker in spiked buffer solutions.[75]

Xiao *et al.* investigated the use of a 3D-printed smartphone-based reader to improve sensitivity for the detection of three analytes - cadmium ion, clenbuterol (CL) and porcine epidemic diarrhea virus (PEDV).[76] They exploited the fact that all smartphones have an in-build ambient light sensor that could measure the transmitted light intensity produced by the test line of a LFIA strip when the strip was placed beneath an LED light source and the sensor was placed beneath the strip. The transmitted light decreased with increasing analyte concentration as more AuNPs accumulated on the test line. An app was designed for use with the smartphone for assay analysis. Their method displayed good correlation with ImageJ colourimetric analysis but did not require the use of any external software other than the smartphone. Additionally they demonstrated quantitative analysis achieving an LODs of 0.16 ng/mL, 0.046 ng/mL and 0.055 μg/mL for Cd^{2+}, CL and PEDV respectively.[76]

Fluorescence has also been used as a visual detection technique. Lou *et al.* functionalised polystyrene microspheres with a fluorophore for the detection of cardiac biomarker cardiac troponin 1 (cTn1) and achieved improved detection sensitivity with a reported LOD of 0.032 ng/mL.[67] An aptamer-based fluorometric LFIA was developed by Zhang *et al.* for creatine kinase MB (CKMB), a biomarker for acute myocardial infarction.[68] The authors used a fluorescent reader alongside a fluorescent microscope to confirm their results and were able to gain quantitative information from the assay, the results of which are shown in figure 3.2 (a) (i), (ii) and (iii). They also demonstrated the efficiency and specificity of their assay in serum for CKMB detection in the presence of two other biomarkers.[68]

Magnetic nanoparticles (MNPs) have been used in LFIA devices using a magnet to concentrate the captured NP labels into a smaller region in order to generate a stronger colourimetric response. MNPs were used this way in one study for the detection of vasolin -containing protein, a biomarker for cervical cancer.[72] The MNPs were gold-coated and functionalised with Abs specific to the biomarker. To elicit a colourimetric response, the MNPs were modified with HRP and TMB followed by H_2O_2 was run through the assay giving a blue colour in the presence of HRP. Figure 3.2 (b) (i) and (ii) show a schematic of the assay and quantitative results in the presence and absence of a magnet.[72] The authors explained how

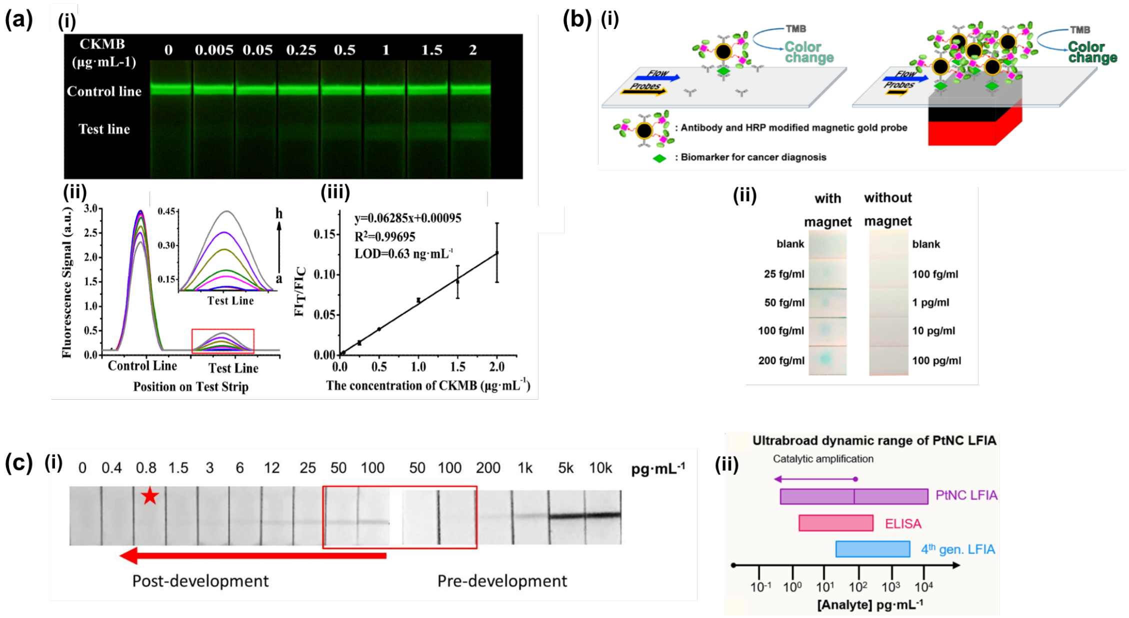

Figure 3.2: Examples of colourimetric techniques developed for quantitative detection and improved sensitivity in LFIAs (a) fluorimetric techniques have demonstrated lower detection limits and quantitative information can be achieved,[68] (b) magnetic nanoparticles have been used to improve sensitivity and quantify biomarker detection[72] (Reprinted with permission from *Analytical Chemistry*, **2019**, *91*, 2876-2884. Copyright 2019 American Chemical Society) and (c) catalytic NPs have been used to increase the dynamic range of LFIAs and for quantitative analysis.[69]

---

the presence of the magnet slowed down the flow rate of the particles, enabling longer incubation time between the conjugates and the analyte. They achieved fg/mL detection limits in buffer and ng/mL levels in tissue samples, generating a 10^6 fold improvement in sensitivity compared with conventional LFIA.[72]

Detection limits of 0.8 pg/mL were achieved for p24, an early-stage biomarker for HIV using platinum core-shell nanocatalysts (PtCNs). In this study, the authors took advantage of the catalytic properties of Pt to increase the dynamic range over which they could detect p24.[69] At high target concentrations, between 100 - 1000 pg/mL, visual detection was possible due to the appearance of a black line at the test line. The test line was then exposed to H_2O_2 and a chromogenic substrate, the captured PtNCs at the test line catalysed the oxidation of the chromogenic species in the presence of H_2O_2 into an insoluble product. Figure

3.2 (c) (i) shows the difference in the colour of the test line before and after treatment across the high and low concentration ranges, the sensitivity of the assay was improved by 2 orders of magnitude by including this amplification step. The dynamic range covered by the assay compared with ELISA and conventional LFIAs is also shown (figure 3.2 (c) (ii)).[69] Using the PtNCs, both concentration ranges of ELISA and conventional LFIA were covered.

While quantification and increased sensitivity were achieved in the all of these cases and the tests demonstrated point-of-care workability, the assay procedures tended to include extra steps like the addition of a colour-developing or amplification reagent. Additionally, none of the techniques are appropriate for multiplexed detection which is necessary for sepsis diagnosis. A LFIA device that can be used at the point-of-care, has a single step sample addition making it user-friendly and is also capable of detecting more than one analyte simultaneously would be ideal. SERS-based LFIA platforms will be discussed in the next section with regards sensitive and quantitative single biomarker detection. Section 4 goes into detail on the development of multiplexed LFIAs using SERS.

3.1.1.3. SERS-based lateral flow immunoassays

SERS-based LFIAs offer increased sensitivity and the ability to gain quantitative information when compared to conventional AuNP-based LF strips. Quantification is important when considering clinically relevant levels of biomarkers present in a biological sample. Biomarkers may be present at low levels, below those considered clinically relevant, whereas increased concentrations of this biomarker may indicate a disease state. Additionally, a decrease in the levels of a biomarker below those considered healthy may also indicate a problem. Using CRP, mentioned in section 1.1.3, as an example, this biomarker has a large dynamic range and its concentration in the bloodstream can give vital information about a patients condition. Normal CRP concentrations lie between 1-3 μg/mL and >10 μg/mL can be indicative of a disease state.[22] But levels as high as 100 μg/mL can indicate a septic event.[13] Additionally, very low levels of CRP, below what is considered normal can be representative of liver problems.[23] Quantitative information can also offer prognostic information for example, IL-6 concentration levels, a biomarker also mentioned in section 1.1.3, can indicate the effectiveness of antibiotic treatment in sepsis patients thereby indicating an improved prognosis.[7,8]

To incorporate SERS analysis into the LFIA, the AuNPs are functionalised with a Raman reporter and detection moiety that is specific to the analyte/biomolecule of interest. After the LFIA is run, the test line can then be analysed using a Raman spectrometer at an appropriate laser excitation. The Raman reporter attached to the AuNPs will provide a SERS signal, the intensity of which is dependent upon the amount of immunoreactions occurring at the test line. The SERS intensity can be then be related to the concentration of analyte/biomolecule present, allowing quantitative information to be obtained. SERS analysis can take place using a portable, point and shoot spectrometer while Raman mapping of the test line can also be performed to build false colour SERS intensity images.

Many investigations into SERS nanotags for biomarker detection on LFIAs have demonstrated the capability of the platform to reach concentration limits beyond what has been observed for colourimetric analysis. Tran *et al.* developed a SERS LFIA for human chorionic gonadotropin (hCG), the pregnancy hormone commonly detected in commercial pregnancy tests. The authors showed their technique was 15 times more sensitive compared to home pregnancy tests and their analysis time was approximately 5 s using a 785 nm laser attached to a spectrometer, the optics of which had been custom-designed to generate a horizontal laser line rather than a spot.[77] Their optical filter probe is shown in figure 3.3 (a). Quantitative detection was also achieved.

Similarly, Wang *et al.* detected the stroke biomarker, S100-beta using AuNPs functionalised with a Raman reporter and Abs specific to the target.[78] Their assay could detect a concentration range of 1 pg/mL to 40 ng/mL for S100-beta and

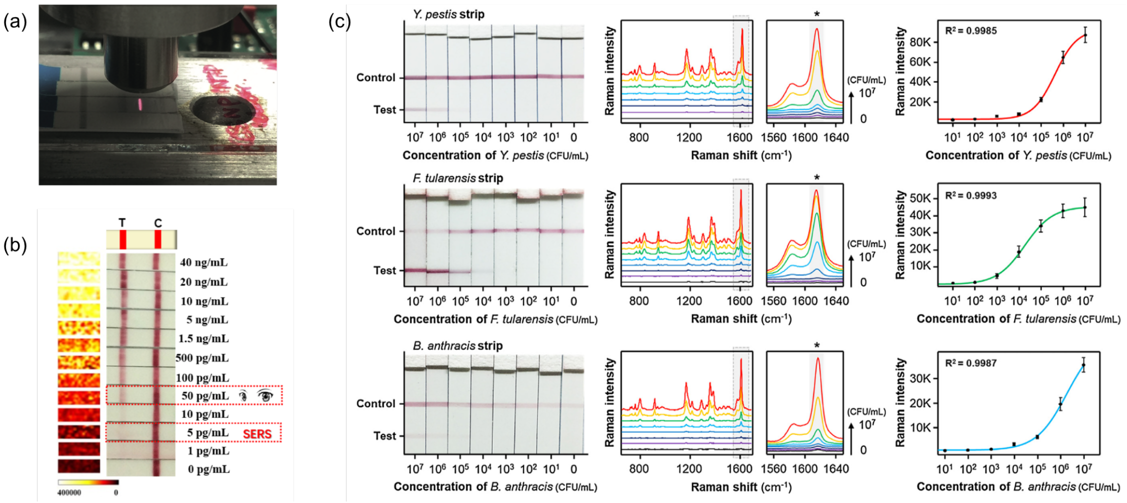

Figure 3.3: AuNPs used in SERS-based LFIAs (a) custom-designed optical filter probe used by Tran *et al.* for the rapid and sensitive detection of hCG,[77] (b) Images of LFIAs for stroke biomarker, S100-beta and correspondong SERS intensity maps comparing visual and SERS detection limits,[78] and (c) LFIA images of the detection of three bacteria, *Y. pestis*, *F. tularensis*, and *B. anthracis* independently where the authors demonstrated sensitive and quantitative detection using SERS. SERS spectra from each concentration of bacteria is shown alongside calibration curves of Raman intensity at 1616 cm^{-1} peak of MGITC reporter against bacteria concentration.[61]

---

a LOD of 0.14 pg/mL was calculated. Scanned images and corresponding SERS intensity maps are shown in figure 3.3 (b) demonstrating the difference between colourimetric and SERS-based detection. They reported that their assay was a factor of 3 more sensitive than colourimetric and fluorimetric techniques for the same biomarker. Additionally, they compared the assay to a commercially available ELISA kit and demonstrated that their SERS-based LFIA device had higher sensitivity over a lower concentration range and a lower LOD.[78]

AuNPs and SERS have combined in other investigations for the detection of HIV-1 DNA, thyroid-stimulating hormone (TSH) and a variety of bacterial pathogens.[61,79,80] For HIV-1 DNA, a LOD of 0.24 pg/mL was achieved, 1000 times more sensitive than colourimetric and fluorescent detection techniques.[79] TSH was detected with LOD of 0.025 μIU/mL. The authors also demonstrated the ability of their assay to detect for hyperthyroidism as well as hypothyroidism, for which there is not a commercially available test as detection limits of TSH using alternative techniques are not sensitive enough.[80] Wang *et al.* were able to detect three different bacteria independently using their SERS-based LFIA. Compared with commercially available LFIA rapid kits their detection limits were improved by 3-4 orders of magnitude with LODs for *Y. pestis*, *F. tularensis*, and *B. anthracis* estimated to be 43.4 CFU/mL, 45.8 CFU/mL, and 357 CFU/mL respectively. Additionally, their assay run-time was found to be 15 mins with a very small sample volume of 40 μL required. Low detection limits acquired in a rapid time frame for bacteria demonstrated a much improved platform compared with culture, colony counting and RT-PCR techniques.[61]

Other types of NPs have also been used as SERS substrates for improved sensitivity. Core-shell particles using Au and Ag have been used for the detection of avian influenza A (H7N9) and CRP, figure 3.4 (a) shows a schematic representation of nanotag synthesis for H7N9 detection.[34,76] Russo *et al.* used hollow AuAg nanoshells for the detection of Myxovirus protein A (MxA), a biomarker that can differentiate between bacterial and viral infections.[70] In this they utilised a dip-stick type LFIA platform with test and control spots as shown in figure 3.4 (b). Their assay covered the concentration range required for differential diagnosis (figure 3.4 (b)) and they demonstrated the ability to detect MxA in human serum with a LOD of 51.8 ng/mL compared with 135.8 ng/mL for visual detection.[70]

Hwang *et al.* reported a LOD of 0.001 ng/mL for staphylococcal enterotoxin B (SEB), a high-priority toxin, that was 3 orders of magnitude lower than ELISA-based methods using hollow gold nanospheres (HGNs) in a LFIA device.[71] While Lu *et al.* used gold nanorods (AuNRs) for the quantitative and ultra sensitive detection of cancer biomarker, alpha-fetoprotein (AFP), achieving a 9.2 pg/mL LOD and improved sensitivity compared with ELISA techniques and conventional AuNP-based LFIAs.[82]

It should be noted in all these examples, with the exception of the custom-designed spectrometer for hCG detection[77], a benchtop Raman microscope was used for the Raman analysis of the LFIAs. While SERS-based methods may

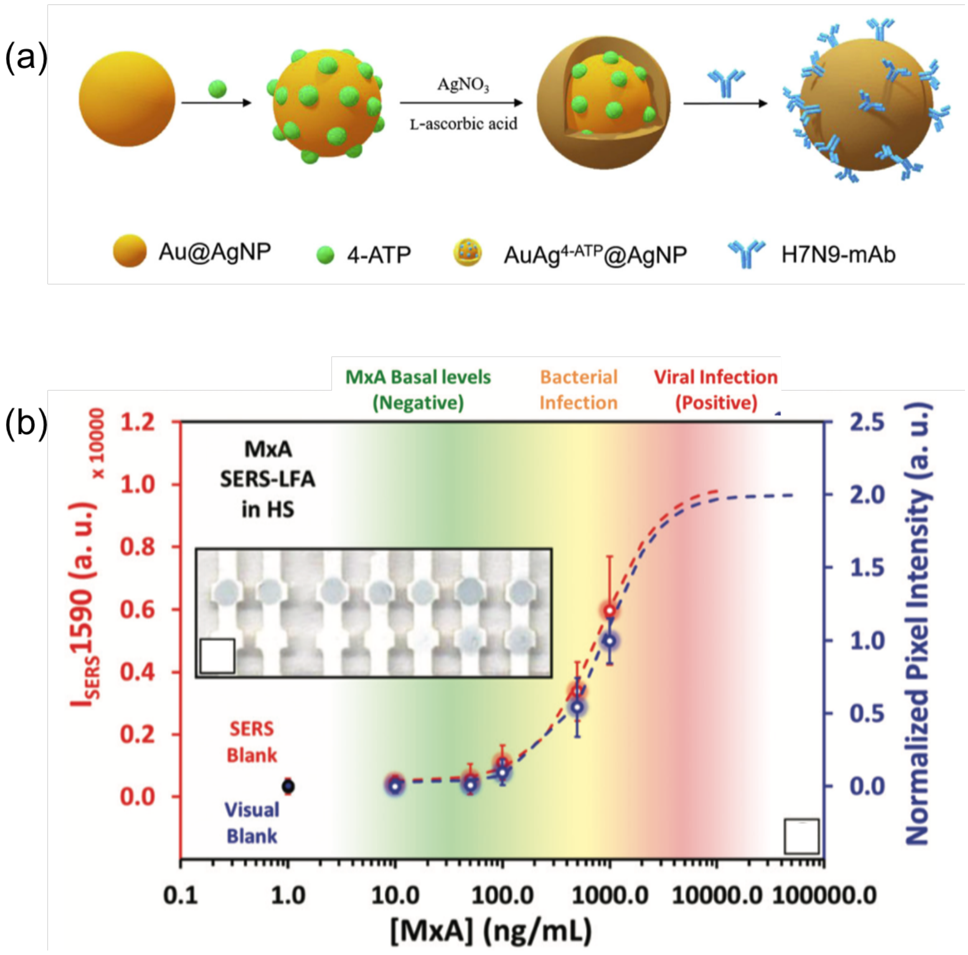

Figure 3.4: (a) Schematic representation of the synthesis of SERS-active AuAg core-shell particles used by Xiao *et al.* for the sensitive detection of avian influenza A[81], the assay time of which was found to be 20 mins and (b) hollow AuAg nanoshells functionalised with Raman reporter 4-MBA were used for the detection of MxA, detection of this biomarker over a larger concentration range meant differential analysis between bacterial and viral infection was possible as shown in the dose response curve.[70]

tick the boxes for quantification and sensitivity, portable, point-of-care analysis needs to be implemented. There are many commercially available handheld spectrometers across a range of laser excitation wavelengths. In this chapter, a handheld spectrometer will be used for analysis of all samples and compared with results from a benchtop microscope in order to demonstrate the viability of using a handheld device in conjunction with a LFIA platform for point-of-care biomarker detection using SERS.

3.2 Chapter Aims

SERS is a valuable tool for implementation into a LFIA platform. AuNPs are already commonly used in conventional LFIAs and the addition of a Raman-active reporter molecule has demonstrated that quantification and improved sensitivity can be achieved using SERS.[34,61,70,71,76–80,82] The aim of this chapter is to firstly show that sepsis-associated biomarker, CRP can be successfully detected using a SERS-based LFIA platform and that quantitative information can be gained from the assay.

AuNPs were synthesised and functionalised with Raman reporter, MGITC and Abs specific to CRP. These were used on the LFIA platform. All analyses of LFIA strips were performed on both a benchtop Raman microscope system and a handheld spectrometer. The benchtop instrument may offer a more accurate representation of the SERS response however, it is not appropriate for use in the field and the analysis can take up to 30 minutes depending on what parameters are set *e.g.* laser power, acquisition time, type of analysis. Therefore, the second aim of this chapter was to compare results with a handheld spectrometer in order to validate the use of a portable Raman instrument for use at the point-of-care.

Finally, human serum and plasma clinical samples were tested on the LFIA strips to ensure that the assay could be used with legitimate biological samples. CRP has a wide dynamic range depending on the cause of inflammation. Normal CRP levels in the blood are between 1-3 μg/mL while in the event of sepsis, concentrations can reach as high as 100 μg/mL.[13,22] Therefore, it was hoped that the assay would be suitable for use across a concentration range that was clinically relevant for human samples.

3.3 Results and Discussion

3.3.1 Gold Nanoparticle Synthesis and Functionalisation

The initial aim of the SERS-LFIA development was to synthesise Raman-active AuNPs and functionalise these with CRP-specific detection Abs. It was important that the AuNPs functionalised with the Raman reporter generated a strong and distinct SERS signal. Additionally, Ab conjugation success was evaluated by testing the assay using the LFIA platform, both with CRP only immobilised on the nitrocellulose (NC) membrane and in the sandwich-assay format with a capture Ab immobilised on the membrane.

AuNPs were synthesised using a citrate reduction protocol adapted from the Turkevich-Frens method.[48,49] Figure 3.5 shows the results from characterisation of AuNPs using extinction spectroscopy, dynamic light scattering (DLS) and zeta potential measurements. Two batches of AuNPs were synthesised and both were used exclusively in all experiments during this work. The AuNPs produced were 38.2 nm and 37.5 nm in size for batch 1 and 2 respectively and had zeta potentials of -42.2 mV and -32.3 mV respectively. Zeta potentials less than -30 mV indicated that the nanoparticles were strongly anionic and electrostatically stable.[83] Both batches had a concentration of approximately 0.14 nM. The LSPR peak for both batches had a λmax at around 520 nm. The bands were sharp and narrow with a full-width half-maximum (FWHM) of approximately 100 nm for each band, a FWHM of $\leq$100 nm is an indication of monodisperse NPs.[84]

Malachite green isothiocynate (MGITC) was chosen as the Raman reporter molecule for this preliminary study. MGITC, the structure of which is shown in figure 3.6, is a triaryl dye consisting of three functional groups, two tertiary amines (NR_3) and one isothiocyanate (-NCS) group. MGITC is a chromophore with an absorbance maximum at 617 nm and therefore benefits from being resonant with $\sim$633 nm laser excitation.[85] The presence of the -NCS group facilitated the attachment of MGITC to the surface AuNPs through the S atom.

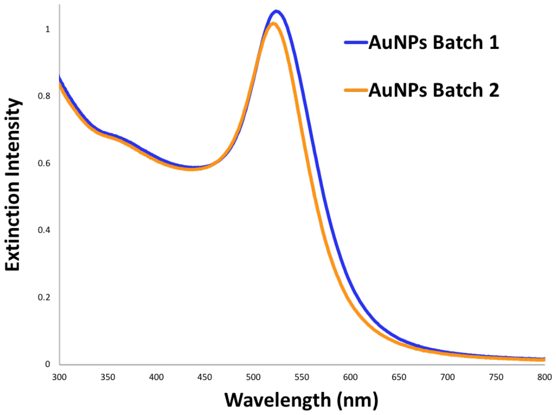

Batch	λmax (nm)	Size (nm)	Zeta Potential (mV)	Concentration (nM)
Batch 1	523	38.22 ± 0.63	-42.2 ± 8.81	0.14
Batch 2	520	37.45 ± 1.3	-32.33 ± 9.61	0.13

Figure 3.5: Results from extinction spectroscopy characterisation for each batch of AuNPs. The sharp, narrow LSPR band observed for both batches indicated low polydispersity. The table shows values for λmax, size, zeta potential and concentration of each batch. Both batches had a λmax of approximately 520 nm with a particle size of just under 40 nm. Both batches were stable with zeta potentials of -42 mV and -32 mV respectively. The size value given is the mean value +/- the standard deviation from 3 repeats measurements using dynamic light scattering (DLS).

As described in section 2.3, passive adsorption was used for attaching Abs to the AuNPs surface. Briefly, AuNPs were corrected to pH 9 with 0.1 M Na_2CO_3. This enabled the protonation of amine groups (pKa 10.53) present on the lysine residues of the monoclonal Abs (mAbs) specific to CRP.[86,87] Correcting the pH may also have consequences on the stability of the AuNPs. The surface is stabilised and capped by citrate ions which have three different pKa's - 3.1, 4.7 and 6.4. At pH 9, all of the carboxylic acid groups of the citrate ion will be deprotonated.[86,88] Therefore Ab attachment was achieved through electrostatic interactions between the negatively charged AuNP surface and positively charged protonated amines on the Ab. Bovine serum albumin (BSA) was used to passivate any exposed AuNP surface thereby stabilising the functionalised particles and preventing non-specific binding. A schematic representation of AuNP functionalisation is shown in figure 3.6. A final concentration of 2.5 μg/mL CRP Ab

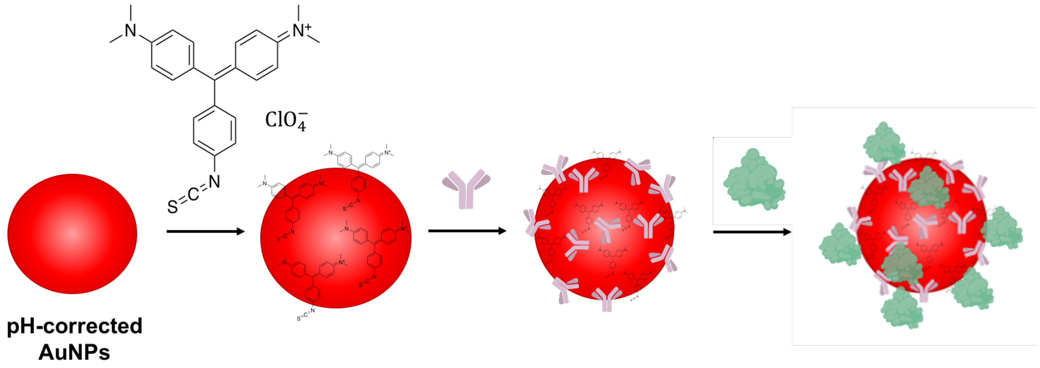

Figure 3.6: Schematic representation (not to scale) of the steps involved in AuNP functionalisation. AuNPs were firstly corrected to pH 9, MGITC was then functionalised onto the NPs followed by Ab attachment and finally passivation by BSA to inhibit non-specifc binding to any exposed AuNP surface.

was added to AuNPs functionalised with MGITC, this concentration was chosen as the AuNPs remained stable after Ab functionalisation while also generating a strong SERS signal. (Concentration studies for MGITC and CRP Ab can be seen in Appendix A.1 - A.4).

Figure 3.7 (a) shows characterisation of AuNPs using extinction spectroscopy, after functionalisation with MGITC and Abs, and passivation with BSA. The LSPR peak remained sharp and narrow following both functionalisation steps. After MGITC attachment, there was a broad band observed at $\sim$700 nm indicating the presence of slightly larger aggregates however the AuNPs remained stable. After Ab conjugation the peak was observed to red-shift slightly from 527 nm to 529 nm but maintained its characteristic shape. This red-shift indicated an increase in particle size, consistent with the attachment of the Ab. The peak also appeared to be dampened suggesting refractive index changes at the interface between the AuNP surface and surrounding medium.

It should be noted that the ‘control AuNPs’ analysed for comparison had undergone all steps in the conjugation method excluding the addition of MGITC and Ab. This is the reason why the λmax for these AuNPs was red-shifted versus the synthesised AuNPs (figure 3.5) as there was BSA attached to the

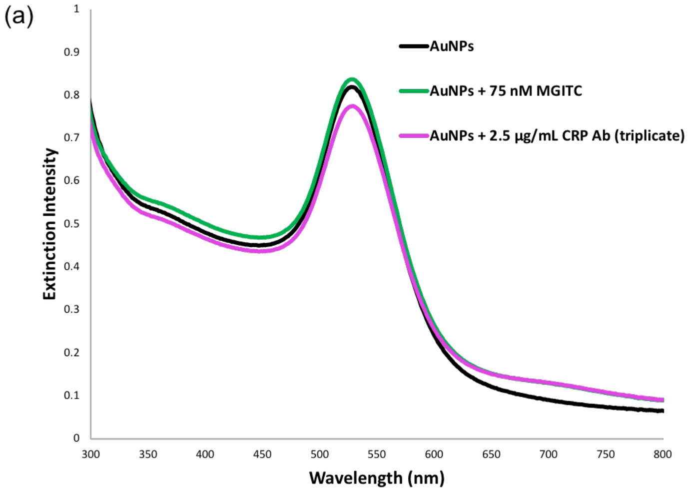

Sample	Extinction Intensity	λmax
AuNPs	0.82	527
75 nM MGITC	0.84	527
2.5 µg/mL CRP Ab	0.78	529

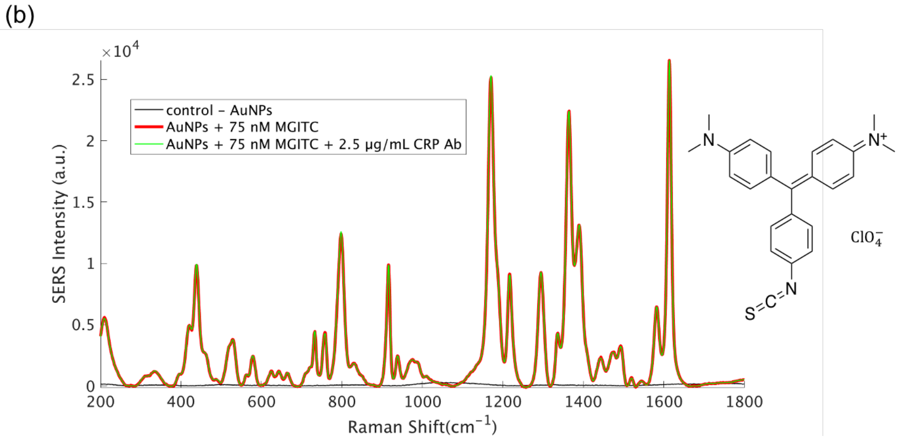

Figure 3.7: Results from the functionalisation of AuNPs with Raman reporter, MGITC and CRP-specific Ab. (a) Extinction spectroscopy results after attachment of MGITC and Ab with table displaying maximum extinction values and the λmax for each LSPR band and (b) corresponding SERRS results with MGITC structure in inset. SERRS spectra were acquired using a 638 nm laser wavelength, an acquisition time of 1 s and 100% laser power. All measurements were taken in triplicate.

surface and additionally, the AuNPs had been centrifuged. The corresponding SERS spectra are shown in figure 3.7(b). There was an intense signal observed after functionalisation with MGITC and this response was maintained following attachment of the Ab. There was a negligible difference in intensity between both spectra which indicated that the AuNPs hadn't aggregated after Ab addition.

To further prove that the Ab had successfully conjugated to the AuNP surface, a LFIA was run. Two LFIA strips were prepared. 0.6 μL of CRP protein (1 mg/mL) was spotted onto the NC membrane of each strip and allowed to dry at room temperature. Figure 3.8(a) shows both LFIA strips after running the assays with the functionalised AuNPs. For the control assay, AuNPs functionalised with MGITC only (AuNP-MGITC) were mixed with LFIA buffer (0.5% BSA, 0.05% Tween 20 in 1.72 mg/mL phosphate buffer powder) in a glass vial and run through the LFIA strip. These NPs did not bind to the CRP spot as there were no Abs bound to the AuNPs. AuNPs functionalised with both MGITC and CRP-specific Abs (AuNP-Ab) were run through the LFIA strip and these NPs were observed to bind to the CRP spot which can be seen from the appearance of the red spot in figure 3.8(a). The LFIA buffer recipe was important for optimum binding of AuNP-Abs to immobilised CRP, BSA discouraged non-specific interactions from occurring while the presence of Tween 20 ensured the AuNP-Abs were properly dispersed in solution.[89] The buffer also maintained a physiological pH of approximately 7.3.

Each spot was analysed using a benchtop Raman microscope at a laser excitation wavelength of 633 nm and SERS intensity maps (figure 3.8(b)) were constructed from the intensity of the 1617 cm^{-1} peak of MGITC (N-Ph ring and C-C vibrational stretch).[90] A handheld Raman spectrometer was also used to characterise the spots, the spectra collected from the spots are shown in figure 3.8(c). There was an intense MGITC spectrum observed for the sample assay (AuNP-Ab) while a very small signal was seen for the control assay (AuNP-MGITC) which is likely due to residual AuNPs in the NC membrane. However, it was clear that the Ab had successfully conjugated to the AuNPs as only AuNP-Abs bound to CRP.

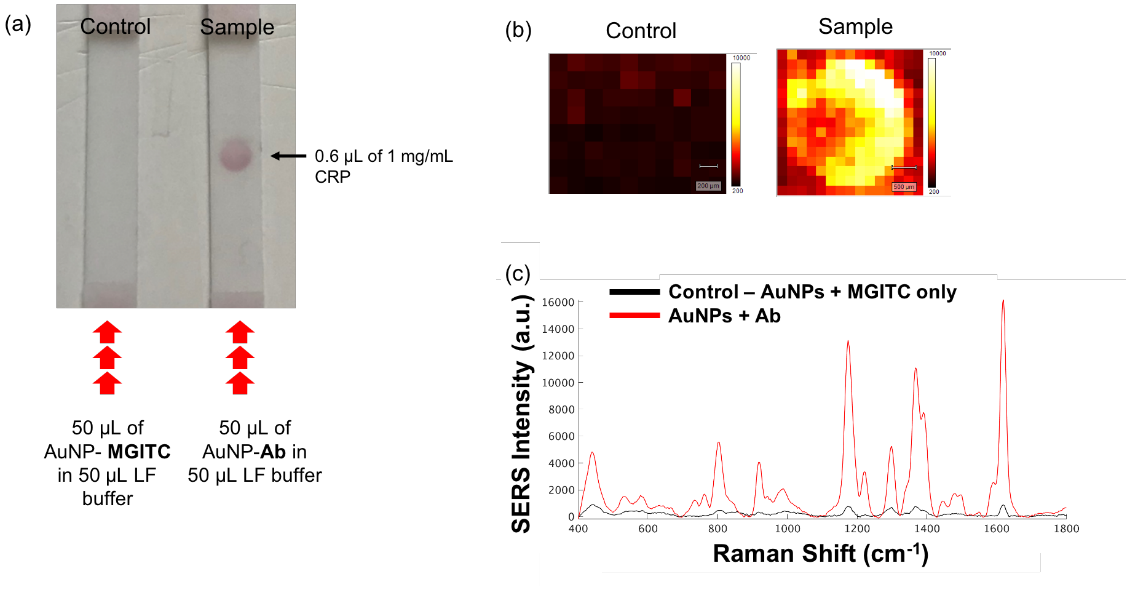

Figure 3.8: LFIAs performed to further confirm successful Ab conjugation (a)Image taken of both LFIA strips after they were run, a red spot was clearly visible only for AuNP-Abs, control AuNPs functionlalised only with MGITC did not bind to CRP, (b) SERS intensity maps from each spot constructed using the intensity of the 1617 cm^{-1} peak of MGITC, Raman mapping was performed on a benchtop instrument using 633 nm laser wavelength, 6 s acquisition time, 0.73 mW laser power and 100 μm step size and (c) handheld Raman analysis for each spot where an intense SERS spectrum was observed only for the sample LFIA strip of Ab functionalised AuNPs. Handheld Raman was carried out at 638 nm laser wavelength, 1 s acquisition time, 27.8 mW laser power and 3 scans were taken of each spot.

3.3.1.1. Sandwich Assay for CRP Detection on Lateral Flow

For the detection of CRP using the LFIA platform, it was necessary to perform a sandwich-type assay using this device. Therefore, CRP-specific Ab was immobilised at a concentration of 360 μg/mL on the NC membrane of two LFIA strips. This Ab would act as a capture site for CRP and would immobilise any AuNP-Ab-CRP immunocomplexes travelling along the strip. Since CRP has 5 identical epitopes, it was possible to use the same Ab for detection *i.e.* conjugated with the AuNPs and for capture of CRP on the LFIA strip. Figure 3.9 shows a schematic of how the sandwich assay was performed. 10 μL of AuNP-Abs were spotted onto the conjugate pad at a concentration of ~0.75 nM, these bound to

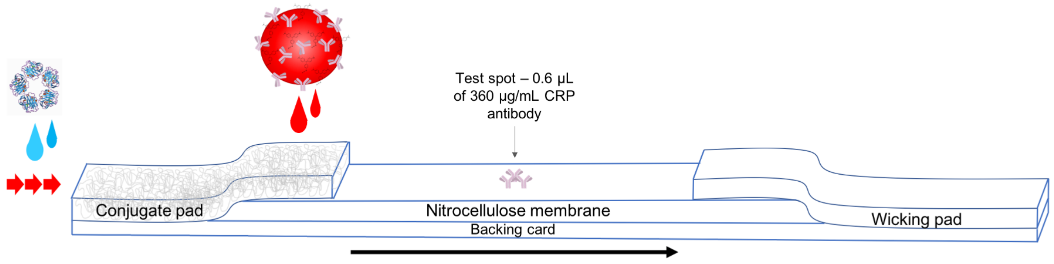

Figure 3.9: Schematic representation of how the sandwich-type assay for CRP was run on a LFIA strip. Firstly, the Ab was immobilised on the NC membrane and concentrated AuNP-Abs were spotted onto the conjugate pad. The LFIA strip was placed in a glass vial containing a solution of CRP prepared in LFIA buffer, this flowed upwards through the strip via capillary action. The CRP should complex with the AuNP-Abs and travel along the strip until these complexes were captured by the immobilised Ab, forming a red spot of accumulated AuNPs. Schematic not to scale

CRP in buffer solution flowing upwards through the strip. In the presence of CRP, a red spot of accumulated AuNPs appeared on the location where the Ab had been immobilised on the NC membrane.

The results from the sandwich assay are shown in figure 3.10, one buffer solution contained 100 ng/mL CRP while the control had no CRP present (0 ng/mL CRP). From the scanned images (figure 3.10(a)), an intense red spot was observed for the sample containing 100 ng/mL CRP only. Colourimetrically, there was no evidence of non-specifc binding of AuNP-Abs to the immobilised Ab in the control assay as no red spot appeared. Raman mapping was performed on each spot and maps were constructed from the intensity of the 1617 cm^{-1} peak of MGITC (figure 3.10(b)), an intense SERS signal was generated from the 100 ng/mL CRP assay while negligible signal was obtained for the control assay. Each spot was also analysed using a handheld Raman spectrometer as shown in figure 3.10 (c). Results from this were consistent with visual and Raman mapping analyses, an intense SERS signal was observed only when CRP was present in the buffer.

Therefore, it was clear that the sandwich assay had worked successfully on

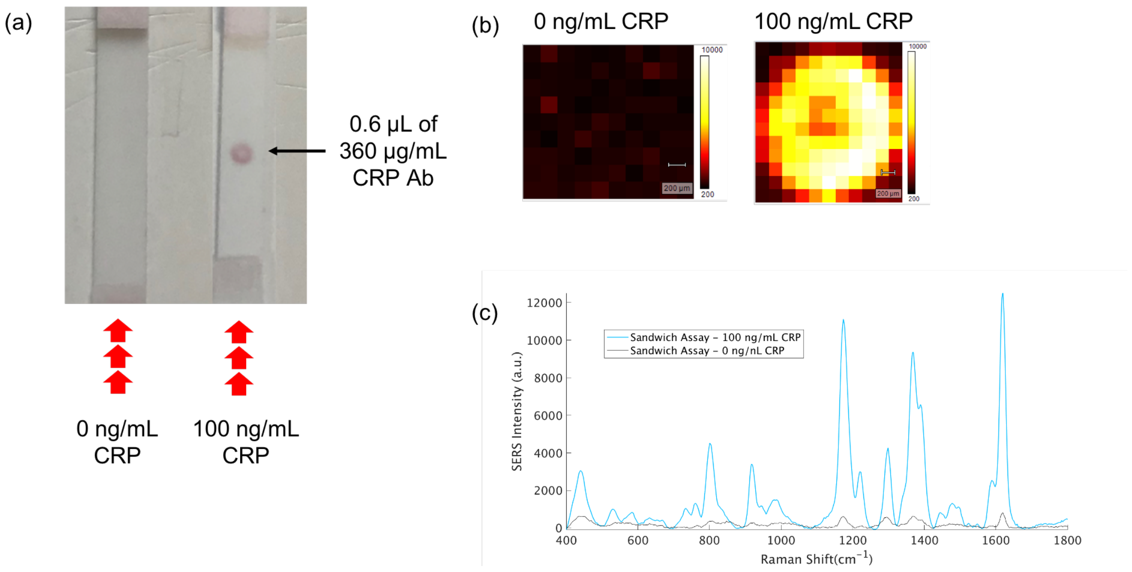

Figure 3.10: Results from on/off sandwich-type assay for CRP detection (a) Images of sandwich assay run for 0 ng/mL CRP vs. 100 ng/mL CRP, 360 ţg/mL CRP Ab was spotted on to the NC membrane and a red spot was observed in the presence of CRP only, (b) SERS intensity maps from each spot constructed from the intensity of the 1617 cm^{-1} peak of MGITC, Raman mapping was performed on a benchtop instrument at 633 nm laser wavelength, 6 s acquisition time, 0.73 mW laser power and 100 μm step size and (c) handheld Raman analysis for each spot where an intense SERS spectrum was observed only for 100 ng/mL CRP. Handheld Raman was carried out at 638 nm laser wavelength, 1 s acquisition time, 27.8 mW laser power and 3 scans were taken of each spot.

the LFIA platform and qualitative information could be obtained confirming the presence or absence of CRP. It was also apparent that the handheld Raman spectrometer results were consistent with the benchtop instrument. Therefore, a CRP concentration study was performed to deduce whether quantitative information could be obtained using this assay platform and how this would compare to colourimetric techniques already widely used for LFIA characterisation. A comparison study of the benchtop Raman system compared with the handheld instrument was also carried out to determine the viability of using the handheld spectrometer, in tandem with this assay platform, with the aim of developing point-of-care biomarker detection for sepsis diagnosis.

3.3.2 CRP Concentration Study - Comparing benchtop and handheld Raman Analyses

A concentration study was carried out using the following concentrations of CRP - 100 ng/mL, 50 ng/mL, 25 ng/mL, 20 ng/mL, 10 ng/mL, 5 ng/mL and 0 ng/mL. LFIA strips were performed as described in section 2.4 and all CRP concentrations were prepared in LFIA buffer. AuNP-Ab conjugates were concentrated by centrifugation (0.75 nM) and 10 μL of this was pipetted onto the conjugate pad. Each strip was placed in a glass vial containing 100 μL of a CRP concentration solution. For all concentrations, excluding the blank (0 ng/mL CRP), red spots were observed on the NC membrane confirming the presence of CRP which can be see from the images shown in figure 3.11 (a). The spots increased in intensity at higher CRP concentrations, more immunoreactions occurred and it appeared, at least visually, that a quantitative response had been achieved.

3.3.2.1. Raman Mapping Analysis and RGB Values

To quantify the results, each spot underwent Raman mapping analysis using laser excitation wavelength of 633 nm. Colourimetric analysis in the form of RGB values was also performed for quantification. The concentration study was carried out in triplicate, figure 3.11 (a) shows scanned images of LFIA strips from one concentration study and the corresponding SERS intensity maps for each spot. From the scanned images, visually, the red spot was observed to diminish in intensity with decreasing CRP concentration and there was no spot observed for the blank (0 ng/mL CRP). The same trend was observed for the mapping analysis. Raman mapping was carried out on a benchtop microscope system and the SERS intensity maps were constructed from the 1617 cm^{-1} peak of MGITC.

The shape of each spot was evident in the Raman maps and their intensity was also clearly observed to decrease with decreasing CRP concentration. It was also observed that as CRP concentration decreased, the SERS response from each spot appeared in a half-moon shape representing the region of highest SERS intensity. This phenomenon was due to the immediate interactions between AuNP-Ab-CRP complexes and immobilised capAbs as soon as contact was made and was indicative of high-affinity binding.[64] As the the AuNP-Ab-CRP complexes flowed along the NC membrane, they bound instantly to the capAbs, rapidly occupying binding sites as they continued to flow further along the strip. At high concentrations of 100 ng/mL CRP, there were enough AuNP-Ab-CRP complexes to form a circular region of SERS intensity as shown in figure 3.11 (a). However, at lower concentrations the high-affinity interactions were more prevalent in the SERS intensity maps as the regions of initial contact appeared as a half-moon area of intense SERS signal. Scanned images and Raman mapping data from all three concentration studies are shown in Appendix A.5.

Figure 3.11 (b) shows the average spectra from triplicate studies for each map at each CRP concentration. There was a clear trend of decreasing SERS intensity with decreasing CRP concentration. To determine the LOD for the SERS analysis, the intensity of the 1617 cm^{-1} peak from figure 3.11 (b) was plotted against CRP concentration across three experiments (figure3.11(c)). The calibration curve was constructed of the linear region of the full concentration range graph shown in the inset of figure 3.11 (c). As shown in the inset, at 50 ng/mL CRP, the relationship between SERS intensity and CRP concentration plateaued indicating binding saturation had occurred *i.e.* AuNP-Ab-CRP complex binding at the capAb region had reached a maximum and no further interactions would occur to contribute to an increase in SERS signal. From the calibration curve, a LOD for CRP from the Raman mapping analysis was calculated using equation3.1:

$$LOD = 3(\frac{SD}{m}) \tag{3.1}$$

where SD is the standard deviation of the blank (0 ng/mL CRP averaged signal)

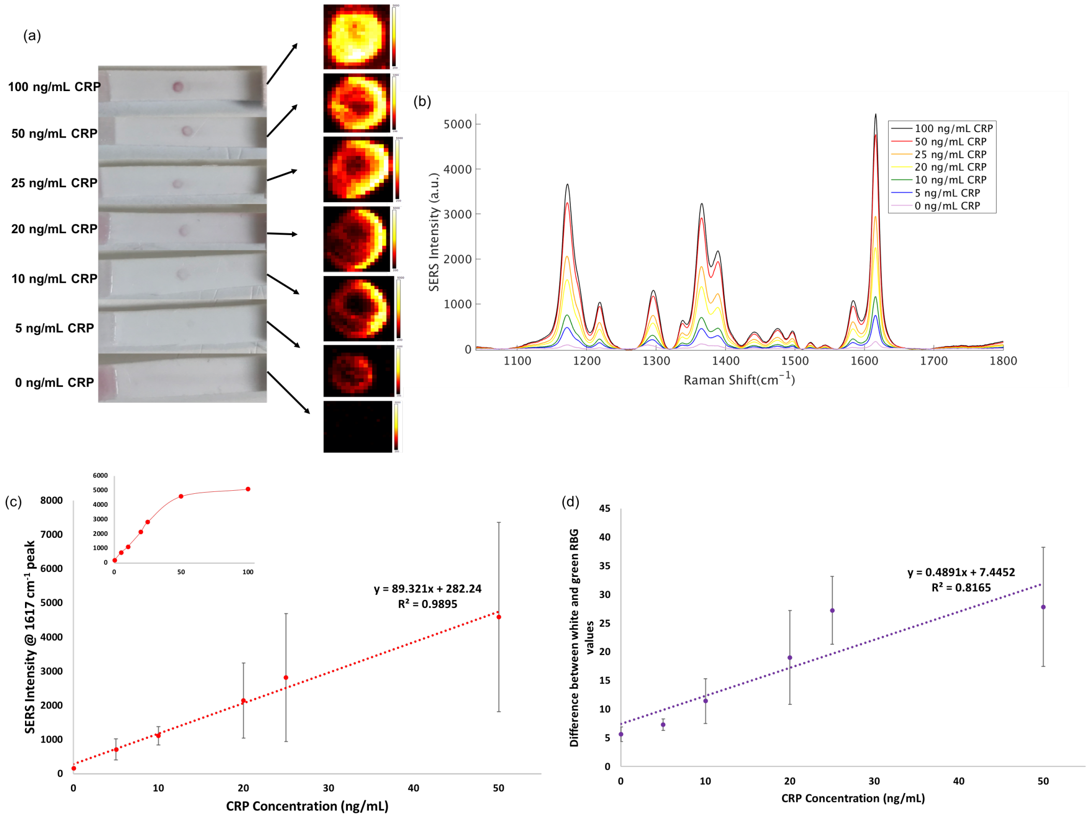

Figure 3.11: Results from using the benchtop Raman instrument for quantitative analysis of CRP concentration study - (a) Images of the LFIAs scanned using an Epson flatbed scanner. The images shown are from one study showing visually the diminishing red spot with decreasing CRP concentrations of - 100 ng/mL, 50 ng/mL, 25 ng/mL, 20 ng/mL, 10 ng/mL, 5 ng/mL and 0 ng/mL CRP. Alongside, are the corresponding SERS maps constructed from the 1617 cm^{-1} peak of MGITC, the SERS intensity decreases with decreasing CRP concentration and there was no signal in the blank. The study was carried out in triplicate and (b) shows the average SERS spectrum for each CRP concentration across the three studies, the SERS signal was observed to increase with increasing CRP concentration, (c) calibration curve from Raman microscope map data from average intensity of the 1617 cm^{-1} peak of MGITC for CRP concentration range 0 - 50 ng/mL with inset showing curve begins to plateau at higher concentrations. An LOD of 1.2 ng/mL was calculated from the curve and (d) RGB values from 0 - 50 ng/mL CRP, a LOD of 16.4 ng/mL was calculated for this analysis. Raman mapping analysis was carried out using 633 nm laser wavelength, 0.73 mW laser power, 6 s acquisition time and 100 μm step size. Data was processed using Matlab and calibration curves were constructed in Excel.

and m is the slope of the calibration curve. The LOD for CRP using SERS mapping data was calculated to be 1.2 ng/mL. Th large error bars for the calibration curve in figure 3.11 (c) should be noted, this large error between experiments may be due to areas of accumulated AuNPs forming regions of SERS hotspots generating very high SERS signals.

RGB values were obtained using a flatbed scanner. The results were analysed using ImageJ software and the green values for each spot were recorded. The green values were chosen because green light is absorbed by 38 nm AuNPs.[91] A calibration curve was constructed based upon the averaged RGB values for each CRP concentration and is shown in figure 3.11(d). The results are in accordance with the Raman mapping, displaying a general decreasing trend with decreasing CRP concentration. Again, the error between the three replicates was large for the RGB analysis where high AuNP accumulation lead to high RGB values. There may be several factors contributing to this such as subtle differences between replicates of how the fluid flows through the membrane of the device. Additionally, the Ab was manually spotted onto the NC membrane therefore homogenous distribution of the Ab was difficult to attain. These issues can be rectified with the use of LFIA assembly instruments such as a membrane plotter for the immobilisation of the capture Ab in a uniform line distribution and a strip cutter to ensure each device is the same width, thereby ensuring the flow rate of each device is the same.

A LOD of 16.4 ng/mL was calculated for RGB analysis using equation3.1. In comparison, Raman mapping data had a LOD of 1.2 ng/mL. Therefore, while both approaches gave a quantitative response, SERS detection out-performed RGB analysis and gave a LOD that was over a factor of 10 lower. However, Raman mapping was carried out on a benchtop microscope system and each map took approximately 30 mins to acquire. For biomarker detection to be clinically feasible and faster, portable methods are essential for use in a point-of-care setting.

3.3.2.2. *Analysis of lateral flow assay strips using a handheld Raman spectrometer*

A handheld CBEx Raman spectrometer from Snowy Range Instruments was used to analyse the lateral flow strips from the triplicate study. The advantages of using a portable instrument over a benchtop microscope instrument include its size and portability but also the time it takes to scan each strip. Each spot was scanned a total of 6 times with an acquisition time of 1 s per scan. This is a much smaller timescale per analysis compared with the 30 minute mapping time on the microscope instrument. An image of both instruments can be found in Appendix A.6 illustrating the size difference between the two instruments. A 3D-printed adaptor designed and printed by Mabbott *et al.* was placed over an attachable objective lens on the handheld instrument.[60] The adaptor has a 4 mm circular opening over which the lateral flow strip was placed. This allowed the LFIA spot to be accurately aligned and focussed with the laser spot from the objective lens. Figure 3.12 shows the design and dimensions of the adaptor as developed by Mabbott *et al.* and how the adaptor was fitted onto the instrument over an attachable objective lens.

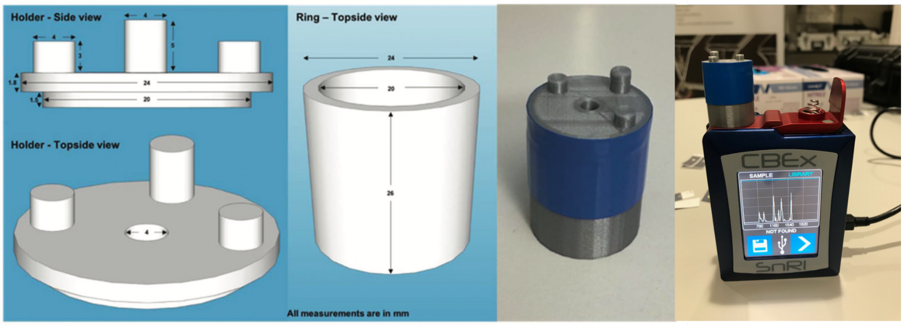

Figure 3.12: The dimensions and design of the 3D-printed adaptor from Mabbott *et al.* with 4 mm aperture opening to allow for analysis of spots on the LFIAs and an image of the handheld Raman instrument with attachable point and shoot lens showing how the adaptor fits over the lens.[60]

Using the adaptor, it was possible to hold the strip in position and scan a selected area on the strip while restricting background light from entering the

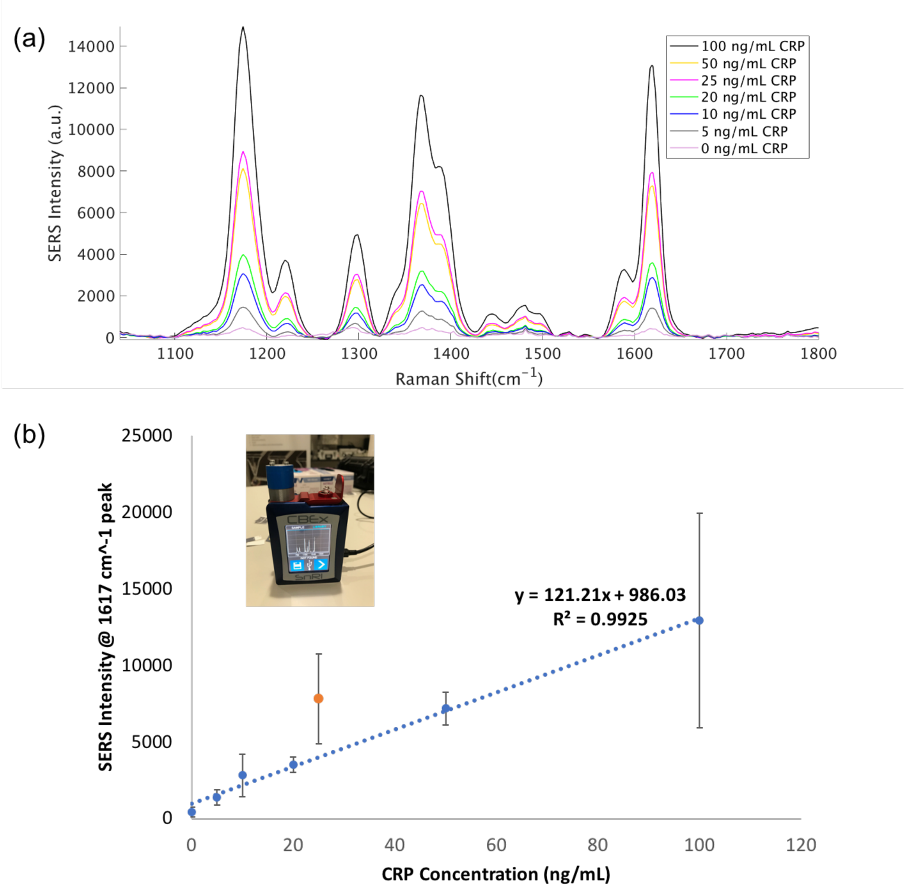

Figure 3.13: Results from handheld Raman analysis of triplicate CRP concentration study - (a) average SERS spectra from each concentration study showing a decreasing intensity trend with decreasing CRP concentration and (b) calibration curve constructed from average intensity of 1617 cm^{-1} peak for each CRP concentration, there was a clear outlier at 25 ng/mL (represented by orange data point) which has been excluded from the trendline calculation. An R^2 value of 0.9925 and LOD of 8 ng/mL were calculated. Handheld Raman scans were performed using a 638 nm laser wavelength, 27.8 mW laser power, 1 s acquisition time with each assay scanned 6 times. Data was processed using Matlab and calibration curves were constructed in Excel.

aperture and hampering the SERS signal. Figure 3.13(a) shows averaged spectra collected across the three concentration studies. The SERS intensity was consistent with the Raman microscope, showing decreasing SERS intensity with decreasing CRP concentration. The calibration curve for SERS intensity of the 1617 cm^{-1} peak with respect to CRP concentration is shown in figure 3.13(b). Excluding an outlier for 25 ng/mL CRP represented by the orange data point (see Appendix A.7), the curve has an R^2 value of 0.9925. The relationship is close to linear, with no plateau occurring at higher CRP concentrations. This indicated the possibility of recording higher dynamic range measurements using the handheld spectrometer. Certainly, handheld analysis can be described as being quick and portable, two criteria which are necessary for point-of-care detection and diagnosis. A LOD of 8 ng/mL CRP was calculated from the handheld SERS data, higher than that calculated from SERS maps, but well within the range considered to be clinically relevant (>10 μg/mL). The handheld spectrometer also offers portability at a much lower cost compared to an expensive benchtop instrument.

3.3.3 Detection of CRP in Human Samples

Clinical and biological studies often use serum and/or plasma as their preferred sample matrix. The choice of which matrix used depends upon what is being measured and the analysis method since serum and plasma differ in their biological and chemical make-up. Essentially, serum is blood plasma that does not contain fibrinogen *i.e.* any clotting factors. To extract serum from a blood sample, coagulation is allowed to happen and the sample is centrifuged to remove the fibrin clots, blood cells and any other clotting factors present. The serum is the supernatant collected from the centrifuged sample. Blood serum primarily consists of water and large proteins like human serum albumin and globulins such as Abs. It also contains hormones and exogenous substances like drugs and invading pathogens.[92,93]

Blood plasma is extracted in much the same way however an anti-coagulant *e.g.* EDTA, heparin or citrate, is added to the blood before centrifugation. This means plasma retains all clotting factors present in the blood. Like serum, all leukocytes and erythrocytes are removed and only the liquid content of the blood remains. Critically, as blood components, both serum and plasma perfuse tissue and therefore biomarkers present in these matrices can give a good indication of disease states.[92,93]

It is important to maintain a standardised sampling method when handling serum and plasma to ensure that pre-analytical variation does not have an effect on the final result. Friebe *et al.* investigated the effect of the anti-coagulant agent used for plasma samples when detecting three cytokines - tumour necrosis factor α (TNFα), IL-6 and IL-8.[94] They also compared their results to serum samples and tracked the time and treatment *i.e.* storage temperature of plasma/serum from the time the blood was taken to when separation of serum/plasma was performed. Their findings showed that the stability of all cytokines was consistent in EDTA plasma while in heparin plasma and serum, increased secretion levels of both TNFα and IL-8 were evident. The authors main finding centred around the time between blood collection and plasma separation where they found cytokine stability remained constant at room temperature for 8 hours, depending on the anti-coagulant used.[94] In a review on pre-analytical variation, Jackson *et al.* outlined all the factors that can introduce variation in blood-related samples; sample type and container, processing and handling *i.e.* how long between blood collection and separation in the case of plasma and how long the blood is left to clot with regards to serum, and storage after processing.[95] While most banks will have a standardised protocol for each step, there is not yet a universal procedure in place and the protocols mainly rely on preference and the analytes being investigated.[95]

The serum and human samples used in this study were gifted by Professor James Dear from the Queen Medical Research Institute (QMRI) at University of Edinburgh where the samples had been collected from the Royal Infirmary Hospital, Edinburgh. The patient samples used were from a paracetemol overdose study therefore all patients had been treated with the protocol for N-acetylcysteine (NAC) prior to having blood samples taken. The blood management SOP used in the trial is attached to the Appendix and specifies the collection of bloods is followed as per the local protocol for NAC.

All samples were centrifuged at 2500 g for 10 minutes at 4°C. Serum samples were left to stand for 30 mins before being centrifuged in order to allow coagulation. Plasma samples were treated with the anti-coagulation agent EDTA. After collection, samples were immediately transferred to a -20°C research freezer. The samples were transported from Edinburgh Royal Infirmary Hospital to QMRI on dry ice. All samples were collected in 2018 and stored at -80°C until use at QMRI.

To determine which matrix worked best with the LFIA platform, CRP detection was trialled initially in both serum and plasma. It should be noted that different version of the Raman microscope instrument was used for all human samples. All LFIA devices and reagents were prepared and the data analysed and processed by myself. All devices were run with serum and plasma samples in the QMRI lab by Dr Sian Sloan-Dennison due to health and safety restrictions. Raman analysis of the clinical samples was also performed by Dr Sloan-Dennison due to health and safety restrictions.

3.3.3.1. CRP detection in human serum samples

Serum samples were spiked with CRP as described in section 2.4. Following a similar protocol as possible to the studies performed in buffer, 100 μL of sample solution was prepared. In the case of serum samples, 25% of the sample was serum and CRP was added to a fixed volume of 25 μL of serum. This was made up to 100 μL with LFIA buffer. Dilution of the serum in buffer was necessary to reduce cross-reactivity, non-specific binding and matrix effects which could have interfered with the binding ability of the Abs. The serum was spiked with the following concentrations of CRP - 0, 1, 5, 10, 25, 50 and 100 ng/mL. The LFIA strips were run as described in section 2.4. A capture Ab concentration of 500 μg/mL CRP Ab was spotted onto the LFIA strips. This concentration was higher than that used when running the assay in buffer (360 μg/mL) and was chosen to encourage immunoreactions to occur in the more complicated biological matrix.

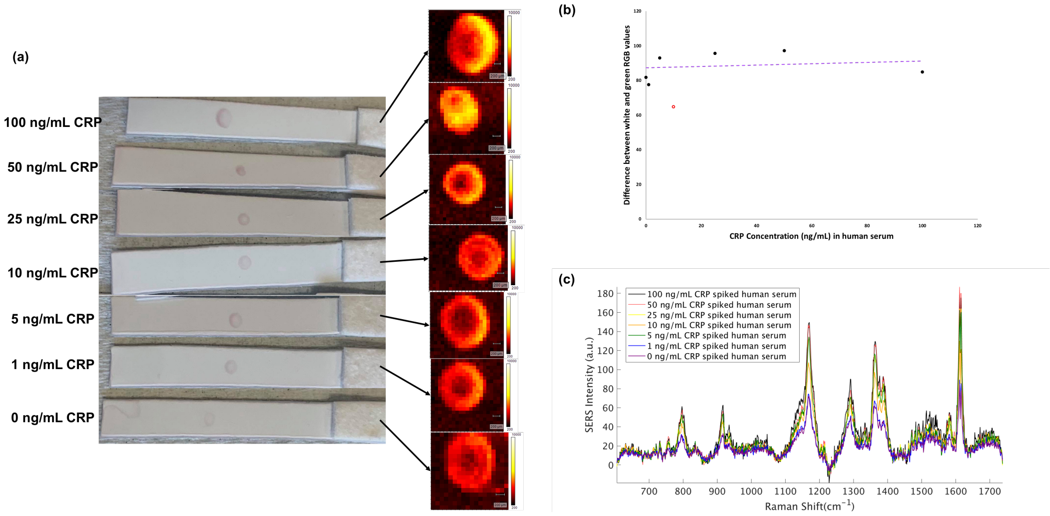

Figure 3.14: Results from CRP concentration study from spiked human serum samples (a) Image taken of LFIAs run for the following concentrations of CRP - 100, 50, 25, 10, 5, 1, and 0 ng/mL and corresponding SERS intensity maps, visually the majority of the red spots look the same with there being only a discernible difference between 100 and 0 ng/mL. From the SERS map data, the signal at higher concentrations was observed to be more intense, particularly for 100 ng/mL however there was still a strong signal for the blank sample, (b) calibration curve of calculated RGB values versus CRP concentration, there was no apparent trend as all values were similar with the exception of an outlier at 10 ng/mL CRP (red data point), this analysis offered no quantitative value and (c) average spectra from each map at each CRP concentration, there appeared to be a general decreasing trend however it was not linear. Raman maps were constructed from the 1617 cm^{-1} peak of MGITC and measurements were carried out at 633 nm laser excitation, 0.1 s acquisition time, 100% laser power and 100 μm step size. RGB values were calculated from scanned images using ImageJ.

Figure 3.14 (a) shows images of each LFIA strip after the assays were run and the corresponding SERS intensity maps for each CRP concentration. The maps indicated that the SERS intensity was indeed higher between 25 - 100 ng/mL CRP compared with the lower concentrations however, it was evident that there was a strong SERS response from the blank sample (0 ng/mL CRP). Since the serum samples used were from human subjects, it was expected that there would be a baseline concentration of CRP present in all of these samples. Normal levels of CRP should be below 3 ug/mL however, these patients may have had higher levels due the presence of inflammation.

A calibration curve of calculated RGB values against CRP concentration is shown in figure 3.14 (b). From this analysis, little difference between RGB values corresponding to each CRP concentration was observed and there was no apparent trend in the results. Therefore, quantitative information could not be appropriated from this analysis.

Figure 3.14 (c) shows the average spectra from each SERS map analysis for each CRP concentration. There appeared to be a general increasing trend in SERS intensity with increasing CRP concentration however, the mapping analysis indicated a SERS signal was observed for the blank sample, similar in intensity to the 100 ng/mL CRP sample. It was thought that this was due to baseline CRP levels already present in the serum which may have been present at approximiately 100 ng/mL CRP. Taking dilution factors into account (1 in 4 diluton of serum sample in buffer), this would be equivalent to 400 ng/mL or 0.4 μg/mL CRP and levels below 3 μg/mL are considered to be healthy therefore it is feasible this level would be present in the serum patient samples.[22]

It should be noted that the 1617 cm^{-1} peak presented as a doublet following analysis of the serum samples using the benchtop Raman instument while it had appeared as a singlet peak in buffer studies. This may have been due to the addition of a complex matrix into the sample. The serum made up 25% of the sample and this may have contributed to changes in vibrational contributions from MGITC resulting in changes in peak ratios of the doublet peak at 1617 cm^{-1}. Therefore, the SERS intesnsity of the 1170 cm^{-1} peak, a singlet peak, was also used to attain quantitative information.

Figure 3.15 shows calibrations curves compared for both SERS intensity peaks at 1617 cm^{-1} and 1170 cm^{-1}. Figure 3.15 (a) and (b) show calibration curves constructed from the 1617 cm^{-1} peak of MGITC where (a) was generated from the data plotted against CRP concentration and (b) was produced from plotting data against $\log_{10}$ of CRP concentration. Using the logarithmic curve, a R^2 value of 0.9310 was calculated compared with $R^2 = 0.8739$ for the linear curve. A similar result was found when plotting the 1170 cm^{-1} peak against CRP concentration

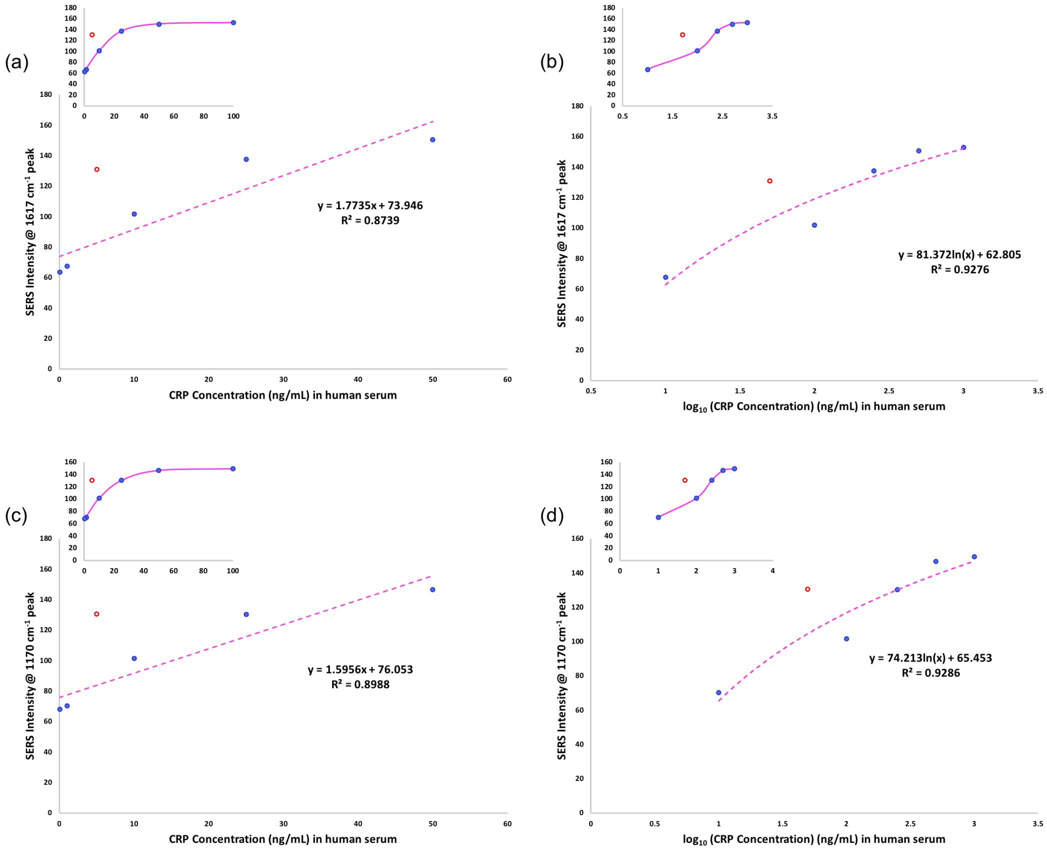

Figure 3.15: Calibration curves from Raman mapping data (a) SERS intensity at 1617 cm^{-1} peak against CRP concentration in human serum across following range - 0, 1, 5, 10, 25, 50 and 100 ng/mL CRP and (b) against log$_{10}$(CRP concentration) which generated an improved R^2 value of 0.9310 when compared with (a) of 0.8739. A clear outlier was identified at 5 ng/mL CRP and is represented by the red data point. Since the doublet peak at approximately 1617 cm^{-1} was more prevalent using serum, the SERS intensity of 1170 cm^{-1} peak was also chosen to construct the calibration curves (c) against CRP concentration and (d) against log$_{10}$(CRP concentration) where again and improved R^2 value was observed for the logarithmic curve of 0.9835 compared with 0.8988 for (c). An outlier at 5 ng/mL CRP was present and is represented by the red data point. Data was processed using Matlab and calibration curves were constructed in Excel.

(3.14 (c) and (d)). R^2 values of 0.8988 for the linear trend and 0.9835 for the logarithmic curve were calculated. It appeared that a logarithmic fit demonstrated improved correlation with the data compared with a linear fit. In all curves, an outlier at 5 ng/mL CRP was represented by the red data point. This may be due to the formation of hotspots regions of accumulated AuNPs generating an enhanced signal compared with the 10 ng/mL sample caused by the heterogenous drying of the immobilised Abs onto the NC membrane. The linear calibration curve including this outlier as a data point is shown in Appendix A7.

From this preliminary concentration study in human serum samples, it was evident that an increase in spiked CRP concentration was necessary to determine whether quantitative information could be gleaned from the assay. Human plasma may be a more representative medium as the blood sample does not undergo coagulation for plasma separation. Therefore, a concentration study using higher concentrations of CRP in human plasma samples was performed.

3.3.3.2. CRP detection in human plasma samples

As previously discussed, plasma is the liquid component of the blood that retains clotting factors *i.e.* fibrinogen. This is because an anti-coagulant is added to the blood before plasma separation. This means the are more biological species present in plasma which may interfere with interactions between AuNP-Ab complexes, CRP and the Ab immobilised on the NC membrane. It was also expected that there would be a baseline concentration of CRP already present in the plasma samples.

The following concentrations of CRP were used - 0, 100, 300, 500 750, 1000 and 2000 ng/mL CRP. The preparation of plasma samples is described in section 2.4, CRP was added to 25 μL of plasma and made up to 100 μL with LFIA buffer, thereby keeping the volume of plasma the same for each sample. When taking into account the 1 in 4 dilution factor of the plasma in buffer, these spiked CRP concentrations would be equivalent to 0, 0.4, 1.2, 2, 3, 4 and 8 μg/mL. CRP concentrations below 3 μg/mL are considered to be normal while increases above this are deemed to be clinically relevant while concentrations greater than 10 μg/mL are indicative of a disease state.[22] Therefore the concentrations chosen for the study in plasma were more representative of clinical CRP blood levels. The LFIA strips were prepared as described in section 2.4, 500 μg/mL of CRP

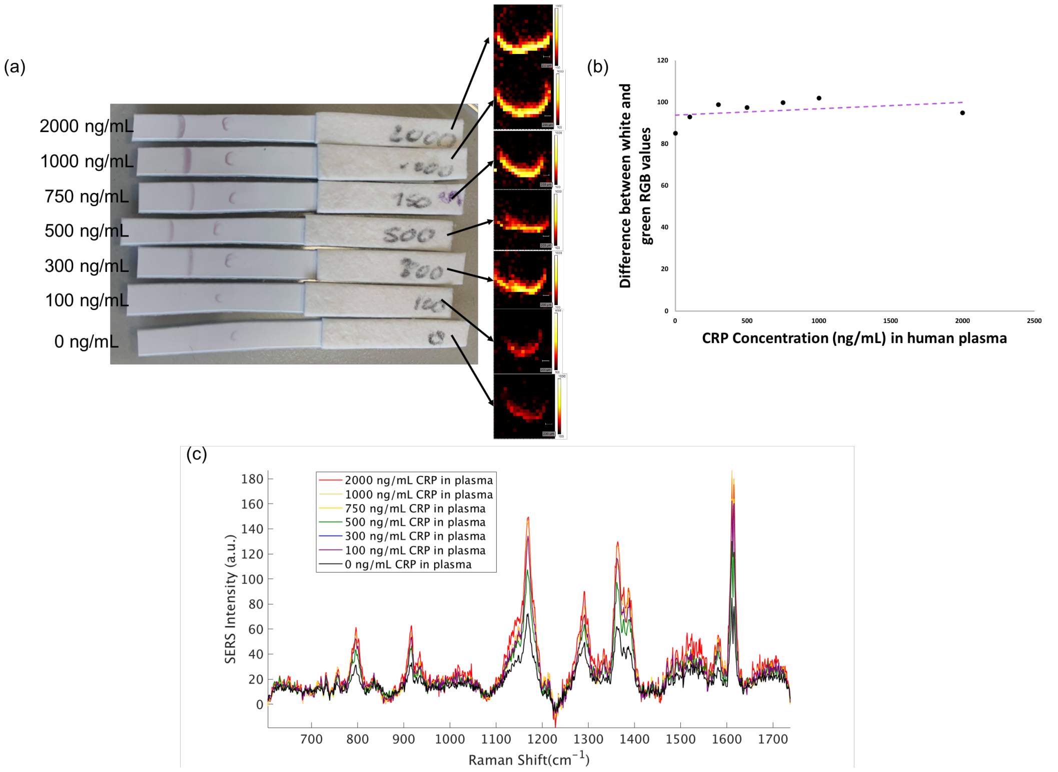

Figure 3.16: Results from LFIA with CRP-spiked human plasma (a) images of LFIA strips and corresponding SERS intensity maps. A half-moon shape was observed for the interaction of AuNP-Ab-CRP complexes with the immobilised Ab which was an indication of highly specific binding, there was a clear decrease in intensity for 100 ng/mL CRP and 0 ng/mL CRP however the maps for these samples appeared visually similar. The maps were constructed from the 1617 cm^{-1} peak, (b) calibration curve of calculated RGB values against CRP concentration, each concentration was observed to give a similar colourimetric response and (c) average spectra from each map for each concentration of CRP where there appeared to be a general decreasing trend in SERS intensity with decreased CRP concentration. Raman map data was performed using 633 nm laser excitation, 0.5 s acquisition time, 10% laser power and 100 μm step size. RGB values were calculated from scanned images using ImageJ.

Ab was spotted onto the NC membrane. The results from the assays along with the corresponding SERS intensity maps are shown in figure 3.16 (a).

The binding observed for the AuNP-Ab-CRP complexes with the immobilised CRP Ab resulted in a half-moon shape. This type of interaction suggested high-affinity binding that was very specific.[64] It was difficult to determine visually from the Raman maps the trend in SERS intensity however it was evident that between

100 ng/mL CRP and 0 ng/mL CRP samples, there was an observable decrease in SERS response. The signal observed for the blank was due to the baseline CRP levels already present in the plasma samples which may have been approximately 0.4 μg/mL or 400 ng/mL (0.1 μg/mL or 100 ng/mL after dilution). These levels would be in line with what is considered normal at below 3 μg/mL.[22]

Figure 3.16 (b) shows the calibration curve constructed from the RGB values calculated for each spot. There was no apparent trend as all concentrations were observed to exhibit a similar colourimetric response, therefore no quantitative information could be gleaned from using this technique.

Figure 3.16 (c) shows the average spectra for each map and a general decreasing trend in SERS intensity was observed. It should also be noted that, as in the case of serum samples, the 1617 cm^{-1} peak, usually observed as a singlet peak in buffer, was again generated as a doublet peak in plasma samples. Therefore both the 1617 cm^{-1} and 1170 cm^{-1} peaks were compared moving forward.

Figure 3.17 shows the calibration curves constructed from the 1617 cm^{-1} and 1170 cm^{-1} peaks of the spectra shown in figure 3.16 (a). A linear trendline was compared to a logarithmic fit to determine which function best fitted the data. In both instances there was an outlier at 300 ng/mL CRP which is represented by the red data point in all graphs, this may have arised due to the preparation of the LFIA resulting in a fault when running the assay. Figure 3.17 (a) and (b) show the linear and logarithmic relationships between CRP concentration and SERS intensity of the 1617 cm^{-1} peak. In (a), the inset curve is across the full concentration range (0 - 2000 ng/mL CRP) and it was from the linear region of this curve (0 - 1000 ng/mL CRP) that a R^2 value of 0.9831 was calculated. This is an improved fit compared with (b) showing the log-linear curve. The same comparison was carried out for the 1170 cm^{-1} peak. Figure 3.17 (c) shows the linear relationship with R^2 value 0.9891 which again appeared to be a better fit than the logarithmic trend in (d).

The LFIA strips from the CRP-spiked plasma concentration study were also

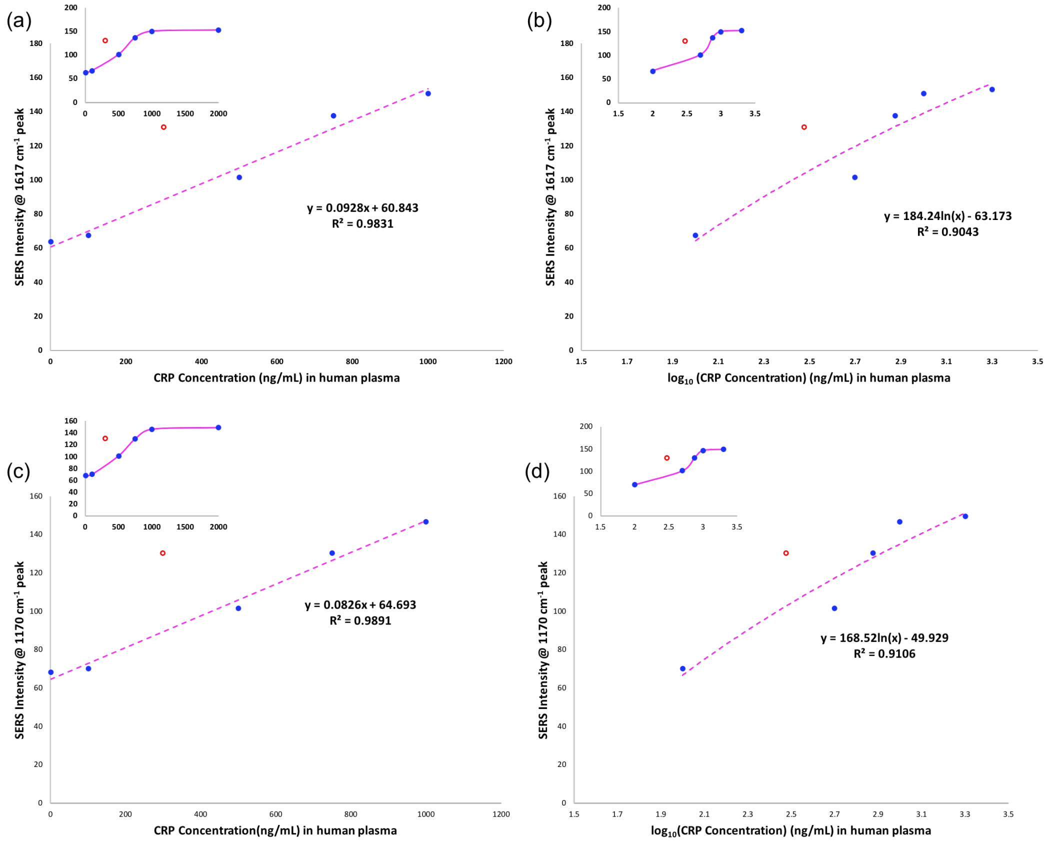

Figure 3.17: Calibration curves from CRP concentration study in human plasma (a) SERS intensity of 1617 cm^{-1} peak against CRP concentration taking linear range of curve shown in inset, a R^2 value of 0.9831 was calculated for this curve, (b) SERS intensity at 1617 cm^{-1} peak against log$_{10}$ of CRP concentration, the logarithmic fit was found to have an R^2 value of 0.9043, (c) SERS intensity at 1170 cm^{-1} peak against CRP concentration across linear range from the inset curve with R$_2$ value of 0.9891 and (d) SERS intensity at 1170 cm^{-1} against log$_{10}$ of CRP concentration with R^2 value of 0.9106. An outlier at 5 ng/mL CRP is shown in each graph, represented by the red data point. Data was processed using Matlab and calibration curves were constructed in Excel.

---

analysed using a handheld spectrometer at 638 nm laser excitation to determine whether the results would be comparable to the benchtop Raman microscope. Figure 3.18 shows the average spectra for a total of 9 scans for each CRP concentration. The average spectra for each concentration (figure 3.18 (a)) showed a general decrease in SERS intensity with decreasing concentration, however, for 2000 ng/mL CRP the signal was observed to diminish indicating that higher con-

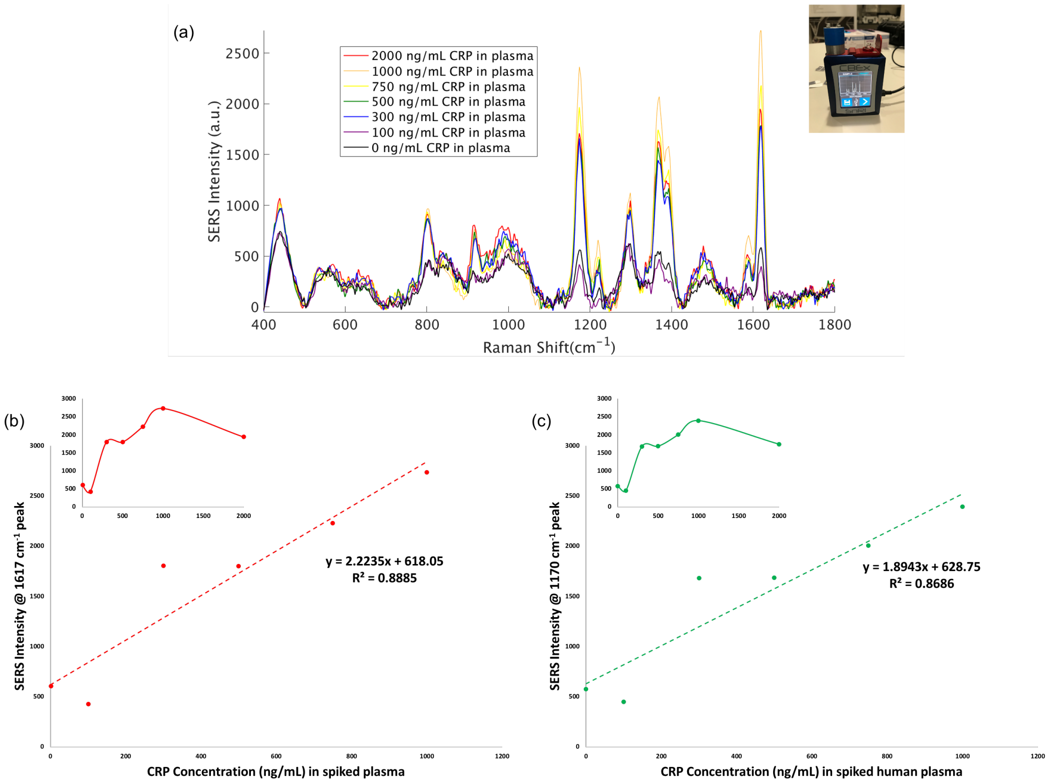

Figure 3.18: Analysis of LFIA from plasma samples using a handheld Raman spectrometer (a) average spectra for each CRP concentration, there was a general decreasing trend of SERS intensity with CRP concentration however, at 2000 ng/mL CRP the SERS response appeared to decrease again, (b) calibration curve (0 - 1000 ng/mL CRP) constructed from the 1617 cm^{-1} peak and the linear region of the graph show in the inset, a R_2 value of 0.8885 was calculated from the linear fit, (c) calibration curve (0 - 1000 ng/mL CRP) constructed from the 1170 cm^{-1} peak and the linear region of the graph show in the inset, a R_2 value of 0.8686 was calculated. Handheld Raman analysis was performed using 638 nm laser excitation, 0.2 s acquisition time and laser power of 27.8 mW. The study was carried out in triplicate and each assay spot was scanned 3 times.

centrations may be outside the range of the assay with regards to handheld analysis. The benchtop instrument demonstrated a plateau in concentration >1000 ng/mL.

Figure 3.18 (b) and (c) show calibration curves of CRP concentration graphed against (b) 1617 cm^{-1} and (c) 1170 cm^{-1} peaks. The linear fit was marginally improved for the 1617 cm^{-1} band compared with the 1170 cm^{-1} band with R^2 values of 0.8885 and 0.8686. This may be due to the resolution of peaks between instruments, the 1617 cm^{-1} peak appeared as a singlet in the handheld spectrometer data making it more consistent with buffer sample results. It also meant there were no ambiguities in SERS response for each concentration when using the handheld instrument as both peaks of the doublet appeared to fluctuate in intensity for plasma sample analysis. The doublet peak observed may have been due to the complex nature of the human samples. The plasma samples were diluted to 25% but this may have been enough to cause changes in the peak ratios of the doublet vibrational band. Therefore, the 1170 cm^{-1} peak was considered alongside the 1617 cm^{-1} peak when performing the investigation in triplicate in plasma samples.

A SERS signal was generated for the blank (0 ng/mL CRP) in the case of both serum and plasma samples. In an effort to diminish this, the triplicate study was carried out using a lower concentration of capture Ab immobilised onto the NC membrane, from 500 μg/mL Ab to 360 μg/mL Ab.

Comparing both studies using human serum and plasma samples, it was decided that a concentration study carried out in triplicate would be performed using plasma. The plasma samples gave an improved linear and logarithmic fit, particularly when using the SERS intensity of the 1170 cm^{-1} peak to construct the calibration curves. Plasma studies were also carried out using much higher concentrations of CRP therefore this concentration range was maintained moving forward.

3.3.3.3. Triplicate Concentration Study

CRP concentration studies were performed in triplicate in human plasma samples using the following spiked concentrations of CRP - 2000, 1000, 750, 500, 300, 100 and 0 ng/mL. These were attempted using the same volume ratio of plasma to LFIA buffer (25 μL:75 μL) however, the conjugates were observed to aggregate during the movement of solution upwards through the LFIA strip. This may be due to a new batch of AuNP-Ab conjugates being used for the triplicate study, the particles may not have been as stable as a result of batch-to-batch variability and crucially more optimisation may be needed for the best conditions *e.g.* plasma dilutionm buffer components, when using the LFIA with human samples. Therefore the plasma:buffer ratio was reduced, a volume of 5 μL plasma was used and made up to 100 μL LFIA buffer.

For each replicate study, the 2000 ng/mL CRP sample was observed to aggregate upon contact with the NC membrane of the LF strips therefore, no data was collected for this concentration. Figure 3.19 (a) shows images from each LF assay in triplicate at each CRP concentration along with all 18 corresponding SERS intensity maps. RGB results are shown in figure 3.19 (b) and display a downward trend with increasing CRP concentration which was not expected. It was concluded that quantitative information could not be determined using this method.

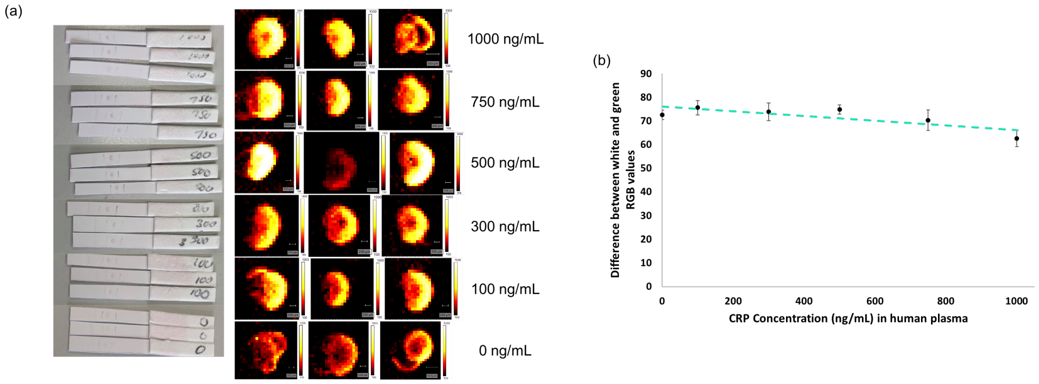

Figure 3.19: Results from CRP concentration study performed in triplicate (a) Images of LFIA strips from all concentration studies and corresponding SERS intensity maps across the following CRP concentrations - 1000, 750, 500, 300, 100 and 0 ng/mL CRP, there was an obvious difference between replicates for 500 ng/mL CRP where a diminished SERS response was observed for a single replicate and (b) calibration curve of calculated RGB values against CRP concentration, this analysis did not offer any quantitative information. RGB values were calculated from scanned images using ImageJ. Raman mapping was performed at 633 nm laser excitation, 0.2 s acquisition time, 50% laser power and a step size of 100 μm.

From the visual appearance of the maps in figure 3.19 (a) it was difficult to ascertain whether there would be differences in SERS signal correlating with CRP concentration. There was also a significant SERS response from the blank due to the residual CRP present. An obvious decrease in SERS response was observed for the second replicate of the 500 ng/mL CRP samples that was not consistent with the other two replicates. The average spectra from the Raman mapping data, across all replicates for each CRP concentration, are shown in figure 3.20 (a). It should be noted that the 1617 cm^{-1} peak which had appeared as a doublet band when using 25 μL of plasma, had now remained as a singlet peak while using 5 μL plasma. This indicated that indeed the percentage of the biological matrix present in the sample was responsible for the appearance of the doublet band. The SERS spectra exhibited a general decrease in SERS signal with decreasing CRP concentration.

Calibration curves constructed from the 1617 cm^{-1} and the 1170 cm^{-1} peaks are shown in figures 3.20 (b) and (c) respectively.

The calibration curves at the 1170 cm^{-1} peak (figure 3.20(c) and (d)) displayed an improved linear fit over the 1617 cm^{-1} peak. The LOD for each curve was calculated using equation 3.1, a LOD of 606.2 ng/mL was calculated for the 1617 cm^{-1} peak and 582.4 ng/mL for the 1170 cm^{-1} peak. These were both high compared with those reported using buffer conditions however, in the event of sepsis, CRP will be present in the blood at levels potentially above 100 μg/mL with clinically relevant levels being $>$ 10 μg/mL.[22] For this study, the plasma samples were diluted 1 in 20 (5 μL plasma in 100 μL LFIA buffer) meaning their detection limits were just within the bounds of clinical relevance at 12.12 μg/mL and 11.65 μg/mL respectively. With this dynamic range in mind, a very low LOD may not prove necessary for the application of sepsis diagnosis with regards to CRP detection as both LOD's are in line with clinically relevant concentrations. It should also be noted that the baseline levels of CRP present in the samples may mean that the actual levels of CRP are higher and that the concentrations observed in this study are higher than those calculated.

Analysis from handheld spectrometer scans are shown in figure 3.21. Average

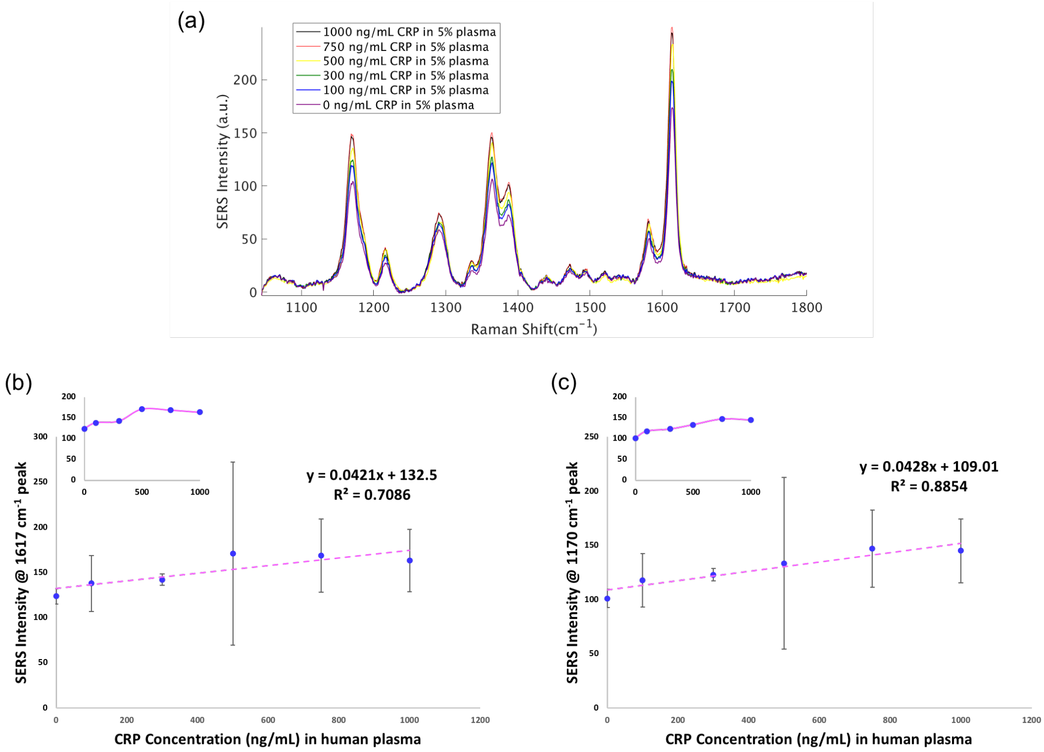

Figure 3.20: Triplicate study in plasma samples (a) Average SERS spectra for each CRP concentration across all replicate studies corresponding to SERS maps shown in 3.19 (a), a decrease in SERS signal was observed with decreasing CRP concentration. Calibration curves were constructed from the (b) 1617 cm^{-1} peak where there was a linear trend observed with a r^2 value of 0.7086 and from the (c) 1170 cm$_{-1}$ peak with a r^2 value of 0.8854. Data was processed using Matlab and calibration curves were constructed in Excel.

spectra across all replicates for each concentration study (figure 3.21 (a)) showed a general decrease in SERS intensity with decreasing CRP concentration. However, the highest SERS response was generated from 500 ng/mL CRP samples. Calibration curves for both 1617 cm^{-1} and 1170 cm^{-1} peaks are shown in figures 3.21 (b) and (c) respectively. The LOD's calculated for each curve were 269.7 ng/mL and 252.3 ng/mL CRP. Again, taking the dilution factor into account these were found to be 5.4 μg/mL and 5.1 μg/mL respectively in the original samples. The size of the error bars for the handheld Raman data were also reduced compared to the benchtop instrument which indicated there was less error between each measurement using the handheld spectrometer. This was a good re-

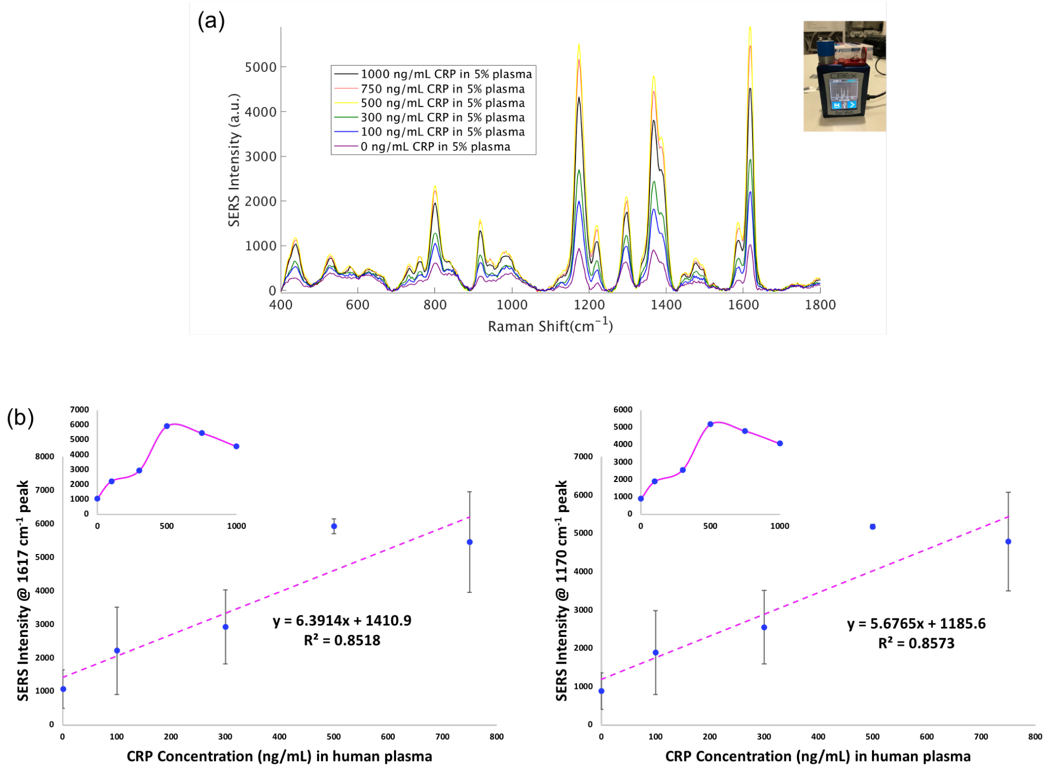

Figure 3.21: Results from handheld spectrometer across replicate plasma studies (a) average spectra for each CRP concentration across all concentration studies, while a general decreasing trend in SERS intensity with concentration was observed, the highest SERS response generated was from 500 ng/mL CRP samples, (b) the calibration curve constructed from the 1617 cm^{-1} peak displayed a linear trend with R^2 value of 0.8581 which was also observed for the (c) 1170 cm^{-1} peak with a slightly improved fit of 0.8573. Handheld SERS measurements were performed using 638 nm laser excitation, 0.2 s acquisition time and 27.8 mW laser power. Average spectra were constructed from 3 scans of each LFIA strip. Data was processed using Matlab and calibration curves were constructed in Excel.

sult as it demonstrated the viability of the portable instrument as a means fr CRP detection when combined with the LFIA platform. The handheld spectrometer was also capable of lower detection limits compared with the Raman microscope and these were still within a concentration range deemed to be clinically relevant.

Immunoturbidimetry and immunonephelometry are commonly used automated techniques for CRP detection in a clinical setting.[96] Both rely upon the aggregation of the biomarker with specific polyclonal Abs to form large particle-like species. Immunoturbidimetry uses the difference in light transmitted before and after interrogating the sample to detect CRP while immunonephelometry uses light scattered by the large particle-like species for qualification and quantification. These methods have sensitivity of approximately 3 - 8 μg/mL but suffer disadvantages associated with long run times and specialised, bulky equipment.[96] Therefore they are not viable for use in the field for example in a resource-limited setting or at the point-of-care in a triage situation.

Commercially available ELISA techniques for CRP detection generally report detection in the pg/mL range (Abcam, Sigma Aldrich, Invitrogen) demonstrating very low detection limits however, clinically relevant levels of CRP are observed to be greater than 3 μg/mL. Biotechne offers CRP ELISA kits in the ng/mL range however the upper limit is 50 ng/mL. This means these commercial ELISA's may not be suitable for detecting high concentrations of CRP indicative of disease states. ELISA analyses also suffer from long analysis times and specialised equipment coupled with extra reagent steps.

While the working range of the LFIA developed in this work is quite small at 0 - 750 ng/mL CRP (0 - 15 μg/mL when taking the dilution factor into account), the platform has demonstrated similar detection limits to immunoturbidimetry and immunonephelometry techniques but was performed on a portable, user-friendly device used in combination with a handheld analysis technique. The detection range also spans both healthy and clinically relevant concentrations which would be an advantage for rapid differentiation between normal levels versus disease states. Additionally the assay run time ranged from 20 - 30 mins including wash steps and each scan took only 0.2 s. While further work is needed to adapt this method to resource-limited and triage settings, it can certainly be said that the handheld Raman spectrometer coupled with a SERS-based LFIA has excellent potential for the rapid detection of CRP at the point-of-care.

3.4 Conclusion

The implementation of SERS-active AuNPs into a LFIA platform offers the ability to obtain quantitative information and improved sensitivity compared with standard colourimetric analysis techniques. Here, the quantitative detection of sepsis-related biomarker, CRP was achieved in buffer solution with calculated LODs of 1.2 ng/mL from benchtop Raman mapping analysis and 8 ng/mL when a handheld spectrometer was used. It was shown that the handheld instrument produced comparable results with the benchtop system and at a significantly reduced analysis time, 30 mins per assay compared with 6 s. Due to its size, the Raman mapping instrument is not suitable for use in the field but the viability of the handheld spectrometer when combined with LFIA devices for point-of-care applications has been demonstrated.

The developed assay was tested using biological samples, both human serum and plasma and the results were again compared between instruments. While further optimisation is undoubtedly needed for human samples, quantitative analysis was somewhat achieved in plasma samples. When the dilution factor of plasma samples was considered, LODs of 11.65 μg/mL and 5.1 μg/mL for benchtop and handheld analysis respectively were observed. The working range of the assay is between 0 - 750 ng/mL CRP which works out at 0 - 15 μg/mL once the dilution factor is accounted for (1 in 20 dilution). Therefore this assay platform spans the healthy and clinically relevant range which is ideal for rapid differentiation of a disease state. CRP concentrations in the event of sepsis have been recorded as being as high as 100 μg/mL, therefore further optimistion of this assay platform would be needed to adapt to a wider working range or, potentially move towards a higher dynamic range which only incorporates very high levels of CRP, indicative of sepsis.

With regard to the working range of the developed SERS-based LFIA, this platform could be used for rapid detection of CRP in an emergency clinical setting *e.g.* in A&E or at the bedside in ICU where abnormal levels could be indicative of inflammation associated with disease states like a cardiac event. With further development the LFIA combined with portablility of the handheld spectrometer would be a valuable commodity in resource-limited settings. For example, out-in-the-field, the LFIA strips could be used initially as a rapid diagnostic at the point-of-need, where visual analysis is the initial indicator of disease. In the event of a positive result, the LFIA device could be transported to a centralised analysis centre and analysed using the handheld Raman spectrometer to obtain quantitative information. Additionally, optimising this platform to work with whole blood samples in the form of a finger-prick test would be extremely valuable in both hospital and resource-limited settings. This development could also allow for home-testing, contributing to pro-active, personalised medical care where CRP levels are monitored regularly by the patient themselves from visual analysis of the LFIA device. A positive test would be an indicator to make a GP appointment where quantification could be performed at the point-of-care using the handheld Raman instrument. This would also be useful for the monitoring of conditions such as Crohns disease in the management of flare-ups and potentially for home-monitoring of the toxic effects of cancer treatment.

Therefore, with further optimisation steps and comparing data with established clinical detection methods *e.g.* immunoturbidimetry/immunonephelometry, this SERS-based LFIA platform holds potential for the development of a point-of-care detection device for CRP. With regards to sepsis diagnosis, however, multiplexed detection of several biomarkers is needed. In the next chapter, the detection of a second biomarker linked to sepsis, interleukin-6 (IL-6) was investigated with the aim of developing a multiplex LFIA device.

4. Multiplexed Detection of CRP and IL-6 using a SERS-based Lateral Flow Assay

4.1 Introduction

Multiplexing, in the context of LFIA devices, is the ability to detect two or more analytes simultaneously and from a single sample, while retaining the benefits associated with the LFIA platform *i.e.* rapid detection, user-friendly format and cost effectiveness. Conventional LFIA devices which rely on colourimetric read-outs are sufficient for single target detection and, as described in section 3.1, signal enhancement techniques have been improved, in may cases overcoming issues with low sensitivity. However, multiplexed analyte detection can deliver more information from one sample which offers obvious benefits for diagnostic accuracy in the case of disease detection. For example the simultaneous detection of IL-10 and MCP-1 cytokines has proven valuable for the monitoring and early diagnosis of atherosclerosis-associated disease, the detection of multiple biomarkers is necessary for sepsis diagnosis as outlined in section 1, the detection of food contaminants such as antibiotics and mycotoxins and for forensic applications.[62,97,98] Additionally, less sample volume is needed for the detection of many analytes simultaneously which lowers the expense and analysis time needed to obtain the final results.[62,99,100] This is also advantageous when a low volume sample only is available such as in the case of cerebral spinal fluid.

A multiplexed detection platform is particularly important in the context of biomarkers for sepsis diagnosis where a panel of biomarkers would need to be detected in order to accurately diagnose the condition and provide a prognostic outlook. There are many different avenues being explored for the multiplexing of LFIA devices, these include changing the device architecture, spatially resolved detection where multiple test lines or an array of test dots are present on a single LFIA strip and signal-resolved detection where multiple labels can be deduced from a single test line.[62,99,100] Examples of these will be described in the following sections.

4.1.1 Manipulating device architecture for multiplexed detection

The manipulation of conventional LFIA device design is the most intuitive and facile method to attain multiplexed detection. In this approach, the physical design of the device has been changed. Fenton *et al.* proposed a variety of different architectural designs of the NC membrane using a computer-controlled knife. They also fabricated protective films for their designs as an alternative to a plastic cassette.[101] These laminate films where only the sample inlet was exposed, would protect the device from contamination, dehydration and make them generally easier to handle. Figure 4.1 (a) demonstrates the workability of one of the authors' proposed templates, which acts as a duplex test for glucose and albumin in spiked artificial urine samples. The square region turned green when glucose was detected, the centre circle was a control and remained colourless while the right-hand circle appeared red when albumin was present.[101]

The combining of LFIA strips has also been attempted for multiplexing. This is where many strips, each for the detection of a specific analyte, are connected through contact with a single sample region. Figure 4.1 (b) shows the device architectures used for rapid and accurate blood typing. The LFIA strips were combined in different ways depending on the test. Single LFIA strips were used for forward-grouping to determine the A/B/O blood group using a colour change reaction with a yellow dye called bromocresol green (BCG). In the event of a positive test, the detection zone, as shown in figure 4.1 (b), turns blue and for a negative test it would turn black. For example, for blood type B, the left detection zone appeared black as there was no A-type red blood cells (RBCs) present in the blood sample while the detection zone on the right of the device appeared blue indicating the presence B-type RBCs and a positive test.[102]

Adding a second LFIA strip to this platform enabled the addition of backward-grouping testing of plasma from the a single whole blood sample thereby achieving plasma separation during the running of the device. In this device, anti-A and anti-B Abs were detected in plasma on the second LFIA strip to validate the result from the forward-grouping test in blood on the first LFIA strip. The third device design was capable of ABO and rhesus (Rh) determination and consisted of 8 LFIA strips joined by a single sample region where an 80 μL sample of whole blood mixed with assay eluent was added (10 μL per strip). This system was mounted on a wheel and could be entered into a production line-type system for running and analysis as shown in figure 4.1 (b). The appearance of the detection zones, whether blue or black, was used as visual determination of blood type for the duplex and octaplex systems and for Rhesus determination in the octaplex.[102]

The inset from the octaplex device shows results from reflectance spectroscopy analysis which the authors used to validate the visual results - a high percentage of reflectance was indicative of the blue colour and a positive result, while low reflectance percentages were observed for the black colour and a negative result. Reflectance spectroscopy was also used in this investigation to determine the time which blood samples could be stored prior to analysis before agglutination of the RBCs began to diminish resulting in false positives for type O blood.[102]

Attempts have also been made to pattern the NC membrane of LFIA strips to create channels for multiplexed detection. Hecht *et al.* used femtosecond laser ablation to etch a microfluidic-type design to act as hydrophobic and air barriers between 4 channels on a single LFIA strip as shown in figure 4.1 (c).[103] They determined the optimum ablation parameters to achieve a process that minimised damage to adjacent membrane and also melted the membrane inside the channel

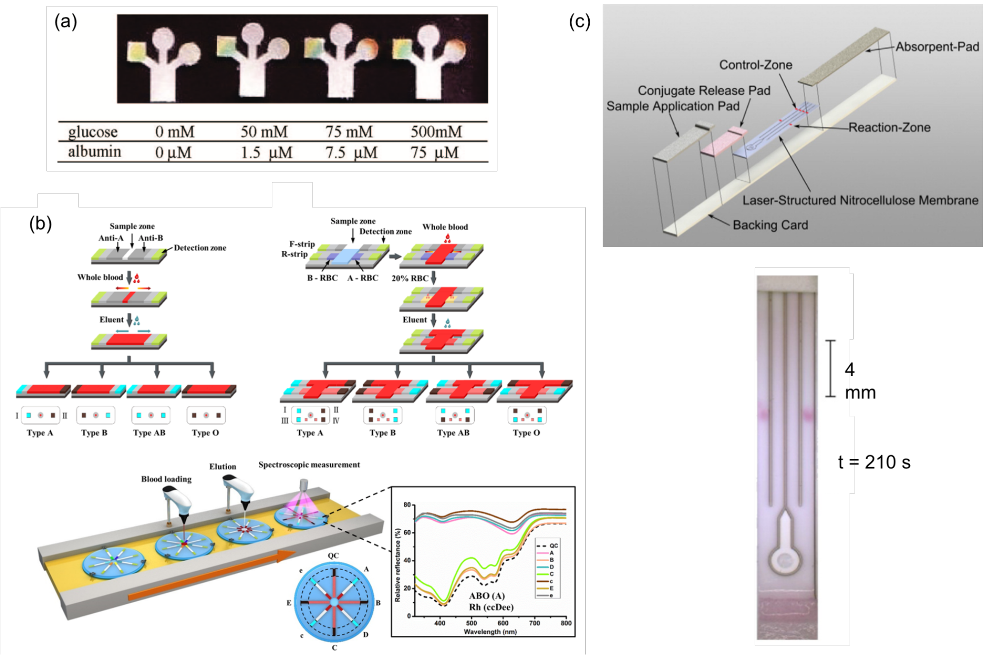

Figure 4.1: Examples where LFIA device architecture has been manipulated to facilitate multiplexing (a) a duplex colourimetric test for glucose and albumin, the square turned green with increasing glucose concentration while the right-hand circle turned red with increasing albumin concentration in spiked artificial urine sample. The authors demonstrated a variety of designs for a multiplexed LFIA platform,[101] (Reprinted with permission from *ACS Applied Materials and Interfaces*, **2009**, *1*, 124-129. Copyright 2009 American Chemical Society) (b) multiplexed LFIA design for accurate and rapid blood type test developed by Zhang *et al.* The first scheme shows a duplex on a single LFIA strip using forward-grouping testing of ABO group of a whole blood sample where the dyed regions on the strip revealed the blood group by showing a certain combination of blue and black. Scheme 2 integrated backward grouping into the device by adding a second LFIA strip with a plasma separation membrane where both LFIAs were connected by a single sample inlet region, scheme 3 shows a wheel-style platform where 8 LFIA strips are connected by a single sample region for ABO and Rh group determination. The device was set up on a production line for sample addition, washing and analysis of the dyed regions on each strip[102] and (c) shows a LFIA platform where a microfluidic-type design with hydrophobic air barriers was shaped onto the NC membrane using femtosecond laser ablation resulting in multiple channels along the membrane capable of multiplexed detection, they demonstrated proof concept by detecting hCG hormone where red spots were observed along the sample channels while the control channels remained blank.[103]

i.e. closing up the pores therefore prohibiting sample fluid entering the channel. They also demonstrated the workability of the device through a hCG hormone detection assay (figure 4.1 (c)) using AuNPs and Abs in a standard sandwich-type interaction where a red spot of accumulated AuNPs was observed in the channels where hCG had been present in the sample and no spot was observed for control channels.[103]

Although a range of changes to the architecture of the conventional LFIA strip have been proposed to facilitate multiplexing and are demonstrated to work, there remains disadvantages with this approach. Since some techniques involve the combination of multiple LFIA strips, more materials are needed for each device, increasing the cost per device on a platform who's unique selling point is that it is cost effective. Sample volume also needs to be considered, where a larger device area would inevitably require a larger sample volume, this would be of particular importance with regards to biological samples. Additionally, fabricating costs come into play when more preparation steps are needed to manufacture the device for example the laser ablation technology used by Hecht *et al.* Therefore alternative methods to multiplex have been explored by controlling the number of interactions occurring on a single LFIA strip.

4.1.2 Multiplexing from spatially resolved detection

Spatially resolved detection involves the placement of multiple test lines or regions on a single LFIA device. This allows the detection of multiple analytes simultaneously on one test strip. In some instances the label for each analyte does not change but this method has also been investigated using adaptable labels that give a specific response depending on the analyte they are designed to detect. Multiplexing using colourimetric analysis of multiple test lines has been explored for the detection of alpha defensin and CRP for the diagnosis of periprosthetic joint infection (PJI).[104] In this study, two independent test lines, consisting of Abs specific to each target were present on the NC membrane along with a control line. The assay worked the same as conventional LFIA tests where AuNPs became immobilised on the test line in the presence of the target and excess AuNPs bound to the control line. Therefore, in the event of a positive test for both targets, three red lines were observed on the LFIA strip. While this method was advantageous compared to ELISA with regards simultaneous detection of alpha defensin and CRP, cost effectiveness and time, quantification was not achieved.[104]

A similar approach was taken for the detection of genomic DNA from two biological agents associated with terrorism, *Francisella tularensis* and *Yersinia pestis*. The authors demonstrated the quantitative capability of the colourimetric assay in both synthetic and genomic DNA samples.[105] Unfortunately, for this type of test that relies solely on colourimetric analysis, a DNA amplification step was needed before utilising the LFIA device which added to the time, cost and expertise needed to perform the test. It should be noted that both techniques demonstrated specificity of the labels for their targets, however the disadvantages associated with conventional colourimetric analysis were prevalent.

Similar to single target LFIA assays, efforts have been made to enhance the signal response for duplex assay platforms Chen *et al.* investigated a dual-readout device for the duplex detection of alpha fetoprotein (AFP) and carcino embryonic antigen (CEA). In their assay they compared the colourimetric readout with a chemiluminescent (CL) analysis by adding a CL substrate after the assay had been run. This extra step to attain CL provided signal amplification from the test lines thereby achieving greater sensitivity.[106] Figure 4.2 (a) shows a schematic of their duplex LFIA assay and the colourimetric and CL readout analyses. Quantitative information was also gained from the assay in both readout techniques with lower limits of detection reported for CL analysis.

Similarly, fluorescence has been used to achieve an enhanced signal through the use of upconversion NPs (UCNPs).[110] Red, green and blue UCNPs were used to demonstrate the triplex detection of Hg^{2+} ions, ochratoxin A and *Salmonella* as proof-of-concept.[110] Although this was a negative assay *i.e.* no signals were observed on any of the test regions when the targets were present, the resulting signal was different for each target introducing the concept of specific responses

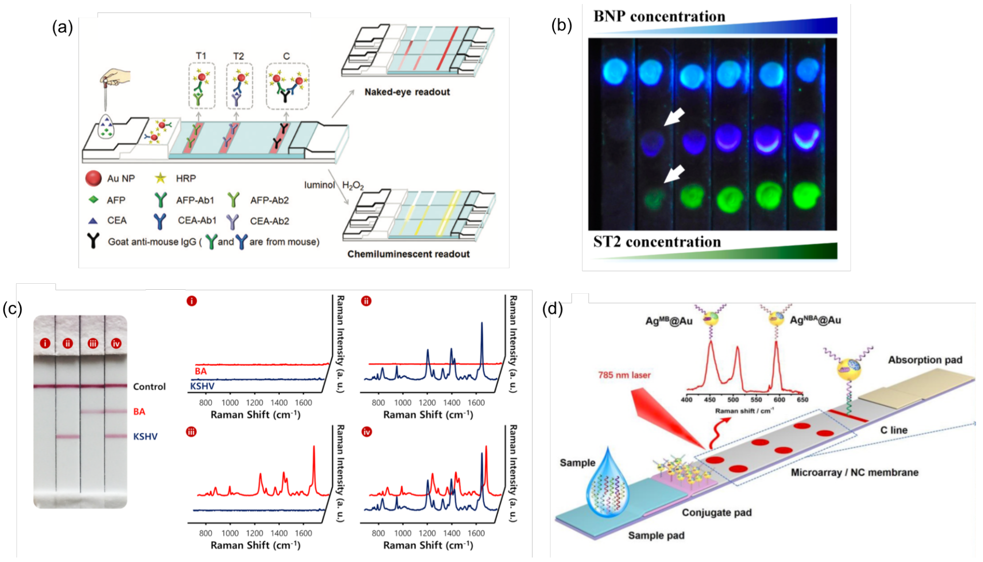

Figure 4.2: Spatially resolved multiplexed detection has been achieved by the placement of two or more test lines on a single LFIA strip (a) dual-readout duplex assay developed for the detection of tumour biomarkers CEA and AFP. Initially the assay returned a colourimetric readout which, with the addition of a CL substrate, generated a CL response that was more sensitive,[106] (b) blue and green UCNPs were used to generate a fluorescent signal for the duplex detection of BNP and ST2, biomarkers of heart failure. Unlike the CL method, each UCNP-probe generated a different signal depending on its target,[107] (c) SERS-based LFIA for the detection of KSHV and BA, the assay demonstrated excellent specificity and was capable of quantitative detection, the same Raman reporter was used for each target,[108] and (d) SERS-based microarray capable of simultaneously detecting 11 nucleic acids, associated with respiratory tract infection pathogens, on a single LFIA strip. Two Raman probes were synthesized each with a different Raman reporter, these were used for the detection of two targets immobilised on one array dot. These regions generated a duplex SERS spectrum in the presence of both targets.[109]

catering for individual analytes, not achievable for colourimteric and CL methods. You *et al.* also used UCNPs in a test for heart failure prognosis. Green and blue particles indicated the presence of the cardiac biomarkers, brain natriuretic peptide (BNP) and suppression of tumorigenicity 2 (ST2), and the assay was capable of quantitative detection of both biomarkers on a single LFIA strip as shown in figure 4.2 (b).[107]

SERS has also been employed for spatially resolved multiplexed detection. Wang *et al.* employed a SERS-based LFIA for the duplex detection of two DNA markers, one associated with Kaposi's sarcoma-associated herpesvirus (KSHV) and the other with bacillary angiomatosis (BA).[108] Figure 4.2 (c) shows visual results for the assay alongside SERS signals for each LFIA strip, these results demonstrated the specificity of the assay and the lack of cross-reactivity. The authors showed that their assay was quantitative, 10,000 times more sensitive than conventional colourimetric methods and demonstrated the potential for multiplexing.[108]

Similarly, triplex detection has been achieved using SERS. Zhang *et al.* detected three cardiac biomarkers; myoglobin (Myo), cardiac troponin I (cTnI) and creatine kinase-MB isoenzymes (CK-MB) on a single LFIA strip using SERS. Three separate test lines were prepared on the NC membrane along with a control line and quantitative detection of all targets was achieved on a single device.[111] However, as in the detection for KSHV and BA, the same Raman reporter was used for all three targets. While this approach may be suitable for the detection of 2-3 markers, it is not viable when the detection of more targets is necessary.

With regards to the placement of test lines, the highest recorded number is 8 on a single LFIA strip plus a control line. Han *et al.* showed that 8 contaminants commonly found in milk products could be detected simultaneously using visual analysis.[112] However, Zhang *et al.* then developed a SERS-based microarray on LFIAs that was capable of the detection of 11 nucleic acids associated with different respiratory tract infection pathogens.[109] In this approach, microarray dots were placed on the NC membrane along with a control line as shown in figure 4.2 (d). Five of the spots could bind two targets while one of the spots only bound a single target. Two different Raman probes were prepared, each with a different Raman reporter, methylene blue (MB) or Nile[109] Blue A (NBA). For array dots containing capture nucleic acids specific to two different targets, both of the Raman probes bound to this region, each representing a different target. Therefore, the SERS signal from this dot would produce a duplex SERS spectrum from the mixture of both reporter signals. If both targets were present, features from both reporter spectra would be observed.[109]

This final example of spatially resolved multiplexed detection also incorporates signal-resolved detection by the use of a duplex signal from a single region which will be described in the next section. While the capabilities of spatially resolved multiplexing have been well demonstrated, this approach has some disadvantages. For example, the number of test lines that can be incorporated into a single device is finite and having an increasing number of test regions will undoubtedly increase the overall analysis time. There is an option to incorporate an architecture change of the device to make the NC membrane physically longer however, this would increase the flow time of the device thereby increasing the time of the test. Because of these concerns, signal-resolved detection has been attempted where the detection of multiple analytes from a single analysis region is attainable.

4.1.3 Multiplexing from signal-resolved detection

Signal-resolved detection occurs when multiple labels are immobilised at a single test zone and can be identified through their specific signals, this can be either from analysis of a visual response, light emission or a spectral signal response. The key factor is that all signals are collected from the same region simultaneously offering rapid analysis and return of results. With regards to LFIA devices, this also means no deviation from the device architecture incurring increased materials costs.

Chemiluminescence (CL) has been used in the duplex detection of β-agonists ractopamine (RAC) and clenbuterol (CLE) as proof-of-concept.[113] Two different CL kinetics strategies were employed called flash type and glow type reactions which represented RAC and CLE respectively. The CL intensity of the flash type reaction (RAC) was at a maximum of 3 seconds after CL co-reactants were flowed through the LFIA strip while the glow type reaction (CLE) reached a maximum CL intensity after 300 seconds. In this way, the time delay between intensity maxima could be used to code for each of the β-agonists. The authors demonstrated quantitative detection for the competitive assay as the CL intensity maxima decreased with increasing β-agonist concentration.[113] While signal-resolved detection was shown in this case, it is difficult to imagine how this approach could be applied to more than two analytes, particularly without increasing the analysis time.

Figure 4.3 (a) shows colourimetric-style signal-resolved detection on a LFIA dipstick device. Yen *et al.* used multicoloured silver nanoparticles (AgNPs) of orange, red and green for the triplex detection of proteins associated with yellow fever, Ebola and dengue viruses respectively. The coloured AgNPs were synthesised from spherical seeds which appeared yellow. Size increases and morphological changes towards triangular-plate shaped AgNPs resulted in different wavelengths of light being scattered and the subsequent colour changes observed in each batch of AgNPs. When running the LFIA, if all proteins were present in the test sample, the test line appeared brown due to each coloured AgNP being immobilised at the test line. RGB values were used to analyse the colourimetric response and compared to single target LFIAs of each protein at the same concentration. The results determined that the device could indeed be used for signal-resolved multiplexed detection.[114] However, their LOD was reported to be 150 ng/mL for each viral protein suggesting that a signal enhancement method *e.g.* SERS could be coupled with this approach to achieve greater sensitivity.

Danthanarayana *et al.* used persistent luminescent nanophosphors (PLNPs) to demonstrate duplex detection of hCG and prostate-specific antigen (PSA). The LFIAs were analysed using a custom-designed app on a smartphone camera that had been coupled with an attachment, enabling the camera's LED flash to act as an excitation source. Using this setup, the synthesised PLNPs were observed as green and blue when bound to the test line.[115] Figure 4.3 (b) shows how the LFIA strip was analysed after running the duplex assay. RGB analysis and ImageJ were used to deduce the signals from the blue and green channels and

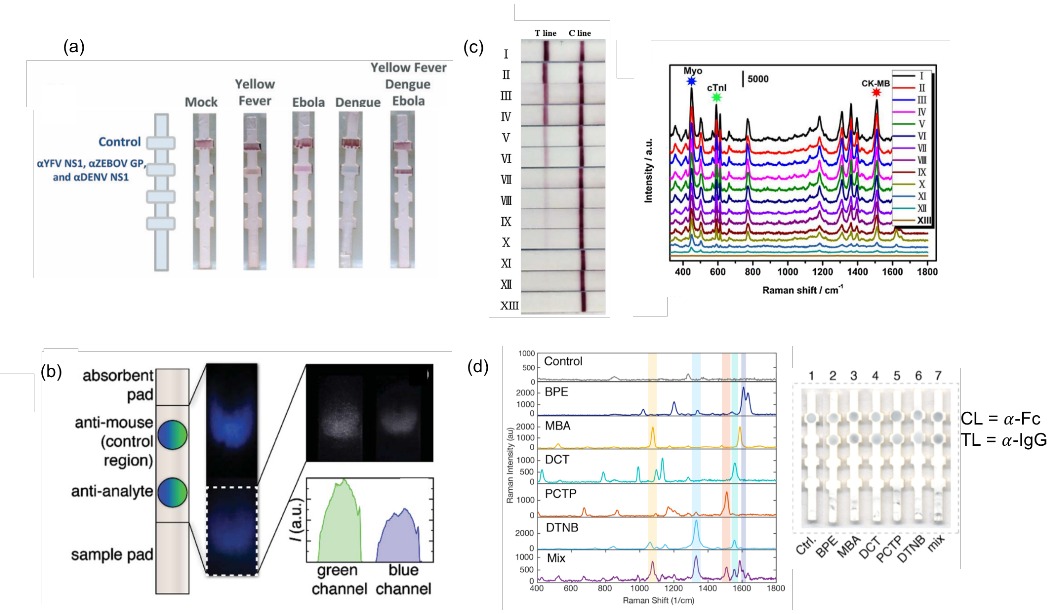

Figure 4.3: Signal-resolved multiplexed detection has been realised through the analysis of a single test region where multiple signals from different labels can be detected simultaneously for the detection of multiple analytes. (a) Colourimetric triplex detection was achieved using AgNPs of orange, red and green for the detection of protein biomarkers of yellow fever virus, ebola virus and dengue virus respectively. When all targets were present in the sample solution the test region appeared brown and RGB values were used to determine the presence of a target,[114] (b) PLNPs of blue and green were used for duplex detection of hCG and PSA respectively. A smartphone camera with an attachment was used with an app to obtain a coloured photo allowing colourimetric analysis to be achieved through RGB values,[115] (c) SERS was used for the detection of three cardiac biomarkers; Myo, cTnI and CK-MB from a single test line. Quantitative analysis was also achieved in the ng/mL range. The graph shows the characteristic peaks for each Raman reporter in the multiplex spectrum, representing the three biomarkers present in the test samples[116] and (d) proof-of-concept pentaplex deomnstrating that at least four analyytes can be detected from a single test region using SERS, each peak from each Raman reporter is clearly represented in the multiplex spectrum. The test region appears as blue on the dipstick LFIA as gold nanostars were used as SERS substrates.[117] (https://pubs.acs.org/doi/full/10.1021/acsomega.8b01499 further permissions related to the material excerpted for figure 4.3 (d) should be directed to the ACS.)

signal-resolved detection was achieved. The assay was also capable of attaining quantitative information and the PLNPs were chosen as they offered photostability and improved sensitivity.[115] However, multiplexed detection may be limited to the number of different coloured PLNPs that can be synthesised.

SERS has also been used for signal-resolved multiplex detection. SERS benefits from the fact that a range of different Raman reporters exist, generating characteristic, “fingerprint" spectra specific to the reporter molecule. If a number of different Raman reporter-functionalised NPs are mixed together in a sample, distinct peaks from each of their individual spectra can be picked out of the multiplexed spectrum generated from the mixture and the individual reporters can be identified. This way, different reporters can be used to represent multiple analytes in a single sample. The presence of characteristic peak of the reporter in the multiplex spectrum can be used for qualitative analysis and the intensity of the peak can be used to gain quantitative information. Signal-resolved detection using SERS can be achieved in solution and on paper-based assay platforms. Of course considerations must be made for optimum excitation wavelength, resonance effects and the relative SERS intensities between Raman reporters. Wu *et al.* used AuNPs functionalised with two reporters, DTNB and 4-MBA for the duplex detection of *L. monocytogenes* and *S. typhimurium* respectively on a single LFIA strip. Quantitative information was attained based on decreasing intensities of DTNB and 4-MBA peaks present in the multiplex spectrum with decreasing concentrations of the targets.[118]

Following on from spatially resolved triplex detection,[111] Zhang *et al.* used Raman reporters NB, NBA and R6G to code for the presence of cardiac biomarkers myoglobin (Myo), cardiac troponin I (cTnI) and creatine kinase-MB isoenzymes (CK-MB) respectively in a signal-resolved detection assay.[116] Figure 4.3 (c) shows results from a concentration study for all three biomarkers demonstrating the quantitative capability of the assay. The SERS spectra collected from each test line are shown and each peak representing each reporter is highlighted in the multiplexed spectrum. The authors achieved low detection limits, well within the clinical ranges of each biomarker.[116]

Sanchez-Purra *et al.* achieved duplex detection of dengue and Zika virus using SERS. Their dipstick LFIA platform was also capable of quantitative analysis.[119]

In a different publication, the same author's demonstrated as proof-of-concept, that a pentaplex SERS signal could be obtained from a single test region.[117] Figure 4.3 (d) shows the five Raman reporters chosen for functionalisation to gold nanostars. A generic capture protein was immobilised on the test region of the LFIA device (α-IgG) and the control line consisted of a second capture protein (α-Fc). Peaks from each of the individual SERS spectra were clearly visible in the pentaplex spectrum therefore implying that signal-resolved pentaplex detection can be achieved using SERS.[117]

The advantages of signal-resolved multiplexed detection include rapid analysis for the detection of multiple analytes therefore the results offer more information in the time it takes to run a single LFIA device. Smaller quantities of reagents are used both in the preparation and running of the device and finally the device architecture does not need to be drastically changed lowering the cost associated with materials. However, the immunoreactions taking place must be highly-specific and ensure cross-reactivity is at a minimum. Depending on the analysis method, this approach may also be limited to the amount of signals that can be generated from a single region and how these can be separated. This is why SERS offers the greatest potential for signal-resolved multiplexing as a range of Raman reporters can be used. It should be noted, that in all of the SERS examples described above, analysis was performed using Raman microscopes and no signal-resolved detection studies were found to use a portable instrument. For point-or-care multiplexed detection, instrument portability is vital for the viability of the assay platform.

4.2 Chapter Aims

Sepsis diagnosis requires the development of a multiplexed detection platform. This can be achieved by the combination of a LFIA device and SERS where a range of different Raman reporters can be used to code for different analytes. Additionally, this platform benefits from the advantages associated with LFIAs, namely, rapid analysis times, cost effectiveness and a user-friendly format. The potential for multiplexing using SERS-LFIA devices has been discussed and this chapter aims to investigate spatially resolved and signal-resolved detection of two biomarkers associated with sepsis.

We have shown that CRP can be detected successfully using a SERS-based LFIA where sensitivity and quantitative analysis were attained. In order to meet the criteria for sepsis diagnosis, we attempted to detect a second biomarker associated with sepsis, interleukin-6 (IL-6) using the same technique. For this, AuNPs were functionalised with a different Raman reporter, rhodamine B isothioscyante (RBITC) and the initial aim was to demonstrate quantitative detection of IL-6 in a single target LFIA.

The second aim of this work was to attempt to detect both CRP and IL-6 on a single LF strip. While architecture changes to LFIA devices have shown the potential for multiplexing, this technique demanded a larger sample volume, the use of more materials and reagents and longer analysis times. Therefore, we aimed to use a single LFIA strip for duplex detection of CRP and IL-6. Spatially resolved duplex detection was first attempted where two different test regions were present on a single LFIA strip. Signal-resolved duplex detection was then investigated with the aim of also attaining quantitative analysis of both biomarkers simultaneously on a single LFIA strip.

Raman mapping analysis was used to visualise the binding of both biomarkers in each duplex technique while handheld Raman results were also obtained to demonstrate the viability of the method as a portable and point-or-care technique.

4.3 Results and Discussion

4.3.1 Gold Nanoparticle Functionalisation with RBITC and IL-6 Ab

IL-6 is a cytokine associated with the innate immune system, the release of which up-regulates CRP production in the liver.[7,20] It is also strongly linked to sepsis and has been shown to hold prognostic value for the condition.[7,8] For the detection of a second biomarker, a different Raman reporter was chosen. The criteria for this reporter molecule centred around the presence of peaks that could be distinguished from the MGITC spectrum and that it gave a strong SERS signal capable of competing with MGITC which is resonant at ~633 nm laser excitation wavelength.

Rhodamine B isothiocyanate (RBITC) was chosen as the reporter that would code for IL-6 in the multiplex assay. RBITC is a chromophore with an absorbance maximum at ~550 nm (absorbance spectrum is shown in Figure A.8 of the Appendix) therefore to satisfy resonant conditions a 532 nm excitation would be ideal. However, RBITC exhibits strong fluorescence at this laser excitation wavelength which swamps the SERS response making it challenging to detect. 633/638 nm laser excitation wavelengths were used in the previous chapter for CRP detection and was also used for this investigation. Since this wavelength is off-resonance for RBITC, fluorescence interference was greatly reduced and a sharp, distinct SERS spectrum was generated for AuNPs functionalised with RBITC.

The chemical structures of RBITC and MGITC are shown in figure 4.4 along with SERS spectra of each reporter functionalised to AuNPs in solution overlaid on the same graph. The SERS spectra have been normalised to 1 to highlight the different peak positions distinct to each reporter. As the 1617 cm^{-1} peak had been chosen for data anaylsis for MGITC in chapter 2, the 1650 cm$_{-1}$ peak was chosen as the characteristic peak for RBITC which represented C=C and aromatic C-C stretching vibrations.

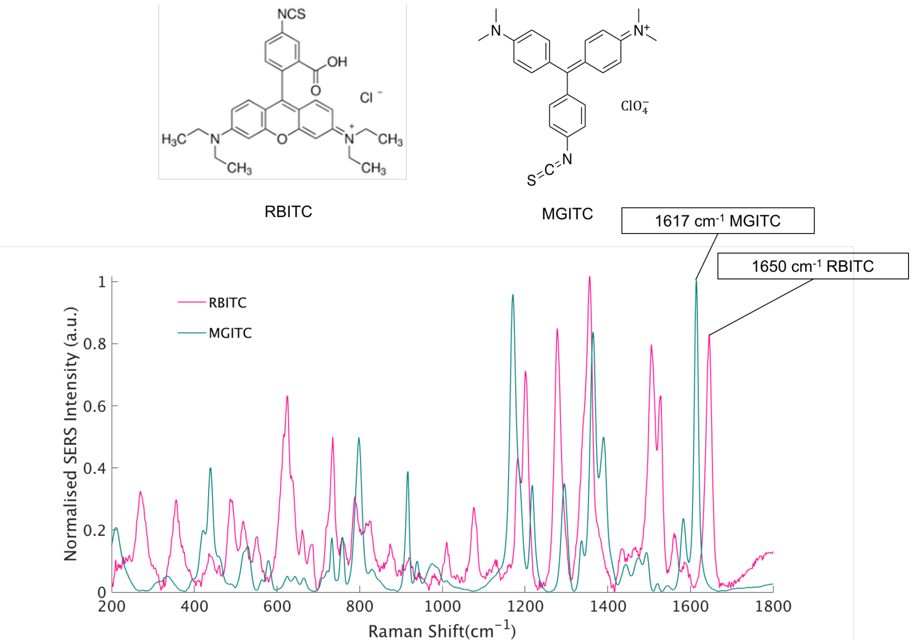

Figure 4.4: Chemical structures of Raman reporters RBITC and MGITC and below, overlaid SERS spectra from each reporter in solution. The spectra were normalised to 1 to highlight the different peaks characteristic to each reporter, the 1617 cm^{-1} peak of MGITC (N-Ph ring and C-C stretch) is highlighted as this was the peak used for analysis in section 3.1 for CRP detection. For RBITC, the 1650 cm^{-1} peak (C=C and aromatic C-C stretch) was chosen as it was an intense band, distinct from the MGITC spectrum. Both reporters were attached to AuNPs, MGITC at a concentration of 75 nM and RBITC at 0.75 μM. SERS spectra were collected using 638 nm laser excitation, 1 s acquisition time and 100% laser power. The data was processed and normalised using Matlab.

The reporter molecule contains an isothiocyanate group which means it attaches to AuNPs through the S atom, in the same way as MGITC. Figure 4.5 shows characterisation of AuNPs after functionalisation with RBITC and IL-6 specific Abs. The Abs were conjugated to AuNPs using a method developed by Wang *et al.*[61] Briefly, 990 μL AuNPs were added to 10 μL of 0.75 μM RBITC solution, the particles were shaken for 30 mins followed by the addition of 100 μL of 0.1 M borate buffer. The function of the borate buffer was to pH correct the RBITC-functionalised AuNPs to pH 9 thereby facilitating passive adsorption of the Ab onto the AuNP surface (described in section 3.3.1). 4 μL of IL-6 Ab was then added to give a final Ab concentration of 3.6 μg/mL. The NPs were shaken for 2 hours, 10% BSA solution was added to passivate any exposed AuNP surface, followed by shaking for 30 mins. The NPs were centrifuged and resuspended in 1 mL of 0.1 M borate buffer.

The AuNPs were analysed using extinction spectroscopy and SERS. Figure 4.5 (a) shows the extinction spectroscopy results, peak broadening was observed after attachment of both RBITC and IL-6 Ab indicating increases in particle size and dispersivity however the table shows there was no shifts in the LSPR peak from the control which may have indicated refractive index changes between AuNPs and their surrounding environment due to the attachment of the Ab. Control AuNPs had been through the entire conjugation protocol but H_2O was added instead of RBITC and IL-6 Ab. SERS spectra are shown in figure 4.5 (b), no signal was observed for control AuNPs and an intense SERS response was seen after the attachment of RBITC. This signal was observed to diminish slightly following Ab conjugation however these analyses provided no definitive evidence for Ab attachment. Therefore, a LF sandwich immunoassay test was performed.

Figure 4.6 shows SERS analysis from LFIAs run with two different capture Ab concentrations - 360 μg/mL and 450 μg/mL. There was no clear on/off signal observed in the SERS intensity maps for 360 μg/mL IL-6 capture Ab and this was also shown in the average spectra from each map (figure 4.6 (a)). Comparing this to mapping results when 450 μg/mL (figure 4.6 (b)), the map showed the outline of the spot demonstrating an obvious on/off signal which was also evident from the average spectra for each map. It appeared that at a lower capture Ab concentration, a problem was occurring with the binding between AuNP-Ab-IL-6 complexes and the immobilised Ab at the test region. This may have been due to the hook effect.[120] This phenomenon happens on LFIAs and produces falsely low results when analytes are present at high concentrations. At the lower capture Ab concentration of 360 μg/mL, excess IL-6, that had not complexed with the AuNP-Ab conjugates, may have been occupying immobilised Ab sites on the NC membrane and therefore blocking binding sites for AuNP-Ab-IL-6 complexes.

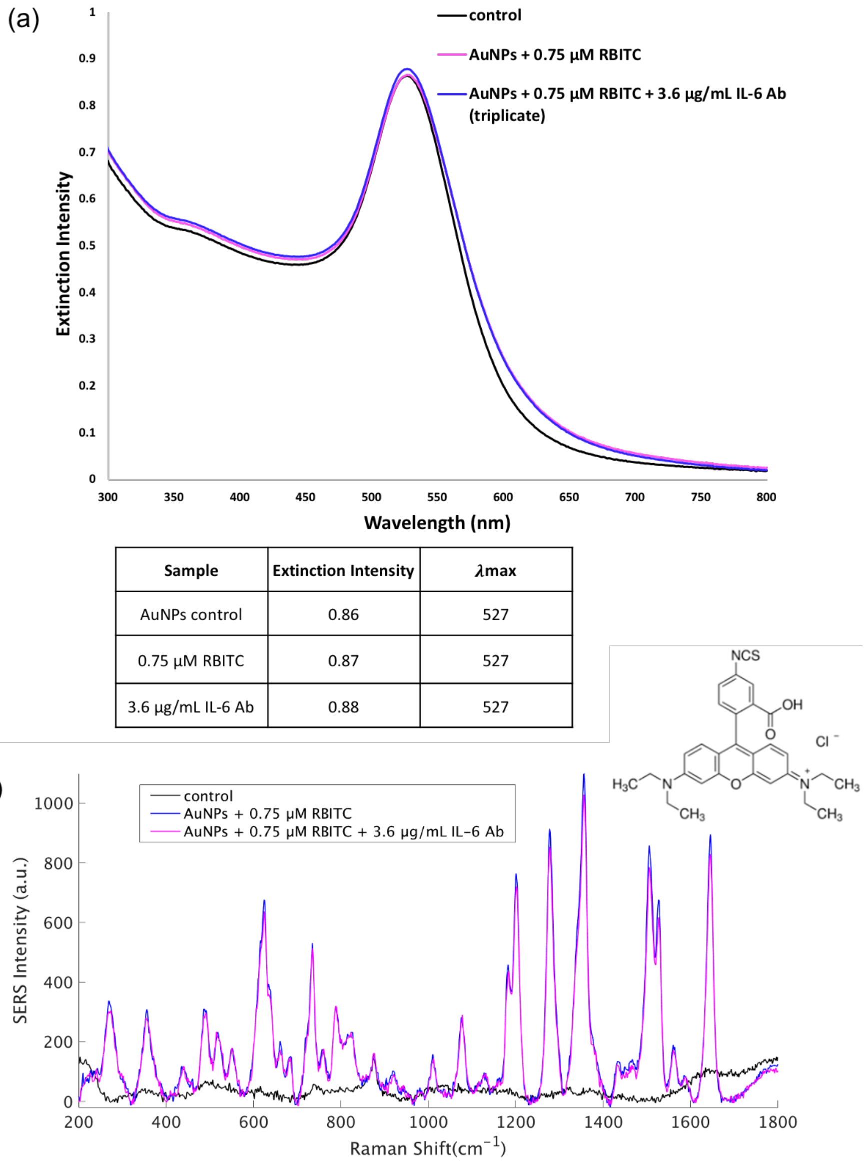

Sample	Extinction Intensity	λmax
AuNPs control	0.86	527
0.75 μM RBITC	0.87	527
3.6 μg/mL IL-6 Ab	0.88	527

Figure 4.5: Characterisation results from AuNP functionalisation with Raman reporter RBITC and IL6-specific Ab (a) extinction spectroscopy of AuNPs after functionalisation, the table shows extinction intensity and λmax for at each step. There was slight peak broadening and changes in extinction intensity after attachment of both species however no shift of the LSPR peak was observed and (b) corresponding SERS spectra from each sample, intense response was observed after RBITC functionalisation which decreased slightly in intensity after attachment of the Ab. SERS analysis was performed at 638 nm laser excitation, 100% laser power, 1 s acquisition time and each sample was scanned 3 times.

With the these complexes unable to successfully bind at the test region, a greatly diminished SERS signal was generated giving a false negative result.[120] 360 μg/L was evidently too low a concentration for this test. Using a higher concentration of 450 μg/mL of immobilised Ab meant that there were more sites available for binding with the AuNP-Ab-IL-6 complexes and the hook effect was overcome, achieving a positive result. All maps were constructed the intensity of the 1650 cm^{-1} peak of RBITC. This result for 450 μg/mL capture Ab demonstrated that Ab conjugation had been successful and that the assay worked.

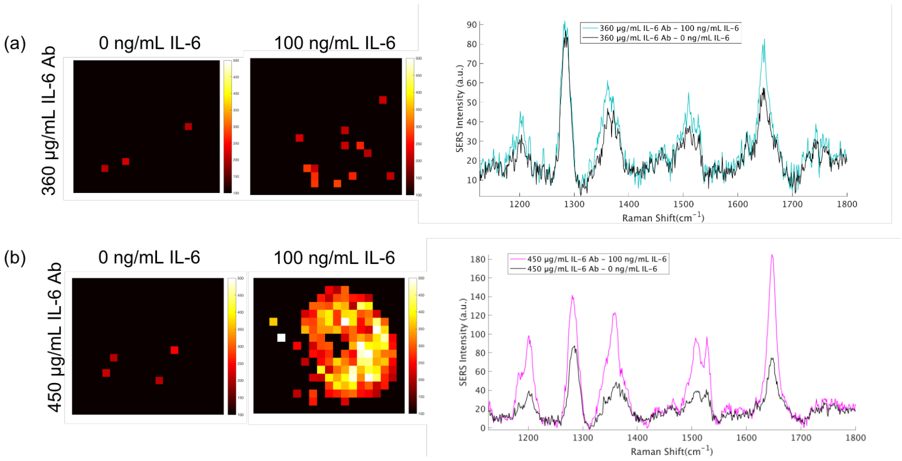

Figure 4.6: Results from LF sandwich immunoassay for IL-6 detection - SERS intensity maps and corresponding average SERS spectra from each Raman map (a) using 360 μg/mL IL-6 capture Ab and (b) using 450 μg/mL IL-6 capture Ab. Raman mapping was performed at 633 nm excitation wavelength, 6 s acquisition time, 0.73 mW laser power and 100 μm step size.

4.3.1.1. IL-6 Concentration Study

A concentration study was performed in triplicate for IL-6 on LFIA strips, the following concentrations of IL-6 were used - 100, 50, 25, 10, 5, 1 and 0 ng/mL. In the event of sepsis, IL-6 levels in the blood can exceed 1 ng/mL.[32] LFIA strips were prepared as described in section 2.4 where 450 μg/mL of IL-6 capture Ab was spotted onto each strip. The LFIAs were analysed using RGB values, Raman mapping and handheld SERS measurements. The SERS analyses were compared with RGB values to demonstrate the improved quantitative capabilities of SERS for this assay and Raman mapping measurements were used to validate the handheld Raman instrument for portable, point-of-care analysis.

Figure 4.7 (a) shows scanned images from one of the replicate studies with corresponding SERS intensity maps. The maps were constructed from the intensity of the 1650 cm^{-1} peak of RBITC (aromatic C-C stretching, C=C stretching).[121,122] There was a clear decrease in SERS signal observed from the maps with decreasing IL-6 concentration. Appendix figure A.11 shows scanned images and Raman maps from all three replicate studies. RGB values are shown in figure 4.7 (b) and show a similar trend of decreasing values with decreasing IL-6 concentration. However, the error between measurements was large and at lower IL-6 concentrations there was no obvious trend. An LOD of 123 ng/mL IL-6 was calculated from the RGB analysis. The reason this value was so high may have been as a result of the inconsistent signal observed at lower IL-6 concentrations, where the colourimetric response was close to the value calculated for the blank. This demonstrated that RGB values were not an effective analysis method for gaining quantitative information from this assay.

Figure 4.8 (a) shows spectra from the Raman mapping experiment for each IL-6 concentration averaged across all replicates. There was a clear decrease in SERS intensity with decreasing IL-6 concentration and this was demonstrated in the calibration curve shown in (b). The inset shows the relationship between intensity of the 1650 cm^{-1} peak and IL-6 concentration across the full concentration range. The calibration curve was constructed from the linear portion (0 - 50 ng/mL) of this graph and the data produced a LOD of 13.7 ng/mL. Figure 4.8 (c) and (d) show data from handheld Raman analysis. The average spectra for each IL-6 concentration demonstrated the same decreasing intensity trend observed in the Raman mapping data and the calibration curve was constructed in the same way. However, a lower LOD of 10.5 ng/mL was calculated for handheld instrument across the 0 - 50 ng/mL range.

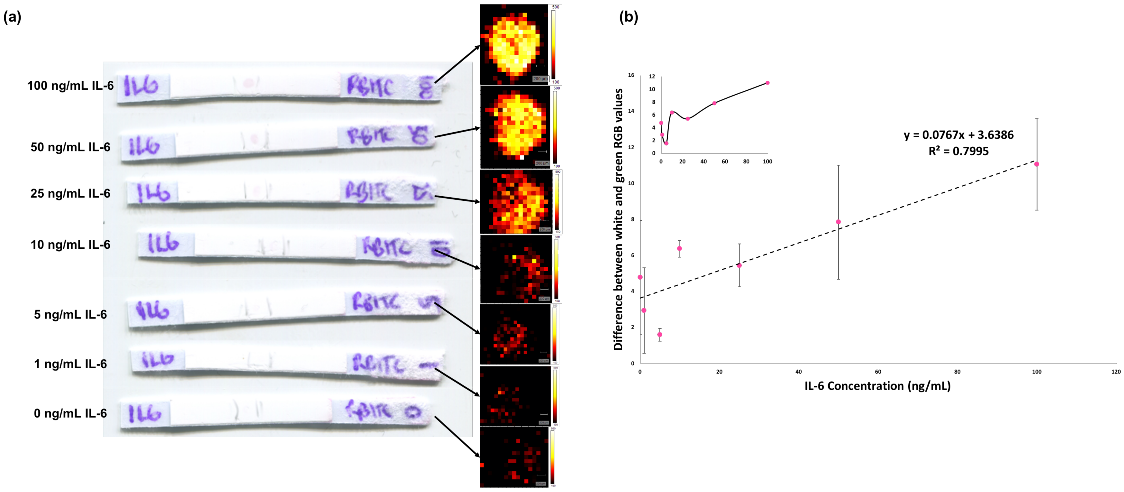

Figure 4.7: (a) Flatbed scanned images and corresponding Raman mapping results from one replicate study for IL-6 concentrations - 100, 50, 25, 10, 5, 1 and 0 ng/mL, a decreasing SERS signal was observed with decreasing IL-6 concentrations. Raman maps were constructed using the intensity of the 1650 cm^{-1} peak of RBITC and (b) calibration curve of average RGB values versus IL-6 concentration across triplicate studies, a LOD of 123 ng/mL was calculated using this analysis. Raman analysis was performed using a 633 nm laser excitation, 0.73 mW laser power, 5 s acquisition time and 100 μm step size. RGB values were calculated from scanned images using ImageJ software.

Therefore, from the three analysis methods, RGB values, Raman mapping and handheld measurements, the latter generated the lowest LOD. While the calculated value may not have been low enough for clinically relevant detection (pg/mL - ng/mL), the IL-6 assay could be used as a proof-of-concept assay for the duplex detection of both IL-6 and CRP. In this way, both biomarkers could be detected simultaneously on a single LFIA strip using a portable spectrometer. This duplex assay can act as a preliminary step towards developing a multiplexed assay platform for sepsis diagnosis at the point-or-care.

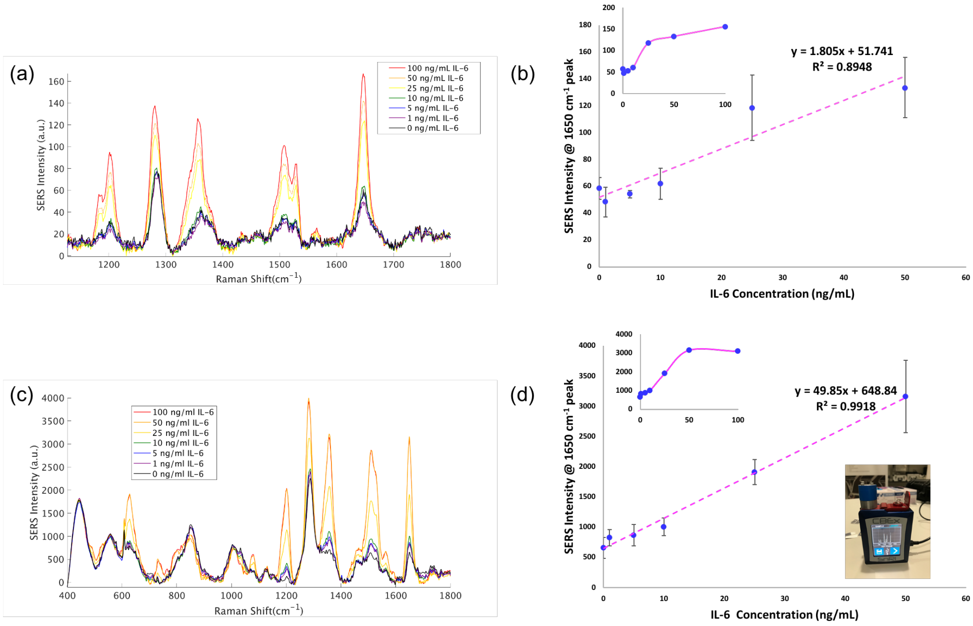

Figure 4.8: SERS analysis results from triplicate IL-6 concentration studies (a) average spectra for each IL-6 concentration from SERS mapping data which showed a decrease in SERS intensity with decreasing IL-6 concentration, (b) calibration curve of 1650 cm^{-1} peak against IL-6 concentration (0 - 50 ng/mL) with shape of curve across full concentration range shown in inset. A LOD of 13.7 ng/mL was calculated from the SERS mapping analysis data, (c) results from handheld Raman analysis showing average spectra for each IL-6 concentration where a decreasing trend of SERS intensity with IL-6 concentration was observed and (d) corresponding calibration curve (0 - 50 ng/mL IL-6) constructed from average intensity of the 1650 cm^{-1} peak across all replicates, a LOD of 10.5 ng/mL was calculated from the handheld Raman data. Raman mapping was performed using 633 nm laser excitation, 0.73 mW laser power and 5 s acquisition time, the data was processed using WiRE and Matlab. Handheld Raman analysis was carried out at 638 nm laser excitation, 27.8 mW laser power and 0.75 s acquisition time. The data was processed using Matlab. All calibration curves were constructed in Excel.

4.3.2 Duplex Detection of CRP and IL-6 using a Lateral Flow Assay Platform

4.3.2.1. Spatially resolved duplex detection

The first duplex assay format to be investigated, spatially resolved detection, is shown in figure 4.9. IL-6 specific Ab and CRP specific Ab were spotted onto different regions of the NC membrane of a single LFIA strip as shown in figure

4.9 (a). Both biomarkers (CRP and IL-6) and both AuNP-Ab conjugates were mixed together in LFIA buffer, CRP present in the sample bound to the AuNP-Abs conjugated with CRP-specific Ab and IL-6 bound to AuNP-Abs conjugated with IL-6-specific Ab, forming AuNP-Ab-CRP and AuNP-Ab-IL-6 complexes. At this point during the assay, there was a risk of cross-reactivity where the biomarkers could potentially bind to AuNP-Abs non-specifically. This would result in the wrong AuNP probe binding at the wrong test region and generating a SERS response representative of the wrong biomarker. If this was the case, a mixed spectrum with peaks from both Raman reporters would be collected from either of the test regions and in this instance, duplex detection would not be possible. However, highly specific, monoclonal Abs had been used for conjugation with AuNPs for the detection of both biomarkers, therefore it was expected that cross-reactivity would not occur.

The buffer solution of biomarkers and AuNP-Ab conjugates was allowed to flow upwards through the strip and if both biomarkers were present, two red spots appeared on the strip as shown in figure 4.9 (b). However, if only one biomarker *e.g.* CRP was present and there was no IL-6 in the sample mixture, one red spot would appear on the NC membrane at the region where the capture Ab specific to CRP had been spotted. For the schematic in 4.9(b), this would mean a red spot was visible on the region closest to the wicking pad where the CRP capture Ab was immobilised and no spot would be observed where the IL-6 capture Ab was immobilised, (region closest to the conjugate pad). The opposite would be true if IL-6 was present and CRP was absent from the sample mixture and if neither biomarker was present, no spots would be observed. SERS analysis was carried out on each region where the Abs had been immobilised and a different spectrum was recorded for each biomarker *i.e.* MGITC for CRP and RBITC for IL-6.

The double-spot, spatially-resolved duplex was attempted on four separate LFIA strips with three of the devices acting as control assays to demonstrate the

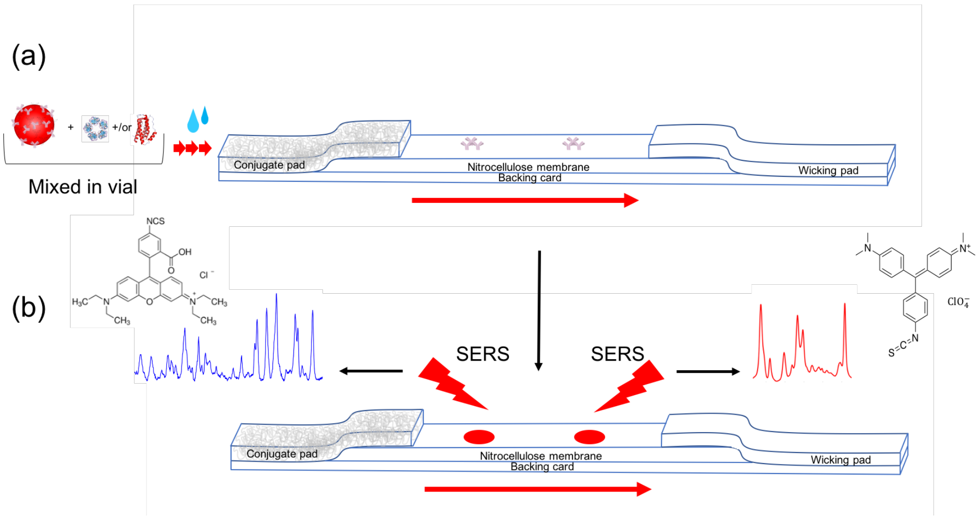

Figure 4.9: Schematic representation of how a double-spot duplex assay was prepared on a single LFIA strip (a) IL-6 specific Abs and CRP specific Abs were immobilised onto different regions of the NC membrane, a sample solution containing both biomarkers and both conjugates was prepared in LFIA buffer and the strip was placed in the mixture and (b) the appearance of the NC membran eafter the duplex assay was run, two red spots have appeared on each Ab region as both biomarkers were present in the sample, these can be analysed using SERS to determine which conjugates have bound to which area, with MGITC representing CRP and RBITC representing IL-6. Schematic not to scale.

lack of non-specific binding between Abs and conjugates. These also showed the specificity of the synthesised conjugates for their biomarker. The LFIA strips were prepared as described in section 2.4. The IL-6 specific Ab was immobilised closest to the conjugate pad at a concentration of 450 μg/mL followed by 360 μg/mL of CRP specific Ab immobilised closer to the wicking pad. The following sample mixtures were prepared in 100 μL of LFIA buffer for the four LFIA strips with 10 μL of each conjugate being added at an approximate concentration of 0.75 nM -

- LF A - both biomarkers at 100 ng/mL each + both conjugates
- LF B - 100 ng/mL CRP only + both conjugates
- LF C - 100 ng/mL IL-6 only + both conjugates
- LF D - no biomarkers present + both conjugates

Figure 4.10 shows results from the double-spot duplex assays. Figure 4.10 (a) shows scanned images following each assay run on LF A, LF B, LF C and LF D with the black-outline boxes indicating the location of the immobilised IL-6 Ab and the CRP Ab on each strip. Two red spots were observed to appear on LF A. This was expected as both biomarkers were present in the sample mixture. LF B and LF C displayed a single red spot each, as only one biomarker was present in each sample solution. Furthermore the spots were in the correct Ab region corresponding to their specific biomarker. No spots were observed for LF D as no biomarkers were present in the sample. Colourimetrically, these results indicated that there was no non-specific binding occurring and that the conjugates were binding specifically.

Raman mapping data is shown in figure 4.10 (b). The schematic shows arrows pointing at each Ab region indicating which spots have been analysed. In order to confirm the lack of non-specific binding observed visually, separate maps were constructed of each spot using both the intensity of the 1617 cm^{-1} peak of MGITC (representing CRP) and the 1650 cm^{-1} peak of RBITC (representing IL-6). For the CRP Ab spots, intense SERS maps were generated of the 1617 cm^{-1} peak for LF A and LF B, these were the two assays where CRP was present in the sample. No signal was recorded at this peak intensity for LF C and LF D. The corresponding maps generated from the 1650 cm^{-1} peak of RBITC at the same locations, gave a negligible SERS response deemed to be background signal from residual AuNPs left on the NC membrane.

Figure 4.10 (b) also shows maps generated from the IL-6 Ab spots on the LFIA strips. Intense SERS signals for maps constructed using the 1650 cm^{-1} peak were observed for LF A and LF C as IL-6 was present in both sample mixtures. As expected, no definitive SERS signal was observed in LF B and LF D at the same peak intensity. When maps at the same locations were constructed using the 1617 cm^{-1} peak representative of MGITC and CRP detection, no SERS response was generated.

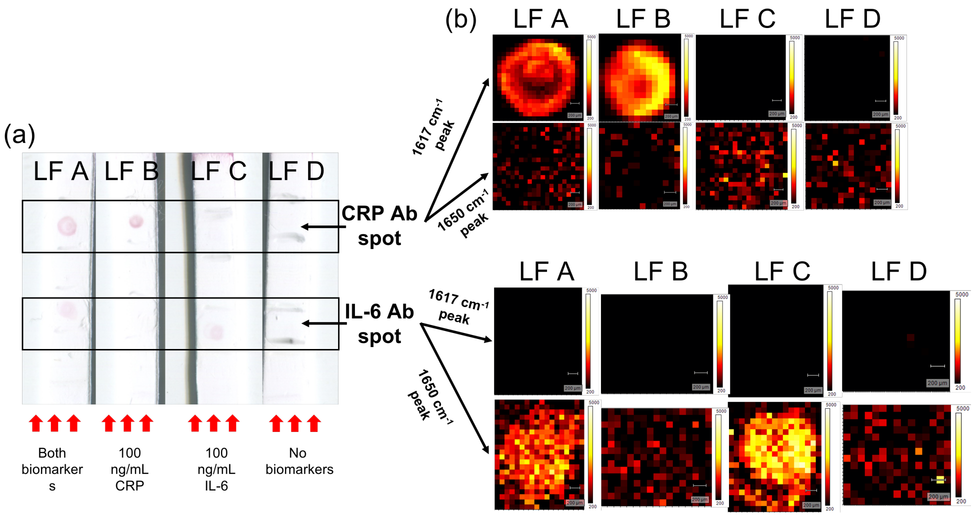

Figure 4.10: Results from a double-spot duplex assay run on LFIA for CRP and IL-6 detection (a) scanned images from each assay; LF A - both biomarkers at 100 ng/mL each + both conjugates mixed together in LFIA buffer, LF B - 100 ng/mL of CRP only + both conjugates mixed together in LFIA buffer, LF C - 100 ng/mL of IL-6 + both conjugates mixed together in LFIA buffer and LF D - no biomarkers present + both conjugates mixed together in LFIA buffer. Each strip was spotted with 450 μg/mL of IL-6 Ab and 360 μg/mL of CRP Ab in the regions shown on the schematic, red spots were observed at these locations only when the corresponding biomarker was present and (b) corresponding SERS intensity maps for each spot, maps were constructed from the 1617 cm^{-1} peak (MGITC) and from the 1650 cm^{-1} peak (RBITC) as indicated by the arrows. For the CRP Ab spot, the spot was only observed in the map for the MGITC 1617 cm^{-1} peak and similarly for the IL-6 Ab, this was the case for the RBITC 1650 cm^{-1} peak. The other maps displayed negligible background signal and demonstrated no evident non-specific binding. Average SERS spectra from each map are shown in Appendix A.11. Raman mapping was performed at 633 nm laser excitation, 6 s acquisition time, 0.73 mW laser power and 100 μm step size.

Raman mapping results confirmed the specificity of each of the conjugates towards IL-6 and CRP while demonstrating no evidence of non-specific binding when both biomarkers and their corresponding conjugates were mixed together. Average SERS spectra from each of the maps can be seen in figure 4.11. The spectra generated from each of the spots from LF A are shown in figure 4.11 (a), an intense SERS spectrum characteristic of MGITC was observed for the CRP Ab spot as expected, with the 1617 cm^{-1} peak clearly distinguishable. The RBITC spectrum collected from the IL-6 Ab spot was identifiable however it was aproximately 6 times less intense than the MGITC spectrum. This was due to MGITC being resonant at 638 nm laser excitation which contributed to a more intense SERS spectrum. Despite this, the 1650 cm^{-1} peak was visible in the RBITC spectrum.

It should also be noted that there appeared to be no cross-reactivity occurring between AuNP-Ab conjugates and the incorrect biomarker as no evidence of the MGITC signal was observed in the SERS spectrum collected from the IL-6 Ab region and vice versa, RBITC in the CRP Ab spot, although this may have been due to the resonant MGITC signal overcoming any residual RBITC signal.

Figure 4.11 (b) shows spectra from each of the spots on LF B, where only CRP was present in the sample. Again, an intense SERS spectrum was generated at the CRP Ab region while a negligible signal was collected from the IL-6 Ab region. The peak at approximately 1288 cm^{-1} was attributed to enhancement of the NC membrane from NO_2 groups present in the nitrocellulose material.[123] Spectra collected from each spot on LF C where only IL-6 was present in the sample are shown in figure 4.11 (c). Residual MGITC signal was observed for the CRP Ab spot with contributions from the NC membrane. There was also a small peak present at 1650 cm^{-1} which represented minor non-specific binding between AuNP-Ab conjugaes specific to IL-6 with CRP. The spectrum generated for the IL-6 Ab spot was observed to be an intense RBITC spectrum which was expected as IL-6 was present in the sample.

For LF D (figure 4.11 (d)), where no biomarkers had been present in the sample, negligible background spectra similar to those observed in LF B and LF C were generated for each of the spots with peaks representative of NC membrane enhancement and residual MGITC and RBITC peaks. These residual signals may have been generated by AuNPs that had not been removed after washing steps but had become immobilised in the NC membrane.

Handheld Raman analysis was performed on each of the assay spots. Figure 4.12 (a) shows results from LF A, where both biomarkers were present in the

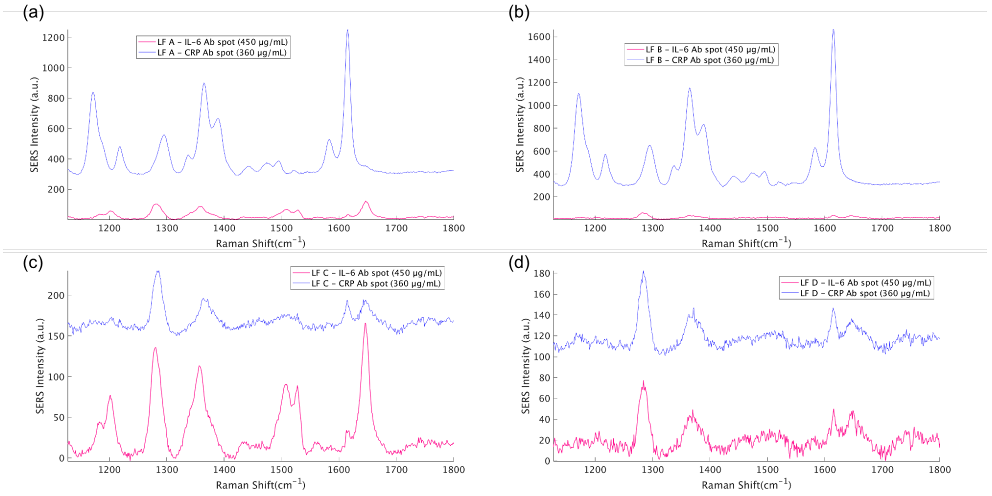

Figure 4.11: Average spectra from Raman maps for each spot of double-spot duplex LF assays (a) LF A - both biomarkers at 100 ng/mL each + both conjugates mixed together in LF buffer. The average spectra from each spot showed a clear spectrum for RBITC (pink line - IL-6 Ab spot) and for MGITC (blue line - CRP Ab spot) which was expected as both biomarkers were present in the sample solution, (b) LF B - 100 ng/mL of CRP only + both conjugates mixed together in LF buffer. Since only CRP was present in the sample solution, the MGITC spectrum was observed (blue line - CRP Ab spot). The characteristic RBITC spectrum was not observed (pink line - IL-6 Ab spot), (c) LF C - 100 ng/mL of IL-6 + both conjugates mixed together in LF buffer. No MGITC spectrum was observed (blue line) but a clear RBITC spectrum was observed (pink line) as IL-6 was the only biomarker present in the sample solution and (d) LF D - no biomarkers present + both conjugates mixed together in LF buffer. Neither spots generated SERS spectra characteristic of MGITC or RBITC which was as expected as neither biomarkers were present in the sample solution. There was no evidence of non-specific binding in any of the assays. Raman mapping analysis was carried out at 633 nm laser excitation, 6 s acquisition time, 0.73 mW laser power, 100 μm step size.

sample mixture. The characteristic SERS spectrum for RBITC was collected from the IL-6 Ab spot while an MGITC spectrum was observed from the CRP Ab spot. Again, this indicated that the duplex assay had successfully detected both biomarkers on a single LFIA device, both at a concentration of 100 ng/mL, and that the handheld instrument was viable for analysis. Figure 4.12 (b) and (c) show results from LF B and LF C respectively. The CRP Ab spot on LF B generated a clear MGITC signal while no RBITC signal was observed on the IL-6 Ab spot. Two peaks were present on the IL-6 Ab spot at 855 cm^{-1} and 1288

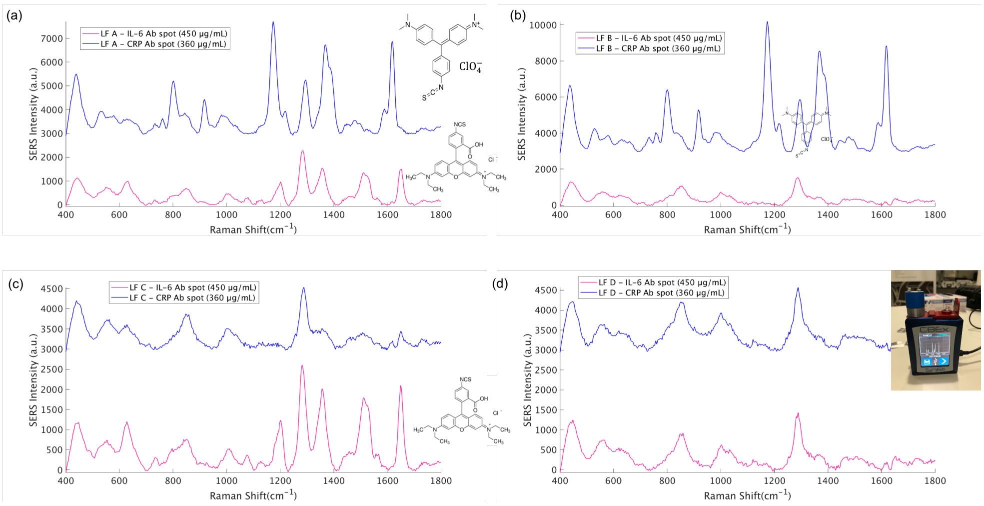

Figure 4.12: Results from handheld Raman analysis of double-spot duplex LFIAs (a) LF A - both biomarkers at 100 ng/mL each + both conjugates mixed together in LFIA buffer. The handheld scans showed clear spectra for RBITC (pink line - IL-6 Ab spot) and MGITC (blue line - CRP Ab spot) which was expected as both biomarkers were present in the sample solution, (b) LF B - 100 ng/mL of CRP only + both conjugates mixed together in LFIA buffer. Since only CRP was present in the sample solution, MGITC spectrum was observed (blue line - CRP Ab spot). The characteristic RBITC spectrum was not observed (pink line - IL-6 Ab spot), (c) LF C - 100 ng/mL of IL-6 + both conjugates mixed together in LFIA buffer. No MGITC spectrum was observed (blue line) but a clear RBITC spectrum was observed (pink line) as IL-6 was present in the sample solution and (d) LF D - no biomarkers present + both conjugates mixed together in LFIA buffer. Neither spots generated SERS spectra characteristic of MGITC or RBITC which was as expected as neither biomarkers were present in the sample solution. Handheld Raman analysis was carried out at 638 nm laser excitation, 0.5 s acquisition time, 27.3 mW laser power and each spot was scanned 6 times.

cm^{-1}, these were due to background signal of NO and NO_2 groups present in the NC membrane material[123]. These may have undergone slight SERS enhancement from AuNPs that had not been removed from the porous matrix after washing and, as in the case for the Raman mapping results, appear as a background signal. For LF C, no MGITC signal was generated from the CRP Ab spot while a clear RBITC signal was collected from the IL-6 Ab spot as expected.

No characteristic SERS spectra were recorded from either spot on LF D as no biomarkers were present in the sample mixture. The peaks observed at 855 cm^{-1} and 1288 cm^{-1} were again representative of the background signal generated from the NC membrane.

The results from the spatially resolved duplex assay showed that both CRP and IL-6 could be detected simultaneously on a single LFIA strip using a handheld Raman spectrometer. These results correlated well with Raman mapping data and the results from both analysis techniques were very promising. They indicated the specificity of the duplex assay with little evidence of non-specific binding or cross-reactivity and this was especially good for the development of a signal-resolved duplex assay as for multiplexed detection of biomarkers associated with sepsis, the number of different Abs spatially immobilised on the NC membrane would be limited by the size of the membrane. Therefore, we investigated the possibility of immobilising both CRP Abs and IL-6 Abs in the same area to achieve signal-resolved duplex detection. The aim of demonstrating this would act as preliminary work towards the detection of multiple biomarkers from a single spot on a single LFIA membrane. SERS analysis could then be used to collect a multiplexed spectrum from the spot to identify the biomarkers present in the sample from characteristic Raman reporter bands found in the multiplexed spectrum.

4.3.2.2. Signal-resolved duplex Detection

As shown from the spatially-resolved detection results for CRP and IL-6, negligible cross-reactivity and non-specific binding was observed. This was promising for the signal-resolved approach as it meant a duplex spectrum would only be observed if both biomarkers wee present in the sample. Figure 4.13 shows what the duplex SERS spectrum of MGITC and RBITC looks like and indicates which peaks are assigned to each reporter molecule. Unique peak contributions from MGITC occurred at 801 cm^{-1} (benzene C-H bend), 1177 cm^{-1} (ν_9 benzene in plane), 1364 cm^{-1} (N-Ph ring stretch) and 1617 cm^{-1} (N-Ph ring and C-C stretch). Those from RBITC were identified to be - 628 cm^{-1} (xanthene, aromatic bending), 1288 cm^{-1} (C-C bridge bands stretch), 1364 cm^{-1} (aromatic C-C

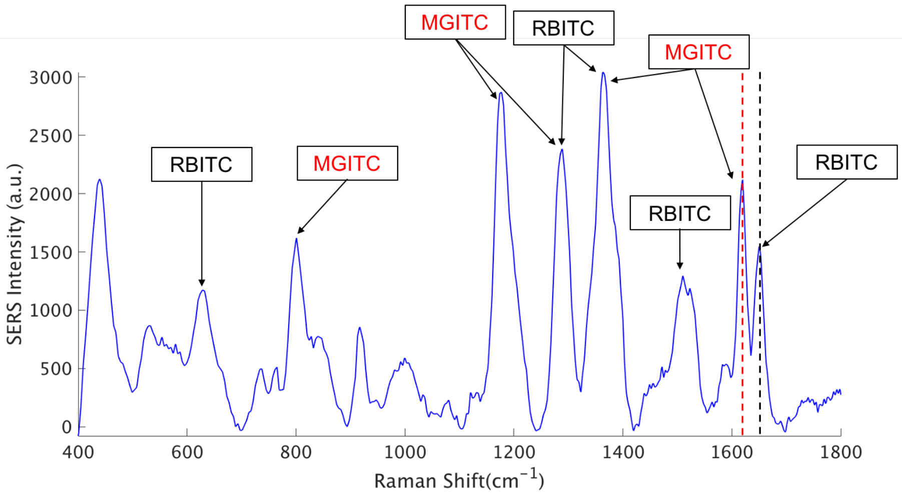

Figure 4.13: Duplex SERS spectrum of MGITC and RBITC showing main peak contributions from each Raman reporter. MGITC peaks - 801 cm^{-1} (benzene C-H bend), 1177 cm^{-1} (ν_9 benzene in plane), 1364 cm^{-1} (N-Ph ring stretch) and 1617 cm^{-1} (N-Ph ring and C-C stretch) peak indicated by the red dotted line which was used for SERS analysis to represent the presence of CRP. RBITC peaks - 628 cm^{-1} (xanthene, aromatic bending), 1288 cm^{-1} (C-C bridge bands stretch), 1364 cm^{-1} (aromatic C-C stretch), 1510 cm^{-1} (aromatic C-C stretch) and 1650 cm^{-1} (aromatic C-C stretch and C=C stretching) peak indicated by the black dotted line which was used for SERS analysis to represent the presence of IL-6. It was clear from the duplex spectrum that the 1617 cm^{-1} and 1650 cm^{-1} peaks used for duplex analysis were easily identifiable and well separated in the duplex spectrum. SERS spectrum was generated using laser excitation wavelength of 638 nm, 1 s acquisition time and 100% laser power.

stretch), 1510 cm^{-1} (aromatic C-C stretch) and 1650 cm^{-1} (aromatic C-C stretch and C=C stretching). The two peaks used for differentiation of the two reporters are highlighted by the dotted lines, the red dotted line shows the 1617 cm^{-1} peak from MGITC ad the black dotted line shows the 1650 cm^{-1} peak from RBITC. Crucially, both peaks are easily distinguishable and well separated in the duplex spectrum therefore signal-resolved analysis using SERS was indeed possible for these reporter molecules.

A schematic representation of a single-spot, signal-resolvable duplex LFIA is shown in figure 4.14. Section 2.4 describes the method for preparing a single-spot assay. Before spotting onto the NC membrane, CRP Abs and IL-6 Abs were mixed together. The mixed Abs were then immobilised onto the NC membrane.

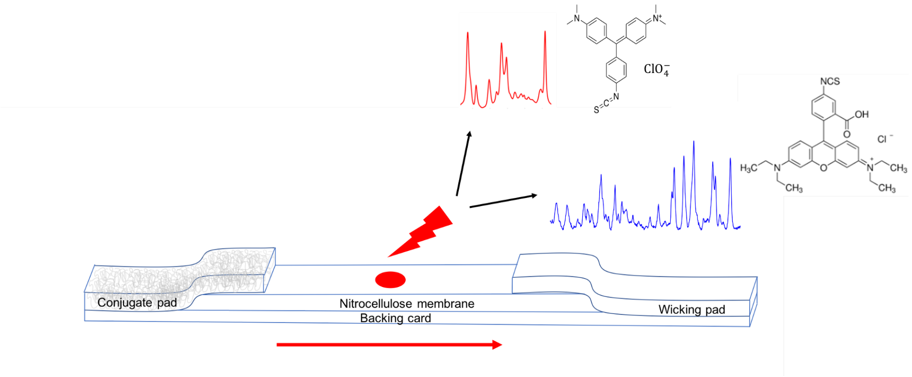

Figure 4.14: Schematic representation of a single-spot duplex LFIA. Both CRP Abs and IL-6 Abs were mixed together in solution and immobilised on the NC membrane where a red spot appeared after running the assay. The sample solution contained 100 ng/mL of both biomarkers + both conjugates mixed together in LFIA buffer. The spot was analysed using SERS, the response of which was a combination of both MGITC and RBITC spectra *i.e.* a duplex spectrum. Schematic not to scale.

The sample mixture was prepared the same way as for the spatially resolved assay, both biomarkers were mixed with both conjugates in LFIA buffer and allowed to flow upwards through the strip. A single red spot of accumulated AuNPs was observed to appear on the NC membrane after running the assay and this could be analysed using SERS. As both biomarkers were present in the sample, both conjugates should have been captured by the immobilised Ab mixture. Therefore, signals from both MGITC and RBITC will be detected following analysis of the spot. As shown in figure 4.13, this signal will be a combination of both SERS responses resulting in a unique duplex SERS spectrum, different from either spectrum separately. From this, characteristic peaks from each reporter, representing each biomarker, can be identified in the spectrum, the intensities of which can be used to obtain quantitative information about both CRP and IL-6.

To confirm that the single-spot duplex assay worked, four LFIAs were performed in 100 μL of LFIA buffer:

- LF A1 - both biomarkers + both conjugates
- LF B1 - 100 ng/mL CRP + both conjugates

- LF C1 - 100 ng/mL IL-6 + both conjugates
- LF D1 - no biomarkers + both conjugates

CRP Abs and IL-6 Abs were mixed together at concentrations of 360 μg/mL and 450 μg/mL respectively and spotted onto the NC membrane of each LFIA strip.

Figure 4.15 (a) shows scanned images after all the assays were run, with the black box outlining the region where the Ab mixture had been spotted. Red spots were observed on all LFIA strips with the exception of LF D1. As no biomarkers were present in the sample for this assay, this result was expected. Therefore, colourimetrically it can be seen that in LF A1, LF B1 and LF C1 there was at least one biomarker present due to the appearance of a spot. However, differentiating which biomarkers were present could not be achieved colourimetrically.

Raman mapping analysis was therefore carried out on all four LFIA strips to achieve duplex detection and to determine whether maps could be separated into the characteristic SERS peaks of MGITC (1617 cm^{-1}) and RBITC (1650 cm^{-1}). Appendix A.12 shows the average SERS spectra generated from each map, the duplex SERS spectrum was observed for LF A1. Figure 4.15 (b) shows SERS intensity maps for each assay spot where maps had been constructed from both peak intensities. The 1617 cm^{-1} peak intensity maps are shown in pink and represented CRP. LF A1 and LF B1 displayed strong SERS responses from this peak as CRP was present in both samples. No signal was observed in maps for LF C1 and LF D1 from the 1617 cm^{-1} peak.

The 1650 cm^{-1} peak intensity maps are shown in turquoise and represented IL-6. Strong SERS signals at this peak were observed in maps for LF A1 and LF C1 which was expected as both assays had IL-6 present in the sample mixture. No signals were observed from the 1650 cm^{-1} peak for LF B1 and LF D1 as IL-6 was not present in either sample. Figure 4.15 (c) shows images of the maps from (b) overlaid. When both biomarkers were present (LF A1), the map appeared purple indicating the presence of both MGITC and RBITC peaks. When only

CRP was present (LF B1) in the sample, the map remained pink as only the SERS signal from the 1617 cm^{-1} peak (MGITC) was present. Similarly for IL-6 (LF C1), only the 1650 cm^{-1} peak signal was collected therefore the map remained turquoise. Finally when no biomarkers were present (LF D1), no SERS signal was obtained from either peak position.

The duplex was successfully detected using Raman mapping, however to test if the assay could be portable, the sensitivity of handheld analysis was investigated. Handheld Raman analysis from each LFIA strip is shown in figure 4.16. The stacked spectra are the SERS signals collected from each assay averaged across 6 scans. The spectrum generated from LF A1 (blue spectrum) was a combination of both MGITC and RBITC spectra *i.e.* the duplex spectrum. The black dotted lines (figure 4.16) indicate the position of the 1617 cm^{-1} peak (representing CRP) and the 1650 cm^{-1} peak (representing IL-6). Both peaks were observed in the handheld spectrum collected from LF A1, indicating the presence of both biomarkers which correlated with Raman mapping data (Appendix A.12). As shown in figure 4.13, the peak contributions from each of the reporters was evident especially when compared to the SERS signals generated from the three control LFIAs. It should be noted that, despite the biomarkers being present at the same concentrations, the 1617 cm^{-1} peak of MGITC (representative of CRP) was of a higher intensity than the 1650 cm^{-1} peak of RBITC (IL-6). This was due to MGITC being resonant at 638 nm laser excitation and geneating a more intense SERS spectrum. However, as already seen, the MGITC signal did not swamp the RBITC signal as the concentrations of each reporter attached to AuNPs had been optimised to adjust for resonance effects, *i.e.* a much higher concentration of RBITC was used, and the peak signals were quite close in relative intensity.

For LF B1, only CRP was present in the sample, therefore it was expected that the spectrum for MGITC only would be obtained and the 1650 cm^{-1} peak of RBITC would be absent. This was indeed the case, as can be seen from LF B1 SERS signal (yellow spectrum). Similarly, only IL-6 was present in the

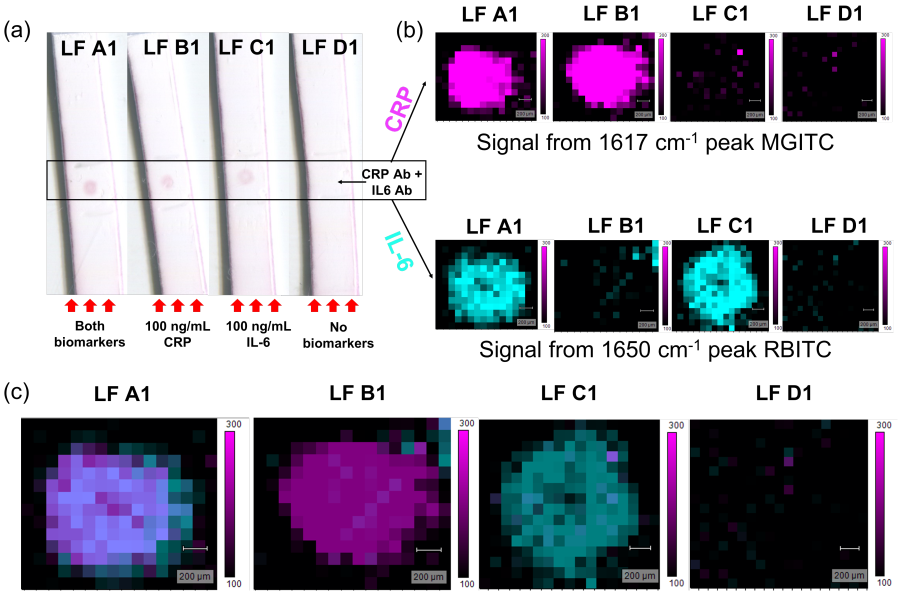

Figure 4.15: Raman mapping results from the single-spot duplex assay (a) scanned images from each assay. Each LF strip was run with 100 μL of the following sample mixtures prepared in LFIA buffer: LF A1 - both biomarkers at 100 ng/mL each + both conjugates, LF B1 - 100 ng/mL CRP only + both conjugates, LF C1 - 100 ng/mL IL-6 + both conjugates and LF D1 - no biomarkers present + both conjugates. The black-outlined box indicates the position of the immobilised Ab mixture, red spots were observed on LF A1, B1 and C1. There was no red spot present on LF D1 as no biomarkers were present in the sample solution, (b) SERS intensity maps constructed from each of the spots with caption indicaing which SERS peak was used. In pink, maps were constructed from the intensity of the 1617 cm^{-1} peak of MGITC (representing CRP) and showed high intensity at this peak for LF A1 and LF B1 as CRP was present in both samples. Below, in turquoise, maps were constructed from the 1650 cm^{-1} peak of RBITC (representing IL-6), the maps showed intense signals for this peak from LF A1 and LF C1. This was expected as both assays had IL-6 present. No signal from either peak intensity was observed in LF D1 as no biomarkers were present in the sample mixture and (c) shows the maps from (b) overlaid for each LFIA, when both biomarkers were present (LF A1), overlaying the maps produced a purple colour from both peak intensities being present on the spot. When only CRP was present (LF B1), the map remained pink representing MGITC and for LF C1 when only IL-6 was present, the map remained turquoise (RBITC). Raman mapping was performed at 633 nm laser excitation, 0.73 mW laser power, 5 s acquisition time and 100 μm step size.

sample for LF C1, therefore the SERS spectrum for RBITC only was observed (red spectrum) and there was no appearance of the 1617 cm^{-1} peak of MGITC.

Finally for LF D1, both peaks were absent from the SERS spectrum (black spectrum) as expected, as neither biomarkers were present in the sample. As

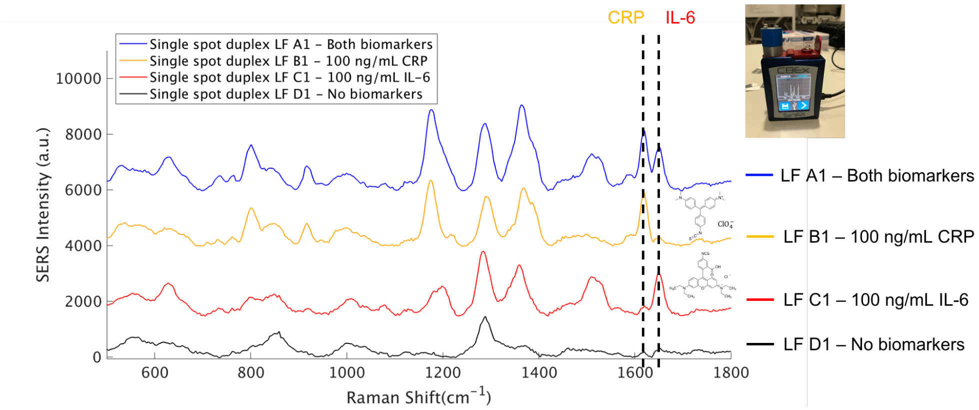

Figure 4.16: Results from handheld Raman analysis of the single-spot duplex assay for each LFIA strip. The blue spectrum was collected from LF A1 where both biomarkers were present in the sample and represents the duplex spectrum of both reporter (MGITC and RBITC) signals together. Black dotted lines indicate the peaks which represent each biomarker, 1617 cm^{-1} peak (MGITC)for CRP and 1650 cm^{-1} peak (RBITC) for IL-6, the appearance of both peaks means both biomarkers are present. In the yellow spectrum (LF B1), only the 1617 cm^{-1} peak was present because only CRP was present in the sample. Similarly, in the red spectrum (LF C1), only the 1650 cm_{-1} peak was observed as only IL-6 was present. Neither peak appeared in the black spectrum (LF D1) as neither biomarker was present in the sample. Handheld Raman analysis was carried out at 638 nm laser excitation, 27.8 mW laser power, 0.5 s acquisition time and all spots were scanned 6 times.

was seen in the spatially resolved duplex assay, when no biomarkers were present (figure 4.12 (d)), peaks at 855 cm^{-1} and 1288 cm^{-1} were observed in the spectrum for LF D1. Again, these may be due to SERS enhancement of the NO and NO_2 groups of the NC membrane by residual AuNPs that were not removed during the the washing step.

Raman mapping results and handheld Raman analysis indicated that the signal-resolved duplex LFIA had been successful and a clear duplex spectrum of MGITC and RBITC was generated in the presence of both biomarkers at 100 ng/mL. Therefore, a concentration study was performed in order to determine whether quantitative information could be gained for each biomarker using this assay platform.

4.3.2.3. Signal-resolved Duplex Assay - Quantitative Detection of CRP and IL-6

Quantitative detection of CRP and IL-6 was attempted to demonstrate that quantification could be achieved and detection limits could be attained for these biomarkers using the signal-resolved duplex LFIA platform. This would also show that more information could be obtained from a single sample using handheld SERS analysis for quantification. The following concentrations of CRP and IL-6 were prepared as a mixture in 100 μL of LFIA buffer - 500, 250, 100, 50, 25, 5 and 0 ng/mL. The LFIA strips were prepared as described in section 2.4 with CRP Ab and IL-6 Ab mixed together and immobilised onto the NC membrane of each LFIA strip. The concentration study was performed in triplicate.

Figure 4.17 (a) shows scanned images from one of the triplicate studies. Red spots were observed for all biomarker concentrations except for the blank, 0 ng/mL CRP and IL-6. The corresponding overlaid SERS intensity maps for each concentration are also shown in (a). Maps were constructed using both the 1617 cm^{-1} (MGITC) and the 1650 cm^{-1} peak (RBITC) for each concentration and overlaid to give a blended SERS intensity map. When both SERS signals were contributing to the signal, the image appeared purple. As shown in previous figure 4.15 (b), 1617 cm^{-1} contributions appeared as pink while 1650 cm^{-1} contributions appeared as turquoise.

From the map generated for 500 ng/mL of CRP and IL-6, there was a much larger region of the spot contributing to the 1650 cm^{-1} signal as shown by the turquoise area. The purple area indicated the region where both SERS signals were contributing but also showed the area of the spot that was generating a signal at the 1617 cm^{-1} peak representative of CRP. Both biomarkers were present at the same concentrations however there appeared to be more IL-6 specific AuNP conjugates binding to the mixture of immobilised Abs. This may be due to the difference in size between both biomarkers. The molecular weight of CRP is ~118 kDa while IL-6 is approximately 4 times smaller at ~26 kDa.[124,125] CRP also has 5 identical epitopes available for binding whereas IL-6 only has 2 which are non-identical.[21,29] Therefore, as AuNP-Abs conjugates interact with more and more CRP proteins as they travel along the LFIA strip, the complexes may become larger and heavier resulting in a slower flow time through the strip. AuNP-Ab-IL6 complexes will lighter and move at a faster speed resulting in these complexes reaching the Ab region more quickly.

These complexes then bind to the IL-6 specific Abs and take up space, in effect blocking the immobilised Abs that could bind to CRP due to the size difference between AuNP-Ab-IL6 complexes (approximately 70 - 80 nm) and the immobilised Abs (approximately 10 nm). It can also be argued that, at this high CRP concentration, when the AuNP-Ab-CRP complexes come into contact with the immobilised CRP specific Abs, they bind immediately and with high affinity forming a half-moon shaped accumulation of AuNPs.[64] It may also be possible that both of these effects contributed to a smaller region of AuNP-Ab-CRP complex binding. The hook effect could also be contributing to the loss in signal at higher concentrations, where excess, unbound CRP interacts with immobilised Abs effectively blocking these sites where AuNP-Ab-CRP complexes could have bound.

As CRP concentration decreases, a larger purple region was observed in the maps which could be due to the complexes flowing faster along the strip as there was less CRP present and additionally, less unbound CRP to generate a hook effect. Since there was also less IL-6 present, there may also have been less of these interactions happening with immobilised IL-6 Abs on the NC membrane allowing space for AuNP-Ab-CRP complexes to bind. Appendix A.13 - A.15 shows scanned images and Raman map data from all three concentration studies

constructed at the 1617 cm^{-1} peak, the 1650 cm^{-1} peak and overlaid maps across replicate studies.

Figure 4.17 (b) shows average duplex spectra from handheld Raman analysis for each concentration across the replicate studies. The peaks of interest from MGITC (1617 cm^{-1}) and RBITC (1650 cm^{-1}) are indicated on the graph. A

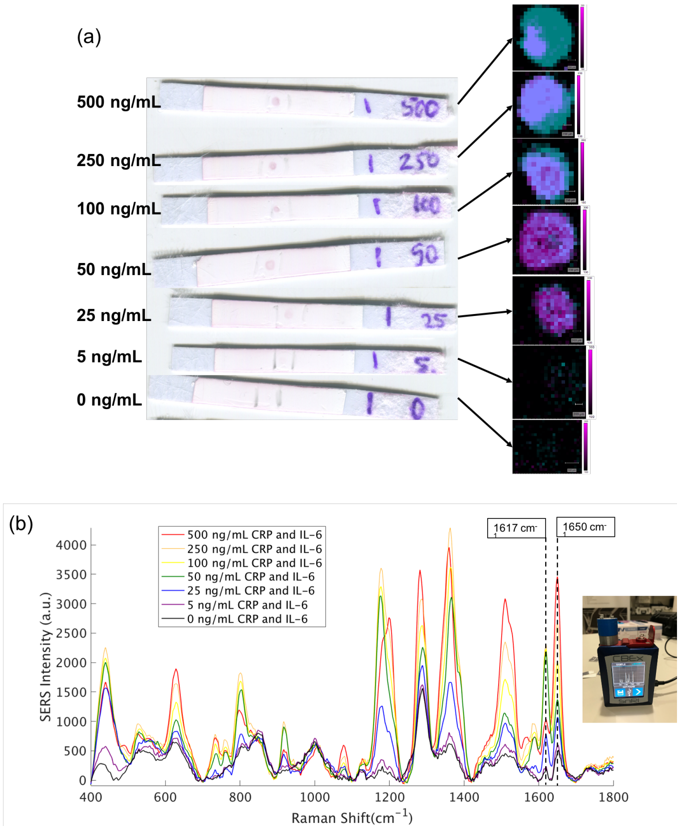

Figure 4.17: SERS analysis results from a CRP and IL-6 concentration study carried out in triplicate on a single-spot, signal-resolved duplex LFIA platform (a) scanned images from one of the replicate studies of the LFIA strips after the assays were performed. The following CRP and IL-6 concentrations were used: 500, 250, 100, 50, 25, 5, 0 ng/mL, red spots were visible on all LFIA strips excluding 0 ng/mL. The corresponding overlaid SERS intensity maps are also shown in (a) where maps were constructed from both peaks of interest, 1617 cm^{-1} MGITC peak representing CRP and 1650 cm^{-1} RBITC peak representing IL-6. Maps appeared purple when both biomarkers were present, pink when only CRP was present and turquoise when only IL-6 was present. These maps indicated that with increasing CRP concentration, the 1617 cm^{-1} peak (MGITC) contributed less to the overall SERS response and was confined to a specific region. Appendix A.16 shows average SERS spectra from mappig results along with calibration curves constructed from 1617 cm^{-1} (MGITC) and 1650 cm^{-1} (RBITC) peaks, (b) average handheld SERS spectra across the triplcate studies for each concentration, the peaks of MGITC and RBITC are highlighted with the black-dotted lines. The 1650 cm^{-1} peak displayed a decrease in SERS signal with decreasing IL-6 concentration however, the 1617 cm^{-1} peak intensity decrease only followed a decreasing trend from 100 - 0 ng/mL CRP. Raman mapping was performed using 633 nm laser excitation, 0.73 mW laser power, 5 s acquisition time and 100 μm step size.

decreasing trend of SERS intensity of the 1617 cm^{-1} peak with decreasing CRP concentration was observed from 100 ng/mL and below. This was also demonstrated in the calibration curve shown in figure 4.18 (a). The inset shows the relationship between SERS intensity at the 1617 cm^{-1} peak and CRP concentration across the full concentration range. At higher CRP concentrations, the SERS signal was observed to plateau and eventually diminish rapidly at 500 ng/mL CRP. This was in correlation with the mapping data which demonstrated that at higher CRP concentrations, the contribution from the 1617 cm^{-1} peak to the overall SERS signal was lower than expected. A LOD of 7.2 ng/mL was calculated (equation 3.1) from the CRP concentration range of 0 - 100 ng/mL using the handheld spectrometer.

With regards to the 1650 cm^{-1} peak highlighted in figure 4.17 (b), a decrease in SERS intensity was observed with decreasing IL-6 concentration. Figure 4.18 (b) shows the calibration curve from 1650 cm^{-1} peak intensity with respect to IL-6 concentration, constructed from the linear region (0 - 100 ng/mL IL-6) of the graph shown in the inset. The LOD calculated for IL-6 was 14.1 ng/mL (0 - 100 ng/mL range) using handheld Raman analysis.

Comparing the detection limits calculated for handheld analysis with Raman mapping analysis, the results are somewhat in line with one another. Average spectra from Raman maps across triplicate studies are shown in figure A.16 of the Appendix along with calibration curves for CRP and IL-6 with respect to the 1617 cm^{-1} peak and 1650 cm^{-1} peak intensities respectively. LOD's for these were calculated to be 6.5 ng/ml for CRP and 7.5 ng/mL for IL-6. The mapping data demonstrated improved sensitivity particularly with regards to IL-6 detection however, each map took ~30 mins to run on a bulky benchtop

instrument while handheld analysis took 3 s per LFIA strip (6 scans x 0.5 s) on a portable instrument. The LODs calculated for each biomarker independently were 8 ng/mL for CRP (0 - 100 ng/mL range) and 10.5 ng/mL for IL-6 (0 - 50 ng/mL range), comparing these with the values calculated for the duplex assay,

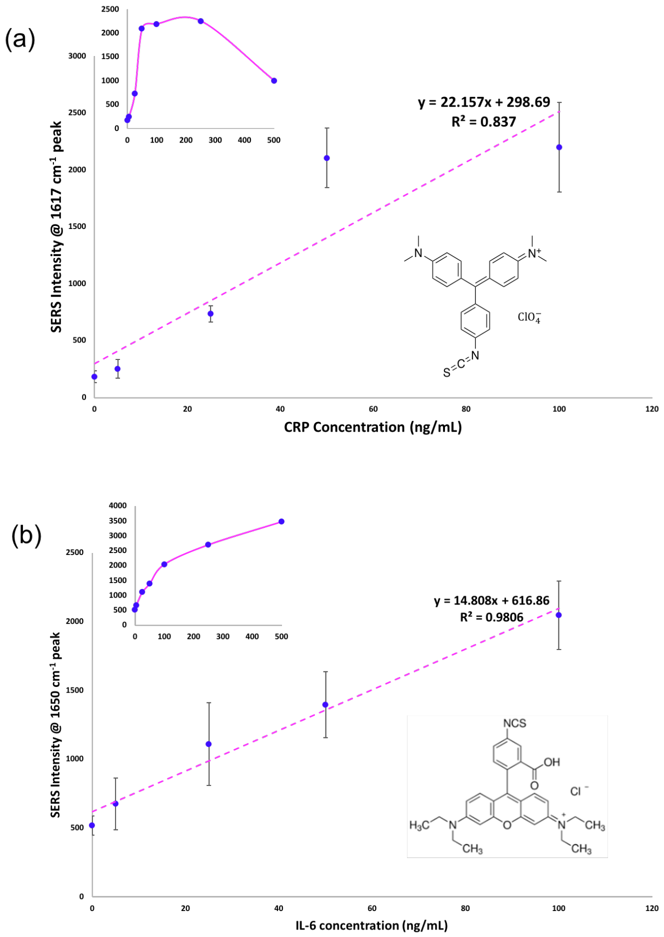

Figure 4.18: Calibration curves constructed from handheld SERS analysis (a) calibration curve of SERS intensity of the 1671 cm^{-1} peak against CRP concentration constructed from the linear region of the graph shown inset, a LOD of 7.2 ng/mL was calculated for CRP and (b) calibration curve of SERS intensity of the 1650 cm^{-1} peak against IL-6 concentration constructed from the linear region (0 - 100 ng/mL) of the graph shown inset, a LOD of 14.1 ng/mL was calculated for IL-6. Handheld Raman analysis was carried out using 638 nm laser excitation, 27.8 mW laser power, 0.5 s acquisition time and each spot was canned 6 times.

they are quite close. The detection limit for CRP was slightly lower at 7.5 ng/mL across the same concentration range. For IL-6, there was a loss in sensitivity with the detection limit increasing from 10.5 ng/mL to 14.1 ng/mL however this was across a larger concentration range of 0 - 100 ng/mL of IL-6. This was a promising result using the signal-resolved duplex assay and indicated that the interactions remained highly specific even when reagents were mixed together, with negligible cross-reactivity and non-specific binding occurring.

The frustration encountered with this assay was that it appeared to work better for lower concentrations of CRP but for higher concentrations of IL-6. When taking into account the clinically relevant levels associated with each biomarker, it would have been more beneficial if the reverse was true. CRP is present at higher concentrations in the blood during an inflammatory condition *i.e.* > 10 μg/mL while high levels of IL-6 are reported to be close to 1 ng/mL in the event of sepsis. Therefore, while this assay platform demonstrates the potential of developing multiplexed biomarker detection simultaneously, on a single LFIA strip and from analysis of a single region, further optimisation is needed for these particular biomarkers. Further thought would need to go into the dynamic range required for the sensitive detection of each biomarker and how that could be applied to a single LFIA device. Certainly it is possible to collect a multiplex SERS signal from a single spot and this signal-resolved duplex assay will act as preliminary work towards developing a LFIA platform that is capable of multiplexed biomarker detection at clinically relevant concentrations.

Additionally, the application of a SERS-based, signal-resolved LFIA platform can be used for the multiplexed detection of biomarkers associated with many different disease states such as atherosclerosis and other cardiac related issues, be they for monitoring or diagnostic purposes, cancer biomarker detection and diagnosis of viral infections.[97,111,114,115,126]

4.4 Conclusion

Quantitative detection of IL-6 was demonstrated using a SERS-based LFIA platform. RBITC was chosen as the Raman reporter to represent IL-6 with the aim of developing a duplex detection assay for CRP and IL-6. An intense SERS signal was generated for AuNP-IL6-Ab conjugates using 638 nm laser excitation. Quantitative detection of IL-6 was achieved with a LOD of 10.5 ng/mL from handheld Raman analysis using the 1650 cm^{-1} peak intensity of RBITC for quantification. Although this detection limit was above the range considered to be clinically relevant for IL-6 ($\sim$1 ng/mL in the event of sepsis), these results could be used for preliminary development of a SERS-based duplex detection assay on a single LFIA device.

A spatially resolved duplex assay was demonstrated on a single LFIA strip by firstly spotting CRP Ab and IL-6 Ab onto individual regions of the strip. This approach showed the specificity of the AuNP conjugates for their distinct biomarker and that non-specific binding or cross-reactivity was not occurring. However, with the need for multiple biomarkers to be detected simultaneously for sepsis diagnosis there is only a finite amount of NC membrane for the spatial immobilisation of different Abs. Therefore, it was investigated whether signal-resolved duplex detection could be obtained by immobilising a mixture of Abs on a single spot.

For the signal-resolved duplex assay, CRP Abs and IL-6 Abs were mixed together and immobilised on the same region of the membrane allowing analysis to be performed on a single test region. Duplex detection was achieved for CRP and IL-6 using this approach and quantitative information was also obtained for both biomarkers using SERS. LODs of 7.2 ng/mL and 14.1 ng/mL were observed for CRP and IL-6 respectively. These were found to be close to detection limits calculated for individual LFIAs performed for each biomarker in a singleplex assay, where LODs of 8 ng/mL and 10.5 ng/mL were calculated for CRP and IL-

6 independently. It was noted that, again, clinically relevant IL-6 detection limits could not be achieved but nevertheless, the results demonstrated the specificity of the assay for each of the biomarkers and that multiplex detection can be accomplished using SERS. A handheld Raman spectrometer was used for analysis of the assays with time of 3 s per assay. The combination of the LFIA platform with a portable spectrometer shows the viability of this system for point-or-care, multiplexed detection.

From this investigation, it is clear that further optimisation is needed for clinically relevant detection of both biomarkers simultaneously. One aspect that could be improved is the immobilisation of capture Abs onto the NC membrane. The Abs were spotted on at 0.6 μL using a pipette resulting in little control over how the Ab dispersed through the porous matrix and also how it dried. As a consequence of this, the spots were heterogenous in shape and size between replicate assays which may be of crucial importance with regards to assay reproducibility, particularly for the signal-resolved duplex assay. To overcome this, it would be beneficial to use a precision line dispensing system for the plotting of an Ab test line onto the NC membrane in future investigations.

Taking into account the range of detection for both CRP and IL-6 for this assay, biomarkers present in the ng/mL concentration range in the event of sepsis may be ideal for use with this LFIA platorm. For example, procalcitonin (PCT) is another biomarker with links to sepsis, where levels >2 ng/mL indicate the presence of severe localised bacterial infection and possible sepsis. PCT also holds prognostic value for the condition where decreasing levels can suggest resolution of the illness.[127] Matrix metalloproteinases or MMPs have shown value as biomarkers for cancer, stroke and inflammatory conditions such as osteoarthritis.[128–131] They are present in blood serum/plasma at concentrations in the ng/mL range, where high concentrations exceed 30 ng/mL for most MMPs.[131] These levels are well within the working range of the assay developed here and furthermore may benefit from skipping a sample dilution step before running the assay.

As demonstrated by Sanchez-Purra *et al.* (figure 4.3 (d)), pentaplex signal resolution is possible from a single test area using five different Raman reporters with characteristic peaks that can be identified in a multiplex SERS spectrum.[117] Although the authors did not detect any protein specifically in this experiment and used a generic capture species to bind with the SERS probes, they demonstrated what can be achieved using SERS as part of a signal-resolved assay platform. If multiple test regions were placed on the NC membrane of a LFIA, combining spatial and signal-resolved multiplexing, the potential exists, for example, to detect 10 biomarkers simultaneously from a single sample when two test regions are present. Incorporating array-type test regions,[109] as demonstrated by Zhang *et al.* (figure 4.2 (d)) could theoretically allow for the detection of 30 biomarkers simultaneously from a single sample using a handheld Raman spectrometer.

While the application for a multiplexed LFIA coupled with SERS analysis holds enormous potential, much work is needed for optimising these assays - ensuring the assay works for biomarker concentrations that are clinically relevant, choosing reporters that can be identified in a multiplex spectrum, ensuring the relative intensities of the reporters are close to one another and one signal does not dominate the spectrum, the hook effect must also be taken into account, the interactions must be highly specific with negligible cross-reactivity and non-specific binding and the biomarkers chosen for detection must all give information about the disease state, be it diagnostic and/or prognostic.

5. Optimisation of a 3D Paper-based device for Biomarker Detection

5.1 Introduction

The 3D paper-based device used in this investigation was the result of a large amount of research into paper-based microfluidics which has spanned the past 13 years. Microfluidic paper-based analytical devices or μPADs were first conceived by George Whitesides and co-workers with the aim of developing low-cost, portable assays that only required a small sample volume to run. Their vision was for these devices to be used in rapid diagnostics in developing countries, triage and emergency situations and personalised health care at home.[132]

Initial μPAD protocols involved a photoresist template that was impregnated into chromatography paper. The photoresist design acted as a hydrophilic barrier that could direct liquid along the paper channels in a controlled way. The advantage of this was that multiple assays could be performed on a single device depending on the design of the photoresist and only a single, small sample volume was required.[132] Martinez *et al.* demonstrated this in one of Whitesides' group's early μPADs, where the simultaneous detection of glucose and BSA was achieved through visual colour changes in the test zones of a branched template design. The test zones were pre-treated to visualise the colour change for each analyte, in the case of glucose the colour changed from clear to brown due to the oxidation of an iodide treatment species to iodine. Similarly, for BSA the test zone was partially treated with tetrabromophenol blue (TBPB) which changed from yellow to blue in the presene of BSA. They also showed another advantage of the μPAD as having the capability to separate sample from debris such as dirt, plant pollen and graphite powder, large contaminants that may be found in the field.[132]

Figure 5.1 (a) shows an early design of a 3D μPAD by Whitesides and co-workers with two sample entry points on the top layer. The entry points begin at channels placed at the corner of the device which enables the wicking of fluid by dipping the corners of the 3D μPAD into the sample. This also eliminates the need for a pipette which may not be readily to hand in the field. As the sample flows through the five layers of the device, the template design facilitates the channelling of the fluid into two sections of eight readout spots, four spots for the control and four spots for the sample. The readout regions were pre-treated with reagents for the colourimetric detection of glucose and BSA simultaneously from the same sample thereby enabling the replicate detection of two analytes on one device.[133]

In addition to this, slight changes were made to the 3D μPAD to facilitate the analysis of four samples with the inclusion of four sample entry points. The two devices, two sample and four sample 3D μPADs, are shown in figure 5.1 (b) after running assays for glucose and BSA, with a table displaying the results. The sample entry points are evident at the corners of each device. The images shown are of the bottom of the devices which were analysed prior to running and drying. An Epson scanner was used to scan the devices and Adobe Photoshop was used to analyse the colour intensity at each test spot.[133]

Ellerbee *et al.* demonstrated the detection of BSA using a μPAD coupled with a specially designed transmittance reader in which the device could be housed for analysis.[135] In this way, the device could be read by a rapid, handheld, point-of-care system without the need for external equipment. The μPAD incorporated four reaction zones including one control region. The device was run and placed in a plastic slip containing oil. The function of the oil was to reduce the difference in refractive index between the paper device and the surrounding environment.

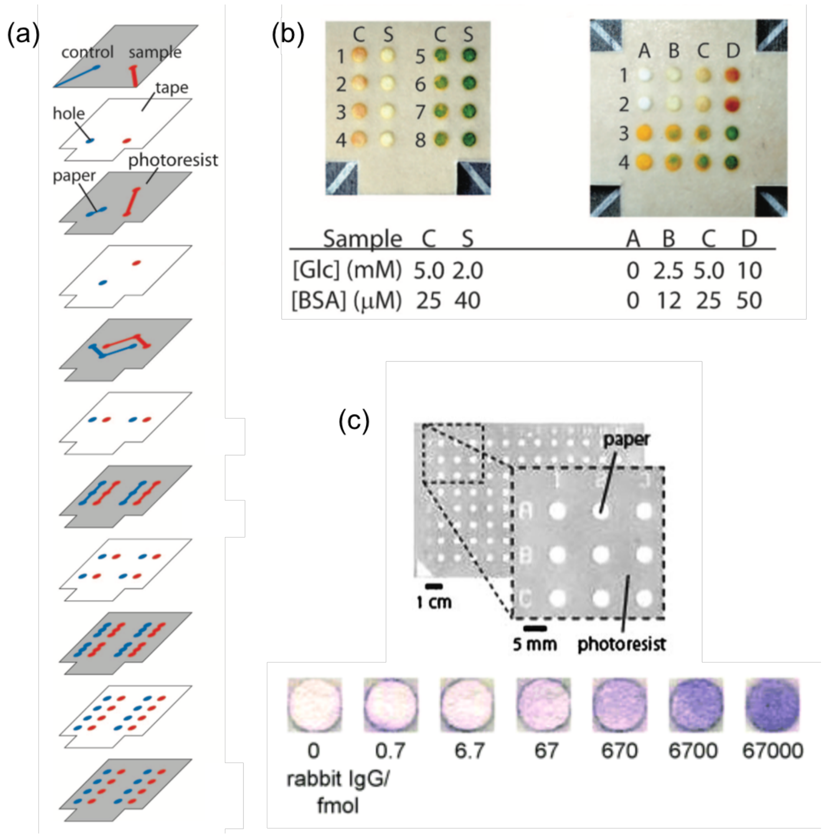

Figure 5.1: Examples of Whitesides and co-workers work using paper as microfluidics devices (a) manifestation of first 3D μPAD for running assays simultaneously, in parallel for the detection of glucose and BSA. A photoresist was used for the design template of each layer (shown in grey) and tape layers were placed in between each paper layer (white) to allow for controlled flow of liquid along specific, hydrophobic channels.[133] Replicate assays for glucose and BSA were carried out on this device with the results shown in (b). The device was turned over to reveal the results of the assay. The assay on the left was carried out for high (S) and low (C) concentrations of glucose and BSA and the device allowed for four replicates to be performed simultaneously. The device on the right demonstrated simultaneous, quantitative detection of both glucose and BSA in duplicate on a single device. The cut-out corners of each device were the areas which drew in the sample fluid which consisted of spiked artificial urine.[133] A paper-based ELISA is shown in (c) also developed by Whitesides and co-workers. The image shows a 96-well plate in paper form, zoomed in to demonstrate the paper and photoresist areas. Below, results for the detection of rabbit IgG demonstrate the workability of the ELISA on paper with quantitative information being obtained.[134]

The slip was placed in the colourimetric reader equipped with an LED light to interrogate the test zones, an external screen then gave a digital readout of transmittance. The transmittance was then normalised against a control which adjusted for background attenuation. This normalised value, T_N, was used to construct a calibration curve of T_N versus analyte concentration.[135] While the μPAD-reader combination is ideal for point-of-care detection, this particular design encountered problems with the need for an index-matching medium and the fact the device could not be run while being housed in the reader system. Whitesides and co-workers also showed that a camera phone could be used alongside colourimtetric analysis for the portable detection and quantification of glucose and BSA.[136]

Figure 5.1 (c) shows a paper-based ELISA (P-ELISA) developed by Cheng *et al.* The 96-well template design was again impregnated into the paper using a hydrophobic photoresist. To prove the workability of this new approach to ELISA, the authors immobilised rabbit IgG antigen of increasing concentration onto the P-ELISA. They then washed through IgG Abs labelled with alkaline phosphatase (ALP) which produced a colourimetric readout. The results from the concentration study are also shown in figure 5.1 (c), the purple colour was observed to increase in intensity with increasing IgG concentration. Additionally, the P-ELISA was capable of detecting and quantifying the HIV-1 specific Abs in human serum by immobilising HIV-1 antigen gp14 on the P-ELISA test zones and using an ALP-conjugated anti-human IgG Ab.[134]

Although the P-ELISA was found to be less sensitive than conventional ELISA, it paved the way for further research on paper-based immunoassays which were more cost-effective, user-friendly, portable and much faster than ELISAs. Another revelation in μPAD technology came with the replacement of photoresist patterning techniques used for the design template. Lu *et al.* reported the first use of wax printing for creating a hydrophobic barrier in μPADs. The template was wax-printed onto the paper followed by heating, allowing the wax to melt through the paper forming hydrophobic channels in line with the template design.[137] Whitesides and co-workers published their research on wax printing shortly afterwards.[138]

With wax printing offering a more accessible and low-cost fabrication method and multiplexed detection becoming more essential, research began to focus on developing μPADs for immunoassay and multi-analyte detection while also trying to increase the sensitivity of the devices.

5.1.1 Advances in μPAD development for rapid detection

Distance-based readouts, where distance travelled by the readout solution along a channel is used as a form of measurement, have been investigated for rapid disease detection. In this approach, the sample solution is usually coloured or for example, in the case of hematocrit measurements, the distance travelled by a whole blood sample is measured. Berry *et al.* optimised a double-layer, wax-printed μPAD which consisted of a sample inlet layer placed on top of a single-channel template. The device was used to measure the hematocrit *i.e.* to quantify the liquid component of blood which can be an early indicator of dehydration and anaemia. A low hematocrit, indicative of anaemia, was represented by the whole blood sample travelling a further distance along the channel of the μPAD, while at a high hematocrit, indicative of dehydration, the blood failed to move a small distance from the sample region. Therefore the authors were able to rapidly measure hematocrit by a distance-based readout and without the need for external equipment, although the blood did need to be pre-treated with an anti-coagulant.[139]

Similar μPAD designs have been used for the colourimetric detection of lactoferrin in saliva, where the distance at which the colour change occurred along the channel indicated the amount of lactoferrin present in the sample.[140] Wei *et al.* also used a distance-based readout design for the detection of cocaine in urine samples.[141] However, mutliplexed detection is difficult to achieve using this readout method.

Multiplexed drug detection was achieved using a branched wax-printed template design by Wang *et al.* Three drugs, cocaine, codeine and methamphetamine were detected in an aptamer-based assay where AuNPs were used to generate a colourimetric response. In the absence of the drug targets, the test zones remained red because the drug-specfic aptamers were free to protect the AuNPs surface, while if the drug was present, the test zone appeared blue due to the aggregation of AuNPs.[142] Nanoparticles have also been used to enhance the colourimetric response from a test region for the triplex detection of glucose, glutamate and lactate. A different chromogenic reagent was used for each analyte and the response was intensified by pre-immobilising silica NPs at each of the test zones prior to running the assay.[143]

Advances have also been made in wax printed template design, particularly with respect to 3D μPADs. 3D origami μPADs have been investigated for multiplexed immunnoassays.[144,145] Figure 5.2 (a) shows the design of one such device. This origami-inspired μPAD was used for the simultaneous detection of four tumour biomarkers. Capture Abs were immobilised on the test pad shown in green on the device. The device was run using pre-agglutinated whole blood samples. The filter tab (shown in red) was folded over the test pad and the whole blood samples were introduced to the device through this layer, filtering out the agglutinated red blood cells. The filter tab was then torn away and a wash step was performed using one of the wash tabs (blue). AgNP conjugates functionalised with biomarker-specific Abs and luminol were added to each of the test zones on the test pad followed by a second washing step. Finally the reagent tab was used to stagger the introduction of H_2O_2 to each of the test zones which would generate a chemiluminescence (CL) response. Due to staggering the reaction at each test zone, multiplexed detection of the tumour markers was possible by the time delay in the appearance of the CL response. The intensity of this response was also used to quantify the assay.[145]

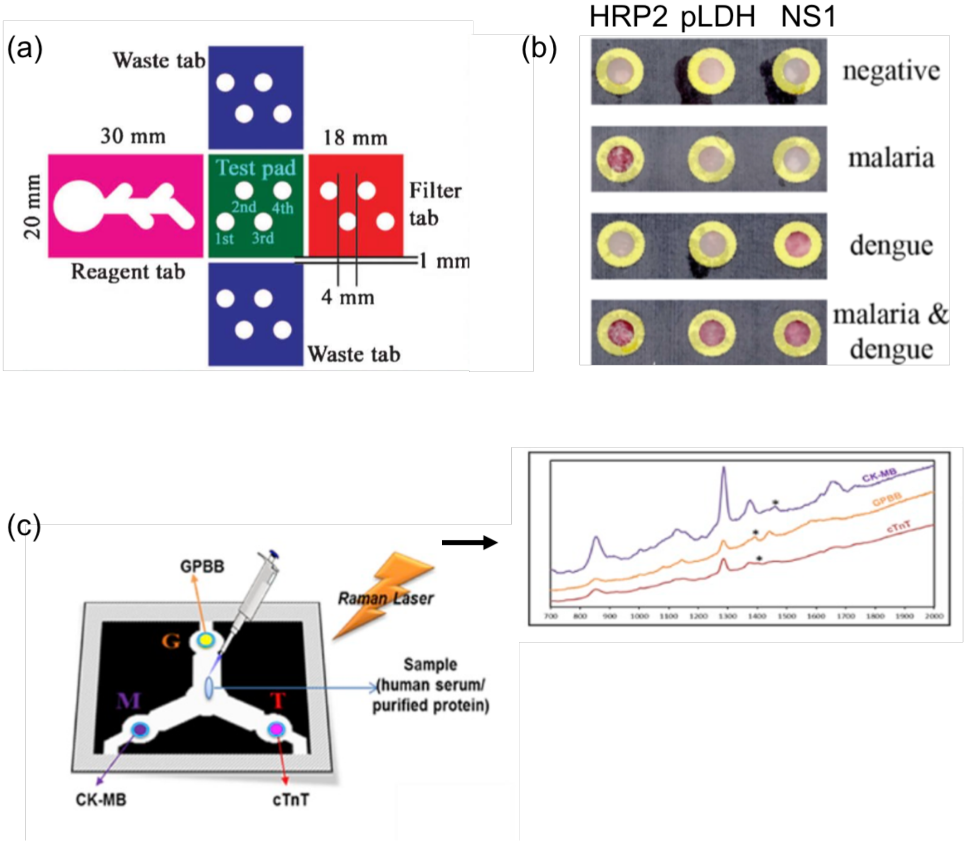

Figure 5.2: Examples of how μPAD research has developed since Whitesides and co-workers work (a) 3D origami μPAD for the simultaneous detection of 4 tumour biomarkers - fetoprotein (AFP), carcinoma antigen 153 (CA153), carcinoma antigen 199 (CA199), and carcinoembryonic antigen (CEA). Using the device involved folding each tab over the test pad (green) as needed and tearing away that tab once it had been used. A plasma filter tab (red) was integrated into the device and an agglutination reagent was used to facilitate detection in whole blood samples. After sample introduction, the device was washed before AgNP-luminol-Ab detection complexes were added to the test areas. Chemiluminescence (CL) was used as the analysis technique where the treatment of each test area with H_2O_2 was staggered using the reagent tab (pink) following a second wash step. This allowed for time differences in CL response to detect and quantify each biomarker,[145] (b) triplex detection of malaria HRP2, malaria pLDH, and dengue NS1 type 2 for the rapid diagnosis of malaria and/or dengue fever. The 3D μPAD used AuNPs as a colourimetric readout and the device was also performed using whole blood samples with the integration of a plasma separation material as the top layer[146] and (c) a single layer μPAD for the simultaneous detection of three cardiac biomarkers using NPs and SERS. The authors used three different Raman reporters to code for each of the biomarkers.[147]

While the authors results demonstrated acceptable accuracy compared with commercially used methods, the folding and removing of layers added an extra level of complexity to the device making it much less user friendly. Additionally the blood sample required pre-treatment before being tested and at each stage of the assay, a housing folder was used to compress the μPAD together for it to run efficiently. A final step was also needed to obtain the CL response.

Deraney *et al.* developed a 3D μPAD for the detection of three markers associated with dengue fever and malaria, where the presence of all three markers indicated both diseases were present.[146] A plasma separation material was integrated into the top layer of the device, eliminating the need to pre-treat whole blood samples. AuNPs were used for colourimetric detection therefore no extra reagent step was needed as in the case of CL. The device consisted of 8 layers including an extremely absorbent wicking pad as the final layer, the function of which was to draw the sample solution through the device. All layers were stuck together using double-sided adhesive. Once the assays had been run, the top five layers of the device were peeled away to reveal the readout/capture layer where target specific Abs had been immobilised prior to running the device. In the presence of the biomakers, Ab-functionalised AuNPs would accumulate at the capture layer generating a red colour, the intensity of which correlated with biomarker concentrated. Three capture regions were present on the capture layer representing each of the malaria and dengue fever markers.[146]

Figure 5.2 (b) shows diagnostic results obtained from the μPAD in each case. When the blood sample was negative for all three markers, only a faint red colour was observed. When a biomarker was present, an intense red colour was observed, therefore the device was capable of diagnosing both malaria and dengue fever independently as well as identifying when both diseases were present.[146] A singleplex version of this μPAD, developed by Mace and co-workers, was used in this investigation for the optimisation of a SERS-based 3D μPAD. Since it has been shown that NPs already work well in μPADs, the incorporation of SERS-active NPs would offer quantitative detection with potentially better sensitivity and scope for an improved multiplexed system.

Figure 5.2 (c) shows one example of a SERS-based single-layered μPAD for the triplex detection of biomarkers associated with acute myocardial infarction - glycogen phosphorylase isoenzyme BB (GPBB), creatine kinase-MB (CK-MB) and cardiac troponin 1 (cTnT). Three different types of NP - AuNPs, Au-urchin NPs and AgNPs were functionalised with three different Raman reporters to code for each of the biomarkers.[147] In a previous publication, the authors had showed they could detect the three cardiac biomarkers colourimetrically with these NPs, obtaining semi-quantitative information.[148] For this investigation, they functionalised the particles with reporter molecules and achieved quantitative results over a larger concentration range with much more sensitive detection limits compared with the colourimetric approach. As shown in 5.2 (c), the serum sample was pipetted into a central inlet of the μPAD and flowed outwards to each of the test zones where capture Abs had been immobilised. The SERS probes were then added to each of their respective reaction zones as shown. The test zones were analysed using a benchtop Raman microscope.[147] For the viabilty of a SERS-based μPAD however, the technique would need to be made portable with the use of a handheld Raman spectrometer.

Mabbott *et al.* incorporated AuNPs into the singleplex μPAD developed by Mace and co-workers, using colourimetric and handheld SERS analysis for the detection of miR-29a, a micro-RNA associated with myocardial infarction.[60] The authors envisioned the use of colourimetric analysis by eye in the field, as a qualitative analysis. Then, in the event of a positive result, the test could be sent to a centralised hub for quantitative SERS analysis using the handheld instrument. Very low detection limits for miR-29a, in the pg/mL range, were attained using SERS analysis while colourimetric results indicated quantitative analysis was not possible using that technique.[60] This again demonstrated the superiority of SERS and its viability for use with the 3D μPADs.

Mace and co-workers had previously used sandwich-like interactions between Ab-functionalised AuNPs and immobilised Abs on the capture layer of the device,[146,149] this study will integrate Raman reporter functionalised AuNPs into the 3D μPAD and use colourimetric and SERS analysis for the detection of CRP with the ultimate aim of developing a rapid, multiplexed, point-of-care diagnosis platform for sepsis.

The following section describes the fabrication of the 3D μPAD developed by Mace and co-workers and demonstrates the workability of the device for this investigation.

5.1.2 Architecture and Assembly of the 3D μPAD for Biomarker Detection

The 3D μPAD used in this investigation was designed and developed by Fernandes *et al.*[150,151] The device consists of 5 paper layers placed on top of a thick, absorbent pad *i.e.* the wick pad. The template for each layer was carefully designed using AutoPAD software to ensure optimum and controlled flow of sample through the device. Each layer must also undergo treatment prior to assembly of the device.

Figure 5.4 shows a schematic of the 3D μPAD where red arrows indicate the flow of sample through the device. Section 2.5 describes in detail the fabrication protocol for the device. The black rectangles represent each paper layer where the template has been wax-printed on. This technique ensures that a hydrophobic barrier is used to control and direct the flow of a sample in a very specific way. Since the template design is simply printed, the template can be patterned in multiple ways to suit the need of the user and with the implementation of many channels, can facilitate multiplexed detection on a single device from a single sample. The templates were printed onto Whatman Grade 4 chromatography paper (pore size 20-25 μm) for all layers except for the capture/readout layer template which was printed onto a nylon membrane (pore size 0.45 μm). The adjacent clear rectangles represent the double-sided adhesive placed between each paper layer. All adhesive layers are permanent with the exception of the adhesive backing the incubation layer which is removable. This way, the top three layers can be removed to reveal the capture/readout layer after running the assay. A knife plotter can be used to circular cut holes, as shown in figure 5.3, into each adhesive layer in specified regions corresponding to the flow direction of the assay.

Layer one, the sample layer, is where the liquid sample is introduced to the device and also protects the conjugate layer, *i.e.* the second layer of the device where the AuNPs are housed. After addition of the sample, the AuNPs are rehydrated and free to interact with target species present in the sample. The incubation layer directs the sample and rehydrated AuNPs in a lateral flow allowing time for further immunoreactions to take place. The channel length dimensions contribute greatly to the performance of the device. Schonhorn *et al.* reported a channel length of 6 mm for optimum device performance, assay run time and reproducibility.[152]

The capture/readout layer differs from the other layers (Whatman Grade 4 paper) as it is made from a nylon membrane. The material has the same functionality as the NC membrane used in LFIAs however, nylon has increased durability meaning it can better withstand the wax printing process compared with NC which is brittle and breaks apart easily.[152] Target-specific capture Abs are immobilised at the capture region and this is where the AuNP-Ab-target complexes will accumulate. Therefore, the region possesses a yellow ring making it easier to identify the red colour of the AuNPs. The function of the wash layer is to draw any unbound AuNPs away from the capture layer and the analysis area. Unbound AuNPs flow laterally along this layer and are drawn vertically towards the wick pad which collects all excess liquid *i.e.* sample and wash fluids.

The device is assembled from the bottom up and undergoes lamination before use to ensure there are no air pockets between each layer. To reveal the capture layer, a removable double-sided adhesive, as shown in figure 5.3, is placed between the incubation and capture layers. All other layers use permanent adhesive. The

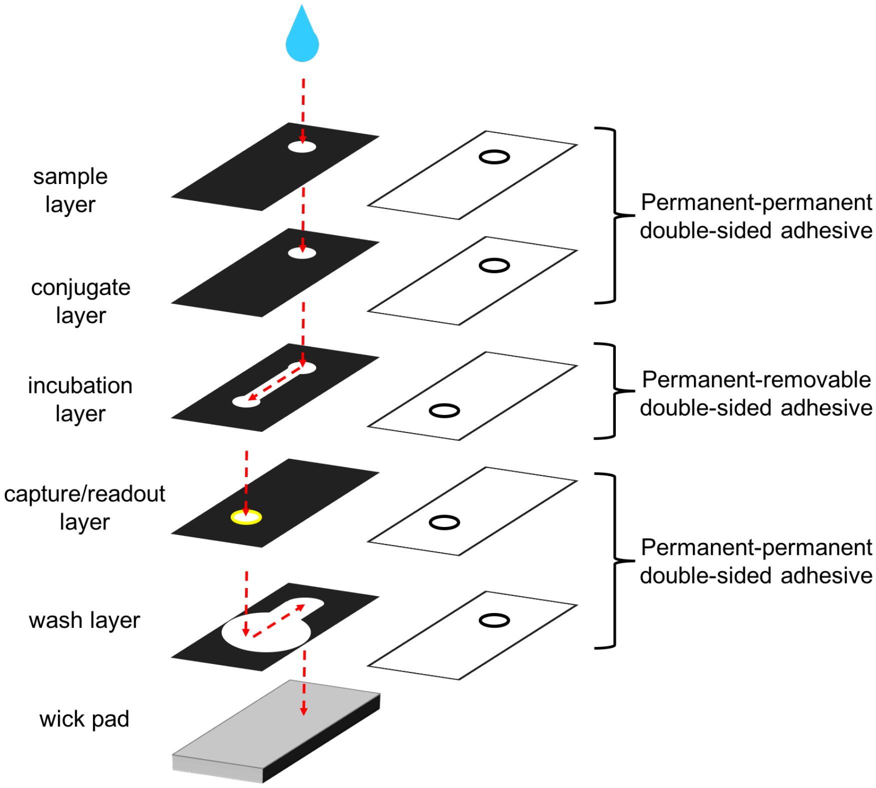

Figure 5.3: Schematic showing the 3D paper-based device used in this investigation. The device consists of 5 layers; sample, conjugate, incubation, capture/readout and wash layers, all backed with double-sided adhesive. A wick pad is placed at the bottom of the device for the collection of excess sample and wash liquids (shown in grey). The black rectangles represent the wax printed template on each of the paper layers. The clear rectangles represent the permanent double-sided adhesive placed on the back of each paper layer, a removable double-sided adhesive is placed between the incubation and capture/readout layer. The sample is directed vertically and laterally through the device in a direction controlled by the hydrophobic wax template design as depicted by the red arrows. AuNPs are typically housed in the conjugate layer, these are rehydrated by the sample, react and complex with the target species while flowing along the incubation layer and the complexes are finally captured on the capture layer. A red colour observed after revealing this layer indicates a positive result. The capture layer is fabricated from a nylon membrane which facilitates protein adsorption. Each layer is approximately 1 cm in width.

---

capture region will appear red if the target is present and will remain white if not. Colourimetric analysis, in the form of RGB values, can the be used to gain quantitative information.

Prior to device assembly, three of the layers must undergo pre-treatment;

the conjugate, incubation and capture layers, which encourages flow of solution through the device while maintaining dispersion of AuNPs. The conjugate layer is firstly treated with a buffer solution containing 10% BSA in 1xPBS, followed by drying (described in section 2.5). AuNPs are then dried on. The incubation layer is treated with a block buffer (5 mg/mL milk powder and 0.1 % Tween 20 in 1xPBS) which is also dried. Finally capture Abs are dried onto the capture layer followed by treatment with the block buffer used for the incubation layer. The device is then ready for assembly. To run the assay, 20 μL of sample is run through the device followed by two consecutive wash steps of wash buffer (0.05 % Tween 20 in 1xPBS). The capture layer is revealed by peeling away the top three layers of the device and can be analysed immediately.[150]

These devices offer many of the advantages associated with LFIAs and the ability to easily change the template design makes them ideal for multiplexed detection. In addition to this, analysis of the capture region using a handheld Raman spectrometer can be readily achieved. Therefore, in this investigation the 3D device was optimised for a SERS-based assay for the detection of CRP with the ultimate aim of further developing multiplexed devices for the rapid diagnosis of sepsis at the point-of-care.

5.2 Chapter Aims

The flexible design of μPADs has demonstrated their great potential for multiplexed detection. While we have already shown signal-resolved duplex detection is achievable using a LFIA platform, the multiplexing ability is limited due to the size of the NC membrane and the number of signals that can be resolved from a single analysis region. With the use of a 3D μPAD, the wax printed design template can facilitate the detection of multiple analytes, and coupling this with SERS, improves the scope for quantitative detection. Additionally, with the future implementation of signal-resolved detection, the number of analytes for detection from a single sample could reach a very high number. This would demonstrate the potential for the identification of more than one disease state simultaneously. It should also be noted that a plasma separation layer can be added to the device which demonstrates its viability for use with whole blood samples.

The aim of this study was to optimise the 3D μPAD, developed by Mace and co-workers, for use with a SERS-based immunoassay.[149,150] CRP was chosen as the proof-of-concept biomarker for detection since the sandwich assay, described in section 3.3, had worked well on the LFIA platform, therefore the same AuNP-Ab conjugates were incorporated into the 3D μPAD. Since colourimetric detection is important for visual confirmation in the field as described by Mabbott *et al.*[60] it was necessary to elicit an effective colourimetric response to initially detect the presence of the target protein. Following this, with the generation of an intense SERS response, quantitative detection could then be achieved using a handheld Raman spectrometer.

Optimisation was performed by altering the AuNP-Ab concentration, the concentration of Ab immobilised on the capture layer and the buffers used for the pre-treatment of the device layers. Once these parameters had been altered to attain the optimum colourimetric and SERS responses, another aim of this work was to achieve quantitative detection of CRP using SERS. It was hoped that by optimising the assay for CRP detection, the 3D μPAD platform could be further developed for portable, rapid detection of multiple biomarkers associated with sepsis from a single small sample volume.

5.3 Results and Discussion

The AuNPs used in this study were the same batch used in the LFIA work, the synthesis for which is described in section 2.3. Extinction spectroscopy, DLS and zeta potential results are given in figure 3.5. As shown in the extinction spectrum, the AuNPs used had a λmax of approximately 520 nm and a FWHM of <100 nm which demonstrated monodispersity.[84] DLS results showed AuNPs were found to have a hydrodynamic radius of 38 nm and zeta potential measurements of <-30 mV, demonstrating the particles were stable.[83] Figure 3.7 shows results from Raman reporter, MGITC and CRP-specific Ab (AuNPs-Ab) conjugation which was performed for AuNPs used in the 3D μPAD. The functionalisation was carried out as described in section 2.3, where MGITC was attached to AuNPs through the S atom of the isothiocyanate group followed by electrostatic attachment of Abs facilitated by pH correction (pH 9) of the AuNPs.

Figure 5.4 shows a schematic representation of the SERS-based assay incorporated into the 3D μPAD. The five layers of the device are shown in (i), AuNPs are dried onto the second layer of the device (conjugate layer) and the capture Ab is immobilised onto the fourth layer (capture layer), as indicated by the grey arrows. The liquid sample, in this case one containing CRP in water, is introduced into the device through the sample layer followed by two wash steps. Figure 5.4 (ii) shows the interactions occurring on the capture layer after running the assay. As the CRP sample flows through the device, it re-hydrates the AuNP-Abs forming AuNP-Ab-CRP complexes. These complexes flow further through the device and are captured by immobilised Abs at the capture layer. Following two wash steps, the capture layer is revealed and RGB and SERS analysis can be performed. Figure 5.4 (iii) shows visual results from the capture layer for two devices, one where the sample contained no CRP (control) and one with CRP present at 100 ng/mL. The red colour was observed when CRP was present in the sample due to the accumulation of AuNP-Ab-CRP complexes binding to immobilised Abs.

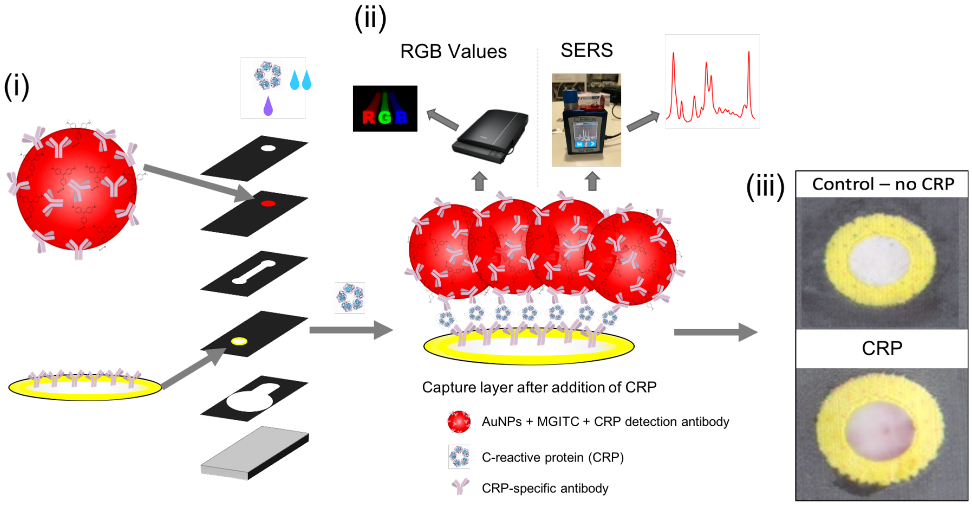

Figure 5.4: Schematic representation of SERS-based 3D device for the detection of CRP - (i) five-layered 3D device, arrows indicate the locations for AuNP-Ab and immobilised Abs, AuNP-Ab probes are dried onto the conjugate (second) layer while the capture (fourth) layer houses Abs to capture AuNP-Ab-CRP complexes, (ii) zoomed in view of the capture layer prior to running the assay where the AuNP-Ab-CRP complexes have bound to the immobilised Abs. This layer was revealed following two wash steps and the region was analysed using RGB and SERS measurements and (iii) visual results from the running of two separate assays, one where no CRP was present in the sample (control) and one where CRP was present resulting in a red colour being observed at the capture zone due to the accumulation of AuNPs. Schematic not to scale.

To determine whether the 3D device needed to be optimised for the integration of a SERS-based assay, assays were initially performed using the same buffer treatments for the layers as Fernandez *et al.* and the same wash buffer.[150] The concentration of capture Ab immobilised onto the capture region was chosen to be 360 μg/mL as this was the optimum concentration used in the LFIA studies for CRP detection. From previous work in the group using the 3D μPAD, AuNP-Ab concentration of 0.4 nM was chosen.[153]

Two assays were performed on separate control and sample devices to test 0 ng/mL and 500 ng/mL CRP samples respectively. The assays were performed as described in section 2.5. 20 μL of wash buffer was run through the control device followed by two consecutive wash steps of 15 μL of wash buffer. A 500 ng/mL CRP sample was prepared in 20 μl of d.H_2O and the wash steps were repeated for the sample device. The wash steps ensured that all of the sample solution was run through the device. Figure 5.5 (a) shows the visual results from revealing the capture layer of each device. The control device appeared white while the sample containing 500 ng/mL CRP was a red colour. This was a good result as it demonstrated a clear off/on evaluation for CRP detection. RGB analysis (figure 5.5 (b)) coincided with visual results where there was a distinct difference between green channel values. As with the LFIAs, the green channel was chosen as it was most sensitive to the colour produced by the AuNPs.[146]

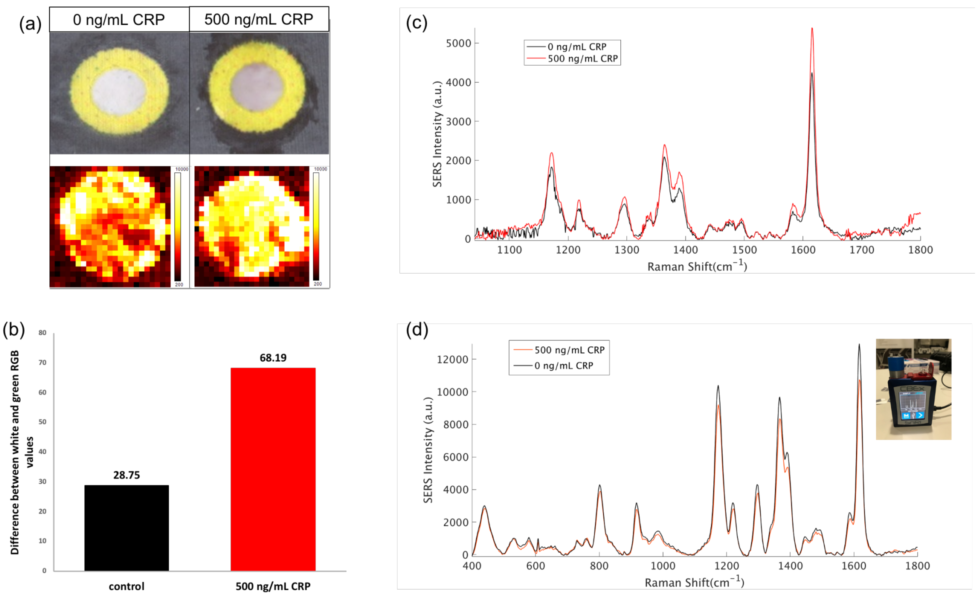

Figure 5.5: Results from the first 3D device assay test for CRP detection (a) scanned images of the control (0 ng/mL CRP) and sample (500 ng/mL) CRP devices after revealing the capture layer and corresponding SERS maps for each device. There was a clear red colour observed in the capture region of the sample device while the control device remained white. The SERS maps were constructed from the 1617 cm^{-1} peak of Raman reporter, MGITC. A strong SERS response was observed for both devices, (b) RGB analysis comparison between each device, a higher value was calculated for the sample device, in accordance with visual results, (c) average SERS spectra from each SERS map analysed using the benchtop microscope system, a slightly higher signal intensity was observed for the sample device and (d) handheld Raman analysis of each device. Intense SERS signals were observed for both, although the signal was more intense for the control device. Raman mapping analysis was performed at 633 nm laser excitation, 0.73 mW laser power, 6 s acquisition time and 100 μm step size. Handheld Raman analysis was carried out at 638 nm laser excitation, 27.8 mW laser power, 1 s acquisition time and each spectrum was an average of 6 scans.

The results from Raman mapping analysis of each of the devices is also shown in figure 5.5 (a). The SERS maps were constructed from the 1617 cm^{-1} peak of MGITC and a strong signal was observed for both devices. This was an anomalous result when compared to visual analysis. It was evident from observing the devices that no AuNPs were visually present on the capture region of the control device however a strong SERS response was generated. The corresponding average SERS spectra from each map is shown in (c) where the SERS signal generated was slightly higher for the sample device (500 ng/mL CRP). Handheld analysis was also performed on each device (figure 5.5 (d)), although both SERS signals were intense, a higher signal was recorded for the control device (0 ng/mL).

From this initial test using the 3D μPAD, it was concluded that the colourimetric response and RGB analyses were as expected, the capture region appeared white in the absence of CRP and appeared red in the presence of CRP. However, there was little difference between the SERS response from each device. This may have been due to the capture Ab concentration being too high. This may have resulted in AuNPs not involved in complexation with the immobilised Abs, becoming stuck in the capture region and contributing to the SERS response. As the aim of this investigation was to combine the 3D μPAD with SERS for improved quantitative and multiplexing capability, it was necessary to optimise the assay conditions to achieve this by diminishing the SERS response from the control device.

5.3.0.1. Capture Ab Concentration study

In order to drastically reduce the SERS response from the control device, a capture Ab concentration study was performed using the following Ab concentrations - 5, 25, 50 and 100 μg/mL. In the initial 3D μPAD assay test, 360 μg/mL capture Ab had been used, therefore lower concentrations were investigated to determine whether at higher Ab concentrations AuNPs not involved in immunoreactions were unable to pass through to the capture/readout layer, contributing to an intense SERS signal in the absence of CRP in the control device.

Figure 5.6 shows visual and RGB results for each Ab concentration. When 5 μg/mL Ab was immobilised on the capture layer, a darker red colour was observed

for the control device compared to the sample device as shown in the scanned images of each μPAD in figure 5.6 (a). The RGB analysis was consistent with this where a larger value of 62.17 was calculated for the control compared with 38.92 for the sample. Therefore, this Ab concentration was deemed too low to facilitate optimum complex interactions.

Figure 5.6 (b) shows results when 25 μg/mL Ab was used. Visually, there was an obvious colour difference between the devices with a darker red colour observed for the sample device. Additionally, a higher RGB value of 61.45 was calculated for the sample device compared with 31.52 for the control. 50 μg/mL and 100 μg/mL Ab studies showed similar results (figure 5.6 (c) and (d)) however, 100 μg/mL Ab exhibited an improved RGB analysis with a larger difference in values between the control (33.75) and sample (72.79) device. Therefore, handheld Raman analysis was performed on the 25 μg/mL Ab and the 100 μg/mL devices respectively to determine whether the intensity of the SERS signal from the control devices had diminished.

Figure 5.7 shows results from handheld Raman analysis of 25 and 100 μg/mL Ab devices. The same 3D-printed adaptor that was used to position the LFIAs in the laser beam (section 3.3.2.2) was used to analyse the 3D μPAD devices as shown in figure 3.12. This adaptor was specifically designed for use with the 3D μPAD therefore the dimensions of the collection aperture (4 mm) is the exact diameter of the capture region, ideally excluding the yellow ringed region.[60] This means the analysis area was of the entire capture region only and no excess area was being analysed. The spectrometer was also set to a rastor function enabling collection of SERS signal from the whole area.

The SERS signal for the 25 μg/mL Ab control device was observed to be more intense than for the sample device as shown in figure 5.7 (a). A broad band was

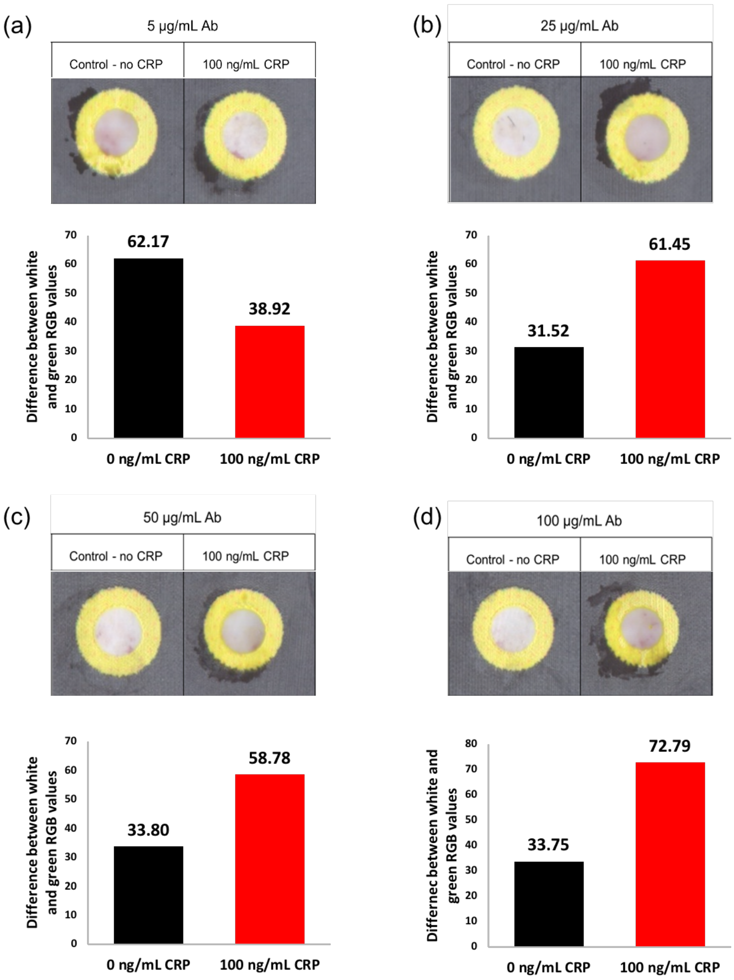

Figure 5.6: Results from capture Ab concentration study where the following Ab concentrations were investigated - 5, 25, 50 and 100 μg/mL, (a) 5 μg/mL Ab - scanned images of visual results after revealing the capture layer and corresponding RGB analysis from each device, the control device was visibly more red than the sample (100 ng/mL CRP) device and the RGB value for the sample device was also much lower, (b) 25 μg/mL Ab - visual improvement compared with 5 μg/mL Ab as the control device appeared lighter in colour, this was supported by RGB analysis, (c) 50 μg/mL Ab - a visual difference was again observed however, areas of mottled AuNPs were observed in the control device close to the yellow ring. RGB analysis comparison was not as good as 25 μg/mL and (d) 100 μg/mL Ab - a clear visual difference was observed with the sample device appearing a darker red in colour. While mottled areas were again observed in the control, 100 μg/mL gave the largest difference in RGB values for control versus sample device.

present at $\sim$600 cm^{-1} which was attributed to enhancement of the background signal from the nylon membrane.[154] Therefore, using 25 μg/mL Ab concentration had not aided in the lowering of the SERS response from the control device.

Figure 5.7 (b) shows handheld scans from the 100 μg/mL Ab devices. The SERS signal generated in the sample device was observed to be more intense than for the control device, particularly with regards to the 1617 cm^{-1} peak. The broad background band at ~600 cm^{-1} was, however, again present. In the SERS spectrum from the control device, an intense, broad band was also observed at ~1100 cm^{-1} which represented enhancement of the C-C backbone chain of the nylon 6,6 membrane.[155] This band was not as intense in the corresponding 25 μg/mL Ab control device which may have bee due to different background bands being enhanced depending on the immobilised Ab concentration.

Since a more intense signal was observed for the sample compared with the control device for 100 μg/mL Ab, next it was determined whether changing the AuNP-Ab concentration would result in a more intense SERS signal from the sample device while maintaining a diminished control device SERS response. The AuNP concentration used was 0.4 nM and had remained constant in all previous 3D μPAD experiments. A range of AuNP-Ab concentrations was therefore tested while using 100 μg/mL capture Ab concentration.

5.3.0.2. AuNP concentration study with 100 μg/mL capture Ab concentration

The following concentrations of AuNPs were used - 0.13 nM, 0.23 nM, 0.4 nM, 0.5 nM and 0.65 nM. 100 μg/mL capture Ab was used and all the buffer treatments for the device layers remained the same. Figure 5.8 shows results from the AuNP concentration study, showing visual and handheld SERS analysis from the control (0 ng/mL CRP) and sample (100 ng/mLCRP) devices at each concentration. At 0.13 nM AuNPs (figure 5.8 (a)), the scanned images appeared to be visually similar after revealing the capture layer. The SERS signal collected from the control device was more intense than that observed for the sample device. However, the intensity of the background peak at ~600 cm^{-1} was noticeably diminished in the sample spectrum.

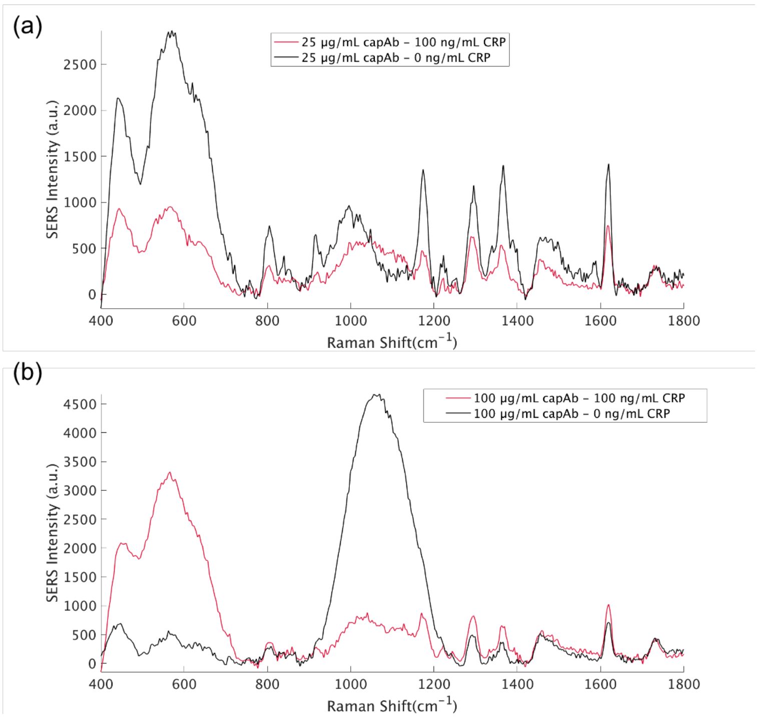

Figure 5.7: Handheld Raman analysis from (a) 25 and (b) 100 μg/mL capture Ab concentrations from control (0 ng/mL CRP) and sample (100 ng/mL CRP) devices. A more intense SERS signal was observed for the control device in (a) and a large background signal was observed for both the control and sample device with an intense band at approximately 600 cm^{-1} which can be attributed to enhancement of the nylon membrane.[154] For 100 μg/mL capture Ab, when looking at the intensity of the 1617 cm^{-1} peak, the SERS spectrum was more intense. Again, an intense band at 600 cm^{-1} was observed for the sample device. This was greatly diminished however in the control device where a broad band was present at approximately 1100 cm^{-1}, attributed to enhancement of the C-C backbone chain of the nylon 6,6 structures.[155] Handheld Raman analysis was performed using 638 nm laser excitation, 27.8 mW laser power, 1 s acquisition time and the spectra were averaged across 3 scans.

This was also observed for 0.23 nM AuNPs as shown in figure 5.8 (b). Both devices appeared visually similar and the SERS signals from both had similar intensities with the exception of the 1100 cm^{-1} peak in the control device spectrum. This band again diminished in intensity for 0.4 nM AuNPs (figure 5.8(c)), however the SERS signal for the control was still more intense than for the sample device. Visual results had improved for this AuNP concentration where the sample device was noticeably more red in colour than the control. It should be noted that 0.4 nM AuNP concentration had been used in the previous capture Ab concentration study and the spectra collected here were visibly different from those observed previously. This may be because a new batch of AuNP-Abs had been synthesised for the AuNP concentration experiment and batch-to-batch variability may be causing a problem with spectra reproducibility.

Sampling may also be contributing to changes in SERS signals. The 3D-printed adaptor being used for signal collection was designed for analysis of the entire capture region, areas of SERS hotspots may be present that will not be the same between replicates. This phenomenon may be contributing to changes in the average SERS signal. Further optimisation of the sampling method may therefore be needed to ensure assays run under the same conditions and with the same concentration of CRP, generate SERS signals of similar intensities.

Figure 5.8 (d) shows results from 0.5 nM AuNPs. The sample device was visibly more red than the control device and the SERS analysis of the sample device demonstrated a more intense SERS signal. However, the background band at ∼600 cm^{-1} was enhanced in both the control and sample spectra. Results from 0.65 nM AuNPs are shown in figure 5.8 (e). Both capture regions generated a red colour and looked visually similar. However, the SERS signal from the sample device was more intense than the control device and in both spectra the 600 cm^{-1} peak had disappeared. This suggested that the increased AuNP concentration had generated an enhanced SERS spectrum for both the control and sample devices thereby overcoming any enhancement of the nylon background. At this AuNP concentration, it was also evident that SERS provided an on/off result. However, the SERS signal from the control device remained high and it was next investigated whether the AuNPs, at all concentrations, were blocking or 'sticking' to the nylon membrane.

The following AuNP concentrations were used - 0.13 nM, 0.4 nM, 0.65 nM and 0.9 nM. As in all previous experiments, the AuNPs were functionalised with 75 nM MGITC. All devices were prepared as normal however, the capture layer was

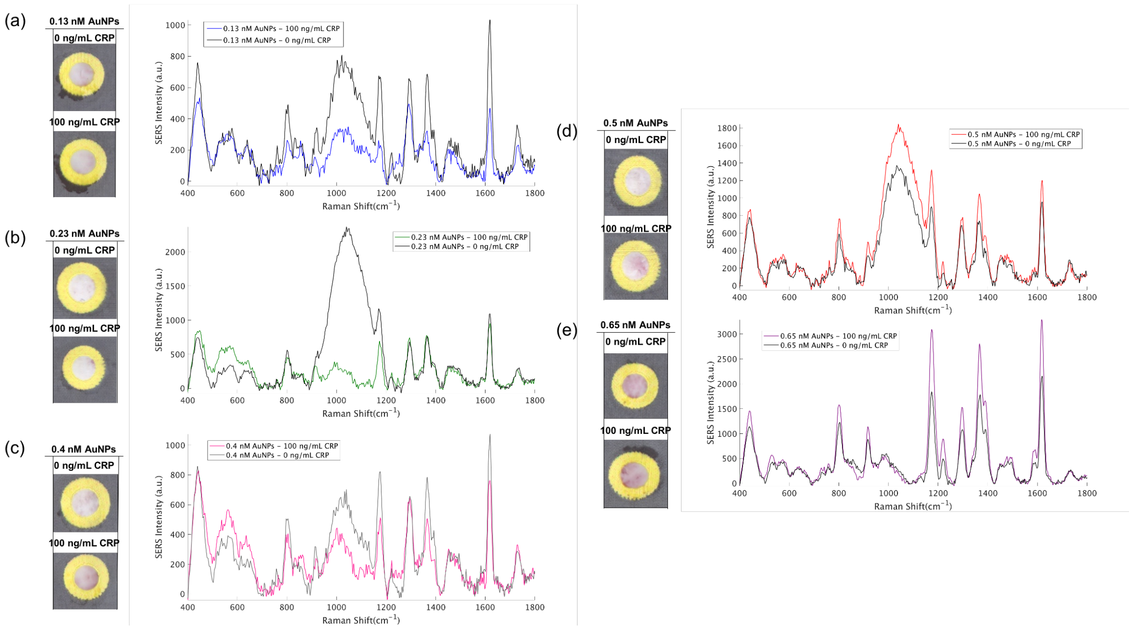

Figure 5.8: Results from AuNP concentration study (a) scanned images and corresponding handheld SERS analysis of control (0 ng/mL CRP) and sample (100 ng/mL CRP) devices when 0.13 nM AuNPs were dried onto the conjugate layer. Visually, the revealed capture regions appeared the same while the SERS spectrum generated for the control device was more intense than for the sample, (b) scanned images and corresponding SERS spectra when 0.23 nM AuNPs were used. The devices looked the same and the SERS spectra were of similar intensities however there was a broad band at $\sim$600 cm^{-1} from the nylon background signal that was not present in the sample spectrum, (c) results from 0.4 nM AuNPs. Visually, the result had improved with a darker red region observed for the sample device however the SERS spectrum for the control remained more intense. It should be noted that in the control spectrum the $\sim$600 cm^{-1} band greatly diminished in intensity compared with 0.23 nM AuNPs, (d) 0.5 nM AuNPs generated a more intense SERS spectrum for the sample device, however the $\sim$600 cm^{-1} band was enhanced in both spectra and (e) using 0.65 nM AuNPs this band disappeared from both spectra owing to the MGITC spectrum dominating and the SERS signal from the sample device was clearly enhanced compared with the control device. However, visually both capture regions were similar and displayed an obvious red colour. Handheld Raman analysis was performed at 638 nm laser excitation, 27.8 mW laser power, 1 s acquisition time and each device was scanned 3 times.

treated with 10% BSA in 1xPBS buffer only, capture Abs were not immobilised on the capture region. Wash buffer (0.05% Tween 20 in 1xPBS) was run through each device three times, 20 μL followed by two 15 μL increments. The capture layer of each device was revealed and RGB analysis was performed.

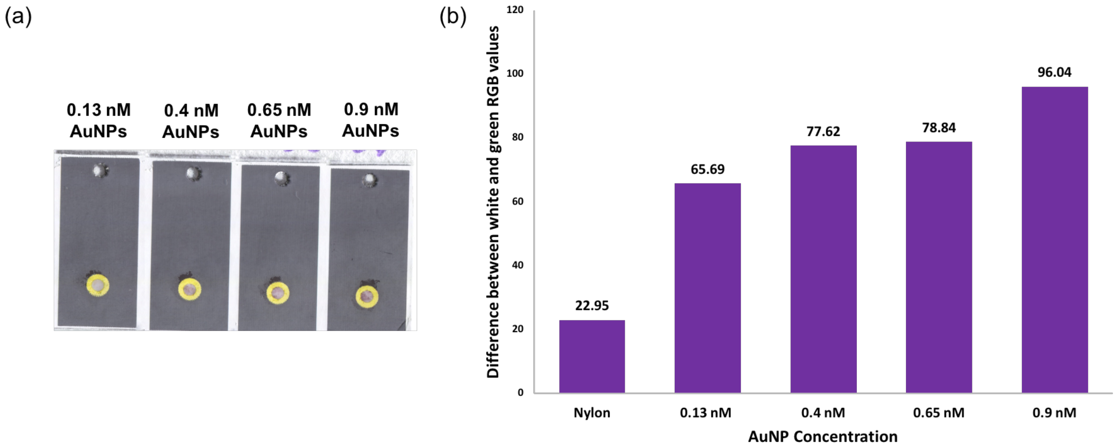

Figure 5.9: Results from AuNP-Ab concentration to determine whether AuNPs were sticking to the nylon membrane in the absence of CRP. The nylon membrane had been treated with 10% BSA in 1xPBS buffer but no capture Ab was immobilised on the capture region (a) scanned images from each 3D device where the following AuNP concentrations had been used - 0.13 nM, 0.4 nM, 0.65 nM and 0.9 nM. There was evident colouration in the capture region of all device, which appeared to darken with increasing AuNP concentration. This was consistent with RG analysis in (b) where the highest value was calculated for 0.9 nM AuNPs. The values from each device are compared with an untreated nylon membrane to show the AuNPs are clearly interacting with the nylon membrane in the absence of CRP.

Figure 5.9 (a) shows scanned images of each device after revealing the capture layer. Visually, it was clear that the capture region of all the devices was coloured, the intensity of which increased with increasing AuNP-Ab concentration. RGB analysis of each device was compared with the value calculated for an untreated nylon membrane (figure 5.9 (b)) and the highest value was calculated for the the highest AuNP concentration of 0.9 nM. In the absence of CRP and capture Ab, it was evident that the AuNP-Abs were interacting with and sticking to the nylon membrane. This suggested that in the control devices, AuNP-Abs sticking to the nylon were contributing to an enhanced SERS response.

These results indicated that the buffer treatment of the layers needed optimisation. The conjugate layer treatment consisted of 3 μL of 10% BSA in 1xPBS to prevent non-specific interactions occurring, this was quite a high percentage of BSA which may have been preventing the AuNP-Ab complexes from passing through the layer. Additionally, upon rehydration, excess BSA may be interacting with the AuNP-Ab complexes resulting in the formation of a protein corona. When these complexes tried to flow through the nylon membrane, as they were not bound to any CRP, they may have become too large due to the formation of the 'soft' protein corona.

Reducing the concentration of BSA in the buffer treatment could potentially reduce these effects while still promoting specific interactions between AuNP-Ab-CRP complexes and the immobilised Ab. The buffer treatment could also benefit from the addition of a protecting reagent to encourage AuNP-Ab dispersion. Therefore, an alternative buffer treatment for the conjugate layer was investigated.

5.3.1 Alternative buffer treatment

It had already been demonstrated that AuNP-Abs were interacting with the nylon layer at a concentration of 0.9 nM therefore, a high AuNP-Abs concentration of 1 nM was chosen to test the effect of changing the buffer treatment on the conjugate layer. The conjugate layer was originally treated firstly with 10% BSA in 1xPBS buffer and the AuNP-Abs were then dried on. For this optimisation step, the same buffer used for the LFIA strips was used to treat the conjugate layer - 0.5% BSA and 0.05% Tween 20 in 1.72 mg/mL phosphate buffer. The BSA content of this buffer was 20 times lower than used previously and the addition of Tween 20, a non-ionic surfactant, was used to encourage AuNP dispersion following rehydration.[89] All the other layers were treated as normal and as with the first 3D μPAD test (section 5.3), 360 μg/mL of capture Ab was immobilised onto the capture layer.

Figure 5.10 shows results from using the LFIA buffer as treatment for the conjugate layer. Control (0 ng/mL CRP) and sample (100 ng/mL CRP) devices were again run, after revealing the capture layer, the sample device appeared more red in colour than the control device and it was evident that AuNPs were

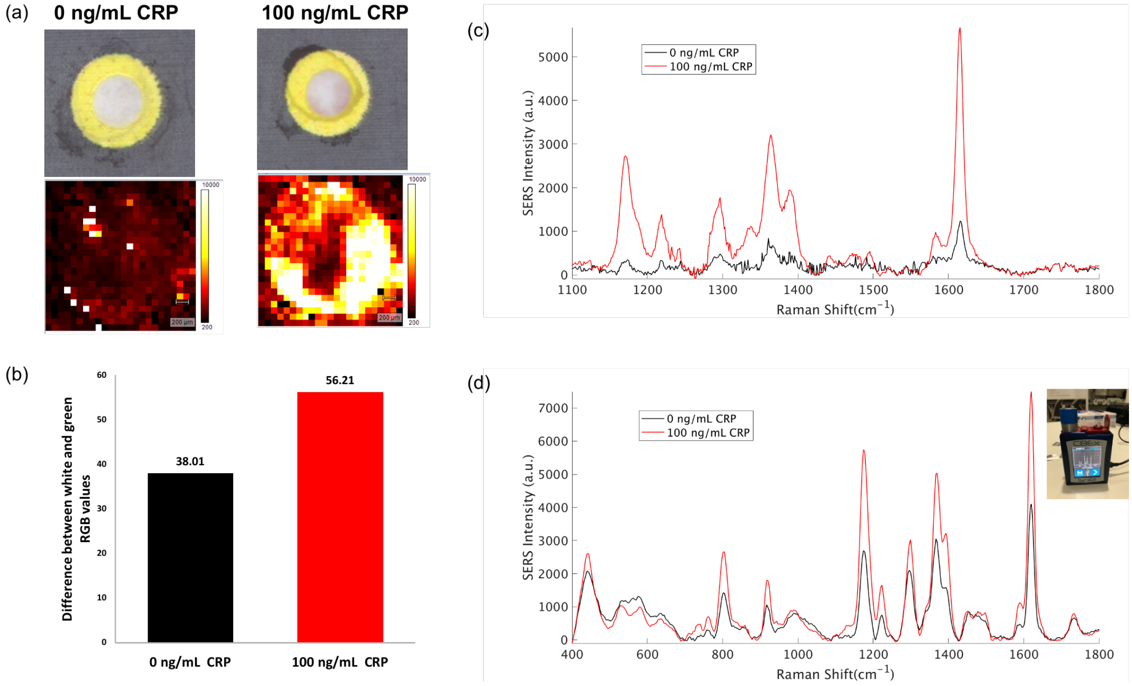

Figure 5.10: Results from changing the buffer treatment of the conjugate region with 0.9 nM AuNPs and 360 μg/mL capture Ab - (a) scanned images and corresponding SERS intensity maps from the control (0 ng/mL CRP) and sample (100 ng/mL CRP) devices, there was an obvious difference in color between the two capture regions and the maps demonstrated a qualitative result with a strong SERS signal generated from the sample device compared with negligible response from the control device, (b) RGB analysis of both devices where a higher value was calculated for the sample device, (c) average SERS spectra from the intensity maps shown in (a), the sample device generated a sharp, intense MGITC spectrum while there was a residual response from the control device in comparison and (d) handheld SERS analysis was consistent with SERS mapping results however, the control spectrum was observed to be higher in intensity. Raman mapping analysis was performed at 633 nm laser excitation, 6 s acquisition time, 0.73 mW laser power with a 100 μm step size. Handheld Raman data was collected using 638 nm laser excitation, 0.25 s acquisition time, 27.8 mW laser power and spectra were constructed from the average of 6 scans per device.

not becoming stuck on the nylon layer in the absence of CRP, even at such a high AuNP-Ab concentration. The scanned images of each device and corresponding SERS intensity maps are shown in figure 5.10 (a). The SERS map for the control device demonstrated negligible signal had been generated, while a bright SERS map was obtained for the sample device. RGB analysis (figure 5.10(b)) showed a higher value was calculated for the sample device, this was consistent with visual and SERS map results. Average SERS spectra from the maps are shown in figure 5.10 (c).

It was evident from these results that the LFIA buffer, with a reduced percentage of BSA, had facilitated the flow of AuNP-Abs unbound to CRP through the capture layer and they were no longer being blocked from passing through the membrane. The LFIA buffer had also contained Tween 20, a non-ionic surfactant that has been used to promote particle stability.[156] In this instance, its presence on the conjugate layer during AuNP-Ab rehydration may have contributed to greater particle dispersion and therefore also aided in uncomplexed AuNP-Ab conjugates passing unhindered through the nylon membrane.[89]

Handheld Raman analysis is shown in (d) and was in accordance with SERS mapping however, a more intense signal was collected from the control device compared with SERS mapping analysis. This may be due to the way in which the handheld instrument scan is collected. The same 3D adaptor was used in this investigation as shown in figure 3.12. This adaptor was specifically designed for use with the 3D μPAD therefore the dimensions of the collection aperture (4 mm) is the exact diameter of the capture region, ideally excluding the yellow ringed region.[60] Therefore, a smaller area was analysed using the adaptor compared with the SERS mapping data. It may be the case that areas of SERS hotspots were contributing more to the overall signal for handheld scans resulting in a more intense average spectrum. The laser power was also higher for the handheld spectrometer as recorded by a portable power metre.

Despite the intense spectrum collected for the control device using the handheld spectrometer, changing the buffer treatment of the conjugate layer had been successful in achieving a clear, qualitative result with respect to SERS analysis. Additionally, at a high AuNP-Ab concentration of 1 nM, AuNP-Abs did not appear to be interacting with the nylon membrane in the absence of CRP. This was an encouraging result and further optimisation steps were performed with the aim of attaining quantitative detection of CRP using the 3D μPAD.

Control (0 ng/mL CRP) and sample (100 ng/mL CRP) devices were run for three AuNP-Ab concentrations - 1.5 nM, 1 nM and 0.5 nM to determine the optimum AuNP-Ab concentration for CRP detection. Figure 5.11 shows visual results and SERS map and RGB data for each device at all AuNP concentrations. At 1.5 nM AuNP-Ab (figure 5.11 (a)), the devices were visually similar while the RGB values showed a slightly higher value for the sample device. SERS intensity maps demonstrated more promising results with a visibly greater SERS response generated for the sample device compared with the control. However, it was evident that at this high AuNP concentration, the SERS signal collected for the control device was noticeably enhanced compared with 0.9 nM AuNP-Ab concentration used previously.

Using 1 nM AuNP-Abs, the SERS map generated from the control device showed a decrease in SERS signal compared with 1.5 nM while the sample device generated a brighter intensity map compared with 1.5 nM. Visually, however, and with regard to RGB analysis, the results were similar to (a). Finally, at 0.5 nM AuNP-Abs (figure 5.11 (c)), visual and RGB results remained similar to (a) and (b). The SERS map generated for the sample device at this concentration demonstrated a diminished SERS response where AuNPs appeared predominantly to collect at the edges of the capture region.

Figure 5.12 (a) - (c) show the corresponding average spectra from each SERS map and from handheld Raman analysis of each device. In both analyses, the best signal discrimination between the control and sample devices was observed when using 1 nM AuNP-Abs as shown in figure 5.11 (b). Therefore, 1 nM was chosen as the optimum AuNP concentration for CRP detection using the 3D devices. Additionally, these results showed that SERS analysis offered improved discrimination between control and sample device compared with RGB values. Quantitative detection of CRP using SERS was investigated and again compared to RGB analysis.

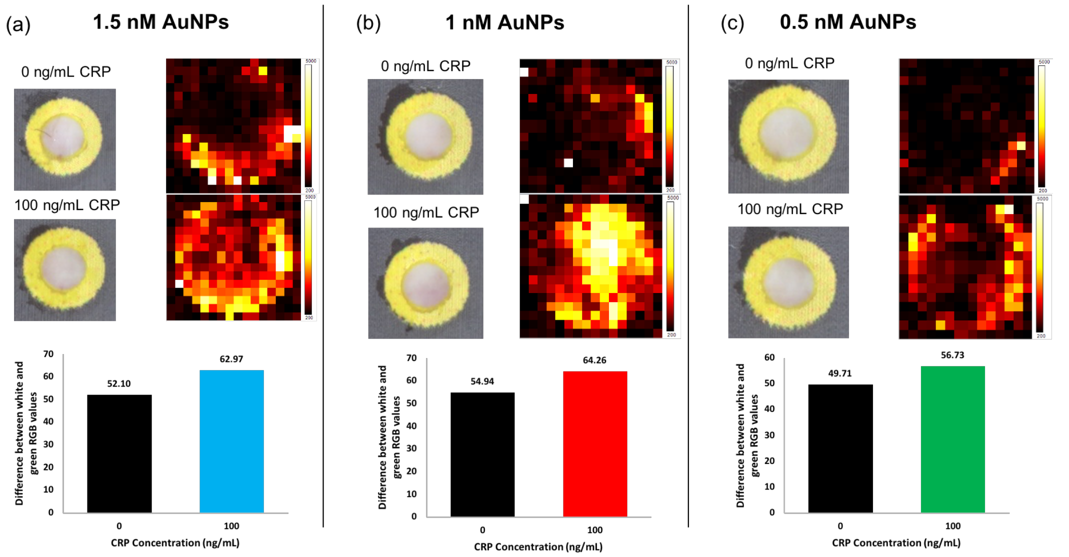

Figure 5.11: Results from AuNP-Ab concentration study with LFIA buffer used for treatment of conjugate layer - (a) 1.5 nM AuNP concentration visual, Raman mapping and RGB analysis results. There was no obvious difference visually between the capture regions however, RGB values demonstrated higher values for the sample (100 ng/mL CRP) device. SERS intensity maps also indicated a greater SERS response from the sample device, (b) results from 1 nM AuNPs, visually the sample device appeared slightly more red in colour compared with the control (0 ng/mL CRP) device which was consistent with RGB analysis. SERS mapping however showed a much greater response from the sample device and (c) 0.5 nM AuNPs, visual and RGB analyses were similar to (a) and while there was a difference between the SERS maps, the lower AuNP concentration used resulted in a diminished SERS response in the sample device. Raman mapping analysis was performed at 633 nm laser excitation, 6s acquisition time, 0.73 mW laser power with a step size of 100 μm.

5.3.2 CRP concentration study using the 3D device assay platform

Since the optimisation steps had been successful in the qualitative detection of CRP using SERS, quantitative detection was therefore attempted. For this, all reagents were freshly prepared which included the preparation of all buffer treatments and the synthesis of a new batch of Ab-functionalised AuNPs. The following concentrations of CRP were used in the experiment - 1000, 500, 100, 50, 10 and 0 ng/mL. These concentrations were chosen based upon the work previously carried out with LFIAs (section 3.3.2) and also to reduce the number of dilution steps needed for clinically relevant concentrations (>10 μg/mL of CRP

(a) 1.5 nM AuNPs

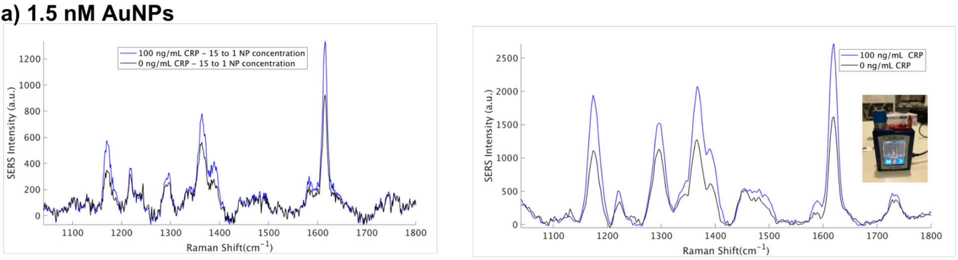

(b) 1 nM AuNPs

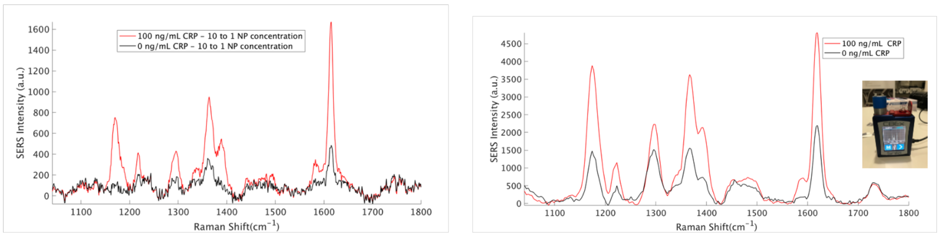

(c) 0.5 nM AuNPs

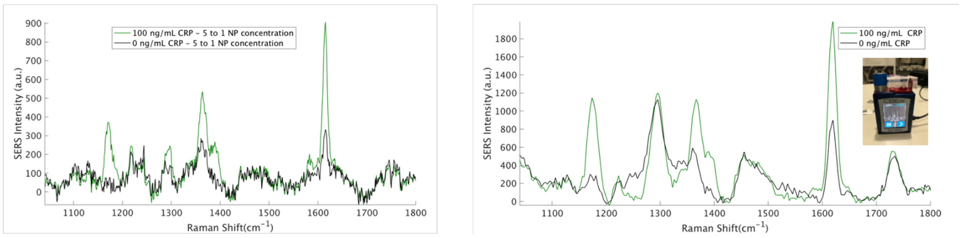

Figure 5.12: Corresponding average spectra from each SERS intensity map shown in figure 5.11 and handheld Raman analysis of each device - (a) 1.5 nM AuNP-Abs, a high SERS signal was observed for the control device relative to the sample device in both the SERS mapping and handheld analyses, (b) 1 nM AuNP-Abs, the best signal discrimination was observed at this concentration with a lower SERS signal collected for the control but a higher signal collected for the sample compared with 1.5 nM AuNPs and (c) 0.5 nM AuNP-Abs, while signal discrimination was observed, the SERS intensity generated for both mapping and handheld analysis across all devices was low. Raman mapping analysis was performed at 633 nm laser excitation, 6s acquisition time, 0.73 mW laser power with a step size of 100 μm. Handheld Raman analysis was carried out at 638 nm laser wavelength, 0.2 s acquisition time and spectra were averaged from 3 scans.

---

is indicative of a disease state.[13])

Figure 5.13 shows results from the concentration study. Visually, it was evident that the capture region intensified in colour with increasing CRP concentration (figure 5.13 (a)). The visual results had improved compared with previous experiments which could be as a result of using all new reagents for this inves-

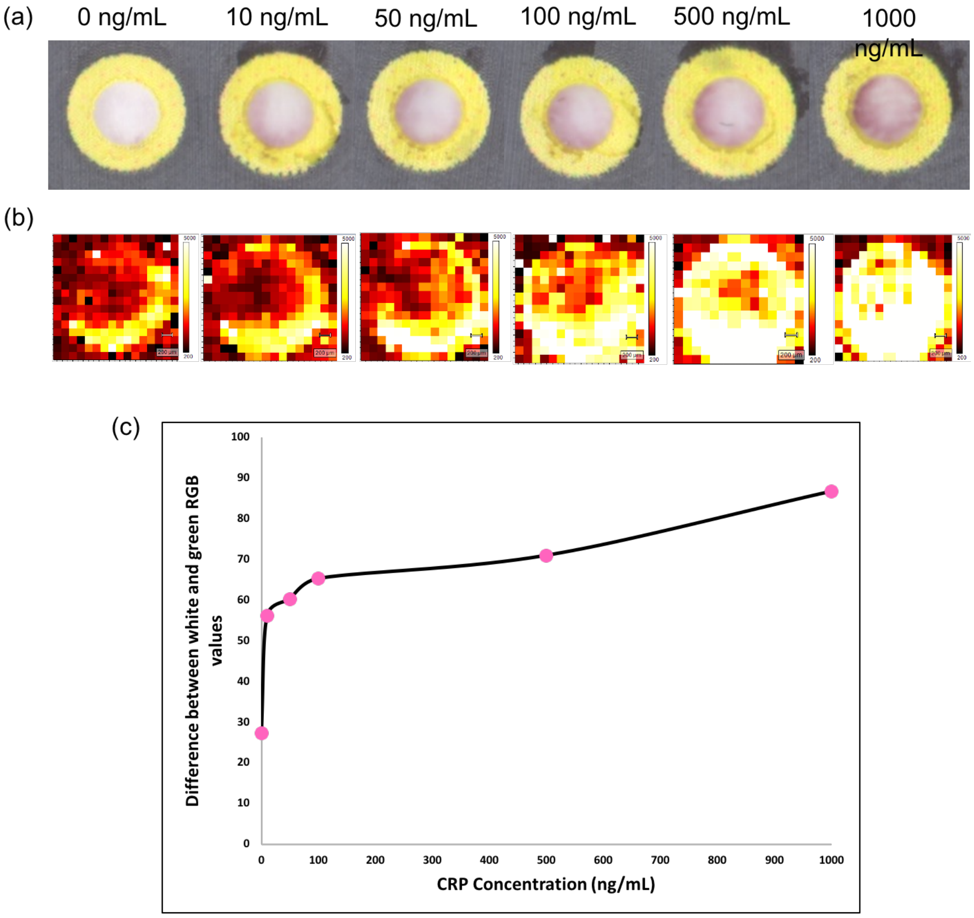

Figure 5.13: Results from CRP concentration study for the following CRP concentrations - 1000, 500, 100, 50, 10 and 0 ng/mL, (a) visual results from revealing capture layer of each device, the red colour of accumulated AuNP-Abs became more prominent with increasing CRP concentration, (b) corresponding SERS intensity maps for each device where a clear increase in SERS response was observed with increasing CRP concentration and (c) RGB analysis also showed a general increasing trend with increasing CRP concentration however, this was evidently not linear. Raman mapping analysis was performed using 633 nm laser excitation, 6s acquisition time, 0.73 mW laser power with a step size of 100 μm.

---

tigation. It may be the case that this analysis relies heavily on the freshness of the reagents. This was a good result as visual analysis could prove beneficial in the field to quickly determine a positive or negative result. This information can then be used to assess whether quantitative analysis is required.

The corresponding Raman maps are shown in figure 5.13 (b). The SERS response was observed to increase with increasing CRP concentration. It should be noted that the signal generated from the 0 ng/mL CRP device appeared noticeably higher than what had been previously observed under similar conditions which may suggests reproducibility issues with the assay. RGB analysis was also performed on each device and was in accordance with the visual and SERS mapping data, showing a general increasing trend with increasing CRP concentration. However, the trend was clearly not linear and it appeared RGB value saturation had been reached at approximately 100 ng/mL CRP. Therefore, it was deduced that RGB analysis was not appropriate for quantitative analysis.

Figure 5.14 (a) shows the average SERS spectra generated for each SERS intensity map in figure 5.13 (b). The intensity of each spectrum was observed to increase with increasing CRP concentration. A calibration curve showing the linear relationship between SERS intensity at the 1617 cm^{-1} peak and CRP concentration is shown in figure 5.14 (b). Handheld Raman analysis was also performed on each of the devices, the results from which are shown in figure 5.14 (c) and (d). Handheld scans were in accordance with Raman mapping data however, there was an outlier at 500 ng/mL CRP (red data point in figure 5.14 (d)) where a diminished SERS intensity was collected from the capture region of this device, averaged across 6 scans. This may have been due to the sampling method used for handheld analysis. The SERS mapping data plainly showed there was an increased SERS signal generated at 500 ng/mL compared with lower CRP concentrations. The maps also indicated that, at lower CRP concentrations, AuNP-Abs were initially binding at the edge of the capture region, closer to the outer yellow ring. As the CRP concentration increased, the SERS signal became more uniform across the capture region as the AuNPs were forced to occupy more centralised Ab binding sites.

This anomaly may be due to the drying of the Ab onto the capture layer. The capture Ab was pipetted onto the capture region and while the hydrophobic barrier of the wax-printed template ensures the Ab solution remains in this area, the drying of the Ab may not be homogenous across the entire region. Additionally,

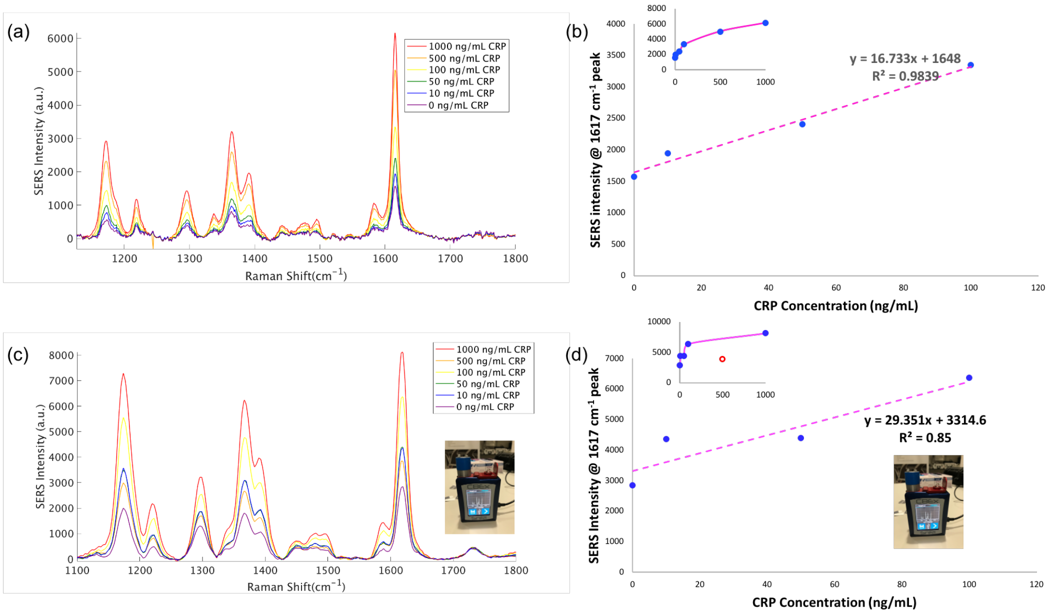

Figure 5.14: (a) Average spectra constructed from SERS intensity maps shown in figure 5.13 (a). The SERS intensity was observed to decrease with decreasing CRP concentration. The corresponding curve shown in the inset of (b) shows CRP concentration with respect to the intensity of the 1617 cm^{-1} peak, taking the linear region of the curve the calibration curve shows reasonable linearity with a R^2 value of 0.907 and (c) handheld Raman results which are in agreement with the average SERS map spectra however, as show by the red data point in (d), there was an outlier at 500 ng/mL CRP for this analysis resulting in a R^2 of 0.85 and diminished linearity. Raman mapping analysis was performed using 633 nm laser excitation, 6s acquisition time, 0.73 mW laser power with a step size of 100 μm. Handheld Raman analysis was carried out with 638 nm laser wavelength, 0.2 s acquisition time and spectra were averaged from 6 scans.

as the liquid sample flows laterally along the incubation layer and then vertically to the capture layer, it encounters the edge of the double-sided adhesive and may initially follow along the edge of the circular area that has been cut out, before the rest of the liquid spreads across the entire circle at the end of the incubation layer. This may mean that the AuNP-Abs in the sample liquid interact with Ab immobilised at the edge of the capture region first which would explain the binding pattern seen in both the visual and SERS mapping results.

For handheld Raman analysis, this phenomenon may cause also problems when scanning the larger capture region ultimately resulting in a loss of SERS signal. The sampling procedure is inconsistent, particularly with regards to alignment of the aperture of the 3D printed adaptor, and by extension the laser, with the capture region. Further work using this platform with handheld SERS would need to be carried out to optimise the interface between the analysis spot on the capture layer and the handheld spectrometer.

Despite issues with handheld analysis, it was found that using the 3D μPAD, a SERS-based assay had been successful in the quantitative detection of CRP. SERS analyses, both the benchtop instrument and handheld spectrometer, were superior to RGB values as a quantitative method as the relationship between SERS intensity of the 1617 cm^{-1} peak and CRP concentration demonstrated improved linearity compared with RGB analysis. This final result demonstrated that visual analysis can be combined with SERS results to obtain qualitative and potentially quantitative detection in the field. In addition to this, SERS offers the ability of multiplexed detection from a single sample and single test region which cannot be attained using RGB values.

It should be noted that the CRP concentration range chosen for this study was too large and the signal appeared to saturate before the upper concentration limit of 100 ng/mL was reached. Additionally, the calibration curve constructed for the handheled Raman analysis was linear across the 0 - 100 ng/mL CRP range. Therefore future work with the 3D μPAD platform would focus on detection at a lower concentration range, potentially achieving lower limits of detection.

By taking steps towards the optimisation of the 3D μPAD for use with a SERS-based assay, the potential for rapid, multiplexed biomarker detection at the point-of-care can be achieved. The flexibility of the template design coupled with SERS makes this device ideal for multiplexed detection of a large number of biomarkers simultaneously. However, the use of a portable Raman spectrometer is vital to the viability of this assay device, therefore further work is needed to ensure the consistency of the sampling method using the handheld instrument. For this a suitable adaptor would be vital for holding the device tightly in place and eliminating human error in the analysis procedure and ensuring a standardised method of reading the device.

5.4 Conclusion

μPADs have demonstrated their viability as immunoassay platforms ideal for multiplexed detection, predominantly using colourimetric readouts as an analysis technique. In this study, we optimised the use of a 3D μPAD developed by Fernandes *et al.*[150] with a SERS-based immunoassay which offers improvements in quantitative detection and increases the scope for multiplexing. CRP was chosen as the proof-of-concept biomarker to be detected as our previous work on the LFIA platform with this protein had been successful (section 3.3.2).

AuNP-Ab concentration, immobilised Ab concentration and buffer treatment were investigated as part of the optimisation process. It was determined that the recipe for the conjugate layer buffer treatment, in which the AuNP-Abs were housed, was particularly important for the success of the assay. The original layer treatment was with 3 μL of 10% BSA in 1xPBS. It was determined that this percentage of BSA was too high and was hindering the subsequent flow of AuNP-Abs through the nylon membrane of the capture layer. This was leading to AuNP-Abs becoming immobilised on the nylon membrane and giving a false positive result in the absence of CRP. The buffer treatment was replaced with treatment using the LFIA buffer (0.5% BSA and 0.05% Tween 20 in 1.72 mg/mL phosphate buffer) where the percentage of BSA was 20 times lower. The buffer also contained Tween 20, a non-ionic surfactant, which contributed to improved AuNP-Ab dispersion following rehydration. The alternative buffer treatment with reduced BSA content meant excess BSA could not form a soft protein corona around the AuNP-Abs but still ensured non-specific binding was prevented while Tween-20 promoted stability and dispersion to prevent clumping or aggregation of AuNP-Abs. These effects ensured the AuNPs-Abs could flow unhindered through the capture layer and only AuNPs-Abs bound to CRP would be captured by Abs immobilised on the membrane and generate a SERS response.

Additionally, a AuNP-Ab concentration of 1 nM and a capture Ab concentration of 360 μg/mL were found to be the optimum amounts for successful running of the 3D μPAD when the alternative buffer treatment was used. These optimisation steps lead to clear discrimination between on/off SERS responses. The freshness of reagents also proved to be important particularly with regards to visual analysis where it was easier to differentiate between a control and sample device as demonstrated by the final set of results. This may have been due to the presence of BSA in the conjugate layer treatment and other proteins in the milk block treatment. As the buffers age, these proteins were observed to be prone to gradual precipitation out of the buffer. This may be starting to happen before it can be observed visually, leading to the aggregated proteins occluding the layers after treatment. Therefore the buffers must be kept in the fridge to maintain their freshness and should not be used past 1-2 weeks following preparation.

Finally, semi-quantitative information was obtained for CRP using the 3D μPAD where a handheld Raman spectrometer was used for SERS analysis. Results also demonstrated that RGB values were not appropriate for quantification and SERS analysis was necessary to obtain quantitative information. It should be noted that previous work using this 3D μPAD with AuNPs for the detection of malaria and dengue fever, has shown that colourimetric analysis is capable of quantification.[146] In the case of the assay investigated here, the colourimetric response was observed to reach saturation at concentrations >100 ng/mL of CRP. The visual response however could be used as an indicator in the event of a positive test as to whether quantitative information is required. This way the 3D μPAD could be valuable in resource-limited settings where both techniques can complement one another.

The 3D μPAD platform offers improvements compared with LFIAs with regards to the flexible design of the wax printed template therefore, there are more options for multiplexing, no plastic housing cassette is required, immobilised AuNPs and biomolecules are protected within the device and whole blood samples can be run by adding a plasma separation layer to the top of the device.

While further work is needed with the 3D μPADs to obtain multiplexed detection using SERS, they remain a potentially viable platform for the development a rapid diagnostic technique for sepsis at the point-of-care.

While there are certain benefits associated with the 3D μPAD platform for point-of-care biomarker detection, the results from the LFIA tests showed that this platform was in fact more successful for the detection of CRP and IL-6. Furthermore, CRP detection was achieved in human plasma and multiplexed detection of both biomarkers simultaneously was also demonstrated using the LFIA devices. Plasma separation is possible for whole blood samples using LFIAs and in the case of this investigation, only one wash step was needed. The 3D μPADs required two wash steps and the removal of the top three layers to reveal the capture layer for analysis was not always straight-forward.

For sepsis detection, LFIAs proved to be more successful for the detection of biomarkers associated with sepsis and duplex detection was achieved using signal-resolved detection of two Raman reporters representing each of the biomarkers. This, coupled with the use of a handheld Raman spectrometer, demonstrated the excellent multiplexing capability of the platform as well as the viability of the SERS-based LFIA platform for use in the diagnosis of sepsis at the point-of-care.

6. Concluding Remarks

We have demonstrated the viability of a SERS-based rapid diagnostics for the detection of biomarkers associated with sepsis. We have also showed that the performance of the Snowy Range CBEx handheld Raman spectrometer was comparable to the Renishaw InVia benchtop Raman microscope instrument, validating the use of portable, handheld SERS as a point-of-care analysis technique. Our SERS-based lateral flow immunoassay platform was successful in the quantitative detection of CRP, achieving a LOD for handheld SERS of 8 ng/mL in buffer. When spiked human plasma samples were analysed, a LOD for handheld SERS of 5.4 μg/mL was calculated, well within levels considered to be clinically relevant (<10 μg/mL). We also investigated multiplexed detection of CRP and IL-6 simultaneously and achieved quantitative, duplex detection of both biomarkers from a single test region. This signal-resolved duplex detection achieved LODs of 7.2 ng/mL and 14.1 ng/mL for CRP and IL-6 respectively. A different rapid diagnostic platform was also investigated in the form of 3D μPADs. These devices were optimised for use with SERS-active AuNPs used for the detection of CRP on LFIAs. Semi-quantitative detection of CRP using SERS was achieved however, the LFIA platform was superior to 3D μPADs for the application of SERS-based rapid diagnostics for biomarker detection. The 3D μPADs show great promise for multiplex detection due to their flexible design that can be easily altered to suit the application. But our results showed much work is needed to optimise them for the application described here and indeed, on how the design flexibility could be exploited to develop a multiplexed platform. For example, for the duplex detection of CRP and IL-6, a signal-resolved detection method could be used but the design of the 3D μPAD template could also be altered to allow for spatially resolved detection. Which method would be ideal for the detection of more than two biomarkers? Would a single sample volume be enough if, for example, the device split into many channels leading to multiple test zones? Or should a combination of both be used? As our investigation showed however, further work is needed to integrate a SERS-based assay into these 3D devices.

Colourimetric analysis in the form of RGB values was used throughout this study as a comparison to SERS. While the RGB response in most cases was found to be quantitative, it was not as sensitive as SERS and when human samples were analysed, no quantitative information could be deduced for CRP. Additionally, for signal-resolved duplex detection of CRP and IL-6, RGB analysis provided no definitive quantitative information regarding the biomarkers individually. A visual and colourimetric response is important when a yes/no answer is needed *i.e.* qualitative information as to whether the biomarker of interest is present in the sample or not. For certain applications *e.g.* pregnancy tests, this type of visual response is all that is required and indeed in some disease diagnostics, with the current SARS-CoV-2 pandemic being a prime example of the need for a rapid, qualitative response only. In the case of sepsis, quantification would be a vital prognostic/clinical outcome indicator and could be used to determine whether treatment was working or not. SERS, with its high multiplexing potential, offers this and has the advantage of providing greater sensitivity compared with colourimetric techniques.

The quantitative ability of SERS also needs to be taken into account and how consistent quantification might be achieved. The reproducibility of SERS in this regard has long been challenged, with NP aggregation and molecular orientation of the Raman reporter being important aspects to consider for quantitative SERS. It has been suggested that, as in the calibration of many analytical techniques, the use of standards for SERS quantification should be employed. These may include the use of an internal standard, isotopologues *e.g.* a deuterated reporter molecule compared with the hydrogenated equivalent and the standard addition method (SAM) as outlined by Goodacre *et al.*[157]

These concerns must also be applied to the instrumentation and how the result of a LFIA will be interpreted and delivered to the user. We have demonstrated the capabilities of the handheld Raman spectrometer as being comparable to a benchtop instrument with the obvious advantage of being compact and portable. However, an interdisciplinary approach would be needed to make handheld SERS truly viable at the point-of-care. This would most likely involve the use of machine-learning methods and specially designed software wherein the instrument itself would have a standard calibration built in and would use this to interpret data collected of unknown biomarker concentrations. This way, the user would be given a response from the instrument that relays the results in a clear way. With regards to a multiplex SERS spectrum, the instrument itself would essentially be capable of processing the data in real-time using specifically designed algorithms that can pick out peaks of interest, while also evaluating their intensity for quantification and what biomarker they represent. At present, handheld Raman spectrometers are predominantly used to identify a whole spectrum, one that it has stored on a spectral library *e.g.* of illicit substances. With the rate at which technology is advancing in the 21st century and with the current pandemic highlighting the urgent need for rapid diagnostics, there is a hope that SERS-based platforms will emerge for sensitive, specific and multiplexed quantitative detection of disease biomarkers. Either from an academic or commercial source but more than likely, a synergistic contribution from both.

With respect to the multiplexed LFIA developed in this work, there are some limitations that need to be considered. The LFIA for IL-6 detection was not sensitive enough to detect clinically relevant concentrations of the biomarker which are in the pg/mL range. Although, in the event of sepsis these have been recorded to be as high as 1 ng/mL, our SERS-based assay was only capable of LODs of 10.5 ng/mL in the singleplex and 14.1 ng/mL in the signal-resolved duplex assay, both using handheld SERS. While these results were used to successfully demonstrate quantitative detection of IL-6 and multiplexed detection of IL-6 and CRP, the lack of sensitivity would need to be amended when moving towards detection in human samples. A simple change would be to increase the concentration of RBITC added to AuNPs, therefore increasing the number of reporter molecules functionalised to the AuNP surface. However, AuNP stability would need to be maintained for Ab attachment to be successful. The use of a resonant reporter like MGITC for IL-6 detection could also improve sensitivity. In effect, the two Raman reporters used could be swapped to code for the other biomarker, with MGITC used for IL-6 detection and RBITC used for CRP. Increasing the reporter concentration could also be investigated in this instance. Core-shell NPs were described in section **??** and have demonstrated their ability to enable increased sensitivity over AuNPs alone. This strategy could also be examined for IL-6 detection.

Another factor to consider for the duplex assay is the clinically relevant concentration range for each biomarker. CRP will be present at concentrations in the μg/mL range during a disease state while IL-6 concentration is much lower at pg/mL levels. Therefore, while a sample dilution step may be necessary for CRP detection, this would certainly not be advisable when detecting IL-6. More thought would need to go into development of the assay to account for this and when introducing the detection of more biomarkers to the assay platform. It may be the case that different biomarkers should be separated depending on their clinically relevant concentration ranges, offering multiplexed detection across two LFIA strips for several different biomarkers.

Regarding the LFIA platform itself, stability of the devices is essential for ensuring their viability out in the field. Therefore, stability tests would need to be run on the final device developed for this application. An operating temperature range would need to be established for the devices and a storage method which allowed the devices to remain dry and uncontaminated prior to use. The performance of the assay would also need to be evaluated, after certain time-points and following storage under certain conditions, to establish whether loss of sensitivity would be an issue. This would indeed be the case for any paper-based rapid diagnostic.

Sepsis is a complicated condition and with it comes the challenges of developing a rapid diagnostic that can deliver as much information about the disease as possible, at an early stage and at the point-of-care. Although much work from an interdisciplinary framework is needed for development, SERS-based multiplex LFIAs indeed hold promise for achieving this in the near future.

References

1 M. Singer, C. S. Deutschman, C. W. Seymour, M. Shankar-Hari, D. Annane, M. Bauer, R. Bellomo, G. R. Bernard, J.-D. Chiche, C. M. Coopersmith, R. S. Hotchkiss, M. M. Levy, J. C. Marshall, G. S. Martin, S. M. Opal, G. D. Rubenfeld, T. van der Poll, J.-L. Vincent and D. C. Angus, *JAMA*, 2016, **315**, 801–810.

2 K. E. Rudd, S. C. Johnson, K. M. Agesa, K. A. Shackelford, D. Tsoi, D. R. Kievlan, D. V. Colombara, K. S. Ikuta, N. Kissoon, S. Finfer, C. Fleischmann-Struzek, F. R. Machado, K. K. Reinhart, K. Rowan, C. W. Seymour, R. S. Watson, T. E. West, F. Marinho, S. I. Hay, R. Lozano, A. D. Lopez, D. C. Angus, C. J. L. Murray and M. Naghavi, *Lancet*, 2020, **395**, 200–211.

3 https://sepsistrust.org/about/about-sepsis/references-and sources/, *Website*, Sepsis trust uk technical report, accessed on 10/07/2020.

4 https://www.cancerresearchuk.org/health professional/, *Website*, Cancer research uk technical report, accessed on 10/07/2020.

5 N. Hex, J. Retzler, C. Bartlett and M. Arber, *The Cost of Sepsis Care in the UK - Final Report*, Yhec - whitewater charitable trust, univeristy of york technical report, 2017.

6 J. E. Gotts and M. A. Matthay, *BMJ*, 2016, **353**, 1–20.

7 J. D. Faix, *Crit Rev Clin Lab Sci*, 2013, **50**, 23–26.

8 C. Russell, A. C. Ward, V. Vezza, P. Hoskisson, D. Alcorn, D. P. Steenson and D. K. Corrigan, *Biosensors and Bioelectronics*, 2019, 806–814.

9 J.-L. Vincent, *PLOS Medicine*, 2016, **13**, 1–10.

10 C. W. Seymour, V. X. Liu, T. J. Iwashyna, F. M. Brunkhorst, T. D. Rea, A. Scherag, G. Rubenfeld, J. M. Kahn, M. Shankar-Hari, M. Singer, C. S. Deutschman, G. J. Escobar and D. C. Angus, *JAMA*, 2016, **315**, 762–774.

11 https://sepsistrust.org/professional resources/clinicaltools/, *Website*, Sepsis trust uk technical report, accessed on 23/07/2020.

12 R. P. Moreno and P. G. H. Metnitz, in *CRITICAL CARE MEDICINE: PRINCIPLES OF DIAGNOSIS AND MANAGEMENT IN THE ADULT*, ed. J. E. Parrillo and R. P. Dellinger, Mosby Elsevier, 3rd edn, 2008, ch. Chapter 74 - Severity Scoring Systems: Tools for the Evaluation of Patients and Intensive Care Units, pp. 1547–1565.

13 C. Pierrakos and J.-L. Vincent, *Critical Care*, 2010, **14**, 1–18.

14 R. M. Califf, *Experimental Biology and Medicine*, 2018, **243**, 213–221.

15 A. Teggert, H. Datta and Z. Ali, *Micromachines*, 2020, **11**, 1–31.

16 W. S. Tillet and T. Francis, *J Exp Med*, 1930, **52**, 561–571.

17 S. Kaptoge, E. D. Angelantonio, G. Lowe, M. B. Pepys, S. G. Thompso, R. Collins and J. Danesh, *Lancet - Emerging Risk Factors Collaboration*, 2010, **375**, 132–140.

18 S. E. Nissen, E. M. Tuzcu, P. Schoenhagen, T. Crowe, W. J. Sasiela, J. Tsai, J. Orazem, R. D. Magorien, C. OShaughnessy and P. Ganz, *N Engl J Med*, 2005, **352**, 29–38.

19 M. B. Pepys, G. M. Hirschfield1, G. A. Tennent, J. R. Gallimore, M. C. Kahan, V. Bellotti, P. N. Hawkins, R. M. Myers, M. D. Smith, A. Polara,

A. J. A. Cobb, S. V. Ley, J. A. Aquilina, C. V. Robinson, I. Sharif, G. A. Gray, C. A. Sabin, M. C. Jenvey, D. T. Simon E. Kolstoe and and S. P. Wood, *Nature*, 2006, **440**, 1217–1221.

20 N. R. Sproston and J. J. Ashworth, *Frontiers in Immunology*, 2018, **9**, 1–11.

21 S. C. Ying, H. Gewurz, C. M. Kinoshita, L. A. Potempa and J. N. Siegel, *J Immunol*, 1989, **143**, 221–228.

22 P. Povoa, L. Coelho, E. Almeida, A. Fernandes, R. Mealha, P. Moreira and H. Sabino, *Clinical Microbiology and Infection*, 2005, **11**, 101–108.

23 J. P. da Silva Silvestre, L. M. da Cruz Coelho and P. M. S. R. Póvoa, *Journal of Critical Care*, 2010, **25**, 657.e7–657.e12.

24 P. Póvoa, *Intensive Care Med*, 2002, **28**, 235–243.

25 https://www.rcsb.org/3d view/ngl/1b09, *CRP Protein Structure*, Rcsb pbd technical report, accessed on 08/08/2020.

26 https://www.rcsb.org/3d view/ngl/2il6, *IL-6 Protein Structure*, Rcsb pbd technical report, accessed on 08/08/2020.

27 A. S. Rose, A. R. Bradley, Y. Valasatava, J. M. Duarte, A. Prlic and P. W. Rose, *Bioinformatics*, 2018, **34**, 3755–3758.

28 M. Murakami, D. Kamimura and T. Hirano, *Immunity*, 2019, **50**, 812–831.

29 J. P. Brakenhoff, M. Hart, E. R. D. Groot, F. D. Padova and L. A. Aarden, *J Immunol*, 1990, **145**, 561–568.

30 T. Kishimoto, *International Immunology*, 2010, **22**, 347–352.

31 L. Ma, H. Zhang, Y. Yin, W. Guo, Y. Ma, Y. Wang, C. Shu and L. Dong, *Cytokine*, 2016, **88**, 126–135.

32 D. M. Franco, I. Arevalo-Rodriguez, M. R. i Figuls and J. Zamora, *Cochrane Database of Systematic Reviews*, 2015, **7**, 1–13.

33 J. Kneipp, H. Kneipp and K. Kneipp, *Chem. Soc. Rev.*, 2008, **37**, 1052–1060.

34 Z. Rong, R. Xiao, S. Xing, G. Xiong, Z. Yu, L. Wang, X. Jia, K. Wang, Y. Cong and S. Wang, *Analyst*, 2018, **143**, 2115–2121.

35 Y. Wang, J. Sun, Y. Hou, C. Zhang, D. Li, H. Li, M. Yang, C. Fan and B. Sun, *Biosensors and Bioelectronics*, 2019, **141**, 1–7.

36 R. S. Krishnan and R. K. Shankar, *Journal of Raman Spectroscopy*, 1981, **10**, 1–8.

37 E. Smith and G. Dent, *Modern Raman Spectroscopy A Practical Approach*, John Wiley and Sons, 2005.

38 K. C. Bantz, A. F. Meyer, N. J. Wittenberg, H. Im, O. Kurtulus, S. H. Lee, N. C. Lindquist, S.-H. Oh and C. L. Haynes, *Phys. Chem. Chem. Phys.*, 2011, **13**, 11551–11567.

39 S. Schlucker, *Angew. Chem. Int. Ed.*, 2014, **53**, 4756 – 4795.

40 X. Huang and M. A. El-Sayed, *Journal of Advanced Research*, 2010, **1**, 13–28.

41 F. Nicolson, L. E. Jamieson, S. M. andKonstantinos Plakas, N. C. Shand, M. R. Detty, D. Graham and K. Faulds, *Analyst*, 2018, **143**, 5965–5973.

42 S. Bayda, M. Adeel, T. Tuccinardi, M. Cordani and F. Rizzolio, *Molecules*, 2020, **25**, 1–15.

43 Y. Liu, J. R. Ashton, E. J. Moding, H. Yuan, J. K. Register, A. M. Fales, J. Choi, M. J. Whitley, X. Zhao, Y. Qi, Y. Ma, G. Vaidyanathan, M. R. Zalutsky, D. G. Kirsch, C. T. Badea and T. Vo-Dinh, *Theranostics*, 2015, **5**, 946–960.

44 D. A. Giljohann, D. S. Seferos, W. L. Daniel, M. D. Massich, P. C. Patel and C. A. Mirkin, *Angew. Chem. Int. Ed*, 2009, **49**, 3280–3294.

45 Y. Xia, Y. Xiong, B. Lim and S. E. Skrabalak, *Angew. Chem. Int. Ed.*, 2009, **48**, 60–103.

46 N. Ajdari, C. Vyas, S. L. Bogan, B. A. Lwaleed and B. G. Cousins, *Nanomedicine: Nanotechnology, Biology and Medicine*, 2017, **13**, 1531–1542.

47 I. Freestone, N. Meeks, M. Sax and C. Higgitt, *Gold Bulletin*, 2007, **40**, 270–277.

48 J. Turkevich, P. C. Stevenson and J. Hillier, *Discuss. Faraday Soc.*, 1951, **11**, 55 – 75.

49 G. Frens, *Nature Physical Science*, 1973, **241**, 20 – 22.

50 M. Brust, M. Walker, D. Bethell, D. J. Schiffrin and R. Whyman, *J. Chem. Soc., Chem. Commun.*, 1994, **7**, 801–802.

51 R. Herizchi, E. Abbasi, M. Milani and A. Akbarzadeh, *Artificial Cells, Nanomedicine, and Biotechnology*, 2016, **44**, 596–602.

52 Z. Farka, T. Jurik, D. Kovar, L. Trnkova and P. Skladal, *Chem. Rev.*, 2017, **117**, 9973 – 10042.

53 M. Arruebo, M. Valladares and A. G. Fernandez, *Journal of Nanomaterials*, 2009, **2009**, 1–24.

54 D. Jacofsky, E. M. Jacofsky and M. Jacofsky, *The Journal of Arthroplasty*, 2020, **35**, S74–S81.

55 https://tinyurl.com/y4ta7atn, *IgG Antibody Structure*, Thermofisher technical report, accessed on 15/08/20.

56 G. T. Hermanson, in *Bioconjugation Techniques*, ed. J. Audet and M. Preap, Academic Press, 2013, ch. Chap 20 - Antibody Modification and Conjugation, pp. 867–920.

57 G. T. Hermanson, in *Bioconjugation Techniques*, ed. J. Audet and M. Preap, Academic Press, 2013, ch. Chap 4 - Zero-Length Crosslinkers, pp. 259–273.

58 M. Shen, J. Rusling and C. K. Dixit, *Methods*, 2018, **116**, 95–111.

59 A. K. Trilling, J. Beekwilder and H. Zuilhof, *Analyst*, 2013, **138**, 1619–1627.

60 S. Mabbott, S. C. Fernandes, M. Schechinger, G. L. Cote, K. Faulds, C. R. Mace and D. Graham, *Analyst*, 2020, **145**, 983–991.

61 R. Wang, K. Kim, N. Choi, X. Wang, J. Lee, J. H. Jeon, G. eun Rhie and J. Choo, *Sensors and Actuators B: Chemical*, 2018, **270**, 72–79.

62 L. Anfossi, F. D. Nardo, S. Cavalera, C. Giovannoli and C. Baggiani, *Biosensors*, 2019, **9**, 1–14.

63 D. Wild, in *The Immunoassay Handbook*, ed. D. Wild, Elsevier, 2013, ch. Immunoassay for Beginners, pp. 7 – 10.

64 B. O'Farrell, in *The Immunoassay Handbook*, ed. D. Wild, Elsevier, 4th edn, 2013, ch. Lateral Flow Immunoassay Systems: Evolution from the Current State of the Art to the Next Generation of Highly Sensitive, Quantitative Rapid Assays, pp. 89–107.

65 S. Kasetsirikul, M. J. A. Shiddiky and N. Nguyen, *Microfluidics and Nanofluidics*, 2020, **24**, 17.

66 Y. Huang, T. Xu, W. Wang, Y. Wen, K. Li, L. Qian, X. Zhang and G. Liu, *Microchimica Acta*, 2020, **187**, 70.

67 D. Lou, L. Fan, Y. Cui, Y. Zhu, N. Gu and Y. Zhang, *Analytical Chemistry*, 2018, **90**, 6502–6508.

68 J. Zhang, X. Lv, W. Feng, X. Li, K. Li and Y. Deng, *Microchimica Acta*, 2018, **185**, 364.

69 C. N. Loynachan, M. R. Thomas, E. R. Gray, D. A. Richards, J. Kim, B. S. Miller, J. C. Brookes, S. Agarwal, V. Chudasama, R. A. McKendry and M. M. Stevens, *ACS Nano*, 2018, **12**, 279–288.

70 L. Russo, M. Sánchez-Purrà, C. Rodriguez-Quijada, B. M. Leonardo, V. Puntes and K. Hamad-Schifferli, *Nanoscale*, 2019, **11**, 10819–10827.

71 J. Hwang, S. Lee and J. Choo, *Nanoscale*, 2016, **8**, 11418–11425.

72 W. Ren, S. I. Mohammed, S. Wereley and J. Irudayaraj, *Analytical Chemistry*, 2019, **91**, 2876–2884.

73 NanoComposix, *Lateral Flow Assay Development Guide*, online, 2017.

74 F. D. Nardo, E. Alladio, C. Baggiani, S. Cavalera, C. Giovannoli, G. Spano and L. Anfossi, *Talanta*, 2019, **192**, 288–294.

75 J. Kim, X. E. Cao, J. L. Finkelstein, W. B. Cárdenas, D. Erickson and S. Mehta, *Malaria Journal*, 2019, **18**, 1–10.

76 W. Xiao, C. Huang, F. Xu, J. Yan, H. Bian, Q. Fu, K. Xie, L. Wang and Y. Tang, *Sensors and Actuators B: Chemical*, 2018, 63–70.

77 V. Tran, B. Walkenfort, M. Kçnig, M. Salehi and S. Schlücker, *Angew. Chem. Int. Ed.*, 2019, **58**, 442–446.

78 Y. Wang, Y. Hou, H. Li, M. Yang, P. Zhao and B. Sun, *Microchimica Acta*, 2019, **186**, 548.

79 X. Fu, Z. Cheng, J. Yu, P. Choo, L. Chen and J. Choo, *Biosensors and Bioelectronics*, 2016, **78**, 530–537.

80 S. Choi, J. Hwang, S. Lee, D. W. Lim, H. Joo and J. Choo, *Sensors and Actuators B: Chemical*, 2017, **240**, 358–364.

81 M. Xiao, K. Xie, X. Dong, L. Wang, C. Huang, F. Xu, W. Xiao, M. Jin, B. Huang and Y. Tang, *Analytica Chimica Acta*, 2019, **1053**, 139–147.

82 L. Lu, J. Yu, X. Liu, X. Yang, Z. Zhou, Q. Jin, R. Xiao and C. Wang, *RSC Adv.*, 2020, **10**, 271–281.

83 J. D. Clogston and A. K. Patri, in *Characterization of Nanoparticles Intended for Drug Delivery*, ed. S. E. McNeil, Humana Press, Springer, 2011, ch. Zeta Potential Measurement, pp. 63 –71.

84 S. Agnihotri, S. Mukherji and S. Mukherji, *RSC Adv*, 2014, **4**, 3974–3983.

85 H. Kitching, A. J. Kenyon and I. P. Parkin, *Phys. Chem. Chem. Phys.*, 2014, **16**, 6050–6059.

86 H. M. Zakaria, A. Shah, M. Konieczny, J. A. Hoffmann, A. J. Nijdam and M. E. Reeves, *Langmuir*, 2013, **29**, 7661–7673.

87 P. Comeau and T. Willett, *Scientific Reports*, 2018, **8**, 12700.

88 R. Höfer, in *Industrial Biorefineries and White Biotechnology*, ed. A. Pandey, R. Höfer, M. Taherzadeh, K. M. Nampothiri and C. Larroche, Elsevier, 2015, ch. 4A, p. 198.

89 Y. Zhao, Z. Wang, W. Zhang and X. Jiang, *Nanoscale*, 2010, **2**, 2114–2119.

90 A. Kamińska, I. Dzięcielewski, J. L. Weyher, J. Waluk, S. Gawinkowski, V. Sashuk, M. Fiałkowski, M. Sawicka, T. Suski, S. Porowskib and R. Hołyst, *J. Mater. Chem.*, 2011, **21**, 8662 – 8668.

91 Y. Liu, J. Ling and C. Z. Huang, *Chem. Commun.*, 2011, **47**, 8121–8123.

92 M. Tuck, D. K. Turgeon and D. E. Brenner, in *Serum and Plasma Collection: Preanalytical Variables and Standard Operating Procedures in Biomarker Research*, ed. H. J. Issaq and T. D. Veenstra, Elsevier, 2013, ch. 5.

93 R. S. Tirumalai, K. C. Chan, D. A. Prieto, H. J. Issaq, T. P. Conrads and T. D. Veenstra, *Molecular and Cellular Proteomics*, 2003, **2.10**, 1096–1103.

94 M. Astrid Friebe and M. Hans-Dieter Volk, *Arch Pathol Lab Med*, 2008, **132**, 1802–1806.

95 D. H. Jackson and R. E. Banks, *Proteomics Clin. Appl.*, 2010, **4**, 250–270.

96 W. M. Fakanya and I. E. Tothill, *Biosensors*, 2014, **4**, 340 – 357.

97 C. Li, Y. Liu, X. Zhouc and Y. Wang, *J. Mater. Chem. B*, 2020, **8**, 3582–3589.

98 D. P. Ramji and T. S. Davies, *Cytokine and Growth Factor Reviews*, 2015, **26**, 673–685.

99 Y. Wu, Y. Zhou, Y. Leng, W. Lai, X. Huang and Y. Xiong, *Biosensors and Bioelectronics*, 2020, **157**, 112168.

100 M. L. Yahaya, N. D. Zakaria, R. Noordin and K. A. Razak, in *Advanced Materials and their Applications: Micro to nano scale*, ed. I. Ahmad, P. D. Sia and R. Raza, ONe Central Press (OCP), 2019, ch. 6, pp. 121–139.

101 E. M. Fenton, M. R. Mascarenas, G. P. Lopez and S. S. Sibbett, *ACS Applied Material and Interfaces*, 2009, **1**, 124–129.

102 H. Zhang, X. Qiu, Y. Zou, Y. Ye, C. Qi, L. Zou, X. Yang, K. Yang, Y. Zhu, Y. Yang, Y. Zhou and Y. Luo, *Sci. Transl. Med.*, 2017, 1–11.

103 L. Hecht, D. van Rossum and A. Dietzel, *Microelectronic Engineering*, 2016, **158**, 52–58.

104 T.-T. Tsai, T.-H. Huang, N. Y.-J. Ho, Y.-P. Chen, C.-A. Chen and C.-F. Chen, *Scientific Reports*, 2019, **9**, 1–8.

105 M. Jauset-Rubio, H. Tomaso, M. S. El-Shahawi, A. S. Bashammakh, A. O. Al-Youbi and C. K. O'Sullivan, *Analytical Chemistry*, 2018, **90**, 12745–12751.

106 Y. Chen, J. Sun, Y. Xianyu, B. Yin, Y. Niu, S. Wang, F. Cao, X. Zhang, Y. Wangb and X. Jiang, *Nanoscale*, 2016, **8**, 15205–15212.

107 M. You, M. Lin, Y. Gong, S. Wang, A. Li, L. Ji, H. Zhao, K. Ling, T. Wen, Y. Huang, D. Gao, Q. Ma, T. Wang, A. Ma, X. Li and F. Xu, *ACS Nano*, 2017, **11**, 6261–6270.

108 X. Wang, N. Cho, Z. Cheng, J. Ko, L. Chen and J. Choo, *Analytical Chemistry*, 2017, **89**, 1163–1169.

109 D. Zhang, L. Huang, B. Liu, Q. Ge, J. Dong and X. Zhao, *Thernostics*, 2019, **9**, 4849–4859.

110 B. Jin, Y. Yang, R. Heb, Y. I. Park, A. Lee, D. Bai, F. Li, T. J. Lu, F. Xu and M. Lin, *Sensors and Actuators B: Chemical*, 2018, **276**, 48–56.

111 D. Zhang, L. Huang, B. Liu, H. Ni, L. Sun, E. Su, H. Chen, Z. Gu and X. Zhao, *Biosensors and Bioelectronics*, 2018, **106**, 204–211.

112 M. Han, L. Gong, J. Wang, X. Zhang, Y. Jin, R. Zhao, C. Yang, L. He, X. Feng and Y. Chen, *Sensors and Actuators B: Chemical*, 2019, **292**, 94–104.

113 W. Wang, X. Su, H. Ouyang, L. Wang and Z. Fu, *Analytica Chimica Acta*, 2016, **917**, 79–84.

114 C.-W. Yen, H. de Puig, J. O. Tam, J. Gómez-Márquez, I. Bosch, K. Hamad-Schifferli and L. Gehrke, *Lab on a CHip*, 2015, **15**, 1638–1641.

115 A. N. Danthanarayana, E. Finley, B. Vu, K. Kourentzi, R. C. Willson and J. Brgoch, *Anal. Methods*, 2020, **12**, 272–280.

116 D. Zhang, L. Huang, B. Liu, E. Su, H.-Y. Chen, Z. Gu and X. Zhao, *Sensors and Actuators B: Chemical*, 2018, **277**, 502–509.

117 M. Sanchez-Purra, B. Roig-Solvas, C. Rodriguez-Quijada, B. M. Leonardo and K. Hamad-Schifferli, *ACS Omega*, 2018, **3**, 10733–10742.

118 Z. Wu, *Food Analytical Methods*, 2019, **12**, 1086–1091.

119 M. Sanchez-Purra, M. Carre-Camps, H. de Puig, I. Bosch, L. Gehrke and K. Hamad-Schifferli, *ACS Infect. Dis.*, 2017, **3**, 767–776.

120 E. G. Rey, D. ODell, S. Mehta and D. Erickson, *Anal. Chem.*, 2017, **89**, 5095–5100.

121 J. Zhang, X. Li, X. Sun and Y. Li, *J. Phys. Chem. B*, 2005, **109**, 12544–12548.

122 S. Lin, W.-L.-J. Hasi, X. Lin, S. qin-gao-wa Han, X.-T. Lou, F. Yang, D.-Y. Lin and Z.-W. Lu, *Anal. Methods*, 2015, **7**, 5289.

123 P.-O. Bussiere, J.-L. Gardette and S. Therias, *Polymer Degradation and Stability*, 2014, **107**, 246–254.

124 D. French and A. H. Wu, in *The Immunoassay Handbook (Fourth Edition) - Theory and Applications of Ligand Binding, ELISA and Related Techniques*, ed. D. Wild, Elsevier, 4th edn, 2013, ch. 9.12 Cardiac Biomarker, p. 825.

125 Y. Luo and S. G. Zheng, *Frontiers of Immunology*, 2016, **7**, 1–7.

126 D. Li, L. Jiang, J. A. Piper, I. S. Maksymov, A. D. Greentree, E. Wang and Y. Wang, *ACS Sens.*, 2019, **4**, 2507–2514.

127 B. Shiferaw, E. Bekele, K. Kumar, A. Boutin and M. Frieri, *J Infect Dis Epidemiol*, 2016, **2**, 1–4.

128 M. Egeblad and Z. Werb, *Nature Reviews*, 2002, **2**, 161–174.

129 L. Lorente, M. M. Martín, M. A. Luis Ramo and, J. J. Cáceres, J. Solé-Violán, A. Jiménez, J. M. Borreguero-León, A. F. González-Rivero, J. Orbe, J. A. Rodríguez and J. A. Páramo, *BMC Neurology*, 2019, **19**, 1–7.

130 A. Rosell and E. H. Lo, *Current Opinion in Pharmacology*, 2008, **8**, 82–89.

131 K. Masuhara, T. Nakai, K. Yamaguchi, S. Yamasaki and Y. Sasaguri, *Arthritis and Rheumatism*, 2002, **46**, 2625–2631.

132 A. W. Martinez, S. T. Phillips, M. J. Butte and G. M. Whitesides, *Angew. Chem. Int. Ed.*, 2007, **46**, 1318–1320.

133 A. W. Martinez, S. T. Phillips and G. M. Whitesides, *PNAS*, 2008, **105**, 19606–19611.

134 C.-M. Cheng, A. W. Martinez, J. Gong, C. R. Mace, S. T. Phillips, E. Carrilho, K. A. Mirica and G. M. Whitesides, *Angew. Chem. Int. Ed.*, 2010, **49**, 4771–4774.

135 A. K. Ellerbee, S. T. Phillips, A. C. Siegel, K. A. Mirica, A. W. Martinez, P. Striehl, N. Jain, M. Prentiss and G. M. Whitesides, *Analytical Chemistry*, 2009, **81**, 8447–8452.

136 A. W. Martinez, S. T. Phillips, E. Carrilho, S. W. T. III, H. Sindi and G. M. Whitesides, *Analytical Chemistry*, 2008, **80**, 3699–3707.

137 Y. Lu, W. Shi, L. Jiang, J. Qin and B. Lin, *Electrophoresis*, 2009, **30**, 1497–1500.

138 E. Carrilho, A. W. Martinez and G. M. Whitesides, *Analytical Chemistry*, 2009, **81**, 7091–7095.

139 S. B. Berry, S. C. Fernandes, A. Rajaratnam, N. S. DeChiara and C. R. Mace, *Lab On a Chip*, 2016, **16**, 3689–3694.

140 H. Kudo, K. Maejima, Y. Hiruta and D. Citterio, *SLAS Technology*, 2020, **25**, 47–57.

141 X. Wei, T. Tian, S. Jia, Z. Zhu, Y. Ma, J. Sun, Z. Lin and C. J. Yang, *Analytical Chemistry*, 2016, **88**, 2345–2352.

142 L. Wang and B. McCord, *Analytical Biochemistry*, 2020, **595**, 1–3.

143 E. Evans, E. F. M. Gabriel, T. E. Benavidez, W. K. T. Coltro and C. D. Garcia, *Analyst*, 2014, **139**, 5560–5567.

144 H. Liu and R. M. Crooks, *J. Am. Chem. Soc.*, 2011, **133**, 17564–17566.

145 L. Ge, S. Wang, X. Song, S. Gea and J. Yu, *Lab On a Chip*, 2012, **12**, 3150–3158.

146 R. N. Deraney, C. R. Mace, J. P. Rolland and J. E. Schonhorn, *Analytical Chemistry*, 2016, **88**, 6161–6165.

147 W. Y. Lim, C.-H. Goh, T. M. Thevarajah, B. T. Goh and S. M. Khor, *Biosensors and Bioelectronics*, 2020, **147**, 1–11.

148 W. Y. Lim, T. M. Thevarajah, B. T. Goh and S. M. Khor, *Biosensors and Bioelectronics*, 2019, **128**, 176–185.

149 S. C. Fernandes, G. S. Logounov, J. B. Munro and C. R. Mace, *Anal. Methods*, 2016, **8**, 5204–5211.

150 S. C. Fernandes, D. J. Wilson and C. R. Mace, *J. Vis. Exp.*, 2017, **121**, e55287.

151 N. S. DeChiara, D. J. Wilson and C. R. Mace, *Scientific Reports*, 2017, **7**, 16224.

152 J. E. Schonhorn, S. C. Fernandes, A. Rajaratnam, R. N. Deraney, J. P. Rolland and C. R. Mace, *Lab On a Chip*, 2014, **14**, 4653–4658.

153 L. Frame, *PhD Thesis*, Department of Pure and Applied Chemistry, University of Strathclyde, 2017.

154 J. V. MILLER and E. G. BARTICK, *Applied Spectroscopy*, 2001, **55**, 1729–1732.

155 N. Sharma, B. Tripathi, A. Shrivastava and R. Chauhan, *I.J.E.M.S.*, 2014, **5**, 128–139.

156 M. R. Hormozi-Nezhad, P. Karami and H. Robatjazi, *RSC Adv.*, 2013, **3**, 7726–7732.

157 R. Goodacre, D. Graham and K. Faulds, *Trends in Analytical Chemistry*, 2018, **102**, 359–368.

158 https://www.youtube.com/watch?v=IX Na7fn6Zk, *John M Cimbala*, Pennsylvania state university technical report, accessed on 22/08/2020.

159 https://www.discoveringstatistics.com/repository/linearmodelsbias.pdf, *Andy Field*, Discovering statistics technical report, accessed on 22/08/2020.

A. Appendix

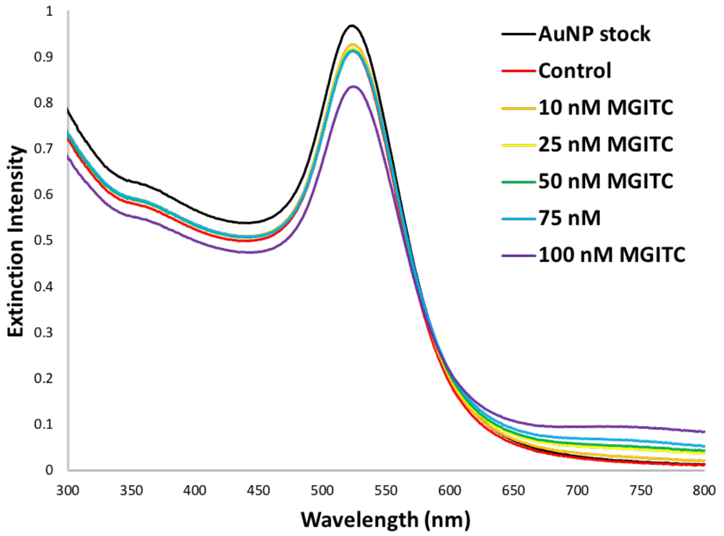

Sample	Max Extinction	λ_{max}
Stock AuNPs	0.96	524.98
control	0.91	524.98
10	0.93	524.98
25	0.92	524.98
50	0.91	524.98
75	0.91	524.98
100	0.84	524.98

Figure A.1: Extinction spectroscopy results from concentration on AuNPs with MGITC. Table below shows the LSPR peak did not shift with increasing MGITC concentration however peak dampening was evident. A broad band at ∼700 nm indicated the generation of larger AuNP aggregates, the extinction intensity of this band increased with increasing MGITC concentration which suggested destabilisation of the AuNP surface as more MGITC molecules became attached.

Table A.1: MGITC Concentration Study showing concentrations used and how they were prepared.

Concentration of MGITC (nM)	Vol. of MGITC solution (1x10^{-5} M) (μL)	Vol. of H_2O
0	0	100
10	1	9
25	2.5	7.5
50	5	5
75	7.5	2.5
10	10	0

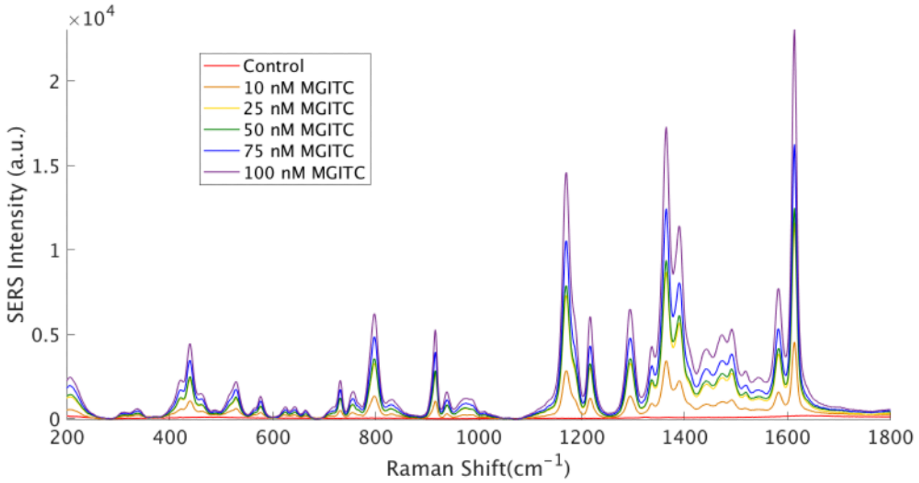

Figure A.2: SERS analysis from MGITC concentration study, SERS intensity was observed to increase with increasing MGITC concentration. 75 nM MGITC was chosen as the optimum concentration as it generated an intense SERS signal without compromising the stability of AuNPs.

Table A.2: CRP-Ab Concentration Study showing concentrations used and how they were prepared.

Concentration of CRP Ab (μg/mL)	Vol. of Ab (μg/mL) (μL)
0	0
0.05	0.1
0.25	0.5
0.5	1
1	2
2.5	5

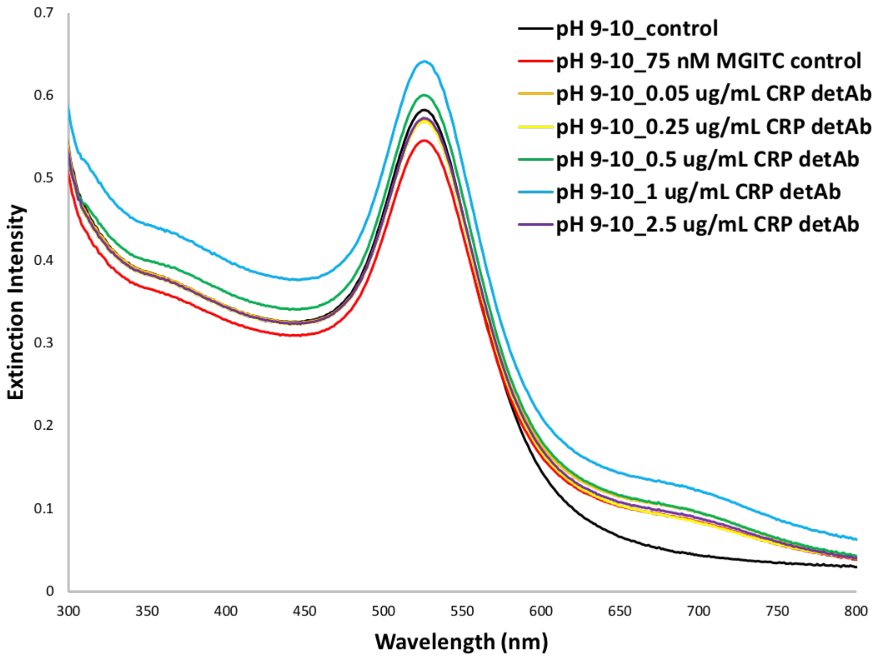

Sample	Max Extinction	λmax
control	0.58	526.00
75 nM MGITC	0.55	526.00
0.05 µg/mL	0.57	527.01
0.25 µg/mL	0.57	525.02
0.5 µg/mL	0.60	525.02
1 µg/mL	0.64	526.00
2.5 µg/mL	0.57	525.02

Figure A.3: Extinction spectroscopy results from CRP-Ab concentration study. The following concentrations were added to AuNPs - 2.5 μg/mL, 1 μg/mL, 0.5 μg/mL, 0.25 μg/mL, 0.05 μg/mL, 0 μg/mL, the optimum concentration of Ab was found to be 2.5 μg/mL as the particles remained stable and the LSPR peak deviated little from that of the control sample.

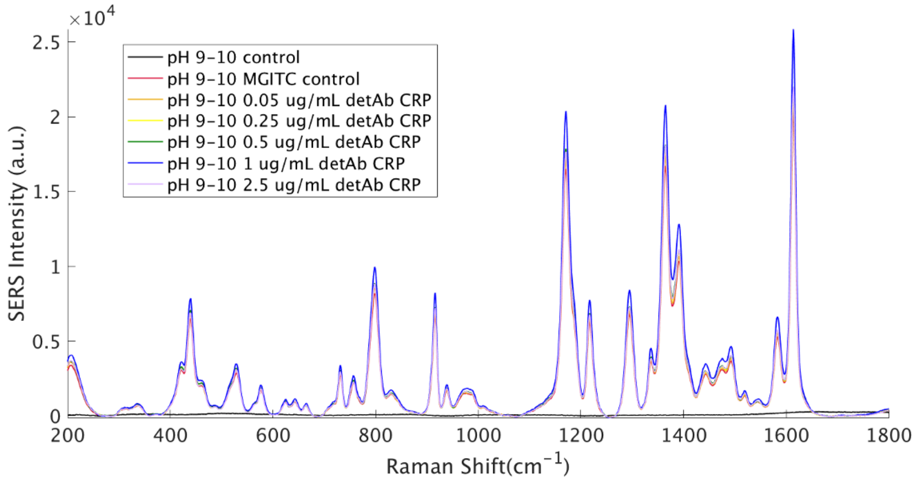

Figure A.4: SERS results from CRP-Ab concentration study. Most intense spectrum was observed for 1 μg/mL Ab which was consistent with extinction spectroscopy results where there was a broad band at ~700 nm indicated the presence of AuNP aggregates. This band was more prominent when compared with other Ab concentrations. Therefore 2.5 μg/mL was chosen as the optimum Ab concentration as it had an intense SERS signal while remaining stable. This was the highest Ab concentration in the the study and it was considered advantageous to have a higher Ab concentration to increase the number of sites available for binding with CRP.

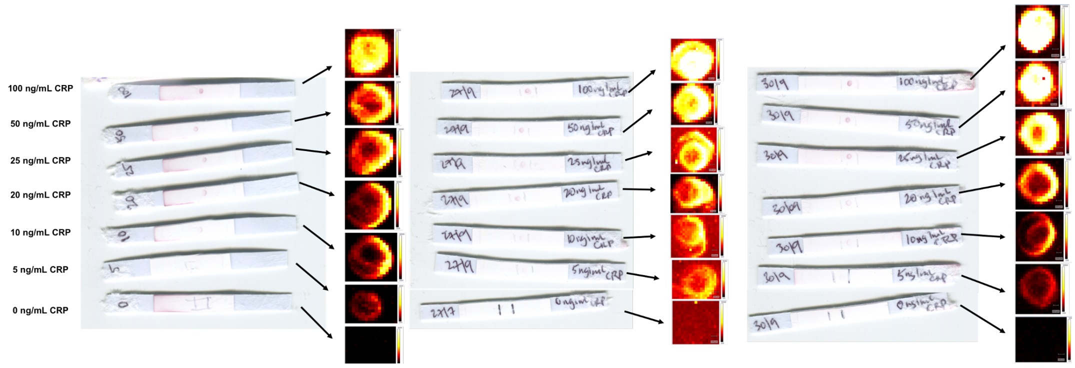

Figure A.5: Scanned images of lateral flow assays and corresponding SERS intensity maps from each CRP concentration study. The images were scanned using an Epson Perfection V370 flatbed scanner with each scan taken at a resolution of 800 dpi. The scanned images were analysed using ImageJ to calculate RGB values for each spot. The SERS maps were generated from the intensity of 1617 cm^{-1} peak of Raman reporter MGITC. The map analysis was carried out on a Renishaw InVia Raman Microscope at laser wavelength 633 nm, 0.73 mW power, integration time 6 s with a stepsize for each map of 100 μm.

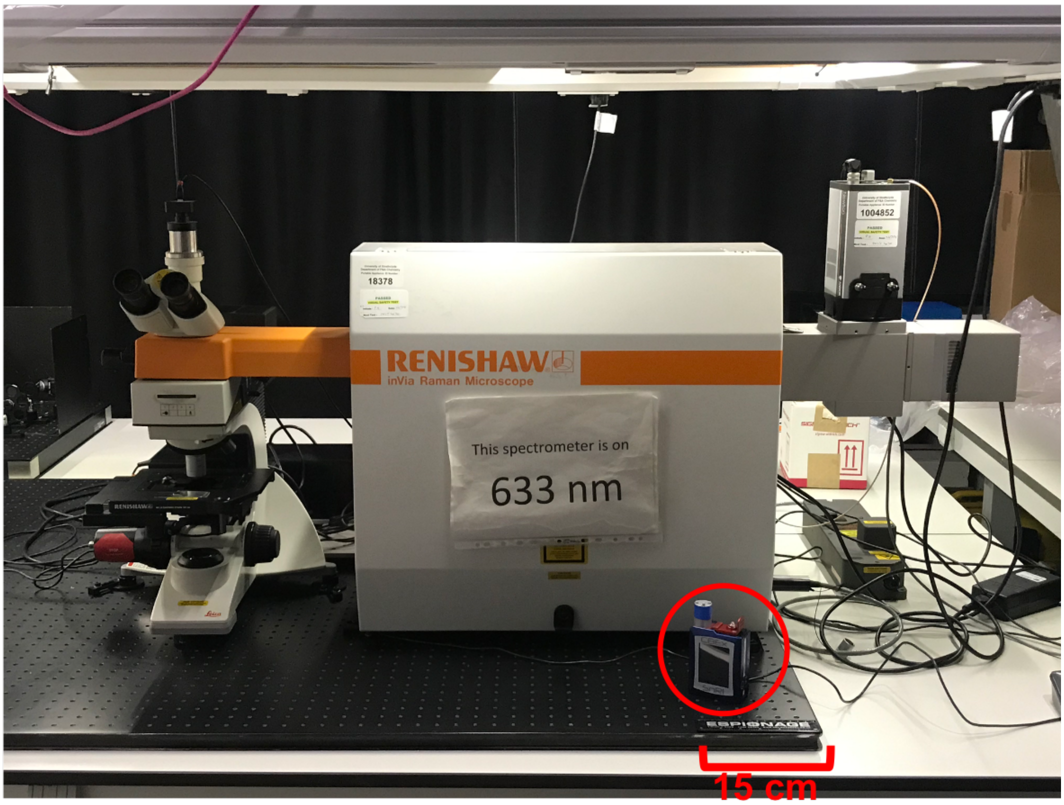

Figure A.6: Renishaw InVia Raman Microscope and CBeX Handheld Raman spectrometer from Snowy Range Instruments placed alongside one another to emphasis the difference in size and portability between the instruments.

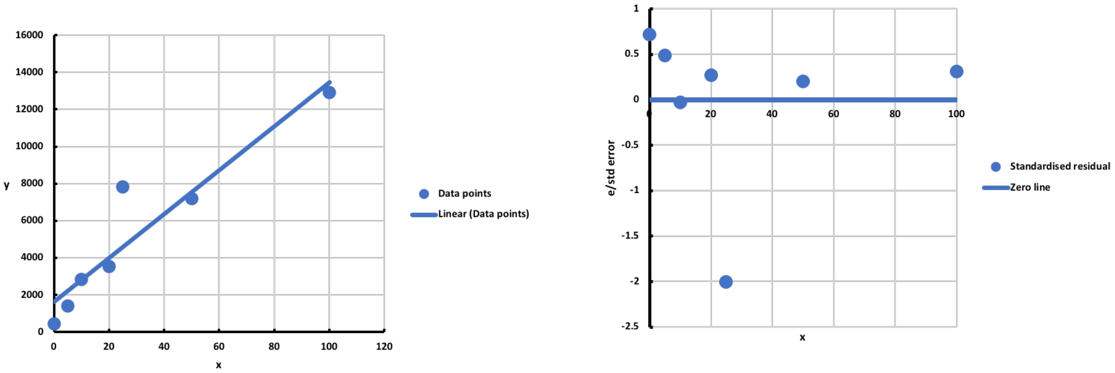

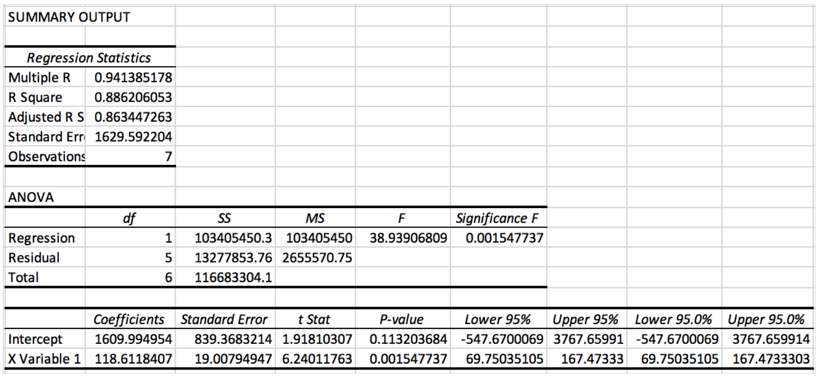

SUMMARY OUTPUT								
Regression Statistics								
Multiple R	0.941385178							
R Square	0.886206053							
Adjusted R S	0.863447263							
Standard Err	1629.592204							
Observations	7							
ANOVA								
	df	*SS*	*MS*	*F*	*Significance F*			
Regression	1	103405450.3	103405450	38.93906809	0.001547737			
Residual	5	13277853.76	2655570.75					
Total	6	116683304.1						
	Coefficients	*Standard Error*	*t Stat*	*P-value*	*Lower 95%*	*Upper 95%*	*Lower 95.0%*	*Upper 95.0%*
Intercept	1609.994954	839.3683214	1.91810307	0.113203684	-547.6700069	3767.65991	-547.6700069	3767.659914
X Variable 1	118.6118407	19.00794947	6.24011763	0.001547737	69.75035105	167.47333	69.75035105	167.4733303

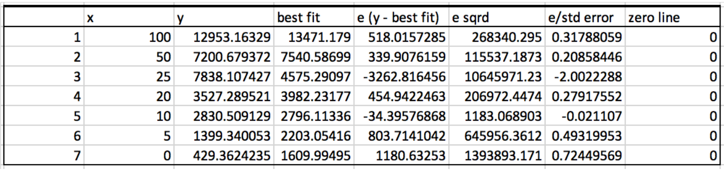

	x	y	best fit	e (y - best fit)	e sqrd	e/std error	zero line
1	100	12953.16329	13471.179	518.0157285	268340.295	0.31788059	0
2	50	7200.679372	7540.58699	339.9076159	115537.1873	0.20858446	0
3	25	7838.107427	4575.29097	-3262.816456	10645971.23	-2.0022288	0
4	20	3527.289521	3982.23177	454.9422463	206972.4474	0.27917552	0
5	10	2830.509129	2796.11336	-34.39576868	1183.068903	-0.021107	0
6	5	1399.340053	2203.05416	803.7141042	645956.3612	0.49319953	0
7	0	429.3624235	1609.99495	1180.63253	1393893.171	0.72449569	0

Figure A.7: Linear regression analysis was used to identify the outlier at 25 ng/mL CRP in the triplicate CRP concentration study using the handheld Raman spectrometer. Standardised residuals (e/standard error) were calculated using the difference between the actual SERS intensity versus the value calculated for the best fit of the linear model (e) and dividing this by the standard error. This was plotted against CRP concentration and any value greater than or less than 2 was deemed to be an outlier as 2 standard deviations is approximately 95% confidence. The linear regression analysis was performed using Excel.[158,159]

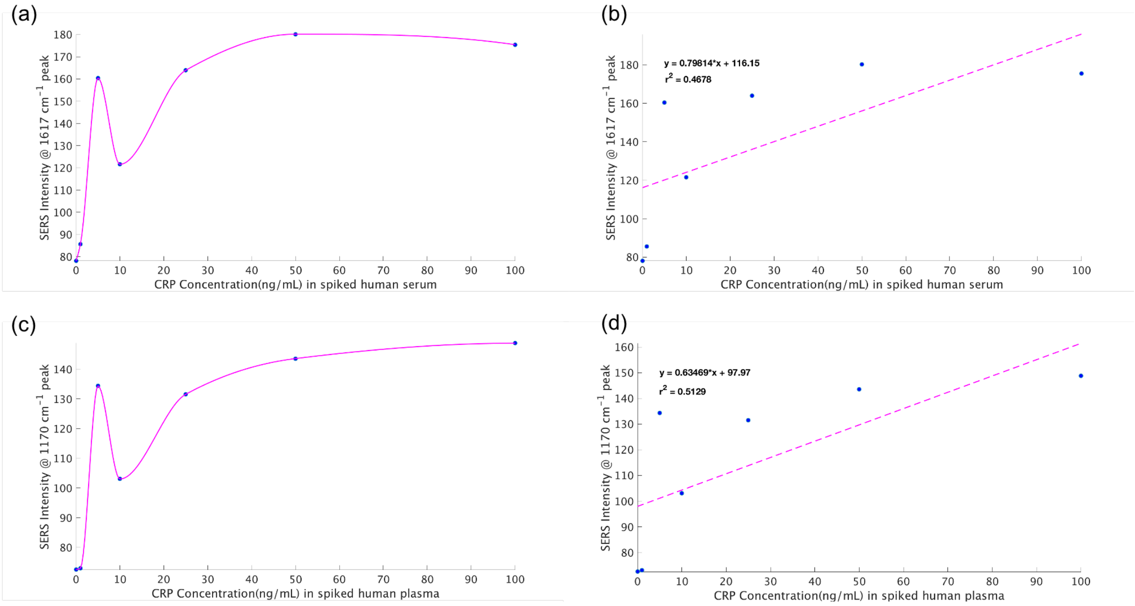

Figure A.8: Calibration curves from CRP concentration study in human serum (a) and (b) concstructed from 1617 cm^{-1} peak and (c) and (d) constructed from the 1170 cm^{-1} peak of MGITC. (a) shape of curve showing outlier at 5 ng/mL CRP and corresponding calibration curve with R^2 value of 0.4678, this is low due to the presence of the outlier which does not follow the general trend of the data, (c) shape of curve for 1170 cm^{-1} peak where outlier at 5 ng/mL CRP was again evident and (d) corresponding calibration curve with R^2 value of 0.5129. Data was processed using Matlab.

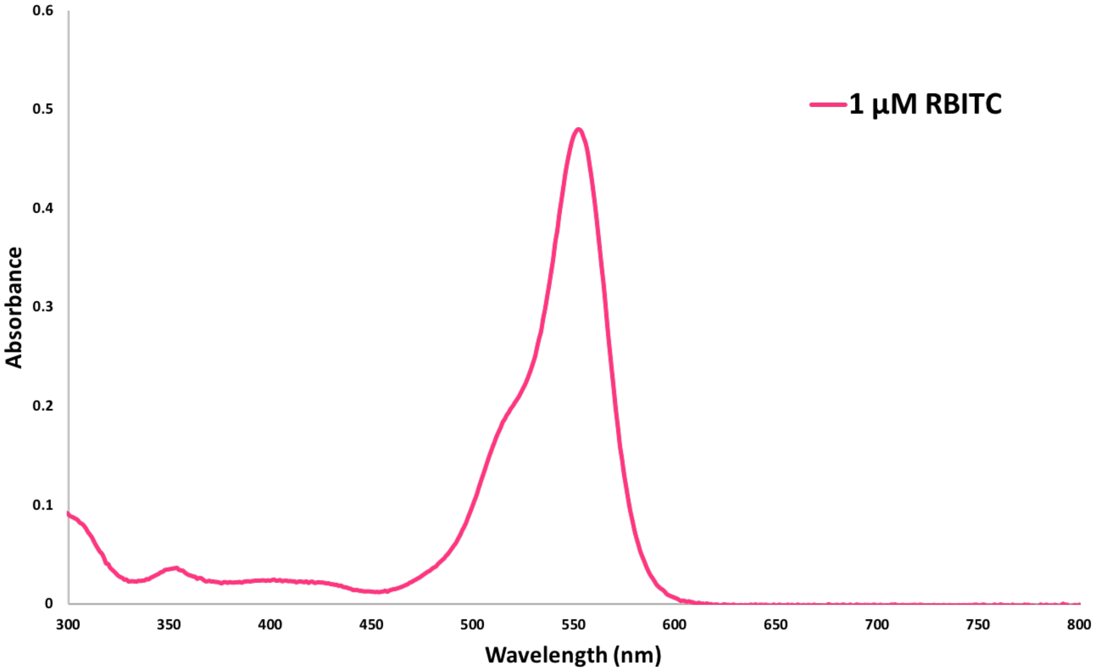

Figure A.9: Absorbance spectrum for 1 μM RBITC diluted in H_2O from 1 mM stock prepared in MeOH.

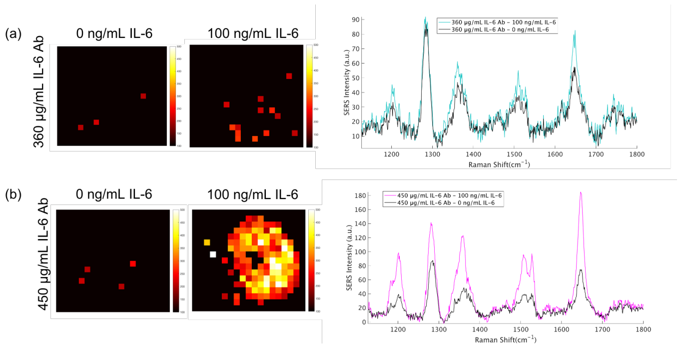

Figure A.10: SERS spectra for AuNPs functionalised with 0.75 μM RBITC using (a) 532 nm laser excitation and (b) 638 nm laser excitation. Due to RBITC being resonant at ~532 nm, broad fluorescence was observed and overcame the SERS signal and quenching at the AunP surface. Off-resonance at a higher wavelength of 638 nm, a clear SERS spectrum was collected with sharp defined peaks characteristic of RBITC. Both spectra were collected at 100% laser power, 1 s acquisition time and 3 scans of each sample were averaged to generate the resulting spectra.

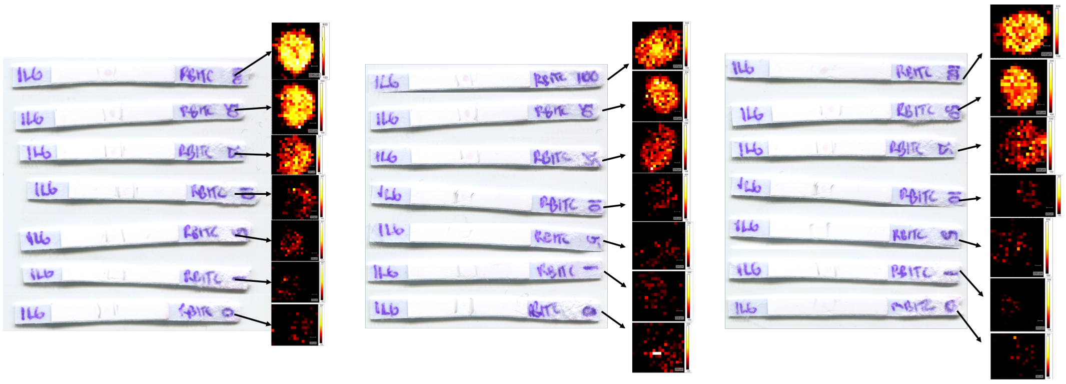

Figure A.11: Scanned images of LF strips and corresponding SERS intensity maps from each study. Maps were constructed from the intensity of the 1650 cm^{-1} peak at 633 nm laser wavelength, 0.73 mW laser power, 5 s acquisition time and 100 μm step size.

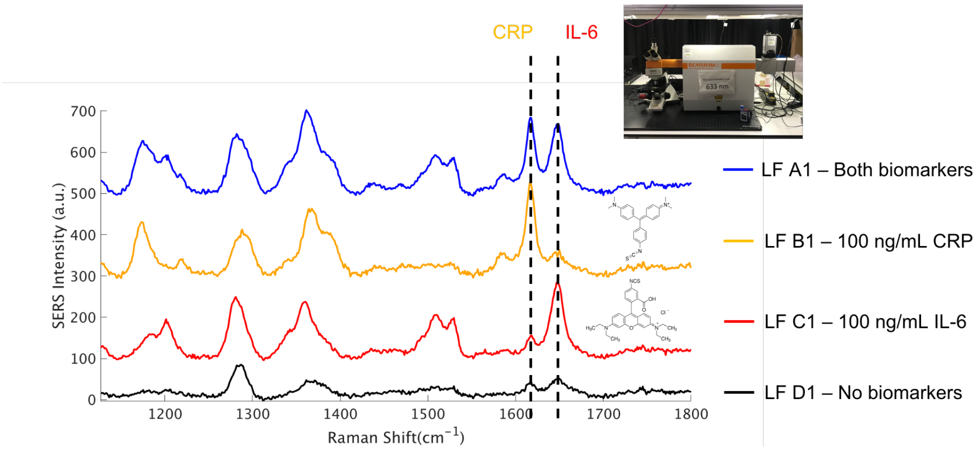

Figure A.12: Average SERS spectra from Raman mapping data for LF A1 - both biomarkers at 100 ng/mL each + both conjugates (blue spectrum), LF B1 - 100 ng/mL CRP only + both conjugates (orange spectrum), LF C1 - 100 ng/mL IL-6 + both conjugates (red spectrum) and LF D1 - no biomarkers present + both conjugates (black spectrum). Black-dotted lines indicate the positions of the peaks of interest, 1617 cm^{-1} peak of MGITC representing CRP and 1650 cm^{-1} peak of RBITC representing IL-6. Both peaks were present only for LF A1 as both biomarkers were present in the sample mixture. For LF B1, only the 1617 cm^{-1} peak was present as only CRP was in the sample mixture. Similarly, IL-6 was the only biomarker present for LF C1 therefore only the 1650 cm^{-1} peak was observed. Both peaks were absent from the SERS spectrum for LF D1 as there were no biomarkers present in the sample mixture. Raman mapping analysis was performed at 633 nm laser excitation, 0.73 mW laser power, 5 s acquisition time and 100 μm step size.

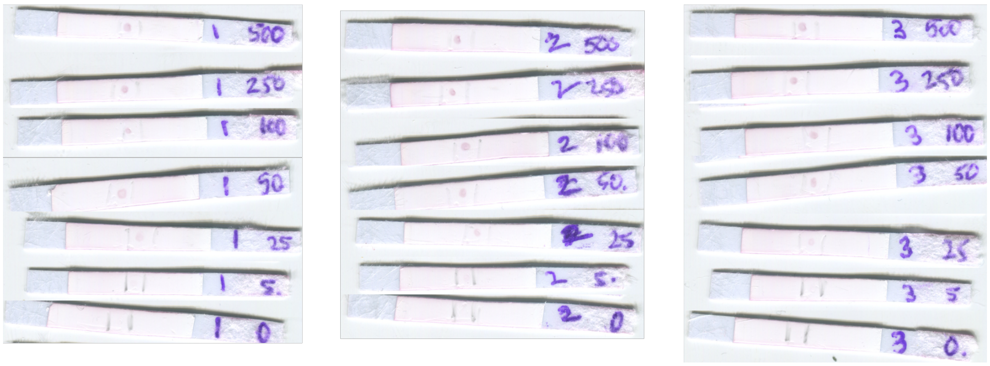

Figure A.13: Scanned images of LF strips from triplicate concentration study of CRP and IL-6 on the single-spot duplex assay platform. The following concentrations of CRP and IL-6 were investigated - 500, 250, 100, 50, 25, 5 and 0 ng/mL.

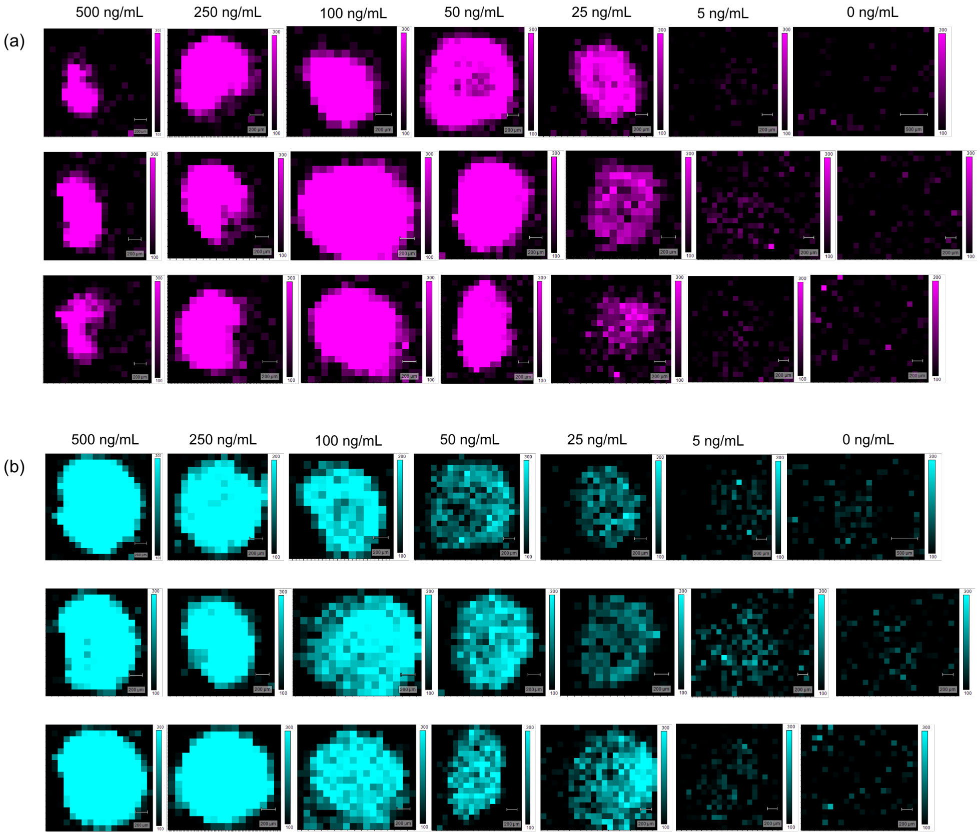

Figure A.14: Results from Raman maps of each spot constructed from (a) 1617 cm^{-1} peak of MGITC representing the presence of CRP for all concentrations across all replicates and (b) the same spot constructed from the 1650 cm^{-1} peak of RBITC representing IL-6 for all concentrations across all replicates. Raman mapping was performed at 633 nm laser excitation, 0.73 mW laser power, 5 s acquisition time and 100 μm step size.

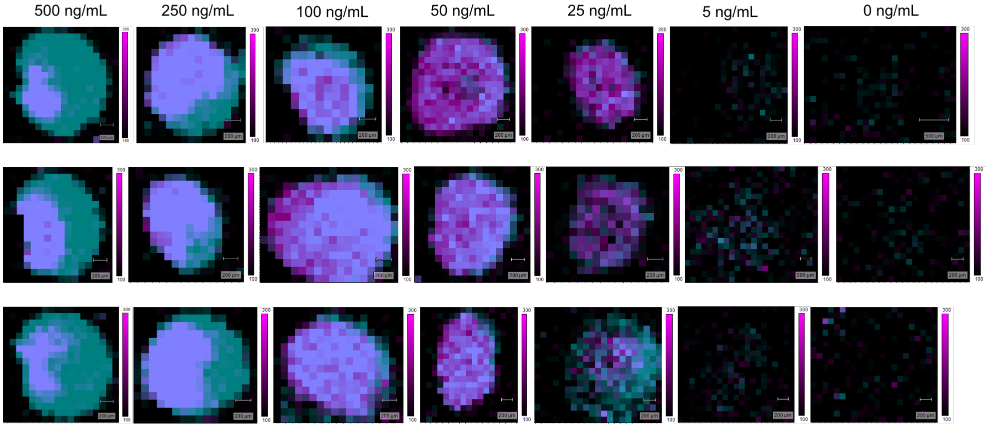

Figure A.15: Results from overlaying Raman maps shown in figure A.13 to demonstrate the duplex capability of the assay. When there was contribution from both the 1617 cm^{-1} and 1650 cm^{-1} peaks, the overlaid maps appeared purple.

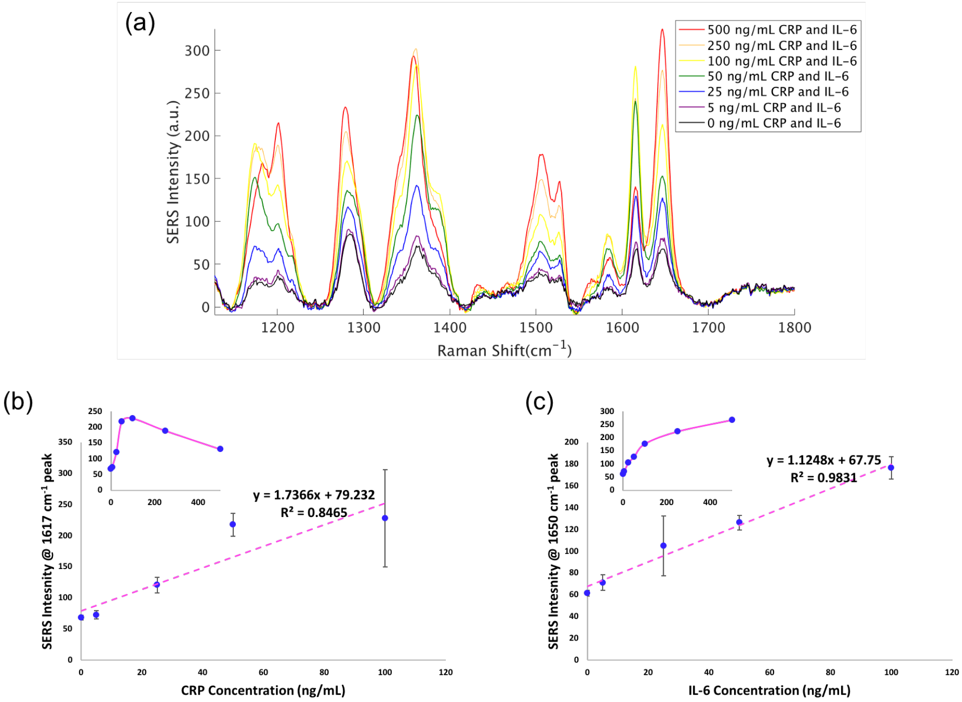

Figure A.16: Results from Raman mapping analysis (a) average spectra for each biomakrer concentration across the triplicate studies, (b) calibration curve for SERS intensity of the 1617 cm^{-1} peak with respect to CRP concentration constructed from the linear region (0 - 100 ng/mL CRP) of the inset graph. A LOD of 6.5 ng/ml was calculated for CRP and (c) calibration curve for the SERS intensity of the 1650 cm^{-1} peak with respect to IL-6 concentration across the entire concentration range (0 - 500 ng/mL IL-6). A LOD of 7.5 ng/mL IL-6 was calculated. Raman mapping was performed at 633 nm laser excitation, 0.73 mW laser power, 5 s acquisition time and 100 μm step size.

Study Specific Blood Sample Management SOP
POP Trial Biomarker Sub-study

Version number:	1.1
Effective date:	18/05/2017

Signature	**Date**
Author: Bernadette Gallagher (EMERGE Senior Research Nurse)	
Reviewed By: Dr. James Dear (Chief Investigator POP study)	
Reviewed By: Miranda Odam (EMERGE Research Nurse Manager)	
Approved By: Dennis Henriksen (Sponsor POP study)	

1. PURPOSE

The purpose of this Standard Operating Procedure (SOP) is to ensure that the correct procedures are used in all aspects of sample management, including obtaining, processing and transferring samples for the POP biomarker sub-study while adhering to Good Clinical Practice (GCP), Good Laboratory Practice (GLP) and Study Specific Guidelines.

2. SCOPE

This SOP applies to the POP biomarker sub-study where research staff is involved in obtaining, processing and transferring samples of blood.

3. PROCEDURES

3.1 Blood sampling

- Routine clinical bloods will be taken by either clinical or research staff at the time specified in the local protocol for N-Acetyl Cysteine (NAC).

- Study specific blood samples will be taken by research staff at the following time-points:

	Blood Tube & Size	2hrs after NAC commenced (+/- 15mins)	10hrs after NAC commenced (+/- 30mins)	20hrs after NAC commenced (+/- 30mins)
Sub-study samples: **EDTA**	Red - 2.7ml	1 x tube	1 x tube	1 x tube
Sub-study samples: **SERUM**	Brown - 4.9ml	1 x tube	1 x tube	1 x tube
*Clinical samples: **EDTA** **Coagulation** **Li-Heparin**	Red - 2.7ml Green - 3ml Orange - 4.9ml	1 x tube (each)	1 x tube (each)	1 x tube (each)
*Clinical bloods are listed here for clarity only				

Table1. Details of study specific biomarkers and clinical blood samples

- Stand <u>sub-study</u> samples in rack and leave samples to settle for at least 30 minutes

- Send <u>clinical</u> blood samples to the lab as per NHS Lothian guidelines

- Sub-study samples should then be spun in accordance with EMERGE SOP 002 Centrifuge
- Centrifuge all sub-study samples at **2500G for 10 minutes. Temperature setting of 4°C**
- Process sub-study samples and transfer to fridge ensuring all safety precautions are taken in accordance with NHS Lothian health and Safety policies

3.2 Processing: Sample preparation

- Wear protective gloves, apron and disposable mask/visor
- Prepare aliquot with pre-prepared POP study labels
- Aliquot samples immediately (maximum 30 minutes from end of spin). Document time into aliquot on sample processing log
- Pipette supernatant from EDTA and Serum equally into 3 separate labelled aliquots each (as below)
- Holding blood tube in one hand, pipette in the other, squeeze tip of pipette then gently insert pipette into blood tube taking care that no contact is made with the whole blood
- Gradually release pressure from the bulb of the pipette and draw the supernatant up into the pipette, then transfer the supernatant into the aliquot. Repeat equally into 3 separate aliquots for EDTA and Serum
- Once completed, discard blood tubes into sharps bin and safely dispose of used gloves, pipette and disposable mask/visor
- Label each aliquot with the pre-printed labels immediately after transfer of the supernatant. A separate label for each of the six aliquots will be available for each time-point
- Transfer samples immediately to the second shelf of the -20 EMERGE research freezer in exam as per the grid reference in the lab folder. Document time into -20 freezer on sample processing log

3.3 Transfer of Samples to QMRI/Pledpharma

- Sample will be transferred to the Queen's Medical Research Institute on dry ice for storage in research freezers (-80^{0}C)

- At the end of the study serum will be shipped for analysis of PP100-01 concentration

4. BLOOD SPILLAGES

1. All spillages should be cleaned immediately as per NHS Lothian guidelines: Accessed from: http://www.nipcm.hps.scot.nhs.uk/documents/sicp-management-of-blood-and-body-fluid-spillages-in-the-hospital-setting/

2. All patient samples should be labelled at the bedside using the patients study ID number as per NHS Lothian policy: Accessed from: http://www.edinburghlabmed.co.uk/UsingTheService/CollectingSample/Label lingSamples/Pages/default.aspx

5. DOCUMENT HISTORY

Version Number:	Effective Date:	Reason(s) for change(s):
1		New document

POP STUDY

Sub – Study Biomarker Sample processing log

Participant Number:
Date:

Blood sample Time-point	Type (EDTA or Serum)	Actual time taken	Time into centrifuge	Time aliquoted	Total number of Aliquot tubes (x3 for each blood sample)	Time into -20 Freezer		Date transferred to QMRI/Pledpharma	
2hr	EDTA						Signature		Signature
	Serum								
10hr	EDTA								
	Serum								
20hr	EDTA								
	Serum								